# Ice, Cloud, and Land Elevation Satellite 2 (ICESat-2) Project

# Algorithm Theoretical Basis Document for Precision Pointing Determination

## Version 2.0

**Prepared By:**

**Sungkoo Bae, Lori Magruder, Noah Smith, Bob Schutz**

**University of Texas Applied Research Laboratories**

**Goddard Space Flight Center**
**Greenbelt, Maryland**

**National Aeronautics and**
**Space Administration**

# Abstract

The Advanced Topographic Laser Altimetry System onboard the Ice, Cloud and Land Elevation Satellite-2 (ICESat-2) will collect measurements at 10 kHz using 6 laser beams. The geolocation knowledge requirement of ATLAS is 6.5 m on the surface, a requirement that is a combination of both the precision orbit determination and precision pointing knowledge. Pointing knowledge consists of time series of laser pointing unit vectors and their uncertainties expressed in the celestial reference frame. During processing the laser pointing vectors are expressed in the Laser Reference Sensor coordinate frame and then in the celestial frame using the estimated Laser Reference Sensor attitude. The Laser Reference Sensor is a custom instrument designed specifically for laser pointing determination and plays the central role for pointing knowledge. It simultaneously observes the altimetry lasers, stars, and reference signals, all in its own instrument coordinate frame. The star observations along with observations from the spacecraft star trackers and gyro unit are used to estimate the rotation between the Laser Reference Sensor coordinate frame and the celestial frame. Processing is similar to the original ICESat altimetry mission, which also centered on a custom Laser Reference Sensor tying laser pointing to the celestial frame.

# CM Foreword

This document is an Ice, Cloud, and Land Elevation (ICESat-2) Project Science Office controlled document. Changes to this document require prior approval of the Science Development Team ATBD Lead or designee. Proposed changes shall be submitted to the ICESat-II Management Information System (MIS) via a Signature Controlled Request (SCoRe), along with supportive material justifying the proposed change.

In this document, a requirement is identified by “shall,” a good practice by “should,” permission by “may” or “can,” expectation by “will,” and descriptive material by “is.”

Questions or comments concerning this document should be addressed to:

ICESat-2 Project Science Office
Mail Stop 615
Goddard Space Flight Center
Greenbelt, Maryland 20771

# Preface

The ICESat-2 Science Development Team, in support of the ICESat-2 Project Science Office (PSO), assumes responsibility for this document and updates it, as required, to meet the needs of the ICESat-2 SIPS. Reviews of this document are performed when appropriate and as needed updates to this document are made. Changes to this document will be made by complete revision.

Changes to this document require prior approval of the Change Authority listed on the signature page. Proposed changes shall be submitted to the ICESat-2 PSO, along with supportive material justifying the proposed change.

Questions or comments concerning this document should be addressed to:

Tom Neumann, ICESat-2 Project Scientist
Mail Stop 615
Goddard Space Flight Center
Greenbelt, Maryland 20771

# Review/Approval Page

***Prepared by:***

*Sungkoo Bae,*
*Lori Magruder,*
*Noah Smith,*
*Bob Schutz*

*Applied Research Laboratories*

## Change History Log

| Revision Level | DESCRIPTION OF CHANGE | SCoRe No. | Date Approved |
|---|---|---|---|
| 1.0 | Initial Release | | |
| 1.1 | Minor Changes | | |
| 2.0 | Added Chromatic Aberration Correction (Section 4.1.5 and Chapter 5) and Ancillary Processing (Chapter 6)<br>Moved original contents (e.g. Chapter 5 and Section 4.1.1) to Appendices | | |

# List of TBDs/TBRs

| Item No. | Location | Summary | Ind./Org. | Due Date |
|---|---|---|---|---|
| | | | | |
| | | | | |
| | | | | |
| | | | | |
| | | | | |
| | | | | |
| | | | | |
| | | | | |
| | | | | |
| | | | | |

# Table of Contents

## List of Figures

# List of Tables

# 1.0 Introduction

The Ice, Cloud and land Elevation Satellite-2 (ICESat-2) uses state of the art onboard laser altimetry technology, ATLAS (Advanced Topographic Laser Altimetry System), to make precision range measurements between the observatory and the surface of the Earth. Pointing determination provides arcsecond-level knowledge of the laser pointing direction for each laser pulse, while orbit determination provides cm-level knowledge of the observatory position in space. The pointing and orbit products are combined with the range measurements to yield the geolocation of the laser spots on the surface of the Earth to a horizontal accuracy of 6.5 meters. This document focuses on the determination of the laser pointing direction in ICRF as an ICESat-2 ground processing. The determination of the geolocation vector, which is the ultimate product of the ICESat-2 elevation product for the science, is the subsequent processing at GSFC SIPS using ICESat-2 position vector and laser range measurement as well as the laser pointing direction vector. The geolocation vector computation is briefly described in Appendix A.

The intended pointing knowledge users are the Planetary Geodynamics Laboratory and the Science Investigator-Led Processing System (SIPS) at NASA's Goddard Space Flight Center (GSFC) for incorporation into the ICESat-2 Level-2A data products. The pointing product consists of 50 Hz time series of laser pointing unit vectors and their uncertainties, expressed in the celestial reference frame for each of the ATLAS six laser beams.

The Precision Pointing Determination (PPD) process is comprised of algorithms that support several sub-systems.  These sub-systems include a Sodern Star Tracker (SST) with two optical heads mounted on the ATLAS instrument, a Scalable Space Inertial Reference Unit (SIRU) and a Laser Reference System (LRS) with two opposing optical axes with back to back focal planes (stellar-side and laser-side) as shown in Figure 1: one tracking stars near the zenith, and one tracking laser and reference spots near the nadir. Ideally, the LRS has a single coordinate frame for the two fields of view. The physical joint between the star and laser sides is designed to be stable and the two coordinate frames are ideally equivalent to a single LRS frame, but pointing determination accounts for the possibility of relative motion.

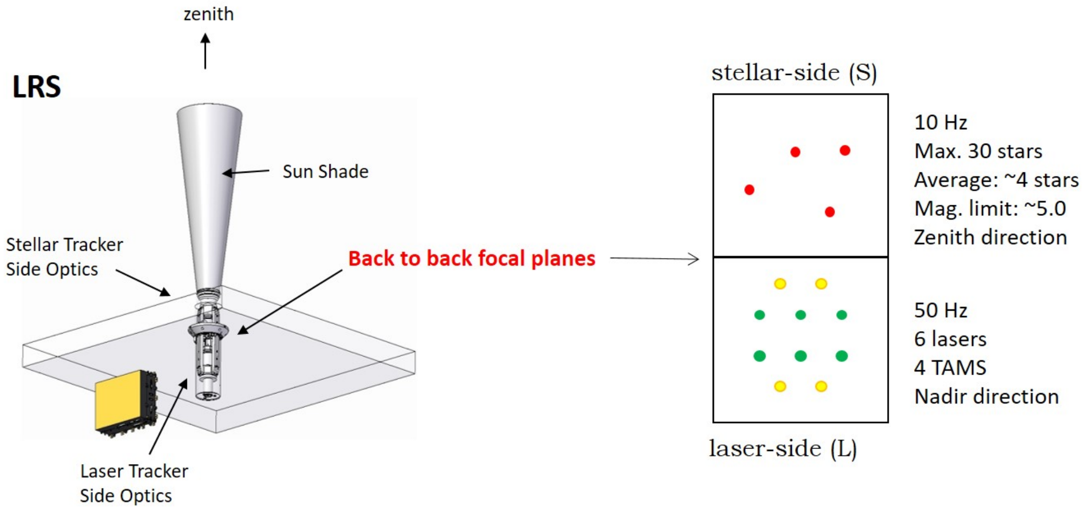

**Fig. 1 LRS**

The transformation of the pointing vectors from the LRS coordinate frame to the celestial reference frame (CRF) relies on the the observatory precision attitude determination (PAD). The PAD solution will use the data streams from the SIRU, the SST and the LRS (stellar-side) in a~~n~~ Kalman Filter process. The LRS stellar-side will provide the input to the PAD process as the primary star tracker. The two SST optical heads are designed for real-time attitude determination for on-board attitude control, but will provide quaternion observations to the PAD algorithm, as additional attitude input specifically during times when the LRS stellar-side experiences solar blinding. The SIRU provides angle data to calculate the body rates, a critical component of propagating the attitude solution between the other instrument measurements.

The estimated uncertainties of the laser pointing vectors are important for downstream processing, particularly calculation of geolocation uncertainties. The empirical information about pointing uncertainties due to high frequency motion will be realized by the SIRU output, which is recorded at 50 Hz and provides more bandwidth than the 10 Hz LRS and SST attitude observations. The SIRU is also used to propage the pointing vector estimates to the 50 Hz rate required in the pointing product.

One significant source of error in ICESat-2 PPD is a chromatic aberration in the LRS stellar-side which distorts the radial position of the star observation on the focal plane and significantly impacts the ability to locate star positions accurately. The radial distortion depends on the wavelength of the starlight or star color. As such, in addition to the algorithm describe herein for PAD, is the approach to mitigate the impact of the LRS chromatic aberration on the final PPD product.

Overall the pointing and attitude determination algorithms are similar to those used in on the original ICESat algorithms, which also centered on an Laser Reference Sensor to transform the laser pointing determination to the celestial reference frame (Take note of the 'Sensor' versus 'System'). The ICESat heritage means that many pointing methods are mature and that their complexities are understood. The algorithms for the ICESat-2 ATLAS LRS attitude estimation carry over directly from the ICESat LRS, although the presence of the chromatic aberration will require an additional step within the software architecture which may not be finalized until on orbit data is available. As such, the most specific questions for ATLAS pointing determination and implementation are related to the unique characteristics of the sensors, and the color correction required for the LRS stellar-side measurements.

Verification and quality measures for the pointing product are based on LRS star residuals and ocean scan altimetry range residuals. LRS attitude estimates are equivalent to predictions of the LRS star observations, and the observed minus predicted residuals reflect the attitude estimate accuracy. Ocean scan residuals reflect the accuracy of the estimated laser pointing vectors. Given accurate LRS attitude estimates, biases in the ocean scan residuals reflect biases in the measurement model used to express laser observations in the LRS coordinate frame. Pointing quality is also assessed using cross-over analysis or verified with other validation methodologies.

# 2.0 Overview

The pointing algorithm uses the LRS observations with support from the SSTs and SIRU to determine the pointing of the altimetry laser. The primary sensors used for the PPD are illustrated in Figure 2. The LRS is a custom instrument designed specifically for laser pointing determination of the ICESat-2 and plays the central role in pointing knowledge. It simultaneously observes the altimetry lasers, stars, and reference signals, all in the LRS coordinate frame. The star observations, along with the SST attitude observations, are used to estimate the rotation between the LRS coordinate frame and the ICRF.

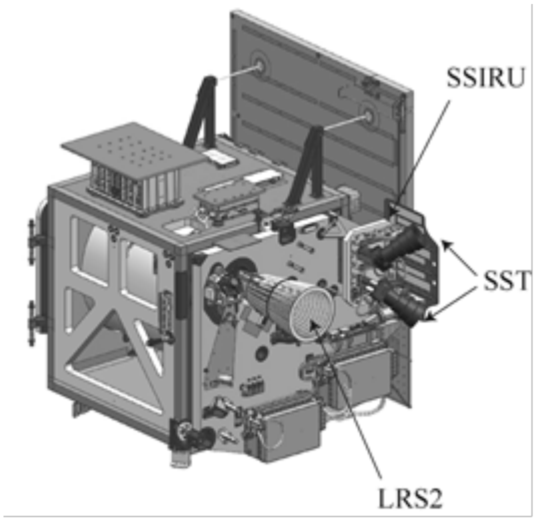

**Fig. 2 PPD Sensors in ATLAS**

The processor is a filter moving sequentially forward in time through the input observations. A propagation and update cycle is performed for each incoming observation and the sensors can be roughly divided into two groups corresponding to cycle phase and measurement type. The LRS (stellar side) and SSTs make 10 Hz vector observations and are used for measurement updates, which generally tend to decrease pointing uncertainty. The SIRU provides the 50 Hz angle and inferred-rate observations and is used for propagation, which tends to increase pointing uncertainty. The LRS (laser-side) provides the pointing vectors of each of the six beams at 50 Hz, similar to the SIRU.

One question concerns the LRS measurement model for interpreting the observations of the lasers and reference signal spots as three-dimensional unit vectors in the LRS coordinate frame. This geometric transformation from two-dimensional image measurements to three-dimensional unit vectors requires calibration, preferably repeatedly throughout the mission. The design of the LRS originally aimed to observe the star and laser in a single body (or single coordinate frame) with the assumption of the rigidity between two sides, however, the alignment variation between two sides is expected during the mission, even during an orbit. The LRS coordinate frame is officially defined by the LRS laser tracker (or laser-side) frame (LT) to make it close to the ATLAS coordinate frame defined in the ICESat-2 Coordinate System Documents [1]. The difference between ATLAS frame and LRS frame is discussed in Section 4.3.1. The LRS stellar-side observes stars in its own star tracker (or stellar-side) frame (ST). Alignment variations between the stellar-side and laser-side are difficult to observe directly, but the effects are corrected with information from ocean scan calibrations.

The star observations themselves are a significant question. The catalog of predicted star observations for the LRS indicates that there are regions of the sky where LRS stars will be sparse. Figure 3 illustrates a number of stars in the field of view (FOV) viewed by LRS across full sky, shown as right ascension (RA) and declination of simulated ICESat-2 with magnitude cut at 5.0. ICESat LRS star observations were inherently sparse and heritage algorithms for incorporating observations from other star trackers based on their time-varying relative alignments carry over here. In actuality, the sparse star situation is less impactful than the LRS chromatic aberration phenomenon which remains one of the primary PPD related risks in the mission. This LRS stellar-side chromatic aberration causes a radial distortion of the star observation on the focal plane, dependent on the wavelength of the star color, or color index. The developers of the LRS have provided a color correction formula that utilizes the color index of each star in the LRS star catalog to remove the position error. This dedicated color correction plan will use an interlaced batch least squares approach to estimate an adjusted optical center, focal length and coefficients to produce a corrected PAD solution.

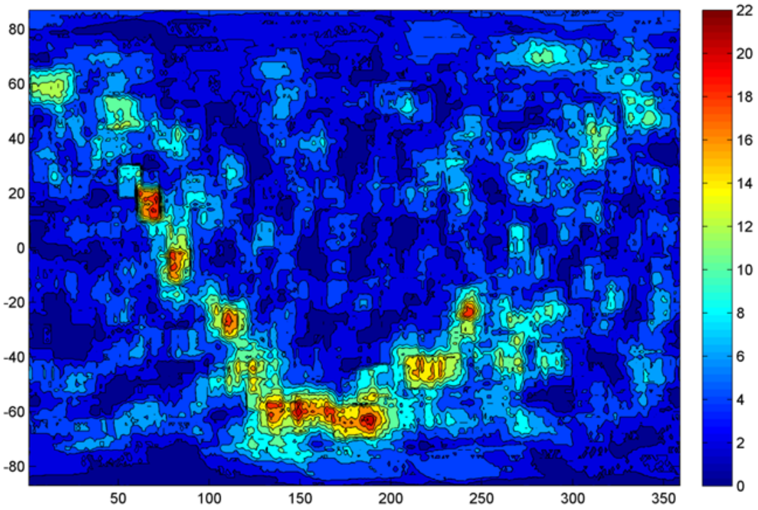

**Fig. 3 Number of stars views by LRS across the whole sky**

Fully utilizing the SIRU is another question. The 50 Hz telemetry from the SIRU and the LRS laser-side are monitored in both the time and frequency domains for evidence of high frequency pointing variations. Correlations with entering and exiting eclipse, solar panel motion, maneuvers, and other changes of state are of particular interest.

## 2.1 Telemetry

Telemetry is received as HDF5 data files containing 10 Hz star telemetry from the LRS stellar-side and SSTs, 50 Hz laser measurements from the LRS laser-side, and 50 Hz sense-axes angular increment measurements from the SIRU. Supporting inputs from telemetry concern the spacecraft state including position and velocity, onboard attitude estimates, solar array motion,–the housekeeping information such as temperature, and the laser/star images by request for the analysis purpose. These data are packaged as ATL02, a Level 1B product that contains science unit converted telemetry. ATL02 is provided at a frequency of 10 times per orbit for 16 orbits a day. The total data volume for ATL02 is estimated to be140 GB/ day, but PPD does not require the complete product.

The term star telemetry is used here for all telemetry entering the processor as measurement updates to determinethe propagation time intervals and filter cycle boundaries. It is a generic term for 10 Hz star measurements from the LRS and 10 Hz attitude estimates from the SSTs (which are based on SST star measurements). The data from the two SST are an attitude estimate used to support the PAD determination from the LRS star tracker.

The processor can be viewed as treating the SSTs as support components for the LRS stellar-side. Each SST is a black box that outputs an attitude estimate. The processor filter states represent the time-varying alignment rotations between the SSTs and the LRS star tracker, in effect joining the SSTs with the LRS by tracking the alignment rotations and replacing physical joints with a software model of the physical geometry. This parallels the way two trackers are physically joined in the LRS to form a single LRS frame.

Laser telemetry is received from the LRS laser-side, which measures laser and reference spot centroids at 50 Hz. The laser spots represent the directions of the lasers in the laser-side coordinate frame. The directions in the LRS frame are then known, assuming that the alignment between the LRS star and laser sides is known.

Gyro telemetry is received from the SIRU and used for propagation between measurement updates. The SIRU is a gyro unit and measures angular increments about its four sense axes. It provides greater angular resolution over short time scales and more information bandwidth than the 10 Hz star telemetry. It consists of four hemispherical resonator gyros arranged with their axes forming an octahedral tetrad pyramid shape. The gyros are of the rate integrating type, outputting an angle expressed as an integer count which wraps as the output register overflows or underflows. One count is equal to 0.05 arcseconds. The overall unit is effectively a black box with four output registers that are updated at 100 Hz, one for each sense axis. The spacecraft records the values in the output registers asynchronously at 50 Hz.

Once the ATL02 data are received from GSFC, the pre-processing algorithms will evaluate the quality of the input data and identify any anomalies.  Once the quality is verified the data will be reformatted and directed to further PPD and PAD processing. The output telemetry, 50 Hz time series of laser pointing vectors in CRF, is packaged in an ancillary product, ANC05, that will be used within the geolocation process for ATL03, a Level 2A product that provides global geolocation estimates for every photon detected.

## 2.2 Measurement and Error Models

Measurement and error models are the equations and parameters necessary for using the LRS, SST, and SIRU telemetry within the processor. Generally, measurement models are deterministic terms for transforming and interpreting the sensor measurements and error models are stochastic terms involving random processes and uncertainties.Initial parameter estimates for the models come from ground testing. The overall pointing knowledge process emphasizes updating both the models and parameter estimates during the mission based on flight data. These updates are shared and documented where possible. Experience with ICESat indicates that problems can arise when the links between telemetry and measurement models become ambiguous or confused.

The key LRS measurements are two-dimensional positions expressed in pixels. The measurement model converts these pixel coordinates to three-dimensional unit vectors in the LRS coordinate frame. For the stellar-side, another measurement model converts brightness counts to instrument magnitudes. The laser-side models have to include the laser to stellar side alignment. This model is complicated by the LRS stellar-side chromatic aberration as the pixel conversion will require a more expansive approach to correct for this distortion.

Because the SSTs provide attitude solutions as quaternions by internally processing star measurements, their measurement models reduce to alignment rotations that relate the telemetered attitude estimates to the LRS frame. The processor tracks these alignment rotations and SST error modeling involves parameter estimation for the alignment process noise in addition to the uncertainties in the telemetered attitude estimates.

The SIRU measurement model combines angular increments from four sense axes and transforms them into a three-dimensional angular rate vector for the SIRU frame. Angular rate is simply calculated as angular increment per unit of time. The SIRU measurement model includes calibration parameters for each sense axis: geometric misalignment from the ideal octahedral tetrad, bias, and scale factors of various types.

SIRU error modeling represents the growth of attitude uncertainty during the propagation phase of the filter cycle. Gyro modeling can be complex but reduces here to three stochastic processes generically referred to as angular random walk (ARW), rate random walk (RRW), and angle white noise (AWN). ARW and AWN are linked to uncertainties over short time scales and can be referred to as noise. RRW is linked to uncertainties over long time scales and can be referred to as bias instability and associated with gyro drift.

## 2.3 Mission Star Catalog

Before the LRS stellar-side data is ingested into the EKF for attitude determination, the observed stars will be linked to an established mission star catalog to interpret the LRS star telemetry and provide reference parameters. Essentially, the catalog is used to identify the stars' associated reference unit vectors in the celestial frame for comparison to the LRS star measurements. Errors in the catalog can cause direct errors in the derived pointing products, so it is important to create a mission catalog of position and magnitude parameters based on analysis of the astronomical star catalogs and ground testing of the LRS.

Stars with measurements that are biased relative to the catalog reference parameters are referred to here as bad stars. The biases can be in position and/or brightness but clearly, the position is the primary concern. Adaptive checks within the filter are used to detect and reject bad stars by comparing the filter predictions and observations before they are used to perform a measurement update, but cases where the measurement bias is near the noise level require large samples to detect and characterize.

The mission catalog is intended to correct for measurement biases wherever possible by providing what is referred to as blended or center of light reference parameters. The catalog positions and instrument magnitudes are predictions of what the LRS actually observes on the sky. For a bad star with a small LRS position measurement bias, the mission catalog record should be corrected as soon as practical to either negate the bias or to flag the star for automatic rejection. The approach to updating the mission star catalog based on the analysis of the measured centroids from the star tracker (i.e., LRS stellar-side) is discussed in Appendix C.

Mission catalog position and magnitude parameters are initially based on analysis of the astronomical star catalogs and ground testing of the LRS. During the mission, the observed minus predicted filter residuals are stored and analyzed in order to improve the catalog records over time. Catalog information comes primarily from the LRS star catalog, Hipparcos catalog, SKY2000 star catalog [2-8]

Ancillary inputs from sources outside the mission are ephemerides for the sun, moon, Earth inertial velocity, fundamental star catalogs (Hipparcos, SKY2000), and luni-solar-planetary ephemerides (DE405 or later version).

## 2.4 Processor and Products

The primary path within the PPD workflow/processor involves cycling sequentially forward in time through the telemetry with a Kalman filter.. Star telemetry determines the cycle boundaries. When a new LRS star measurement or SST attitude estimate is received, a measurement update is performed to incorporate the new information into the filter state. Between updates, the SIRU is used to propagate the filter state forward in time. The conceptual discussion here focuses on the LRS and filter updates.

The combined filter states represent attitude estimates for the LRS and SSTs, along with a correction to the angular rate. The filter also maintains a representation of the uncertainties in the states. The attitude estimates are equivalent to predictions of the star telemetry. The observed minus predicted residuals are used to update the states and uncertainties.

The states represent three attitude estimates but only one is explicit. The other two combine the explicit attitude estimate with alignment estimates. The explicit attitude estimate is often identified with a generic coordinate frame referred to as the body frame. In practice, the body frame can be associated with the LRS frame, an SST, the SIRU, or a combination of several sensor coordinate frames.

The attitude of the LRS coordinate frame is of central importance for the overall pointing product. For the discussion here, the body frame is identified with the LRS coordinate frame unless stated otherwise. The attitude estimates for the SSTs are a combination of the body frame attitude estimate and SST alignment estimates. Other modes of defining and arranging the filter state are possible but are considered contingencies to the primary method.

The pointing products are 50 Hz time series of laser unit vectors and their uncertainties expressed in the celestial frame for each of the six beams. The vectors have two degrees of freedom because of the unit constraint and can be represented by two coordinates. The LRS frame orientation relative to the celestial frame is given by its estimated attitude and alignment correction between the laser-side and stellar-side. A three-dimensional laser unit vector is specified by two coordinates in the LRS frame and then expressed by extension in the celestial frame.

The 50 Hz pointing product time tags correspond to the LRS laser telemetry time tags. In other words, the laser telemetry time tags are the set of times at which the processor needs to estimate the laser unit vectors and uncertainties. The six pointing vectors are the means or first moments of six laser pointing probability distributions which represent the overall pointing knowledge. The

Kalman filter which makes up the main path of the processor models the pointing probability distributions using first and second moments alone. An important question is whether the filter error covariance matrix adequately describes the pointing probability distributions and true laser pointing uncertainties. The pointing vector estimates may be relatively straightforward compared to their uncertainties.Concepts and definitions for describing pointing uncertainty are adopted here from a sequence of papers on the topic [9-11]. Pointing uncertainty is defined for a specified length of time, generally, the time needed for a sensor to make its observation. For an imager the length of time is the exposure or integration time.

For laser pointing knowledge the most significant timescales are a more complex question. The 20 millisecond time scale of the 50 Hz pointing product is adopted here by convention. This is a relatively small time scale and tends to make the question of jitter more significant for pointing uncertainty.The term jitter has a very specific meaning, "motion occurring during an image exposure of specified duration" [10] or "line-of-sight motion within a time interval" [11]. It is rigorously defined as jitter variance, one of two components in the overall variance, along with the variance of the mean. For the pointing product, the estimated pointing vectors are the mean. At longer time scales the variance of the mean becomes smaller and the jitter variance becomes larger which agrees with intuition: the more time and observations available, the more certain the mean value becomes. This is related to the concept of the variance of the sample mean, where the variance for a sample size of $n$ decreases by $1/n$ .

# 3.0 Theory

The theoretical solutions for ICESat-2 PPD are focused on estimation of attitude, instrument alignments, laser pointing, and broader topics related to signal processing. This section begins with a general overview of processor parameters and continues with the analytic theory underlying the processor. Dynamics and dynamical modeling do not play a major role and, in particular, no attempt is made to model the torques and structural dynamics that cause laser pointing variations.

## 3.1 Parameter Overview

The model parameters correspond to the telemetry and phases of the processor filter cycle. The 10 Hz telemetry (LRS stellar-side and SSTs) contributes to the filter measurement updates and the filter propagation process utilizes the 50 Hz telemetry (gyro and LRS laser-side).

The sources of uncertainty that are explicitly modeled from the gyro are the Angular Random Walk (ARW), Angular White Noise (AWN), Rate Random Walk (RRW). The LRS measurement uncertainty, SST attitude uncertainty, and LRS to SST alignment uncertainty are also modeled. Gyro and alignment uncertainties enter the filter as process noise during propagation. LRS and SST uncertainties enter the filter as measurement noise during measurement updates. These sources, particularly gyro ARW and LRS measurement uncertainty, determine the filter model for pointing knowledge uncertainties.

The key sensor telemetry elements and model parameters to this effort are summarized below in Table 1.

**Table 1 Overview of telemetry and model parameters**

| | 10 Hz Star | | 50 Hz Gyro | 50 Hz Laser |
|---|---|---|---|---|
| | LRS Stellar-Side | SSTs | | |
| Telemetry | $x, y$ star centroid detector coordinates, pixels<br>$b$ star brightness, counts | $\mathbf{A}_i^{SST1}, \mathbf{A}_i^{SST2}$ attitude estimates | $\boldsymbol{\theta}_s(t_k)$ sense axes angle increment counts, 0.05 arcseconds/count | $x, y$ laser spot centroid detector coordinates, pixels |
| Deterministic measurement model parameters | $\mathbf{A}_b^{ST}$ alignment rotation from body frame<br>$\mathbf{p}_1$ parameters to convert centroids to unit vectors<br>$\mathbf{u}_1 = \mathbf{f}_1(x, y, \mathbf{p}_1)$<br>$\mathbf{p}_2$ parameters to correct unit vectors<br>$\mathbf{u}_2 = \mathbf{f}_2(\mathbf{u}_1, \mathbf{p}_2)$<br>$\mathbf{p}_{ref}$ mission star catalog reference parameters for stars | $\mathbf{A}_b^{SST1}, \mathbf{A}_b^{SST2}$ alignment rotations from body frame | $\mathbf{A}_b^{SIRU}$ gyro unit alignment rotation from body frame<br>$\boldsymbol{\omega}_s(t_k) = \mathbf{f}(\Delta\boldsymbol{\theta}_s(t_k))$ sense axes angular rates, radians/second<br>$\mathbf{b}(t)$ gyro rate bias expressed in body frame, radians/second<br>$\boldsymbol{\Lambda}$ sense axes scale factors<br>$\mathbf{W}$ sense axes ideal geometry<br>$\mathbf{U}, \mathbf{V}, \boldsymbol{\Delta}_u, \boldsymbol{\Delta}_v$ sense axes misalignments | $\mathbf{A}_{LT}^{ST}$ alignment rotation from LRS laser-side frame to LRS stellar-side frame<br>$\mathbf{p}_{LT}$ parameters to convert centroids to unit vectors<br>$\mathbf{u}_{LT} = \mathbf{f}_{LT}(x, y, \mathbf{p}_{LT})$ |
| Stochastic error model parameters | $\sigma_u^2(b)$ measurement noise variance as a function of star brightness<br>$\sigma_{ST}^2$ alignment rotation process noise, radians$^2$/second | $\mathbf{R}_{SST1}, \mathbf{R}_{SST2}$ uncertainty or effective noise in the attitude estimates<br>$\sigma_{SST1}^2, \sigma_{SST2}^2$ alignment rotation process noise, radians$^2$/second | $\sigma_{awn}^2$ angular white noise variance, radians$^2$<br>$\sigma_{arw}^2$ angular random walk variance, radians$^2$/second<br>$\sigma_{rrw}^2$ rate random walk variance, (radians/second)$^2$/second | $\mathbf{R}_{LT}$ uncertainty of the alignment rotation from LRS stellar-side frame to LRS laser-side frame, radians$^2$<br>$\sigma_{LT}^2$ measurement noise variance, radians$^2$ |

### 3.1.1 Star Model Parameters

These parameters characterize the relevant coordinate frames and telemetry of the three star trackers. A fourth abstract body frame is included in the description. Ideally, the body frame is identified with a stable reference structure such as the Instrument Mounted Spacecraft Component (IMSC). In the case of ICESat-2, one of the tracker frames plays the role of the body frame but it is useful, in practice, to keep the description general.

The three tracker coordinate frames are represented as reference alignment rotations from the body frame $\mathbf{A}_b^{ST}$ , $\mathbf{A}_b^{SST1}$, and $\mathbf{A}_b^{SST2}$. Alignment variations are characterized by the alignment process noises $s_{ST}^{2}$, $s_{SST1}^{2}$, and $s_{SST2}^{2}$ (radians²/second) describing the growth of alignment uncertainty over time. If an alignment has a significant orbital variation its process noise value reflects its magnitude. Any of the tracker frames can be effectively defined as the body frame by assuming that its alignment is constant and that its alignment uncertainty and process noise are zero.Alignment rotations and process noises are effectively the measurement and error models for the SSTs. They are the parameters needed by the processor in order to utilize the SST telemetry.

The LRS stellar-side model is more complex than the SSTs. The simplest possible model converts two-dimensional focal plane positions $x, y$ to three-dimensional unit vectors $\mathbf{u}_1 = \mathbf{f}_1(x, y, \mathbf{p}_1)$ in the LRS stellar-side coordinate frame based on a first-order geometric model (pinhole camera model). The model parameter vector $\mathbf{p}_1$ would contain only one component (the effective focal length) for a true pinhole camera model.- LRS ground calibration provides a quadratic model with multiple components in $\mathbf{p}_1$ which can be used for a more realistic case

Deterministic corrections (for distortion, centroiding errors, aberration, etc.) are included via a second model $\mathbf{u}_2 = \mathbf{f}_2(\mathbf{u}_1, \mathbf{p}_2)$ with parameter vector $\mathbf{p}_2$ . The error model is summarized by $\mathbf{u} = \mathbf{h} + \boldsymbol{\eta}$ where $\mathbf{u}$ is the observed unit vector, $\mathbf{h}$ is the true unit vector, and $\boldsymbol{\eta}$ is zero-mean Gaussian white noise $E\{\boldsymbol{\eta}^T \boldsymbol{\eta}\} = \sigma_u^2 \mathbf{I}$.

Three-dimensional unit vectors $\mathbf{u} = [u_1 \quad u_2 \quad u_3]^T$ are usually represented using $\mathbf{u}_{obs} = [u_{obs,1} \quad u_{obs,2} \quad u_{obs,3}]^T = [h_{obs} \quad v_{obs}]^T$ coordinates in an $\mathbf{ijk}$ tracker frame, where the tracker LOS is the $\mathbf{k}$ axis. Angles $\theta_h$ and $\theta_v$ are defined from the $\mathbf{k}$ axis towards the $\mathbf{i}$ and $\mathbf{j}$ axes. An intermediate vector $\mathbf{u}' = [h \quad v \quad 1]^T$ is defined using $h, v$ coordinates

$$h \equiv \tan \theta_h = u_1 / u_3 \qquad (3.1.1)$$

$$v \equiv \tan \theta_v = u_2 / u_3 \qquad (3.1.2)$$

and $\mathbf{u}$ is the normalized version of $\mathbf{u}'$

$$\mathbf{u} = \begin{bmatrix} h & v & 1 \end{bmatrix}^T \Big/ \left(h^2 + v^2 + 1\right)^{1/2} \qquad (3.1.3)$$

Near the $\mathbf{k}$ axis $h \equiv \tan\theta_h \cong \theta_h$ and $v \equiv \tan\theta_v \cong \theta_v$.

### 3.1.2 Gyro Model Parameters

The four gyro unit sense axes are rate-integrating gyros outputting angular counts $\boldsymbol{\theta}_s(t_k)$, with units of 0.05 arcseconds per count. Angular rates about each sense axis $\boldsymbol{\omega}_s(t_k) = \mathbf{f}(\boldsymbol{\theta}_s(t_k))$ are calculated as observed angular change per unit time. The measurement model parameters describe deterministic effects that are specific to each sense axis. With four sense axes, there are four instances of each type of parameter collected into a parameter vector.

The gyro rate bias vector $\mathbf{b}$ represents the observed rate when the true rate is zero. This is a highly variable parameter. It is always estimated as a time-varying quantity if possible and is therefore always a member of the filter state. It absorbs the effects of multiple sources of error, most notably the alignment between the gyro unit frame and body frame. In effect, the filter estimate of $\mathbf{b}(t)$ includes the effects of alignment variations for the gyro unit as a whole. Note that the components of $\mathbf{b}(t)$ are therefore in practice not strictly mapped one-for-one to the four sense axes.

Variations of $\mathbf{b}(t)$ are referred to as bias instability. Bias instability and gyro drift are closely associated concepts. In general, they are a concern at longer time scales, whereas the concern over shorter time scales is the gyro noise. The effects of gyro drift and bias instability are minimized with measurement updates to the attitude estimation and $\mathbf{b}(t)$ using star telemetry from at least one of the three star trackers. The SSTs are designed not to be simultaneously blinded during normal or near-normal operations.

The rate scale factor vector $\boldsymbol{\lambda}$ represents the scaling between the observed and true rate. A linear scaling factor is often used but more sophisticated models (e.g. asymmetric scaling) are possible. Geometric misalignment vectors $\mathbf{u}, \mathbf{v}$ are used to correct for rate errors introduced when the sense axes do not form a perfect octahedral tetrad pyramid shape. The measurement model combines the four observed sense axes rates using a linear geometric transformation. The misalignments $\mathbf{u}, \mathbf{v}$ describe the deviations of the sense axes away from their ideal directions as two-component rotation vectors, expressed in the plane orthogonal to the ideal direction. Methods have been established for defining the necessary sense axis coordinate frames [12-15].

The basic measurement model for the estimated angular rate $\hat{\boldsymbol{\omega}}(t)$ expressed in the body frame is given by

$$\hat{\boldsymbol{\omega}}(t) = (\mathbf{A}_b^{SIRU})^T \boldsymbol{\omega}_{SIRU}(t) + \hat{\mathbf{b}}(t) \qquad (3.1.4)$$

where the estimate $\hat{\mathbf{b}}(t)$ comes from the filter state and $\mathbf{A}_b^{SIRU}$ is a constant reference alignment rotation from the gyro unit frame to the body frame. Effects from variations in this alignment rotation are absorbed in $\hat{\mathbf{b}}(t)$. The observed gyro unit rate $\boldsymbol{\omega}_{SIRU}(t)$ expressed in the gyro unit frame is given by

$$\mathbf{G}_{4\times 3}\boldsymbol{\omega}_{SIRU}(t) = \boldsymbol{\omega}_s(t) \qquad (3.1.5)$$

where $\mathbf{G}$ is a $4\times 3$ matrix relating the four sense axes rates $\boldsymbol{\omega}_s(t)$ to $\boldsymbol{\omega}_{SIRU}(t)$ using the model parameters for misalighnment and scale factor. In practice $\boldsymbol{\omega}_{SIRU}(t)$ is calculated using the pseudo-inverse of $\mathbf{G}$

$$\boldsymbol{\omega}_{SIRU}(t) = (\mathbf{G}^T\mathbf{G})^{-1}\mathbf{G}^T\boldsymbol{\omega}_s(t) \qquad (3.1.6)$$

$$\mathbf{G} = (\mathbf{I} - \boldsymbol{\Lambda})(\mathbf{W} - \mathbf{U}\boldsymbol{\Delta}_{\mathbf{v}} - \mathbf{V}\boldsymbol{\Delta}_{\mathbf{u}})^T \qquad (3.1.7)$$

where $\boldsymbol{\Lambda} \equiv diag(\boldsymbol{\lambda})$, $\boldsymbol{\Delta}_{\mathbf{u}} \equiv diag(\mathbf{u})$, and $\boldsymbol{\Delta}_{\mathbf{v}} \equiv diag(\mathbf{v})$. The ideal sense axes directions expressed in the gyro unit frame are the columns of $\mathbf{W}_{3\times 4}$.

The error model characterizes uncertainties expressed in the gyro unit frame. It represents the growth of attitude uncertainty during the propagation phase of the filter cycle. The error model parameters are associated with three stochastic processes. Angular white noise (AWN) variance $\sigma_{awn}^2$ is simple noise and has units of radians$^2$. Angular random walk (ARW) variance $\sigma_{arw}^2$ is linked to uncertainties over short timescales. It describes the process noise for the angular output of the gyro unit (or ideally a sense axis) and has units of radians$^2$/second. Rate random walk (RRW) variance $\sigma_{rrw}^2$ describes the process noise for the angular rate observed by the gyro unit (or sense axis). It has units of (radians/second)$^2$/second.

The error model parameters appear in the filter as process noise. As discussed in following sections, the discrete time process noise matrix block associated with the attitude and gyro rate bias estimates is given by

$$\mathbf{Q}_k(t) = \begin{bmatrix} (\sigma_{awn}^2 + t\sigma_{arw}^2 + (t^3/3)\sigma_{rrw}^2)\mathbf{I} & (t^2/2)\sigma_{rrw}^2\mathbf{I} \\ (t^2/2)\sigma_{rrw}^2\mathbf{I} & t\sigma_{rrw}^2\mathbf{I} \end{bmatrix} \tag{3.1.8}$$

It is useful to note that RRW is associated with uncertainties over longer timescales. In fact, the filter uses $\sigma_{rrw}^2$ to model bias instability and the variations of $\mathbf{b}(t)$. The link between $\sigma_{rrw}^2$ and $\mathbf{b}(t)$ is apparent from their units.

### 3.1.3 Laser Model Parameters

The LRS laser tracker observes six laser centroids at a measurement rate of 50 Hz. The measurement model converts the centroids $x_1, x_2$ to unit vectors $\mathbf{u}_{LT}$ in the laser-side coordinate frame. LRS ground calibration provides a quadratic model $\mathbf{u}_{LT} = \mathbf{f}_{LT}(x, y, \mathbf{p}_{LT})$ with parameters $\mathbf{p}_{LT}$. The alignment rotation $\mathbf{A}_{LT}^{ST}$ from LRS stellar-side frame to the laser-side frame is used to express the laser unit vectors $\mathbf{u}_{LT}$ in the star tracker frame and eventually in the ICRF.

The error model represents the uncertainty of the laser directions in the LRS laser-side frame. The uncertainties in the $\mathbf{u}_{LT}$ are characterized by the measurement noise variance $\sigma_{LT}^2$, radians$^2$. The uncertainty in the alignment $\mathbf{A}_{LT}^{ST}$ is the covariance matrix $\mathbf{R}_{LT}$, radians$^2$.

## 3.2 Attitude Filter

The filter is based on a standard attitude filter, referred to by reference [16] as the Multiplicative Extended Kalman Filter (MEKF). The description given here follows references [16] and [17].

Two central MEKF components are the reference attitude quaternion $q_{ref}(t)$, $|q_{ref}(t)| = 1$, and the attitude error quaternion $q(\mathbf{a}(t))$, where $\mathbf{a}(t)$ is a rotation vector and $q(\mathbf{a}(t))$ is a unit-norm quaternion function of the rotation vector. We also define $a \equiv |\mathbf{a}|$. The MEKF performs unconstrained estimation of the rotation vector $\hat{\mathbf{a}}(t)$ during each measurement update phase while maintaining the overall attitude estimate in the constrained (unit-norm) nonsingular reference attitude quaternion $q_{ref}(t)$. The true attitude $q(t)$ is represented as the product

$$q(t) = q(\mathbf{a}(t)) \otimes q_{ref}(t) \tag{3.2.1}$$

The covariance of $\mathbf{a}(t)$ is the covariance of the attitude error in the body frame. The multiplication in Eq. (3.2.1) is the reason for the term Multiplicative EKF. In the standard EKF, the true state $\mathbf{X}$ is represented as the sum of a reference state $\mathbf{X}_{ref}$ and a small error $\mathbf{x}$

$$\mathbf{X} = \mathbf{x} + \mathbf{X}_{ref} \tag{3.2.2}$$

Equation (3.2.1) for the MEKF corresponds directly to Eq. (3.2.2) for the EKF when $q(\mathbf{a}) \cong [\mathbf{a}^T/2 \quad 1]^T$.

The MEKF cycle has three phases: propagation, measurement update, and reset. Reference [16] discusses the relationship between Eq. (3.2.1) and the MEKF reset phase. An analogous EKF reset phase associated with Eq. (3.2.2) is normally absorbed and implicit within the EKF measurement update phase. Before reset $q_{ref}(t)$ is the prior (predicted) estimate $q_{ref}(-)$ of the attitude. After reset $q_{ref}(t)$ is the posterior (updated) estimate. The propagation phase inherently maintains $\hat{\mathbf{a}}(t) = \mathbf{0}$. The measurement update phase assigns a finite value $\hat{\mathbf{a}}(+)$ at $\hat{\mathbf{a}}(t)$ while the reference quaternion retains its pre-update value $q_{ref}(-)$. The update information is moved from $\hat{\mathbf{a}}(+)$ to a post-update reference $q_{ref}(+)$ and $\hat{\mathbf{a}}(t)$ is reset to zero

$$q(\hat{\mathbf{a}}(+)) \otimes q_{ref}(-) = q(\mathbf{0}) \otimes q_{ref}(+) = q_{ref}(+) \tag{3.2.3}$$

The attitude error quaternion $q(\mathbf{a}(t))$ is calculated from the attitude error rotation vector $\mathbf{a}$ as

$$q(\mathbf{a}) = \begin{bmatrix} (\mathbf{a}/a)\sin(a/2) \\ \cos(a/2) \end{bmatrix} \tag{3.2.4}$$

or the second-order approximation

$$q(\mathbf{a}) \approx \begin{bmatrix} \mathbf{a}/2 \\ 1 - a^2/8 \end{bmatrix} \tag{3.2.5}$$

The equivalent attitude error rotation matrix is

$$\mathbf{A}(\mathbf{a}) \approx \mathbf{I}_{3\times3} - [\mathbf{a}\times] - (a^2\mathbf{I}_{3\times3} - \mathbf{a}\mathbf{a}^{\mathrm{T}})/2 \tag{3.2.6}$$

where $[\mathbf{a}\times]\mathbf{b} \equiv \mathbf{a} \times \mathbf{b}$. In practice $q(\mathbf{a})$ is normalized to ensure it is a unit quaternion, and the attitude error rotation matrix $\mathbf{A}$ can be computed from $q(\mathbf{a})$ to ensure it is orthonormal.

### 3.2.1 Attitude and State Propagation

The angular rate and kinematics of the reference attitude $q_{ref}$ are represented by $\boldsymbol{\omega}_{ref}$ and

$$\frac{d}{dt}q_{ref} = \frac{1}{2}\begin{bmatrix} \boldsymbol{\omega}_{ref} \\ 0 \end{bmatrix} \otimes q_{ref} \tag{3.2.7}$$

$\boldsymbol{\omega}_{ref}$ is determined by the requirements that $\hat{\mathbf{a}} = \mathbf{0}$, so that $q_{ref}$ is the optimal attitude estimate. Taking the time derivative of Eq. (3.2.1) and using Eq. (3.2.7)

$$\frac{1}{2}\begin{bmatrix} \boldsymbol{\omega} \\ 0 \end{bmatrix} \otimes q = \frac{d}{dt}q(\mathbf{a}) \otimes q_{ref} + q(\mathbf{a}) \otimes \frac{1}{2}\begin{bmatrix} \boldsymbol{\omega}_{ref} \\ 0 \end{bmatrix} \otimes q_{ref} \tag{3.2.8}$$

$$\left(\frac{1}{2}\begin{bmatrix} \boldsymbol{\omega} \\ 0 \end{bmatrix} \otimes q(\mathbf{a}) \otimes q_{ref}\right) \otimes q_{ref}^{-1} = \left(\frac{d}{dt}q(\mathbf{a}) \otimes q_{ref} + q(\mathbf{a}) \otimes \frac{1}{2}\begin{bmatrix} \boldsymbol{\omega}_{ref} \\ 0 \end{bmatrix} \otimes q_{ref}\right) \otimes q_{ref}^{-1} \tag{3.2.9}$$

$$2\frac{d}{dt}q(\mathbf{a}) = \begin{bmatrix} \boldsymbol{\omega} \\ 0 \end{bmatrix} \otimes q(\mathbf{a}) - q(\mathbf{a}) \otimes \begin{bmatrix} \boldsymbol{\omega}_{ref} \\ 0 \end{bmatrix} \tag{3.2.10}$$

The expectation of this nonlinear function of $\mathbf{a}$ and $\boldsymbol{\omega}$ is approximated by the same nonlinear function of the expectations $\hat{\mathbf{a}}$ and $\hat{\boldsymbol{\omega}}$, normal typical process in EKF

$$2\frac{d}{dt}q(\hat{\mathbf{a}}) = \begin{bmatrix} \hat{\boldsymbol{\omega}} \\ 0 \end{bmatrix} \otimes q(\hat{\mathbf{a}}) - q(\hat{\mathbf{a}}) \otimes \begin{bmatrix} \boldsymbol{\omega}_{ref} \\ 0 \end{bmatrix} \tag{3.2.11}$$

The requirement that $\hat{\mathbf{a}} = \mathbf{0}$ means that $q(\hat{\mathbf{a}})$ is the identity quaternion $q(\hat{\mathbf{a}}) = [0 \quad 0 \quad 0 \quad 1]^T$. Substituting this into Eq. (3.2.11) gives

$$\hat{\boldsymbol{\omega}}(t) = \boldsymbol{\omega}_{ref}(t) \tag{3.2.12}$$

This demonstrates that, because the reference attitude is the attitude estimate, the reference attitude rate is the rate estimate.

The gyro unit outputs time-tagged angular increments which are used to compute the rate vector $\boldsymbol{\omega}_g(t)$. The true rate $\boldsymbol{\omega}(t)$ is modeled using $\boldsymbol{\omega}_g(t)$, a rate bias $\mathbf{b}(t)$, and zero-mean white noise processes $\boldsymbol{\eta}_a(t)$ and $\boldsymbol{\eta}_r(t)$

$$\boldsymbol{\omega}(t) = \boldsymbol{\omega}_g(t) + \mathbf{b}(t) + \boldsymbol{\eta}_a(t) \tag{3.2.13}$$

$$d\mathbf{b}(t)/dt = \boldsymbol{\eta}_r(t) \tag{3.2.14}$$

For the noise processes, $E(\boldsymbol{\eta}_a\boldsymbol{\eta}_a^{\mathrm{T}}) = \sigma_a^2\mathbf{I}\delta(t-\tau)$ where $\sigma_a^2$ is the angular random walk variance, and $E(\boldsymbol{\eta}_r\boldsymbol{\eta}_r^{\mathrm{T}}) = \sigma_r^2\mathbf{I}\delta(t-\tau)$ where $\sigma_r^2$ is the rate random walk variance. The sign convention in Eq. (3.2.13) follows reference [17] rather than reference [16]. The rate estimate is defined as

$$\hat{\boldsymbol{\omega}}(t) = \boldsymbol{\omega}_g(t) + \hat{\mathbf{b}}(t) = \boldsymbol{\omega}_{ref}(t) \tag{3.2.15}$$

The MEKF state vector is

$$\mathbf{x}(t) = \begin{bmatrix} \mathbf{a}(t) \\ \mathbf{b}(t) \end{bmatrix} \tag{3.2.16}$$

The expectation $\hat{\mathbf{x}}$ of the state vector is constant during the propagation phase because $\hat{\mathbf{a}} = \mathbf{0}$ and Eq. (3.2.14) implies $d\hat{\mathbf{b}}/dt = \mathbf{0}$.

The angular rate estimate is $\hat{\boldsymbol{\omega}}(t_k) = \boldsymbol{\omega}_g(t_k) + \hat{\mathbf{b}}(t_k)$ and the rotation vector is given by $\mathbf{a} = (t_{k+1} - t_k)\hat{\boldsymbol{\omega}}(t_k)$, where the time interval $t_{k+1} - t_k$ is short enough that $\hat{\boldsymbol{\omega}}$ is approximately constant. To propagate the attitude and state estimates from $t_k$ to $t_{k+1}$

$$q_{ref}(t_{k+1}) = q(\mathbf{a}) \otimes q_{ref}(t_k) \tag{3.2.17}$$

$$\hat{\mathbf{x}}(t_{k+1}) = \hat{\mathbf{x}}(t_k) \tag{3.2.18}$$

Attitude propagation when the assumption of approximately constant $\hat{\boldsymbol{\omega}}$ is not valid is discussed in references [18].

### 3.2.2 Covariance Propagation

The MEKF covariance matrix $\mathbf{P}$ is defined by

$$\mathbf{P} \equiv E((\mathbf{x}-\hat{\mathbf{x}})(\mathbf{x}-\hat{\mathbf{x}})^{\mathrm{T}} \mid \mathbf{y}) \equiv \begin{bmatrix} \mathbf{P_a} & \mathbf{P_c} \\ \mathbf{P_c} & \mathbf{P_b} \end{bmatrix} \tag{3.2.19}$$

where the vector $\mathbf{y}$ represents star observations and $\mathbf{P}$ is partitioned into $3 \times 3$ attitude, bias, and correlation sub-matrices. The objective here is a discrete-time state transition matrix $\boldsymbol{\Phi}_k(\tau)$ and process noise covariance $\mathbf{Q}_k(\tau)$ to propagate $\mathbf{P}$ over the time interval $\tau = t_{k+1} - t_k$ using

$$\mathbf{P}_{k+1|k} = \mathbf{\Phi}_k \mathbf{P}_k \mathbf{\Phi}_k^T + \mathbf{Q}_k \tag{3.2.20}$$

The following derivation of the linearized state equation follows reference [17]. The time derivative of the attitude error rotation vector $d\mathbf{a}/dt$ is given by the Bortz equation

$$\frac{d\mathbf{a}}{dt} = \boldsymbol{\omega} + \frac{1}{2}\mathbf{a}\times\boldsymbol{\omega} + \frac{1}{a^2}\left(1 - \frac{a\sin a}{2(1-\cos a)}\right)\mathbf{a}\times(\mathbf{a}\times\boldsymbol{\omega}) \tag{3.2.21}$$

which for small $\mathbf{a}$ is approximated by the Bortz equation for small rotations

$$d\mathbf{a}/dt = \boldsymbol{\omega} + (\mathbf{a}\times\boldsymbol{\omega})/2 + (\mathbf{a}\times(\mathbf{a}\times\boldsymbol{\omega}))/12 \tag{3.2.22}$$

Setting aside the bias equation $d\mathbf{b}(t)/dt = \boldsymbol{\eta}_r(t)$, the state equation $\dot{\mathbf{x}} = \mathbf{f}(\mathbf{x},t)$ is

$$\begin{bmatrix} \dot{\mathbf{a}} \\ \dot{\mathbf{b}} \end{bmatrix} = \begin{bmatrix} \boldsymbol{\omega} + (\mathbf{a}\times\boldsymbol{\omega})/2 + (\mathbf{a}\times(\mathbf{a}\times\boldsymbol{\omega}))/12 \\ \mathbf{0} \end{bmatrix} \tag{3.2.23}$$

The objective is to linearize the state equation about a reference trajectory $\mathbf{x}_{ref}(t)$ and form a linearized state equation $\delta\dot{\mathbf{x}} = \mathbf{F}(\mathbf{x}_{ref})\delta\mathbf{x}$ for $\delta\mathbf{x}(t) = \mathbf{x}(t) - \mathbf{x}_{ref}(t)$. Let the reference trajectory $\mathbf{x}_{ref}(t)$ be defined by the solution $\mathbf{a}_{ref}(t)$ from the Bortz equation for small rotations

$$d\mathbf{a}_{ref}/dt = \boldsymbol{\omega}_{ref} + (\mathbf{a}_{ref}\times\boldsymbol{\omega}_{ref})/2 + (\mathbf{a}_{ref}\times(\mathbf{a}_{ref}\times\boldsymbol{\omega}_{ref}))/12 \tag{3.2.24}$$

for the time interval $t_k$ to $t_{k+1}$, where the reference bias is $\mathbf{b}_{ref} = \hat{\mathbf{b}}$, the reference rate is $\boldsymbol{\omega}_{ref} = \boldsymbol{\omega}_g + \mathbf{b}_{ref}$, and the initial condition is $\mathbf{a}_{ref}(t_k) = \mathbf{0}$. The second order term $\mathbf{a}_{ref}\times(\mathbf{a}_{ref}\times\boldsymbol{\omega}_{ref})$ is negligible and the reference trajectory is approximately the solution to the coning equation

$$d\mathbf{a}_{ref}/dt = \boldsymbol{\omega}_{ref} + (\mathbf{a}_{ref}\times\boldsymbol{\omega}_{ref})/2 \tag{3.2.25}$$

From the composition rule for small rotations, the rotation error $\delta\mathbf{a}(t)$ between the true $\mathbf{a}(t)$ from Eq. (3.2.22) and the reference $\mathbf{a}_{ref}(t)$ is

$$\delta\mathbf{a} = \mathbf{a}\circ(-\mathbf{a}_{ref}) \approx \mathbf{a} - \mathbf{a}_{ref} + (\mathbf{a}\times\mathbf{a}_{ref})/2 \tag{3.2.26}$$

where $\delta\mathbf{a}(t_k) = \mathbf{0}$. Differentiating this and discarding higher order terms

$$d(\delta\mathbf{a})/dt = -\boldsymbol{\omega}_{ref} \times \delta\mathbf{a} + \delta\mathbf{b} + \boldsymbol{\eta}_a \qquad (3.2.27)$$

where $\delta\mathbf{b} = \mathbf{b} - \mathbf{b}_{ref}$ .

Including the bias equation $d\mathbf{b}(t)/dt = \boldsymbol{\eta}_r(t)$, the linearized state equation $\delta\dot{\mathbf{x}} = \mathbf{F}\delta\mathbf{x} + \mathbf{G}\boldsymbol{\eta}$ is

$$\begin{bmatrix} \delta\dot{\mathbf{a}} \\ \delta\dot{\mathbf{b}} \end{bmatrix} = \begin{bmatrix} -[\boldsymbol{\omega}_{ref}\times] & \mathbf{I}_{3\times3} \\ \mathbf{0}_{3\times3} & \mathbf{0}_{3\times3} \end{bmatrix} \begin{bmatrix} \delta\mathbf{a} \\ \delta\mathbf{b} \end{bmatrix} + \mathbf{I}_{6\times6} \begin{bmatrix} \boldsymbol{\eta}_a \\ \boldsymbol{\eta}_r \end{bmatrix} \qquad (3.2.28)$$

The discrete-time solution is

$$\delta\mathbf{x}_{k+1} = \boldsymbol{\Phi}_k \delta\mathbf{x}_k + \boldsymbol{\Gamma}_k \mathbf{w}_k \qquad (3.2.29)$$

where the state transition matrix for $\tau = t_{k+1} - t_k$ is

$$\boldsymbol{\Phi}_k(\tau) = \exp(\tau\mathbf{F}(\mathbf{x}_k)) = \begin{bmatrix} \mathbf{R}(\mathbf{a}_k(\tau)) & \mathbf{S}(\mathbf{a}_k(\tau)) \\ 0 & \mathbf{I} \end{bmatrix} \qquad (3.2.30)$$

and where the rotation vector $\mathbf{a}_k(\tau)$ is the solution $\mathbf{a}_{ref}(t_k + \tau)$ to Eq. (3.2.25) with the initial condition $\mathbf{a}_{ref}(t_k) = \mathbf{0}$. For $\mathbf{a} = \mathbf{a}_k(\tau)$, the matrices $\mathbf{R}$ and $\mathbf{S}$ are

$$\mathbf{R}(\mathbf{a}) = (\cos a)\mathbf{I} - \left(\frac{\sin a}{a}\right)[\mathbf{a}\times] + \left(\frac{1-\cos a}{a^2}\right)\mathbf{a}\mathbf{a}^{\mathrm{T}} \qquad (3.2.31)$$

$$\mathbf{S}(\mathbf{a}) = \tau\left[\left(\frac{\sin a}{a}\right)\mathbf{I} - \left(\frac{1-\cos a}{a^2}\right)[\mathbf{a}\times] + \left(\frac{a-\sin a}{a^3}\right)\mathbf{a}\mathbf{a}^{\mathrm{T}}\right] \qquad (3.2.32)$$

The continuous-time process noise covariance $\mathbf{Q}(t)$ is defined by

$$\mathbf{Q}(t) = E(\boldsymbol{\eta}(t)\boldsymbol{\eta}^{\mathrm{T}}(t'))\delta(t-t') = \begin{bmatrix} \sigma_a^2\mathbf{I}_{3\times3} & \mathbf{0}_{3\times3} \\ \mathbf{0}_{3\times3} & \sigma_r^2\mathbf{I}_{3\times3} \end{bmatrix} \qquad (3.2.33)$$

and the discrete-time process noise covariance $\mathbf{Q}_k(\tau)$ for $E(\boldsymbol{\eta}_k\boldsymbol{\eta}_k^T) = \mathbf{I}$ is

$$\mathbf{Q}_k(\tau) = \boldsymbol{\Gamma}_k\boldsymbol{\Gamma}_k^T = \begin{bmatrix} (\sigma_w^2 + \tau\sigma_a^2 + (\tau^3/3)\sigma_r^2)\mathbf{I} & (\tau^2/2)\sigma_r^2\mathbf{I} \\ (\tau^2/2)\sigma_r^2\mathbf{I} & \tau\sigma_r^2\mathbf{I} \end{bmatrix} \qquad (3.2.34)$$

where $\sigma_w^2$ is the gyro angle white noise variance.

### 3.2.3 Update

For filter measurement updates, an observation $\mathbf{y}$ is defined by the measurement model $\mathbf{h}(\mathbf{u})$

$$\mathbf{y} = \mathbf{h}(\mathbf{u}) + \boldsymbol{\varepsilon} = \begin{bmatrix} h \\ v \end{bmatrix} + \boldsymbol{\varepsilon} = \begin{bmatrix} u_1/u_3 \\ u_2/u_3 \end{bmatrix} + \boldsymbol{\varepsilon} \tag{3.2.35}$$

where $\boldsymbol{\varepsilon}$ is zero-mean white noise. The measurement noise covariance matrix $\mathbf{R}$ is

$$\mathbf{R} = \begin{bmatrix} \sigma_h^2 & 0 \\ 0 & \sigma_v^2 \end{bmatrix} \tag{3.2.36}$$

where $\sigma_h^2$ and $\sigma_v^2$ are the horizontal and vertical coordinate variances.

The objective here is the measurement sensitivity matrix $\mathbf{H} = \partial\mathbf{y}/\partial\mathbf{x}$ representing the relationship of the observations to the filter states. The observations are not sensitive to the gyro rate bias, $\partial\mathbf{h}(\mathbf{u})/\partial\mathbf{b} = \mathbf{0}$. They are, however, sensitive to a change of body frame attitude represented by the rotation vector $\mathbf{a}$

$$\mathbf{H} = \begin{bmatrix} \dfrac{\partial\mathbf{h}(\mathbf{u})}{\partial\mathbf{a}} & \dfrac{\partial\mathbf{h}(\mathbf{u})}{\partial\mathbf{b}} \end{bmatrix} = \begin{bmatrix} \dfrac{\partial\mathbf{h}}{\partial\mathbf{u}}\dfrac{\partial\mathbf{u}}{\partial\mathbf{a}} & \mathbf{0} \end{bmatrix} = \frac{\partial\mathbf{h}}{\partial\mathbf{u}}\begin{bmatrix} \dfrac{\partial\mathbf{u}}{\partial\mathbf{a}} & \mathbf{0} \end{bmatrix} \tag{3.2.37}$$

where, from Eq. (3.2.35),

$$\frac{\partial\mathbf{h}}{\partial\mathbf{u}} = \begin{bmatrix} 1/u_3 & 0 & -u_1/u_3^2 \\ 0 & 1/u_3 & -u_2/u_3^2 \end{bmatrix} \tag{3.2.38}$$

To derive $\partial\mathbf{u}/\partial\mathbf{a}$, the rotation from the inertial frame to the body frame can be represented by a rotation vector $\mathbf{a}_i^b$ and equivalent rotation matrix $\mathbf{A}(\mathbf{a}_i^b)$. With the alignment rotation from the body frame to the sensor coordinate frame represented by a rotation matrix $\mathbf{R}_b^s$, the observed unit vector in the sensor coordinate frame $\mathbf{u}$ is related to the same unit vector in the inertial frame $\mathbf{u}'$ by

$$\mathbf{u} = \mathbf{R}_b^s\mathbf{A}(\mathbf{a}_i^b)\mathbf{u}' \tag{3.2.39}$$

For a reference attitude $\mathbf{A}(\mathbf{a}_i^r)$ arbitrarily close to the body attitude $\mathbf{A}(\mathbf{a}_i^b)$

$$\mathbf{A}(\mathbf{a}_i^b) = \mathbf{A}(\mathbf{a})\mathbf{A}(\mathbf{a}_i^r) = (\mathbf{I} - [\mathbf{a}\times])\mathbf{A}(\mathbf{a}_i^r) \tag{3.2.40}$$

where $\mathbf{a}$ is a small rotation vector and the first-order approximation is $\mathbf{A}(\mathbf{a}) \approx (\mathbf{I} - [\mathbf{a}\times])$ with $[\mathbf{a}\times]\mathbf{b} \equiv \mathbf{a}\times\mathbf{b}$. Substituting into Eq. (3.2.40)

$$\mathbf{u} = \mathbf{R}_b^s(\mathbf{I} - [\mathbf{a}\times])\mathbf{A}(\mathbf{a}_i^r)\mathbf{u}' \tag{3.2.41}$$

$$\mathbf{u} = \mathbf{R}_b^s\mathbf{A}(\mathbf{a}_i^r)\mathbf{u}' - \mathbf{R}_b^s[\mathbf{a}\times]\mathbf{A}(\mathbf{a}_i^r)\mathbf{u}' \tag{3.2.42}$$

$$\mathbf{u} = \mathbf{R}_b^s\mathbf{A}(\mathbf{a}_i^r)\mathbf{u}' + \mathbf{R}_b^s[\mathbf{A}(\mathbf{a}_i^r)\mathbf{u}'\times]\mathbf{a} \tag{3.2.43}$$

Taking the partial with respect to $\mathbf{a}$ and noting that $\mathbf{a}_i^r \rightarrow \mathbf{a}_i^b$ as $\mathbf{a} \rightarrow \mathbf{0}$

$$\left.\frac{\partial\mathbf{u}}{\partial\mathbf{a}}\right|_{\mathbf{a}=\mathbf{0}} = \mathbf{R}_b^s[\mathbf{A}(\mathbf{a}_i^b)\mathbf{u}'\times] \tag{3.2.44}$$

and substituting

$$\mathbf{H} = \begin{bmatrix} 1/u_3 & 0 & -u_1/u_3^2 \\ 0 & 1/u_3 & -u_2/u_3^2 \end{bmatrix} \mathbf{R}_b^s[\mathbf{A}(\mathbf{a}_i^b)\mathbf{u}'\times] \tag{3.2.45}$$

After propagation of the state and covariance from $t_k$ to $t_{k+1}$, the measurement update at $t_{k+1}$ is performed using the Kalman filter equations

$$\mathbf{K}_{k+1} = \mathbf{P}_{k+1|k}\mathbf{H}_{k+1}^{\mathbf{T}}(\mathbf{H}_{k+1}\mathbf{P}_{k+1|k}\mathbf{H}_{k+1}^{\mathbf{T}} + \mathbf{R}_{k+1})^{-1} \tag{3.2.46}$$

$$\begin{bmatrix} \Delta\hat{\mathbf{a}}_{k+1} \\ \Delta\hat{\mathbf{b}}_{k+1} \end{bmatrix} = \mathbf{K}_{k+1}(\mathbf{y} - \mathbf{h}(\mathbf{R}_b^s\mathbf{A}(\mathbf{a}_i^b)\mathbf{u}')) \tag{3.2.47}$$

$$\mathbf{P}_{k+1|k+1} = (\mathbf{I} - \mathbf{K}_{k+1}\mathbf{H}_{k+1})\mathbf{P}_{k+1|k} \tag{3.2.48}$$

The estimated bias error is added to the bias estimate

$$\hat{\mathbf{b}}_{k+1} = \Delta\hat{\mathbf{b}}_{k+1} + \hat{\mathbf{b}}_k \tag{3.2.49}$$

and as described above the reset phase moves the estimated attitude error information into the attitude estimate $\hat{q}(t) = q_{ref}(t)$ by multiplication

$$\hat{q}_{k+1} = q(\Delta\hat{\mathbf{a}}_{k+1}) \otimes \hat{q}_k \tag{3.2.50}$$

## 3.3 Alignment Filter

An alignment filter is used to simultaneously predict the measurements from all three star trackers. The measurement residuals are used to update the filter states, which represent the body frame attitude and time-varying corrections to reference alignments. The combined states represent the attitudes of all three trackers. Alignment filtering has been discussed in the literature [19-24], particularly since 2000 by Pittelkau [25-29].

### 3.3.1 Attitude, State, and Covariance

Time-varying rotation vectors $\mathbf{a}_{TRK}(t)$ representing small alignment corrections are included in the attitude models for the three trackers

$$\mathbf{A}_i^{ST}(t) = \mathbf{A}(\mathbf{a}_{ST}(t))\mathbf{A}_b^{ST}\mathbf{A}_i^b(t) \tag{3.3.1}$$

$$\mathbf{A}_i^{SST1}(t) = \mathbf{A}(\mathbf{a}_{SST1}(t))\mathbf{A}_b^{SST1}\mathbf{A}_i^b(t) \tag{3.3.2}$$

$$\mathbf{A}_i^{SST2}(t) = \mathbf{A}(\mathbf{a}_{SST2}(t))\mathbf{A}_b^{SST2}\mathbf{A}_i^b(t) \tag{3.3.3}$$

where $\mathbf{A}(\mathbf{a}_{TRK}(t))$ is a rotation matrix equivalent to a rotation vector $\mathbf{a}_{TRK}(t)$ , and $\mathbf{A}_b^{TRK}$ is a reference alignment.

Normally the ST frame is identified with the body frame by holding $\mathbf{x}(t) = [\mathbf{a}(t)^T \quad \mathbf{b}(t)^T \quad \mathbf{a}_{ST}(t)^T \quad \mathbf{a}_{SST1}(t)^T \quad \mathbf{a}_{SST2}(t)^T]^T$ . This is easily accomplished by setting the uncertainty and process noise associated with $\mathbf{a}_{ST}(t)$ to be very small. The result is $\mathbf{A}_i^{ST}(t) \,@\, \mathbf{A}_b^{ST}\mathbf{A}_i^b(t)$. $\mathbf{a}_{ST}(t)$ is included in the filter state here because in some circumstances it may be useful to identify one of the SSTs with the body frame instead of the LRS, by holding $\mathbf{a}_{SST1}(t) \cong \mathbf{0}$ or $\mathbf{a}_{SST2}(t) \cong \mathbf{0}$.

The state vector is

$$\mathbf{x}(t) = [\mathbf{a}(t)^T \quad \mathbf{b}(t)^T \quad \mathbf{a}_{ST}(t)^T \quad \mathbf{a}_{SST1}(t)^T \quad \mathbf{a}_{SST2}(t)^T]^T \qquad (3.3.4)$$

where $\mathbf{a}(t)$ is the attitude error rotation vector and $\mathbf{b}(t)$ is the gyro rate bias. These states are estimated sequentially using an alignment filter based on the standard attitude filter, referred to by reference [16] as the MEKF. The description here follows references [16, 17, 26, 27].

The filter performs unconstrained estimation of $\mathbf{a}(t)$ during each measurement update phase while maintaining the overall body frame attitude estimate in the unit-norm reference attitude quaternion $q_{ref}(t)$ and $\hat{\mathbf{A}}_i^b(t) = \mathbf{A}(q_{ref}(t))$. The true attitude $q(t)$ is modeled as $q(t) = q(\mathbf{a}(t)) \otimes q_{ref}(t)$ where $q(\mathbf{a}(t))$ is a unit-norm quaternion function of the rotation vector. The measurement update phase assigns a finite value $\hat{\mathbf{a}}(+)$ to $\hat{\mathbf{a}}(t)$ while the reference quaternion retains its pre-update value $q_{ref}(-)$. The update information is moved from $\hat{\mathbf{a}}(+)$ to a post-update reference $q_{ref}(+)$ and $\hat{\mathbf{a}}(t)$ is reset to zero so that $q(\hat{\mathbf{a}}(+)) \otimes q_{ref}(-) = q(\mathbf{0}) \otimes q_{ref}(+)$.

The covariance matrix $\mathbf{P}$ is given by

$$P_{15\times15} \equiv E\{(\mathbf{x}-\hat{\mathbf{x}})(\mathbf{x}-\hat{\mathbf{x}})^T\} = \begin{bmatrix} \mathbf{P_a} & \mathbf{P_{ab}} & & & \\ \mathbf{P_{ab}} & \mathbf{P_b} & & & \\ & & \mathbf{P}_{ST} & & \\ & & & \mathbf{P}_{SST1} & \\ & & & & \mathbf{P}_{SST2} \end{bmatrix} \qquad (3.3.5)$$

where $\mathbf{P}$ is partitioned into $3\times3$ attitude error $\mathbf{P_a}$, gyro rate bias $\mathbf{P_b}$, correlation $\mathbf{P_{ab}}$, and alignment $\mathbf{P}_{TRK}$ sub-matrices. In the continuous-time linearized state equation given by

$$\begin{bmatrix} \delta\dot{\mathbf{a}} \\ \delta\dot{\mathbf{b}} \\ \delta\dot{\mathbf{a}}_{ST} \\ \delta\dot{\mathbf{a}}_{SST1} \\ \delta\dot{\mathbf{a}}_{SST2} \end{bmatrix} = \begin{bmatrix} -[\boldsymbol{\omega}_{ref}\times] & \mathbf{I}_{3\times3} & & & \\ \mathbf{0}_{3\times3} & \mathbf{0}_{3\times3} & & & \\ & & \mathbf{0}_{3\times3} & & \\ & & & \mathbf{0}_{3\times3} & \\ & & & & \mathbf{0}_{3\times3} \end{bmatrix} \begin{bmatrix} \delta\mathbf{a} \\ \delta\mathbf{b} \\ \delta\mathbf{a}_{ST} \\ \delta\mathbf{a}_{SST1} \\ \delta\mathbf{a}_{SST2} \end{bmatrix} + \mathbf{I}_{15\times15} \begin{bmatrix} \boldsymbol{\eta}_{ARW} \\ \boldsymbol{\eta}_{RRW} \\ \boldsymbol{\eta}_{ST} \\ \boldsymbol{\eta}_{SST1} \\ \boldsymbol{\eta}_{SST2} \end{bmatrix} \qquad (3.3.6)$$

the gyro rate bias $\delta\mathbf{b}$ and alignments $\delta\mathbf{a}_{ST}$, $\delta\mathbf{a}_{SST1}$, $\delta\mathbf{a}_{SST2}$ are driven by process noise alone, with $E\{\boldsymbol{\eta}_{ARW}\boldsymbol{\eta}_{ARW}^T\} = \sigma_{ARW}^2\mathbf{I}$, $E\{\boldsymbol{\eta}_{RRW}\boldsymbol{\eta}_{RRW}^T\} = \sigma_{RRW}^2\mathbf{I}$, $E\{\boldsymbol{\eta}_{ST}\boldsymbol{\eta}_{ST}^T\} = \sigma_{ST}^2\mathbf{I}$, $E\{\boldsymbol{\eta}_{SST1}\boldsymbol{\eta}_{SST1}^T\} = \sigma_{SST1}^2\mathbf{I}$,

$E\{\boldsymbol{\eta}_{SST2}\boldsymbol{\eta}_{SST2}^T\} = \sigma_{SST2}^2\mathbf{I}$. The discrete-time process noise matrix for a propagation interval $t \equiv t_{k+1} - t_k$ is given by

$$\mathbf{Q}_k(t) = \begin{bmatrix} (\sigma_{AWN}^2 + t\sigma_{ARW}^2 + (t^3/3)\sigma_{RRW}^2)\mathbf{I} & (t^2/2)\sigma_{RRW}^2\mathbf{I} & & & \\ (t^2/2)\sigma_{RRW}^2\mathbf{I} & t\sigma_{RRW}^2\mathbf{I} & & & \\ & & t\sigma_{ST}^2\mathbf{I} & & \\ & & & t\sigma_{SST1}^2\mathbf{I} & \\ & & & & t\sigma_{SST2}^2\mathbf{I} \end{bmatrix} \qquad (3.3.7)$$

Parameter estimates for the alignment process noises $s_{ST}, s_{SST1}, s_{SST2}$ are discussed in a following section.

### 3.3.2 Propagation

The gyro unit outputs time-tagged angular increments which are used to compute the rate vector $\boldsymbol{\omega}_g(t)$. The true rate $\boldsymbol{\omega}(t)$ is modeled by $\boldsymbol{\omega}(t) = \boldsymbol{\omega}_g(t) + \mathbf{b}(t) + \boldsymbol{\eta}_{ARW}(t)$ where $d\mathbf{b}(t)/dt = \boldsymbol{\eta}_{RRW}(t)$. The angular rate estimate is $\hat{\boldsymbol{\omega}}(t_k) = \boldsymbol{\omega}_g(t_k) + \hat{\mathbf{b}}(t_k)$ and the propagation rotation vector is $\mathbf{a}_p = t\hat{\boldsymbol{\omega}}(t_k)$ where the time interval $t \equiv t_{k+1} - t_k$ is short enough that $\hat{\boldsymbol{\omega}}$ is approximately constant. Attitude propagation when the assumption of approximately constant $\hat{\boldsymbol{\omega}}$ is not valid is discussed in reference [18]. The propagated attitude estimate and state are $q_{ref}(t_{k+1}) = q(\mathbf{a}_p) \otimes q_{ref}(t_k)$ and $\hat{\mathbf{x}}_{k+1} = \hat{\mathbf{x}}_k$.

The discrete-time state transition matrix is given by

$$\boldsymbol{\Phi}_k(t) = \begin{bmatrix} \mathbf{R}(\mathbf{a}_p) & \mathbf{S}(\mathbf{a}_p) & & & \\ \mathbf{0}_{3\times3} & \mathbf{I}_{3\times3} & & & \\ & & \mathbf{I}_{3\times3} & & \\ & & & \mathbf{I}_{3\times3} & \\ & & & & \mathbf{I}_{3\times3} \end{bmatrix} \qquad (\ 3.3.8)$$

$$\mathbf{R}(\mathbf{a}) = (\cos a)\mathbf{I} - \left(\frac{\sin a}{a}\right)[\mathbf{a}\times] + \left(\frac{1-\cos a}{a^2}\right)\mathbf{a}\mathbf{a}^{\mathrm{T}} \qquad (\ 3.3.9)$$

$$\mathbf{S}(\mathbf{a}) = t\left[\left(\frac{\sin a}{a}\right)\mathbf{I} - \left(\frac{1-\cos a}{a^2}\right)[\mathbf{a}\times] + \left(\frac{a-\sin a}{a^3}\right)\mathbf{a}\mathbf{a}^{\mathrm{T}}\right] \tag{3.3.10}$$

and the propagated covariance is $\mathbf{P}_{k+1} = \mathbf{\Phi}_k \mathbf{P}_k \mathbf{\Phi}_k^T + \mathbf{Q}_k$.

### 3.3.3 Update

The input to a measurement update phase consists of one or more observed star unit vectors $\mathbf{u}$ in an $\mathbf{i,j,k}$ sensor coordinate frame with the $\mathbf{k}$ axis along the LOS and the $\mathbf{i,j}$ axes in the focal plane. The star unit vectors are expressed in $h,v$ coordinates using Eqs. (3.1.1) and (3.1.2). The measurement model $\mathbf{h}(\mathbf{u})$ is given by

$$\mathbf{y} = \mathbf{h}(\mathbf{u}) + \boldsymbol{\eta}_y = \begin{bmatrix} h \\ v \end{bmatrix} + \boldsymbol{\eta}_y = \begin{bmatrix} u_1/u_3 \\ u_2/u_3 \end{bmatrix} + \boldsymbol{\eta}_y \tag{3.3.11}$$

where the measurement covariance $\mathbf{R} = E\{\boldsymbol{\eta}_y \boldsymbol{\eta}_y^T\} = \sigma_y^2 \mathbf{I}$. The $j$th sensor attitude is $\mathbf{A}_i^j(t) = \mathbf{A}(\mathbf{a}_j(t))\mathbf{A}_b^j \mathbf{A}_i^b(t)$ and the measurement residuals are $\Delta\mathbf{y} \equiv \mathbf{y} - \mathbf{h}(\mathbf{A}(\mathbf{a}_j(t))\mathbf{A}_b^j \mathbf{A}_i^b(t)\mathbf{u}')$ where $\mathbf{u}'$ is a reference unit vector in the inertial frame.

The measurement sensitivity matrix representing the relationship of the observations to the filter states is

$$\mathbf{H} = \frac{\partial \mathbf{y}}{\partial \mathbf{x}} = \frac{\partial \mathbf{h}}{\partial \mathbf{u}}\frac{\partial \mathbf{u}}{\partial \mathbf{x}} = \frac{\partial \mathbf{h}}{\partial \mathbf{u}}\begin{bmatrix} \dfrac{\partial \mathbf{u}}{\partial \mathbf{a}} & \mathbf{0} & \dfrac{\partial \mathbf{u}}{\partial \mathbf{a}_{LRS}} & \dfrac{\partial \mathbf{u}}{\partial \mathbf{a}_{SST1}} & \dfrac{\partial \mathbf{u}}{\partial \mathbf{a}_{SST2}} \end{bmatrix} \tag{3.3.12}$$

where from Eq. (3.2.35)

$$\frac{\partial \mathbf{h}}{\partial \mathbf{u}} = \begin{bmatrix} 1/u_3 & 0 & -u_1/u_3^2 \\ 0 & 1/u_3 & -u_2/u_3^2 \end{bmatrix} \tag{3.3.13}$$

The factors $\partial\mathbf{u}/\partial\mathbf{a}$ and $\partial\mathbf{u}/\partial\mathbf{a}_j$ represent the sensitivity of star unit vectors to body frame attitude and $j$th sensor alignment variations. Their derivation here follows references [26, 27].

For $\partial\mathbf{u}/\partial\mathbf{a}$ the $j$th alignment is held constant and absorbed in $\mathbf{A}_b^j$. For a reference attitude $\mathbf{A}_i^r(t)$ arbitrarily close to $\mathbf{A}_i^b(t)$ and a small attitude error rotation vector $\mathbf{a}$ with the first-order approximation $\mathbf{A}(\mathbf{a}) \approx (\mathbf{I} - [\mathbf{a}\times])$, the attitude is modeled as $\mathbf{A}_i^b(t) = (\mathbf{I} - [\mathbf{a}\times])\mathbf{A}_i^r(t)$. Observed and reference unit vectors are related by $\mathbf{u} = \mathbf{A}_b^j \mathbf{A}_i^b(t)\mathbf{u}'$ and substitution gives

$$\mathbf{u} = \mathbf{A}_b^j \mathbf{A}_i^r(t)\mathbf{u}' - \mathbf{A}_b^j [\mathbf{a}\times]\mathbf{A}_i^r(t)\mathbf{u}' \qquad (3.3.14)$$

$$\mathbf{u} = \mathbf{A}_b^j \mathbf{A}_i^r(t)\mathbf{u}' + \mathbf{A}_b^j [\mathbf{A}_i^r(t)\mathbf{u}'\times]\mathbf{a} \qquad (3.3.15)$$

$$\partial\mathbf{u}/\partial\mathbf{a} = \mathbf{A}_b^j [\mathbf{A}_i^b(t)\mathbf{u}'\times] \qquad (3.3.16)$$

for $\mathbf{a}_i^r \to \mathbf{a}_i^b$ as $\mathbf{a} \to \mathbf{0}$.

For $\partial\mathbf{u}/\partial\mathbf{a}_j$ with a reference alignment $\mathbf{A}_b^r$ arbitrarily close to $\mathbf{A}_b^j$ and the approximation $\mathbf{A}(\mathbf{a}_j) \approx (\mathbf{I} - [\mathbf{a}_j\times])$, the *j*th sensor alignment is modeled as $\mathbf{A}(\mathbf{a}_j)\mathbf{A}_b^r = (\mathbf{I} - [\mathbf{a}_j\times])\mathbf{A}_b^r$. Observed and reference unit vectors are related by $\mathbf{u} = \mathbf{A}(\mathbf{a}_j)\mathbf{A}_b^r \mathbf{A}_i^b(t)\mathbf{u}'$ and substitution gives

$$\mathbf{u} = \mathbf{A}_b^r \mathbf{A}_i^b(t)\mathbf{u}' - [\mathbf{a}_j\times]\mathbf{A}_b^r \mathbf{A}_i^b(t)\mathbf{u}' \qquad (3.3.17)$$

$$\mathbf{u} = \mathbf{A}_b^r \mathbf{A}_i^b(t)\mathbf{u}' + [\mathbf{A}_b^r \mathbf{A}_i^b(t)\mathbf{u}'\times]\mathbf{a}_j \qquad (3.3.18)$$

$$\partial\mathbf{u}/\partial\mathbf{a}_j = [\mathbf{A}_b^j \mathbf{A}_i^b(t)\mathbf{u}'\times] \qquad (3.3.19)$$

for $\mathbf{a}_b^r \to \mathbf{a}_b^j$ as $\mathbf{a}_j \to \mathbf{0}$.

After propagation of the state and covariance from $t_k$ to $t_{k+1}$ the measurement update at $t_{k+1}$ is performed using the Kalman gain $\mathbf{K} = \mathbf{PH}^T(\mathbf{HPH}^T + \mathbf{R})^{-1}$, estimated state correction

$$\mathrm{D}\hat{\mathbf{x}} = [\mathrm{D}\hat{\mathbf{a}}^T \quad \mathrm{D}\hat{\mathbf{b}}^T \quad \mathrm{D}\hat{\mathbf{a}}_{ST}^T \quad \mathrm{D}\hat{\mathbf{a}}_{SST1}^T \quad \mathrm{D}\mathbf{a}_{SST2}^T]^T = \mathbf{K}\mathrm{D}\mathbf{y} \qquad (3.3.20)$$

and covariance update $\mathbf{P}_+ = (\mathbf{I} - \mathbf{KH})\mathbf{P}_-$. The rate bias estimate is updated by $\hat{\mathbf{b}}_+ = \hat{\mathbf{b}}_- + \Delta\hat{\mathbf{b}}$ and the attitude error estimate is moved into the reference attitude $q_{ref+} = q(\Delta\hat{\mathbf{a}}) \otimes q_{ref-}$. The sensor alignments are updated by $\hat{\mathbf{a}}_{ST+} = \hat{\mathbf{a}}_{ST-} + \mathrm{D}\hat{\mathbf{a}}_{ST}$, $\hat{\mathbf{a}}_{SST1+} = \hat{\mathbf{a}}_{SST1-} + \Delta\hat{\mathbf{a}}_{SST1}$, and $\hat{\mathbf{a}}_{SST2+} = \hat{\mathbf{a}}_{SST2-} + \Delta\hat{\mathbf{a}}_{SST2}$.

### 3.3.4 Alignment Process Noise

Multiple-Model Adaptive Estimation (MMAE) is used to estimate alignment process noise values $s_{ST}, s_{SST1}, s_{SST2}$ by testing a set of candidates. Each candidate is implemented in its own filter $H_i$ and the set of candidates form a filter bank $H_i; i = 1,...,n$. Simulated measurements are input to the filter bank and the results are compared with simulation truth to select the best candidate. The description here follows reference [30].

The simulation represents a sensor frame as a rotation $\mathbf{A}_i^{TRK}(t) = \mathbf{A}(\mathbf{a}_{TRK}(t))\mathbf{A}_i^r(t)$ where $\mathbf{A}_i^r(t)$ is a reference attitude and $\mathbf{A}(\mathbf{a}_{TRK}(t))$ is a rotation matrix equivalent to a small alignment rotation vector $\mathbf{a}_{TRK}(t)$. $\mathbf{A}_i^r(t)$ includes the orbital rate of the stars through the sensor FOV. The simulation state $\mathbf{x}(t)$ is the sensor alignment $\mathbf{a}_{TRK}(t)$ and includes a sinusoidal orbital variation

$$\mathbf{x}(t) \equiv \mathbf{a}_{TRK}(t) = [a\sin(2\pi t / t_p + \theta_0) \quad 0 \quad 0]^T \tag{3.3.21}$$

with amplitude $a$, an orbital period $t_p$, and a random initial phase $\theta_0$. The sensor alignment is driven by zero-mean Gaussian noise $E\{\boldsymbol{\eta}_{TRK}\boldsymbol{\eta}_{TRK}^T\} = \sigma_{TRK}^2\mathbf{I}$ and the continuous-time state equation is $\boldsymbol{\delta}\dot{\mathbf{x}} = \boldsymbol{\eta}_{TRK}$. Filter propagation over an interval $t \equiv t_{k+1} - t_k$ is given by $\hat{\mathbf{x}}_{k+1} = \hat{\mathbf{x}}_k$, $\mathbf{Q}_k = t\sigma_{TRK}^2\mathbf{I}$, and $\mathbf{P}_{k+1} = \mathbf{P}_k + \mathbf{Q}_k$. Measurement updates are performed as in Section 3.2.4 except for the sensitivity matrix which reduces to

$$\mathbf{H} = \frac{\partial \mathbf{y}}{\partial \mathbf{x}} = \frac{\partial \mathbf{h}}{\partial \mathbf{u}}\frac{\partial \mathbf{u}}{\partial \mathbf{x}} = \frac{\partial \mathbf{h}}{\partial \mathbf{u}}\frac{\partial \mathbf{u}}{\partial \mathbf{a}_{TRK}} \tag{3.3.22}$$

After propagation of the state and covariance from $t_k$ to $t_{k+1}$ the measurement update at $t_{k+1}$ is performed using the Kalman gain $\mathbf{K} = \mathbf{PH}^T(\mathbf{HPH}^T + \mathbf{R})^{-1}$, estimated state correction $\Delta\hat{\mathbf{x}} = \Delta\hat{\mathbf{a}}_{TRK} = \mathbf{K}\Delta\mathbf{y}$, and covariance update $\mathbf{P}_+ = (\mathbf{I} - \mathbf{KH})\mathbf{P}_-$.

The measurement probability for a candidate and filter bank member $H_i$ is given by

$$P(\mathbf{y}_k \mid H_i) = (2\pi)^{-m/2} \mid \mathbf{S}_k \mid^{-1/2} \exp(-\Delta\mathbf{y}_k^T\mathbf{S}_k^{-1}\Delta\mathbf{y}_k / 2) \tag{3.3.23}$$

where $\mathbf{S}_k = \mathbf{H}_k\mathbf{P}_k\mathbf{H}_k^T + \mathbf{R}_k$ and $m$ is the number of filter states. At the beginning of a simulation, each of the $H_i$ are assigned the same probability $P_0(H_i) = n^{-1}$ of being the best. The probabilities are updated at each filter measurement update by

$$P_k(H_i) = \frac{P(\mathbf{y}_k \mid H_i)P_{k-1}(H_i)}{\sum_{j=1}^{n} P(\mathbf{y}_k \mid H_j)P_{k-1}(H_j)} \tag{3.3.24}$$

If a $P_k(H_i)$ approaches 1 as $t_k$ increases, it is evidence that the associated filter $H_i$ and candidate are the most correct.

Table 2 shows the simulation results with the orbital rate of 223 arcsecond/second, corresponding to the ICESat orbital period ($t_p$ = 5790 seconds). Two cases are considered here with simulated alignment variation amplitudes $a_1 = 2$ and $a_2 = 10$ arcseconds. In both cases, seven candidates and filter bank members $H_i; i = 1,...,7$ are tested. The candidate values associated with the $H_i$ are shown in the columns 2 and 4.

**Table 2 MMAE results for alignment process noise**

| | $a_1$ = 2, arcsec | | $a_2$ = 10, arcsec | |
|---|---|---|---|---|
| | $\sigma_{TRK}$, arcsec/sec$^{1/2}$ | $P(H_i)$ | $\sigma_{TRK}$, arcsec/sec$^{1/2}$ | $P(H_i)$ |
| $H_1$ | .002 | 0 | .015 | 0 |
| $H_2$ | .005 | 0 | .02 | 0 |
| $H_3$ | .007 | 0 | .025 | 0.001 |
| $H_4$ | .01 | 1 | .03 | 0.985 |
| $H_5$ | .015 | 0 | .035 | 0.014 |
| $H_6$ | .02 | 0 | .04 | 0 |
| $H_7$ | .025 | 0 | .045 | 0 |

The final hypothesis probabilities $P(H_i)$ are used to select the best candidates: $\sigma_{TRK} = 0.01$ arcsec/sec$^{1/2}$ and $\sigma_{TRK} = 0.03$ arcsec/sec$^{1/2}$.

## 3.4 Gyro Parameter Estimation

When the satellite is in science mode – only rotating at a constant angular rate about the pitch axis, and in the absence of maneuvers – the gyro misalignment and the scale factor error are not independently observable, and their effect is absorbed in the gyro bias estimation. When the satellite is maneuvering, however, these gyro errors can degrade the attitude accuracy. As a remedy to the degradation, the EKF can reduce the dependency on the gyro rate by putting more weight on star measurements, which is a proper filter tuning for the given filter model and available data quality. However, this scenario means the loss of an opportunity to achieve better attitude accuracy if the gyro has a relatively large misalignment and scale factor error. Better attitude accuracy would be available if these additional gyro parameters were included in the state vector and estimated for correction separately from bias.

The scale factor error, $\boldsymbol{\delta k}$ is defined, in roll, pitch, and yaw axes, as

$$\boldsymbol{\delta k} = \boldsymbol{k}_{true} - \hat{\boldsymbol{k}} = [\delta k_x \quad \delta k_y \quad \delta k_z]^T \tag{3.3.25}$$

where $\boldsymbol{k}_{true}$ is the true scale factor error vector and $\hat{\boldsymbol{k}}$ is the estimated scale factor error vector. The misalignment error, $\boldsymbol{\delta m}$, is

$$\boldsymbol{\delta m} = \boldsymbol{m}_{true} - \hat{\boldsymbol{m}} = \left[\delta m_{xy} \ \delta m_{xz} \ \delta m_{yx} \ \delta m_{yz} \ \delta m_{zx} \ \delta m_{zy}\right]^T \tag{3.3.26}$$

where $\boldsymbol{m}_{true}$ is the true misalignment vector and $\hat{\boldsymbol{m}}$ is the estimated misalignment vector. Each component $\delta m_{ij}$ represents the misalignment of the $i$ axis toward the $j$ axis direction. The state vector for the EKF is defined as

$$\boldsymbol{\delta x} = [\boldsymbol{\delta\theta}^T \quad \boldsymbol{\delta b}^T \quad \boldsymbol{\delta k}^T \quad \boldsymbol{\delta m}^T]^T \tag{3.3.27}$$

The state equation

$$\frac{d}{dt}\boldsymbol{\delta x} = F(t)\boldsymbol{\delta x} + G(t)\boldsymbol{\eta} \tag{3.3.28}$$

is established with the following matrices [31],

$$F(t) = \begin{bmatrix} [\boldsymbol{\omega}\times] & I_{3\times3} & \omega_d & \omega_u & \omega_l \\ 0_{3\times3} & 0_{3\times3} & 0_{3\times3} & 0_{3\times3} & 0_{3\times3} \\ 0_{3\times3} & 0_{3\times3} & 0_{3\times3} & 0_{3\times3} & 0_{3\times3} \\ 0_{3\times3} & 0_{3\times3} & 0_{3\times3} & 0_{3\times3} & 0_{3\times3} \\ 0_{3\times3} & 0_{3\times3} & 0_{3\times3} & 0_{3\times3} & 0_{3\times3} \end{bmatrix} \tag{3.3.29}$$

$$\omega_d = \begin{bmatrix} \omega_x & 0 & 0 \\ 0 & \omega_y & 0 \\ 0 & 0 & \omega_z \end{bmatrix} \quad \omega_u = \begin{bmatrix} \omega_y & \omega_z & 0 \\ 0 & 0 & \omega_x \\ 0 & 0 & 0 \end{bmatrix} \quad \omega_l = \begin{bmatrix} 0 & 0 & 0 \\ \omega_z & 0 & 0 \\ 0 & \omega_x & \omega_y \end{bmatrix} \tag{3.3.30}$$

$$G(t) = I_{15\times15} \tag{3.3.31}$$

$$\boldsymbol{\eta} = \left[\boldsymbol{\eta}_\theta^T \quad \boldsymbol{\eta}_b^T \quad \boldsymbol{\eta}_k^T \quad \boldsymbol{\eta}_m^T\right]^T \tag{3.3.32}$$

where $\boldsymbol{\eta}_k$ is a white noise vector for the scale factor error, $\boldsymbol{\eta}_m$ is a white noise vector for misalignment.

With additional gyro parameters, the gyro rate vector is obtained by

$$\boldsymbol{\omega} = (I_{3\times 3} - M)\boldsymbol{\omega}_m - \hat{\boldsymbol{b}} \tag{3.3.33}$$

where

$$M = \begin{bmatrix} k_x & m_{xy} & m_{xz} \\ m_{yx} & k_y & m_{yz} \\ m_{zx} & m_{zy} & k_z \end{bmatrix} \tag{3.3.34}$$

The state transition matrix is a 15x15 matrix, where the first 3 rows are, without parenthesis and subscript for simplicity,

$$[\phi \quad \gamma \quad \gamma\omega_d \quad \gamma\omega_u \quad \gamma\omega_l] \tag{3.3.34}$$

and, in the remaining rows, all diagonal terms are 1 and non-diagonal terms zero as noted in the previous section.

### 3.5 Batch Least Squares Differential Correction

Estimation of the gyro rate bias is an essential step in using the SIRU output. A batch least squares method provides an alternative to sequential filtering. This description of batch least squares differential correction follows reference [32].

A time series of attitude estimates $\hat{\mathbf{A}}(t_i)$ is computed by propagating an initial attitude $\hat{\mathbf{A}}(t_0)$ forward in time using $\boldsymbol{\omega}_g(t)$ and $\hat{\mathbf{b}}(t_0)$. The angular rate is $\hat{\boldsymbol{\omega}}(t_i) = \mathbf{A}_g^b \boldsymbol{\omega}_g(t_i) + \hat{\mathbf{b}}(t_0)$ and the rotation vector is given by $\mathbf{a} = (t_{i+1} - t_i)\hat{\boldsymbol{\omega}}(t_i)$, where the time interval is short enough that $\hat{\boldsymbol{\omega}}$ is approximately constant. Propagation is performed using

$$\hat{\mathbf{A}}(t_{i+1}) = \mathbf{R}(t_{i+1}, t_0)\hat{\mathbf{A}}(t_0) \tag{3.4.1}$$

where the state transition sub-matrix $\mathbf{R}(t_{i+1}, t_0)$ is computed recursively beginning with $\mathbf{R}(t_0, t_0) = \mathbf{I}_{3\times 3}$

$$\mathbf{R}(t_{i+1}, t_0) = \mathbf{R}(t_{i+1}, t_i)\mathbf{R}(t_i, t_0) = \mathbf{R}(\mathbf{a})\mathbf{R}(t_i, t_0) \tag{3.4.2}$$

and $\mathbf{R}(\mathbf{a})$ is defined in Eq. (3.2.31). The $\mathbf{R}$ matrices must be orthonormal rotation matrices. This can be ensured by converting to a quaternion, normalizing, and converting back to a rotation matrix. The state transition sub-matrix $\mathbf{S}(t_{i+1},t_0)$ is also computed recursively beginning with $\mathbf{S}(t_0,t_0)=\mathbf{0}_{3\times 3}$

$$\mathbf{S}(t_{i+1},t_0)=\mathbf{S}(t_{i+1},t_i)+\mathbf{R}(t_{i+1},t_i)\mathbf{S}(t_i,t_0)=\mathbf{S}(\mathbf{a})+\mathbf{R}(\mathbf{a})\mathbf{S}(t_i,t_0) \qquad (3.4.3)$$

where $\mathbf{S}(\mathbf{a})$ is defined in Eq. (3.2.32) for $\tau=t_{i+1}-t_i$.

The gyro propagated attitudes $\hat{\mathbf{A}}(t_i)$ are used to compute predictions of the star observations. For a star observation $\mathbf{y}_i$ with an observed vector $\mathbf{u}$ in the tracker coordinate frame and a catalog vector $\mathbf{u}'$ in the celestial coordinate frame, the predicted vector in the tracker coordinate frame is $\mathbf{u}''=\hat{\mathbf{A}}(t_i)\mathbf{u}'$. The measurement noise variance for $\mathbf{y}_i$ is $\sigma_i^2$ and the effective observation is the residual $\Delta\mathbf{y}_i=\mathbf{y}_i-\mathbf{h}(\mathbf{u}_i'')$.

The correction vector is $\Delta\hat{\mathbf{x}}\equiv[\Delta\hat{\mathbf{a}}^{\mathrm{T}} \quad \Delta\hat{\mathbf{b}}^{\mathrm{T}}]^{\mathrm{T}}$ and the observation residual is $\Delta\mathbf{y}_i\equiv\mathbf{H}_i\Delta\hat{\mathbf{x}}+\boldsymbol{\varepsilon}_i$ where the measurement sensitivity is

$$\mathbf{H}_i=\begin{bmatrix} 1/u_3 & 0 & -u_1/u_3^2 \\ 0 & 1/u_3 & -u_2/u_3^2 \end{bmatrix}[\mathbf{u}_i\times][\mathbf{R}(t_i,t_0) \quad \mathbf{S}(t_i,t_0)] \qquad (3.4.4)$$

The least squares solution minimizing the sum of the squares of $\boldsymbol{\varepsilon}_i$ is

$$\Delta\hat{\mathbf{x}}=\left(\sum_{i=1}^{n}\sigma_i^{-2}\mathbf{H}_i^T\mathbf{H}_i\right)^{-1}\sum_{i=1}^{n}\sigma_i^{-2}\mathbf{H}_i^T\Delta\mathbf{y}_i \qquad (3.4.5)$$

To end each iteration the corrections are applied using $\hat{\mathbf{b}}(t_0)_+=\hat{\mathbf{b}}(t_0)_-+\Delta\hat{\mathbf{b}}$ and $\hat{\mathbf{A}}(t_0)_+=\mathbf{R}(\Delta\hat{\mathbf{a}})\hat{\mathbf{A}}(t_0)_-$.

Since all of the observations in batch differential correction are transitioned backward in time to $t_0$, time as a variable and information about variations with respect to time are deemphasized. The useful result here is a single point $\hat{\mathbf{b}}(t_0)$ representing a cluster of observations at $t_0$ and it is natural to interpret this point as a type of expected or mean value given the observations.

## 3.6 Attitude Filter Uncertainty Estimates

The following discussion of attitude filter uncertainties follows reference [33]. The term attitude observer is used interchangeably with the term attitude filter. Here the filter is assumed to be made up of three decoupled single-axis observers and the discussion focuses on one axis.

Single-axis star tracker measurements $y$ are modeled in continuous time as

$$y = \theta + v \qquad (3.5.1)$$

where $\theta$ is a small angle in the instrument coordinate frame and $v$ is zero-mean white Gaussian noise $E\{v(t)v(t+\tau)\} = r\delta(\tau)$. The units of $r$ are $rad^2 / Hz = rad^2 s$. In discrete time with star tracker measurement updates every $\Delta$ second

$$r = \Delta\sigma_{nea}^2 / N \qquad (3.5.2)$$

where $\sigma_{nea}$ is the $1\sigma$ noise equivalent angle in radians per star measured, and $N$ is the number of stars per update.

Single-axis gyro measurements $\omega_g$ are modeled as

$$\omega = \omega_g + b + n_1 \qquad (3.5.3)$$

$$\dot{b} = n_2 \qquad (3.5.4)$$

where $\omega$ is the true rate and $b$ is the gyro bias. The two zero-mean white Gaussian noise terms $n_1$ and $n_2$ represent angular random walk and rate random walk, with $E\{n_1(t)n_1(t+\tau)\} = q_1\delta(\tau)$ and $E\{n_2(t)n_2(t+\tau)\} = q_2\delta(\tau)$. The units of $n_1$ and $n_2$ are $rad / s^{1/2}$ and $rad / s^{3/2}$, and the units of $q_1$ and $q_2$ are $rad^2 / s$ and $rad^2 / s^3$.

For the single-axis observer, the state $\mathbf{x}$ is the angle $\theta$ and gyro bias $b$, $\mathbf{x} = [\theta \quad b]^T$. The state error $\boldsymbol{\varepsilon}$ is the difference between the true and estimated states

$$\boldsymbol{\varepsilon} = \mathbf{x} - \hat{\mathbf{x}} \qquad (3.5.5)$$

and the error covariance is

$$\mathbf{P} = E\{\boldsymbol{\varepsilon}\boldsymbol{\varepsilon}^T\} = \begin{bmatrix} p_{11} & p_{12} \\ p_{12} & p_{22} \end{bmatrix} \qquad (3.5.6)$$

The angle error covariance $p_{11}$ represents the uncertainty in the attitude. Reference [33] demonstrates that if the observer uses the standard Kalman filter gain calculations and is in steady-state, so that $\dot{\mathbf{P}} = \mathbf{0}$, then

$$p_{11} = r^{1/2}(q_1 + 2\sqrt{q_2 r})^{1/2} \qquad (3.5.7)$$

This variance describes the steady-state attitude error in terms of the star tracker and gyro unit characteristics alone. The geolocation error budget, released Feb. 2014, allocates 3.1 microradians $1\sigma$ for attitude determination error in PPD. This can be interpreted as the highest allowable value for $\sqrt{2p_{11}}$.

For the LRS, $\Delta = 0.1$ seconds and a mean value $N = 3.5$ is specified in the geolocation error budget. LRS stellar centroid error as 31.5 microradians (1 σ) per 10Hz sample (16.8 microradians per pattern). For the SIRU, based on documentation from Orbital ATK $n_1 = 4.3633E-8 \ rad/s^{1/2}$ and $n_2 = 2.4241E-11 \ rad/s^{3/2}$. Figure 4 shows $\sqrt{p_{11}}$ from Eq. (3.5.7) for a range of $N$ values on the horizontal axis. The plotted curves are for $\sigma_{nea}$ values of 10, 20, 30 and 40 microradians.

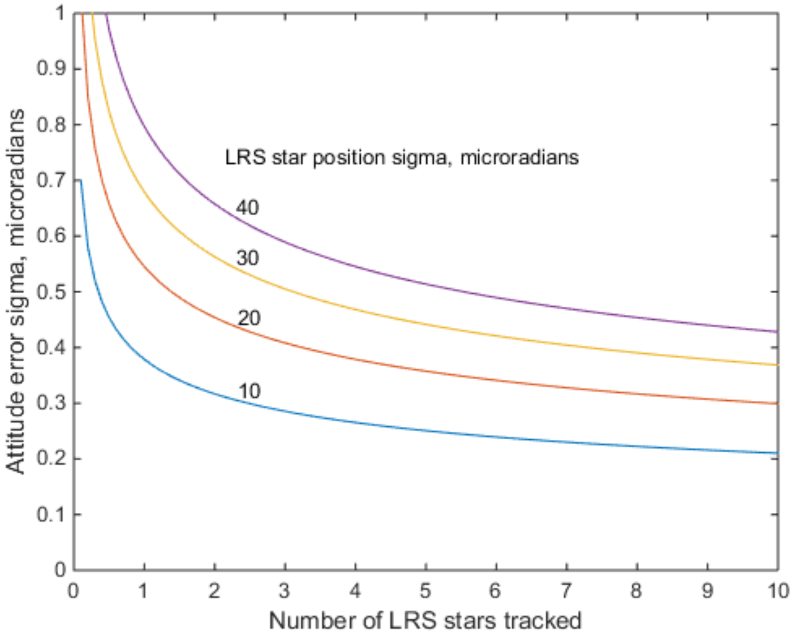

**Fig. 1. PPD filter attitude uncertainty in single axis as a function of the number of LRS stars tracked, and LRS star measurement errors.**

Figure 4 demonstrates that when the LRS is tracking stars so that $N$ is greater than zero, the filter attitude error is significantly less than 2.2 microradians (interpretation of 3.1 microradians to a single axis). However, the actual attitude error could be larger with complexity in the mission data and the realistic simulation.

# 4.0 Implementation

Processing is based on observing the laser pointing vectors in the LRS coordinate frame while estimating the LRS attitude relative to the celestial reference frame. Overview of the procedure is illustrated in Figure 5 with the input, output, and related information. The processor is closely related to the ICESat processor, which also determined laser pointing in the celestial reference frame with a separate instrument. This established heritage means that many of the methods are mature and that their complexities are understood. For example, the direct match technique developed for ICESat Precision Attitude Determination (PAD) [34] continues to be the primary star identification method in the ICESat-2 PAD. The focus of this implementation section is on the unique characteristics of the sensors within the context of the ICESat-2 PPD processor. The discussion is divided by the implementation of each component: star, gyro, and laser telemetry.

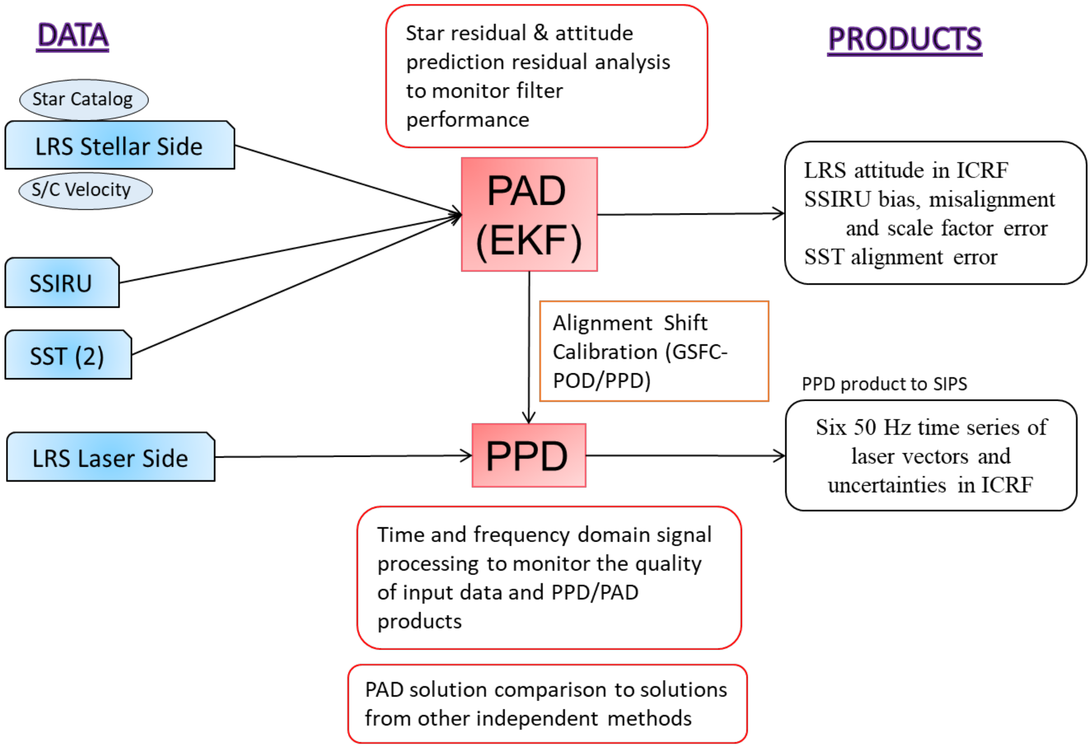

**Fig. 2 PPD System Overview**

## 4.1 Star Telemetry and Model Parameters

LRS stellar-side telemetry provides two-dimensional centroid positions in units of pixels. The FOV is $12^\circ \times 12^\circ$ and the detector is $1024 \times 1024$ with approximately $43.12 arcsec / pixel$ ( $209 \mu rad / pixel$ ). Centroids are converted to unit vectors using the measurement models detailed in this section. The models include deterministic corrections to the measurements that can be thought of as higher-order terms augmenting a first-order geometric model. Some of the important corrections discussed here include integration time, distortion, radial chromatic aberration, centroiding error, and stellar aberration [35-37].

LRS telemetry includes a brightness value (in counts) for each star centroids. The nominal conversion from the LRS stellar-side brightness measurement to instrument magnitude is as follows [38]:

$$I_{mag} = -\log_{10}\left(\frac{\text{brightness counts}}{1060\ \text{counts}}\right) \tag{4.1.1}$$

where the $I_{mag}$ is instrument magnitudes. The anticipated error of the instrument magnitude from the LRS observation is too high (1σ ≈0.85) to use in the star identification as the secondary confirmation information.

The two spacecraft star trackers are closely related to the LRS in an functional sense. Each SST outputs an attitude estimate (quaternion) and uncertainty for its own coordinate frame from the internal processing of the star measurements. Sections 4.1.1-4.1.7 are applied to the star measurements available from the LRS stellar-side. Since the raw star data from the SST will be delivered to the PPD group for the analysis, some of the discussion here is also relevant to the SST star measurement. Section 4.1.8 deals with the SST specific implementation.

### 4.1.1 Unit Vector Representations, Focal Plane and LTP Coordinates

Three-dimensional unit vectors $\mathbf{u}$ have only two degrees of freedom because of the unit constraint $\|\mathbf{u}\| = 1$. One way to take advantage of this is to express a given $\mathbf{u}$ using two coordinates with respect to a reference unit vector $\mathbf{u}_{ref}$. Typically $\mathbf{u}_{ref}$ is the $\mathbf{k}$ axis of an $\mathbf{i},\mathbf{j},\mathbf{k}$ frame and the question is how the $\mathbf{i},\mathbf{j},\mathbf{k}$ frame is defined. A common definition is the $\mathbf{i},\mathbf{j},\mathbf{k}$ frame of a sensor, for example, the LRS stellar-side $\mathbf{i},\mathbf{j},\mathbf{k}$ frame. This case can be referred to as sensor frame coordinates or focal plane coordinates. Another common definition is an $\mathbf{i},\mathbf{j},\mathbf{k}$ frame derived from the body frame and referred to as local tangent plane (LTP) coordinates. Unit vectors in a sensor frame, and their two-coordinate representations, are instrument independent. Conversion from centroids to unit vectors is a conversion from instrument dependent to instrument independent coordinates.

In all cases, within a given $\mathbf{i,j,k}$ frame two coordinates are used to represent unit vectors relative to the $\mathbf{k}$ axis, usually either angles $\theta_h, \theta_v$ or scaled tangent "horizontal and vertical" $h,v$ coordinates. Scaled tangents are often preferable because they can reduce the number of trigonometric function evaluations. In this document, the terms horizontal and vertical coordinates or $h,v$ coordinates indicate that the topic being discussed is associated with three-dimensional unit vectors. Horizontal and vertical coordinates are simply a convenient two-dimensional way to work with three-dimensional unit vectors.

Focal plane coordinates are used here to represent three-dimensional unit vectors in the LRS stellar-side coordinate frame. The LRS coordinate frame, similar to the general case mentioned above, is defined by orthogonal $\mathbf{i,j,k}$ axes in the image or focal plane with the $\mathbf{k}$ axis along the line-of-sight. Star observations are represented by unit vectors $\mathbf{u} = [u_1 \quad u_2 \quad u_3]^T$ pointing from the origin and clustering within six degrees of the $\mathbf{k}$ axis due to the FOV limits. Each unit vector can be specified by an angle $\theta_h$ from the $\mathbf{k}$ axis towards the $\mathbf{i}$ axis, and an angle $\theta_v$ from the $\mathbf{k}$ axis towards the $\mathbf{j}$ axis. The angles $\theta_h$ and $\theta_v$ are given in the output of some commercial star trackers, for example, the two ICESat bus trackers output $a\theta_h$ and $a\theta_v$ where the scaling factor $a \equiv 180 \cdot 60 \cdot 60 / \pi$ . To compute a unit vector $\mathbf{u}$, an intermediate vector $\mathbf{u}' = [h \quad v \quad 1]^T$ is defined using the $h,v$ coordinates

$$h \equiv \tan\theta_h = u_1/u_3 \tag{4.1.2}$$

$$v \equiv \tan\theta_v = u_2/u_3 \tag{4.1.3}$$

and $\mathbf{u}$ is the normalized version of $\mathbf{u}'$

$$\mathbf{u} = \begin{bmatrix} h & v & 1 \end{bmatrix}^T \Big/ \left(h^2 + v^2 + 1\right)^{1/2} \tag{4.1.4}$$

The ICESat LRS computed the ratios $h = x/f$ and $v = y/f$ internally within the instrument and the ICESat GLA04 computed flight data files provided the values $ah$ and $av$ .

Local tangent plane (LTP) coordinates are relative to the body frame $\mathbf{x}$ axis and used to represent clusters of two or more similar unit vectors in the body frame. These clusters of unit vectors can be star observations, star predictions from the filter, sensor LOS vectors, etc. One of the unit vectors is defined as a reference $\mathbf{u}_{ref}$ around which an $\mathbf{i},\mathbf{j},\mathbf{k}$ LTP coordinate frame is formed using

$$\mathbf{i} \equiv \mathbf{j} \times \mathbf{k} \qquad (4.1.5)$$

$$\mathbf{j} \equiv \mathbf{u}_{ref} \times \mathbf{x} \qquad (4.1.6)$$

$$\mathbf{k} \equiv \mathbf{u}_{ref} \qquad (4.1.7)$$

Unit vectors are expressed in an $\mathbf{i},\mathbf{j},\mathbf{k}$ LTP frame by $\mathbf{u} = [u_1 \quad u_2 \quad u_3]^T$ or angles $\theta_h$ and $\theta_v$ from the $\mathbf{k}$ axis towards the $\mathbf{i}$ and $\mathbf{j}$ axes. An intermediate vector $\mathbf{u}' = [h \quad v \quad 1]^T$ is defined using the equations from 4.1.2 and 4.1.3

$$h \equiv \tan\theta_h = u_1/u_3 \qquad \text{~~(4.1.8)~~}$$

$$v \equiv \tan\theta_v = u_2/u_3 \qquad \text{~~(4.1.9)~~}$$

and $\mathbf{u} = \mathbf{u}'/\|\mathbf{u}'\|$. The $\mathbf{i},\mathbf{j}$ plane is tangent to the unit sphere around the body frame origin at the point $\mathbf{k} \equiv \mathbf{u}_{ref}$ and the $h,v$ coordinates are referred to as LTP coordinates. Near the $\mathbf{k}$ axis $h \cong \theta_h$ and $v \cong \theta_v$ and the LTP coordinates are equivalent approximations to angles. The $\mathbf{i}$ axis points as directly as possible (within the tangent plane) towards the body frame $\mathbf{x}$ axis and the $h$ coordinate represents a rotation from $\mathbf{u}_{ref}$ towards or away from the body frame $\mathbf{x}$ axis (depending on its sign). Correlations of the LTP $h,v$ coordinates for LOS variations and measurement residuals (star observations and star predictions) are significant when interpreting filter results.

### 4.1.2 Conversion of Centroids to Unit Vectors

Conversion from centroids to unit vectors is the first step in processing telemetry, partly because it converts from instrument dependent coordinates (centroid position) to instrument independent coordinates (focal plane $h,v$ coordinates).

Consistent with previous sections of this document, the notation here represents the conversion of two-dimensional centroids $x,y$ to three-dimensional unit vectors $\mathbf{u}_1 = \mathbf{f}_1(x,y,\mathbf{p}_1)$ with model parameter vector $\mathbf{p}_1$. Deterministic corrections (for distortion, chromatic aberration, centroiding errors, aberration, etc) are then included via a second model $\mathbf{u}_2 = \mathbf{f}_2(\mathbf{u}_1,\mathbf{p}_2)$ with parameter vector $\mathbf{p}_2$.

The simplest measurement model is based on a pinhole camera and represents the optics as an infinitesimal hole allowing light rays from the stars to pass through with no change of direction [35,39,40]. The focal plane sits behind the pinhole and the minimum distance between the focal plane and pinhole is the focal length $f$ . The point on the focal plane where the distance to the pinhole is a minimum is referred to as the principal point $x_0, y_0$, and is the origin of the two-dimensional focal plane coordinate frame and the three-dimensional instrument coordinate frame. The direction of a light ray hitting the focal plane is specified to first-order by the focal plane coordinates and the focal length.

LRS star position telemetry consists of two-dimensional centroid positions $x, y$ (or H, V) on the focal plane expressed in units of pixels. With parameter estimates for the three pinhole camera model parameters $\mathbf{p}_1 = [f, x_0, y_0]$, a centroid is converted to a unit vector $\mathbf{u}$ by

$$h = (x - x_0)/f \qquad (4.1.8)$$

$$v = (y - y_0)/f \qquad (4.1.9)$$

and $\mathbf{u}_1 = [h \quad v \quad 1]^T / (h^2 + v^2 + 1)^{1/2} = \mathbf{f}_1(x, y, \mathbf{p}_1)$ , taking advantage of the similar triangles

$$h = \tan\theta_h = (x - x_0)/f = u_1/u_3 \qquad (4.1.10)$$

$$v = \tan\theta_v = (y - y_0)/f = u_2/u_3 \qquad (4.1.11)$$

Note that trigonometric functions are not involved and $f, x_0, y_0$ are the only instrument dependent parameters. Once $h, v$ coordinates are computed, $f, x_0, y_0$ are no longer involved, leaving only the instrument independent unit vector $\mathbf{u} = [h \quad v \quad 1]^T / (h^2 + v^2 + 1)^{1/2}$ .

The old version LRS ICD (ICESat-2-LRS-IFACE-1794) defines a different measurement model including a quadratic term to represent a radial deviation from a simple linear model for both the instrument's stellar-side and laser-side. It uses five parameters: $\mathbf{p}_1 = [p_{11}, p_{12}, p_{13}, x_0, y_0]$. The radial distance of a centroid from the principal point is $d = ((x - x_0)^2 + (y - y_0)^2)^{1/2}$. A scaling factor $k$ is given by

$$k = p_{11}d^2 + p_{12}d + p_{13} \qquad (4.1.12)$$

The $h, v$ coordinates of the unit vector are

$$h = \tan\theta_h = \tan(k(x - x_0)) \tag{4.1.13}$$

$$v = \tan\theta_v = \tan(k(y - y_0)) \tag{4.1.14}$$

and $\mathbf{u}_1 = [h \quad v \quad 1]^T / (h^2 + v^2 + 1)^{1/2} = \mathbf{f}_1(x, y, \mathbf{p}_1)$ . The quadratic radial term $p_{11}d^2$ means that similar triangles cannot be taken advantage of to bypass the tan( ) function evaluation during the conversion from instrument dependent coordinates to instrument independent unit vectors. Near the center of the FOV $h \approx \theta_h$ and $v \approx \theta_v$, so $h, v$ coordinates are approximately angular measures with units of radians.

For the stellar-side, the newer version LRS ICD [38] introduces a more sophisticated model to address the radial chromatic aberration. This new model is an evolution of the old version LRS ICD model and is discussed in Section 4.1.5.

### 4.1.3 Integration Time Correction

After conversion to instrument independent three-dimensional unit vectors, an LRS 10 Hz star data packet can consist of up to thirty star observations $\mathbf{u}_i(t - \Delta\tau_i); i = 1,...,30$, each with its own center of integration time offset $\Delta\tau_i$ from the packet time tag $t$ (also referred to as the center of integration base time or simply base time) [38]. The 10 Hz base time $t$ is the sum of two time tag values provided in each packet: the packet header time $t_{\text{Packet Header}}$, and the center of integration base time offset $\Delta t_{\text{COI Base}}$

$$t \equiv t_{\text{Packet Header}} - \Delta t_{\text{COI Base}} \tag{4.1.15}$$

The $i = 1,...,30$ individual star observation time tags $\tau_i$ are

$$\tau_i = t - \Delta\tau_i \tag{4.1.16}$$

And the relation between $t_{\text{Packet Header}}$, $\Delta t_{\text{COI Base}}$ and $\Delta\tau_i$ is illustrated in Figure 6.

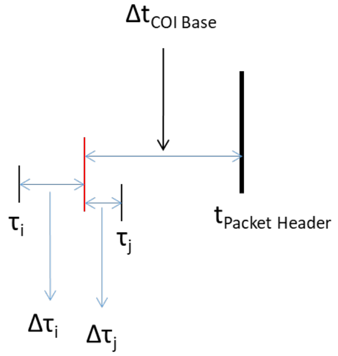

**Fig. 3 LRS Stellar-Side Time-tags**

Integration time correction propagates each unit vector $\mathbf{u}_i(t-\Delta\tau_i)$ over a small time interval $\Delta\tau_i$ Given the observed SIRU coordinate frame angular rate, $\boldsymbol{\omega}_{SIRU}(t)$, the angular rate of the LRS stellar-side coordinate (ST) frame is $\mathbf{A}_b^{ST}(\mathbf{A}_b^{SIRU})^T\boldsymbol{\omega}_{SIRU}$. Over a time interval, the ST frame rotation expressed as a rotation vector $\mathbf{a}$ is given by

$$\mathbf{a}(\mathrm{D}\,\tau_i) = \mathbf{A}_b^{ST}(\mathbf{A}_b^{SIRU})^T\boldsymbol{\omega}_{SIRU}\mathrm{D}\,\tau_i \qquad (4.1.17)$$

where the time interval $\Delta\tau_i$ is short enough that $\boldsymbol{\omega}_{SIRU}(t)$ is approximately constant. The equivalent rotation matrix is $\mathbf{A}(\mathbf{a}(\Delta\tau_i))$. The transpose $\mathbf{A}^T(\mathbf{a}(\Delta\tau_i))$ rotates unit vectors rather than the frame and $\mathbf{u}_i(t)$ is given by

$$\mathbf{u}_i(t) = \mathbf{A}^T(\mathbf{a}(\Delta\tau_i))\mathbf{u}_i(t-\Delta\tau_i) \qquad (4.1.18)$$

Equation (4.1.18) is an exact correction. In practice, approximations can be adequate, for example correcting the $h,v$ coordinates of the unit vectors using their local, observed rate of change $\Delta h/\Delta t$ and $\Delta v/\Delta t$.

### 4.1.4 Distortion Correction

Deterministic corrections to the star unit vectors $\mathbf{u}_1 = \mathbf{f}_1(x, y, \mathbf{p}_1)$ are accommplished using a second model $\mathbf{u}_2 = \mathbf{f}_2(\mathbf{u}_1, \mathbf{p}_2)$ with parameter vector $\mathbf{p}_2$. Since the actual optics and focal plane of the LRS are not adequately represented by an ideal pinhole camera model, the deviations of the real measurements from the first-order transformation require higher-order terms. These higher-order geometric terms, in a generic sense, are described as distortion. The terms and their estimated parameter values comprise most of $\mathbf{p}_2$ and $\mathbf{u}_2 = \mathbf{f}_2(\mathbf{u}_1, \mathbf{p}_2)$.

Distortion errors or low spatial frequency errors (LSFE) refer to deviations from the simple pinhole camera model that are a function of the overall position on the focal plane [36, 39, 41]. These deviations vary slowly over large spatial scales, corresponding to low spatial frequencies. In other words, distortion corrections do not change significantly on the scale of individual pixels, but do change over tens or hundreds of pixels.

Distortion corrections are applied to the measured star unit vectors before utlized in the alignment filter. The ICESat Instrument Star Tracker (IST) distortion correction map is shown in Figure 7 as an example. The largest corrections in the corners of the FOV are approximately 2.5 arcseconds.

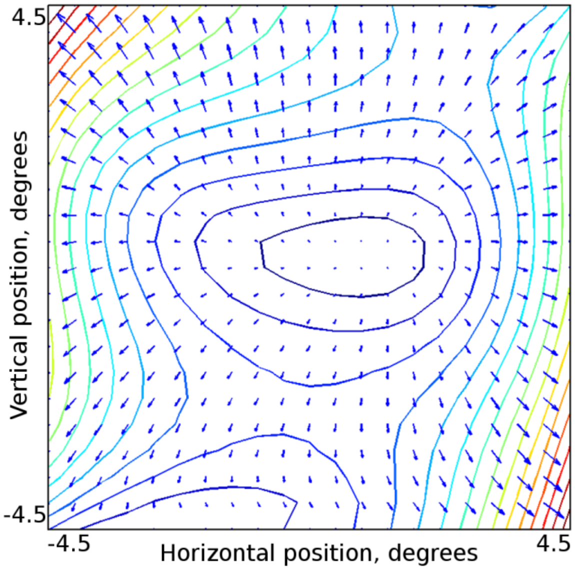

**Fig.4 Distortion corrections of up to 2.5 arcseconds for the IST.**

The PPD algorithm estimates the parameter values by comparing the observed and predicted focal plane $h, v$ coordinates for large numbers of star observations, distributed as uniformly as possible across the focal plane. A three-dimensional surface derived from the observed minus predicted residuals represents the $h, v$ corrections to the observations. Unit vectors are assumed here to be represented by $h, v$ coordinates and all calculations are performed in the two-dimensional $h, v$ plane.

Distortion is based on measurements $\mathbf{u}_1 = [h \quad v]^T$ and measurement residuals $\Delta\mathbf{u}_1 \equiv [\Delta h \quad \Delta v]^T$ calculated during filter measurement updates. A summary of the method for estimating the correction parameters within $\mathbf{p}_2$ is provided here andfollowed by a more detailed discussion of implementation.

As a summary, the measurement residuals are modeled by $\Delta h = \mathbf{h}_h \mathbf{p}_2 + \eta_h$ and $\Delta v = \mathbf{h}_v \mathbf{p}_2 + \eta_v$ where

$$\mathbf{h}_h = \begin{bmatrix} 1 & h & v & h^2 & hv & v^2 & h^3 & h^2 v & hv^2 & v^3 & \mathbf{0}_{1\times10} \end{bmatrix} \tag{4.1.19}$$

$$\mathbf{h}_v = \begin{bmatrix} \mathbf{0}_{1\times10} & 1 & h & v & h^2 & hv & v^2 & h^3 & h^2 v & hv^2 & v^3 \end{bmatrix} \tag{4.1.20}$$

and $\eta_h, \eta_v$ are zero-mean Gaussian white noise. For a sample of measurements and residuals, the observation vector $\mathbf{H}^T \Delta\mathbf{u}_1$ and information matrix $\mathbf{H}^T \mathbf{H}$ are accumulated by $(\mathbf{H}^T \Delta\mathbf{u}_1)_i = (\mathbf{H}^T \Delta\mathbf{u}_1)_{i-1} + \mathbf{h}_h^T \Delta h + \mathbf{h}_v^T \Delta v$ and $(\mathbf{H}^T \mathbf{H})_i = (\mathbf{H}^T \mathbf{H})_{i-1} + \mathbf{h}_h^T \mathbf{h}_h + \mathbf{h}_v^T \mathbf{h}_v$ beginning with $(\mathbf{H}^T \Delta\mathbf{u}_1)_0 = \mathbf{0}_{20\times1}$ and $(\mathbf{H}^T \mathbf{H})_0 = \mathbf{0}_{20\times20}$. The least squares estimate of the distortion parameters $\mathbf{p}_2$ is given by $\hat{\mathbf{p}}_2 = \left(\mathbf{H}^\mathrm{T}\mathbf{H}\right)^{-1} \mathbf{H}^\mathrm{T} \Delta\mathbf{u}_1$.

In more detail, let $\mathbf{u}_{1j}$ be the *j*th measurement and $\mathbf{u}'_{1j}$ be the corresponding prediction

$$\mathbf{u}_{1j} = [u_{11} \quad u_{12} \quad (u_{11}^2 + u_{12}^2)^{1/2}]^T \tag{4.1.21}$$

$$\mathbf{u}'_{1j} = [u'_{11} \quad u'_{12} \quad (u'^2_{11} + u'^2_{12})^{1/2}]^T \tag{4.1.22}$$

The effective observations $\mathbf{y} = \begin{bmatrix} y_h & y_v \end{bmatrix}^T$ are modeled by

$$y_h = u_{11} - u'_{11} = \mathbf{h}_h \mathbf{p}_2 + \eta_h \tag{4.1.23}$$

$$y_v = u_{12} - u'_{12} = \mathbf{h}_v \mathbf{p}_2 + \eta_v \tag{4.1.24}$$

where $\boldsymbol{\eta} = [\eta_h \quad \eta_v]^T$ is zero-mean Gaussian white noise $E\{\boldsymbol{\eta}^T \boldsymbol{\eta}\} = \sigma_y^2 \mathbf{I}$. The information matrix $\mathbf{H}^T \mathbf{H}$ and observations vector $\mathbf{H}^T \mathbf{y}$ are accumulated from $(\mathbf{H}^T \mathbf{H})_0 = \mathbf{0}_{20\times20}$ and $(\mathbf{H}^T \mathbf{y})_0 = \mathbf{0}_{20\times1}$

$$(\mathbf{H}^T\mathbf{H})_j = (\mathbf{H}^T\mathbf{H})_{j-1} + \mathbf{h}_h^T\mathbf{h}_h + \mathbf{h}_v^T\mathbf{h}_v \tag{4.1.25}$$

$$(\mathbf{H}^T\mathbf{y})_j = (\mathbf{H}^T\mathbf{y})_{j-1} + \mathbf{h}_h^T y_h + \mathbf{h}_v^T y_v \tag{4.1.26}$$

and the parameter estimate is given by

$$\hat{\mathbf{p}}_2 = (\mathbf{H}^T\mathbf{H})^{-1}\mathbf{H}^T\mathbf{y} \tag{4.1.27}$$

This generalization allows for various models $\mathbf{h}_h$ and $\mathbf{h}_v$ to be used.

Centroiding errors or high spatial frequency errors (HSFE) refer to deviations away from the pinhole camera model that are a function of small changes of position on the focal plane, on the scale of individual pixels [35, 37]. These deviations vary rapidly over small spatial scales, corresponding to high spatial frequencies, and are generally caused by the spatial quantization of the star images, in other words converting continuous light distributions into discrete pixel brightness values.

The optics are slightly defocused to spread a star image over multiple pixels, making it possible to estimate the centroid at sub-pixel levels, but there remains some centroiding error due to the discrete sampling of the image. This error is visibly apparent as the star image moves across pixel boundaries. If the spacecraft is rotating with a constant rate, a star image moves across the focal plane with approximately the same constant rate (there can be higher-order optical effects near the edges of the FOV). The rate of the measured centroid motion has a small periodic variation as the image moves across pixel boundaries. Deterministic centroiding errors are expected to be at the sub-arcsecond level, per star. For $n$ star observations the effects of these errors on attitude estimation decrease by $1/\sqrt{n}$.

Centroiding error has a significantly smaller effect than distortion and is typically treated as a small stochastic (noise) error that is averaged out by the processor filtering of large numbers of star observations. In effect, it is included in the observation uncertainty $\mathbf{R}$ and is not explicitly treated as a deterministic error and corrected in $\mathbf{u}_2 = \mathbf{f}_2(\mathbf{u}_1, \mathbf{p}_2)$.

### 4.1.5 Chromatic Aberration Correction

The LRS stellar-side optics experiences chromatic aberration, in which light of different wavelengths is imaged at different radial positions in the focal plane. The color correction formula is provided by the LRS developer, to correct the positions of the stellar centroids in the LRS using stars' color indices. The spectral response of the star tracker to the wavelength of the starlight is represented by the color index of each star. The LRS star catalog, also provided by the LRS developer, contains color indices of the entry stars. The formula is basically the variation of the LRS ICD model in Equation (4.1.12), which means that the color correction is applied during the conversion of the raw pixel measurements to the angle unit (radian) measurements. Equations (4.1.28-4.1.36) below are the formula with the original notations with the notations used by the LRS developer [38].

$$H_{angle} = (A\,R_2^2 + B\,R_2 + C)\,H_2 + H_1 \tag{4.1.28}$$

$$V_{angle} = (A\,R_2^2 + B\,R_2 + C)\,V_2 + V_1 \tag{4.1.29}$$

$$R_1 = \sqrt{(H_{pixel} - H_0)^2 + \left(V_{pixel} - V_0\right)^2} \tag{4.1.30}$$

$$R_2 = K_0\,R_1 \tag{4.1.31}$$

$$H_2 = \tan^{-1}\left[\left(H_{pixel} - H_0\right)K_0\right] \tag{4.1.32}$$

$$V_2 = \tan^{-1}\left[\left(V_{pixel} - V_0\right)K_0\right] \tag{4.1.33}$$

$$A = a_1 i^2 + a_2 i + a_3 \tag{4.1.34}$$

$$B = b_1 i^2 + b_2 i + b_3 \tag{4.1.35}$$

$$C = c_1 i^2 + c_2 i + c_3 \tag{4.1.36}$$

The $i$ is a color index of each star, $K_0$ is pixel-to-radian scale factor, $H_0$, $V_0$ are the optical center (i.e. principal point), $H_1$, $V_1$ are tip, tilt angles, and $a_k$, $b_k$, and $c_k$ (k=1,2,3) are color coefficients. The $H_1$, $V_1$ are provided for generality. It is anticipated that they are absorbed into their rotations from HV coordinates to ATLAS coordinate frame described in Section 4.3.1. The original formula applied arctangent function on $K_0\,R_1$ in Eq. (4.1.31) for the calculation of $R_2$ [38]. The application of arctangent is moved to Eq. (4.1.32) and Eq. (4.1.33) to make the definition of focal plane angles coincident with that in the existing PAD software.

Evidence of the chromatic aberration is found in the data from the LRS stellar-side night sky test [42]. Six stars with distinctive wavelengths were effectively observed for about 30 minutes with the rate of Earth rotation. The spectral classes of the measured stars are diverse: K, B, F, M, A, and G. With the corresponding star color, they are W(white), R(red), B(blue), Y(yellow), BW(black-white), and O(orange) stars as indicated in Figure 8. They moved across in near-diagonal direction at different locations of the LRS FOV, but did not move along the normal and expected straight lines. The deviation from the linear motion gets larger as stars move away from the optical center with the maximum of ~250 $\mu$rad based on analysis. Considering that the stars crossed only half of the 12°x12° FOV during the night sky test, the deviation would be much greater if they move across the whole FOV.

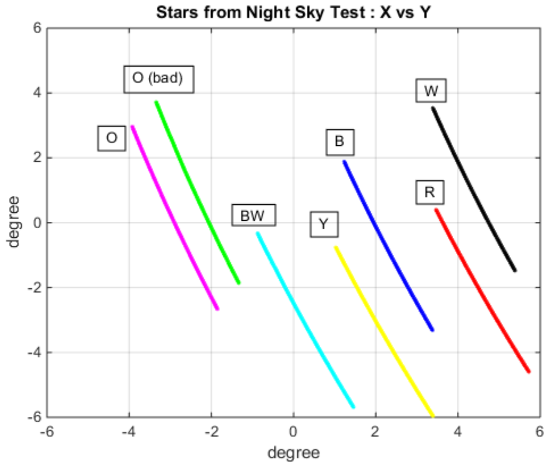

**Fig. 5 Night Sky Test stars with Earth rate angular velocity**

The LRS developer provided the LRS star catalog [2] that is a subset of Hipparcos star catalog by selecting stars brighter than magnitude 6. It includes the color correction index of each star with the uncertainty of 0.1 for blue and red stars and 0.04 for the remaining stars. From 4360 stars in the catalog, about 23.4% of stars fall to blue or red stars. The color (correction) index *i* is not simply an astronomical color index defined by the difference of the star magnitudes measured by two filters sensitive to light at different wavelengths. It also reflects detector's spectral response to the particular star wavelength as well as thermal coating spectral properties of the sunshade. The color index error is important since it eventually limits the accuracy of the color correction.

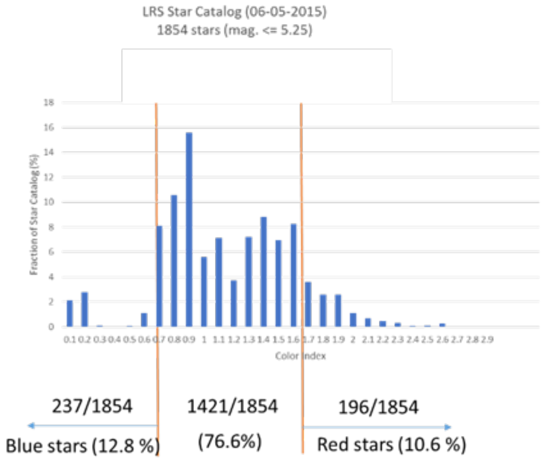

**Fig. 6 Color index distribution of the stars in the LRS star catalog**

The color correction formulas in Eqs. (4.1.28-4.1.36) indicate that the star position error due to the chromatic aberration depends on the color index *i* and the distance from the optical center $R_2$, if the color coefficients $a_k$, $b_k$, and $c_k$ (k=1,2,3) are known. Based on the night sky test data, the LRS developer derived pre-launch color coefficient values for of the initial chromatic aberration corrections once ICESat-2 is operationalin the early stages of the mission.However, the accuracy of these intial coefficients is not reliable for PPD because it is based on only a handful of measured stars over a fraction of the LRS FOV and most notably, the test environment is different from actual flight environment due to technical difficulties. Computation of the color coefficients based on many actual on-orbit star measurements is imperative to meet the PPD requirement of the mission. The color correction algorithm is developed for the determination of the color coefficients using millions of LRS star measurements. The algorithm is described below:

1. Determine attitude with an EKF using LRS stars and SIRU data, initially with the preliminary, pre-launch color coefficients or without color correction. The attitude determination generates the output file that contains information about the measured stars; star centroids in pixel unit, star unit vector at ICRF obtained from star identification, and estimated attitude in quaternion. The attitude determination should be conducted over a long enough time span to collect sufficient amount of star measurements in support of deriving updated color coefficients. The data collected are sorted out to generate multiple files; each of them is allocated for individual stars.

2. Compute $R_1$, $R_2$, $H_2$, and $V_2$ using the measured pixel coordinates ($H_{pixel,}V_{pixel}$) of each star during the measurement period. The initial value of ($H_0$,$V_0$) is from the prelaunch measurement or simply the geometrical center of the FOV. Using the least squares method, estimate $A, B, C$, of each star. It starts with the addition of the square of Eq. (4.1.28) and Eq. (4.1.29) to yield

$$\theta_c = (A\,R_2^2 + B\,R_2 + C)\,\theta_m \qquad (4.1.37)$$

where

$$\theta_c = \sqrt{H_{angle}^2 + V_{angle}^2} \qquad (4.1.38)$$

and

$$\theta_m = \sqrt{H_2^2 + V_2^2} \qquad (4.1.39)$$

$\theta_m$ is easily calculated by Eq. (4.1.32) and Eq. (4.1.33). For $\theta_c$, ($H_{angle}$, $V_{angle}$) is calculated by

$$H_{angle} = \tan^{-1}\frac{W_{c,x}}{W_{c,z}} \tag{4.1.40}$$

$$V_{angle} = \tan^{-1}\frac{W_{c,y}}{W_{c,z}} \tag{4.1.41}$$

where the star vector $[W_{c,x} \quad W_{c,y} \quad W_{c,z}]^T$ is computed by the projection of the star unit vector, $\vec{V}$, in the ICRF, onto the LRS ST coordinate frame by

$$\overrightarrow{W_c} = A_{CRF}^{ST}\,\vec{V} \tag{4.1.42}$$

The $A_{CRF}^{ST}$ is estimated attitude. The only unknown in Eq. (4.1.37) is $A, B$, and $C$. By dividing both sides of the equation with $\theta_m$, $S_\theta$ is defined as $\theta_c/\theta_m$. Then

$$S_\theta = AR^2 + BR + C \tag{4.1.43}$$

where $S_\theta$ is close to 1. If the star is observed near the optical center where the chromatic aberration error is normally pretty small, the singularity problem may arise. Those measurements should be ignored.

Eq. (4.1.43) is for one measurement of the selected star. In the ICESat-2's nominal orbit, without maneuver, the star could be observed for up to ~190 seconds over the LRS FOV in 10 Hz rate. Accumulating the star measurements over multiple orbits, thousands of measurements for the same star will be available, which allow to set up the system of equations;

$$\begin{bmatrix} S_{\theta,1} \\ S_{\theta,2} \\ \vdots \\ S_{\theta,n} \end{bmatrix} = \begin{bmatrix} R_{2,1}^2 & R_{2,1} & 1 \\ R_{2,2}^2 & R_{2,2} & 1 \\ \vdots & \vdots & \vdots \\ R_{n,2}^2 & R_{n,2} & 1 \end{bmatrix} \begin{bmatrix} A \\ B \\ C \end{bmatrix} \tag{4.1.44}$$

where $n$ is the number of measurements for the star. It can be written concisely as

$$Y = R\,X + \varepsilon \tag{4.1.45}$$

by defining

$$Y = [S_{\theta,1} \quad S_{\theta,2} \quad \cdots \quad S_{\theta,n}]^T \tag{4.1.46}$$

(4.1.47)

$$R = \begin{bmatrix} R_{2,1}^2 & R_{2,1} & 1 \\ R_{2,2}^2 & R_{2,2} & 1 \\ \vdots & \vdots & \vdots \\ R_{2,n}^2 & R_{2,n} & 1 \end{bmatrix} \tag{4.1.48}$$

$$X = [A \quad B \quad C]^T$$

and $\varepsilon$ is the $n \times 1$ error vector.

By applying the least squares method to minimize the error vector $\varepsilon$ [43], the estimates of the coefficients vector, $X$, is determined as

$$X = (R^T R)^{-1} R^T\, Y \tag{4.1.49}$$

The coefficients $A$, $B$, and $C$ of the specific star are components of $X$. The same procedure is applied to all other stars that are available in the same time period.

3. The estimated coefficients, $A$, $B$, and $C$ are not the same for different stars. In the LRS star catalog, each star has its own color index number. For multiple stars, Eq. (4.1.34) is expanded to build the system of equations with the coefficient $A$ and color index of each star. Similar derivation described in Step 2 produces the least squares solution for $a_1$, $a_2$, and $a_3$. In the same way, color coefficients in Eq. (4.1.35) and Eq. (4.1.36) are derived. It completes the determination of nine color coefficients.

4. Because the initial estimated attitude $A_{CRF}^{ST}$ has relatively large errors due to the chromatic aberration, iteration of the above procedure is required. Repeat steps 1-3 with the updated color coefficients (and improved attitude) until the termination condition is met. In each iteration, the most recent color coefficients are applied to correct measured star positions.

Figure 10 summarizes the overall color correction procedure. First, the attitude is determined using LRS and gyro data with the initial value of color coefficients, optical center $(H_0, V_0)$ and focal length $f$. Note that the color coefficients cannot be estimated correctly if the three pinhole model parameters $(H_0, V_0, f)$ are not sufficiently accurate. Unlike the color coefficient estimation described above, the determination of the optical center ($H_0$, $V_0$) and the focal length $f$ uses the existent method [44]. It is an independent procedure from the color coefficient estimation and named as *optical center estimation* in Figure 10.

The attitude determination is repeated with the updated optical center and focal length. The new attitude solution is used for the color coefficients estimation. The color correction formula with the updated color coefficients and optical parameters is applied to the star measurements in the next attitude determination. The iterative process is necessary to achieve high accuracy of color correction and attitude solution.

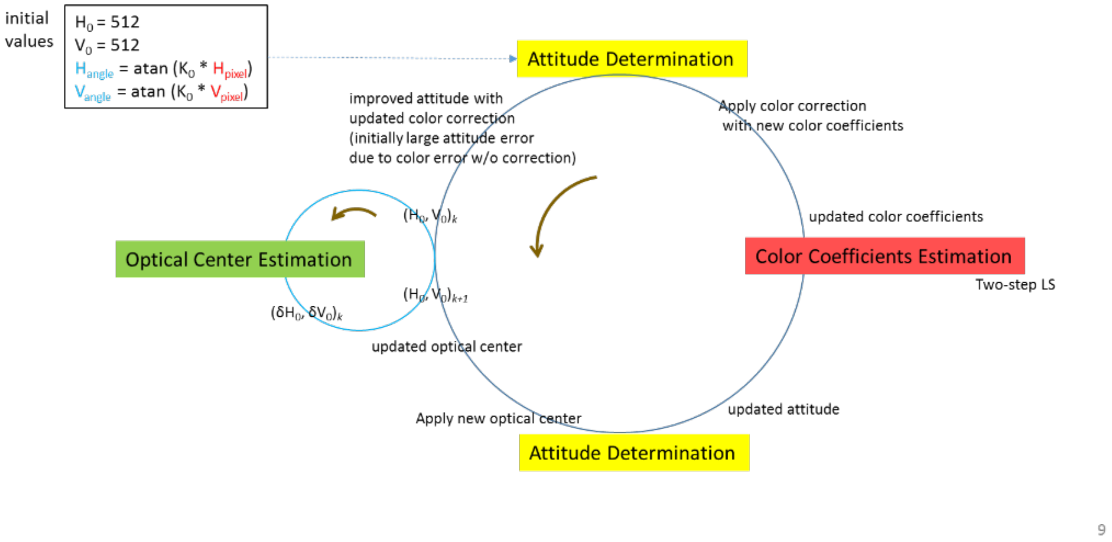

**Fig. 7 Color Correction Diagram**

The star identification in the PAD is based on both pattern matching and direct match technique. The algorithms are described in ICESat PAD ATBD[34]. The ICESat pattern matching performed the star identification successfully with the ICESat star tracker data, however, it sometimes failed when the chromatic aberration is added to the simulated star data. About 4% of the simulation cases, the huge position error of the star centroids obstruct the correct identification at the start of the EKF. Note that the daily EKF (PAD) starts with coarse attitude information. The alternative pattern matching based on K-vector search method is implemented to replace the ICESat pattern matching [45] that eventually showed the successful performance under the chromatic aberration. The direct match technique, which is used for more than 95% of star identification (after the pattern matching is successful), is efficient regardless of the chromatic aberration. It is because the direct match technique is a star tracking method rather than star identification except for the time when the new star enters into the LRS FOV.

### 4.1.6 Stellar Aberration Correction

The telemetry value of the spacecraft velocity vector is used for stellar aberration correction. Supporting telemetry included in HDF5 data that concern the spacecraft state include position and velocity, temperatures, solar array position, and various housekeeping data.In stellar aberration, the observed direction **u** of a star is displaced from its true direction by an amount which depends on the transverse velocity of the observer. In practice this velocity is the sum of the Earth velocity and spacecraft velocity, both expressed in the ICRF. The displacement of the observed star direction can have a magnitude on the order of 20 arcseconds by the Earth velocity. The aberration correction can be applied either to the star predictions or to the star observations [46]. Here all vectors including the observer velocity vector **v** are expressed in the observer's coordinate frame (observer frame). In practice, this is a sensor frame; the LRS stellar-side (ST) frame given the Earth velocity vector in the ICRF $\mathbf{v}_{EARTH,ICRF}$, the spacecraft velocity vector in the ICRF $\mathbf{v}_{SC,ICRF}$, and the LRS attitude $\mathbf{A}_i^{ST}$

$$\mathbf{v} = \mathbf{A}_i^{ST}(\mathbf{v}_{EARTH,ICRF} + \mathbf{v}_{SC,ICRF}) \qquad (4.1.50)$$

For an observed star direction **u** in the stellar-side frame, the direction corrected for stellar aberration is

$$\mathbf{u}' = (\mathbf{u} - \mathbf{v}/c)/\|\mathbf{u} - \mathbf{v}/c\| \qquad (4.1.51)$$

Aberration correction can be incorporated with the deterministic correction $\mathbf{u}_2 = \mathbf{f}_2(\mathbf{u}_1, \mathbf{p}_2)$, but for simplicity and clarity, the implementation is usually separate and easily distinguishable.

### 4.1.7 Noise Estimation Using the Triangle Method

In this section unit vectors are assumed to be represented by $h, v$ coordinates and all calculations are performed in the two-dimensional $h, v$ plane. The error model is $\mathbf{u} = \mathbf{h} + \boldsymbol{\eta}$ where $\mathbf{u}$ is the observed unit vector, $\mathbf{h}$ is the true unit vector, and $\boldsymbol{\eta}$ is zero-mean Gaussian white noise $E\{\boldsymbol{\eta}^T\boldsymbol{\eta}\} = \sigma_u^2\mathbf{I}$. Measurement noise $\sigma_u$ is estimated empirically for use in the measurement covariance $\mathbf{R} = E\{\boldsymbol{\eta}_u\boldsymbol{\eta}_u^T\} = \sigma_u^2\mathbf{I}$. The estimate is based on variations of the angular separations between pairs of stars [47]. The variance of the separations between stars $a$ and $b$ is equal to the sum of their individual noise variances $\sigma_{ab}^2 = \sigma_a^2 + \sigma_b^2$, where $\sigma_{ab}^2$ is calculated directly from a set of simultaneous measurements of stars $a$ and $b$. For a set of simultaneous measurements of three stars $a$, $b$ and $c$ the variances of the separations form 3 equations $\sigma_{ab}^2 = \sigma_a^2 + \sigma_b^2$, $\sigma_{ac}^2 = \sigma_a^2 + \sigma_c^2$

, and $\sigma_{bc}^2 = \sigma_b^2 + \sigma_c^2$ with 3 unknowns $\sigma_a^2$, $\sigma_b^2$ and $\sigma_c^2$. When there are $n > 3$ measured stars over a given time period there is a variable number $m$ of measured angular separations. If $m > n$ the resulting system of equations is solved using the least squares methods. Estimated noise as a function of star brightness for ICESat is shown in Figure 11.

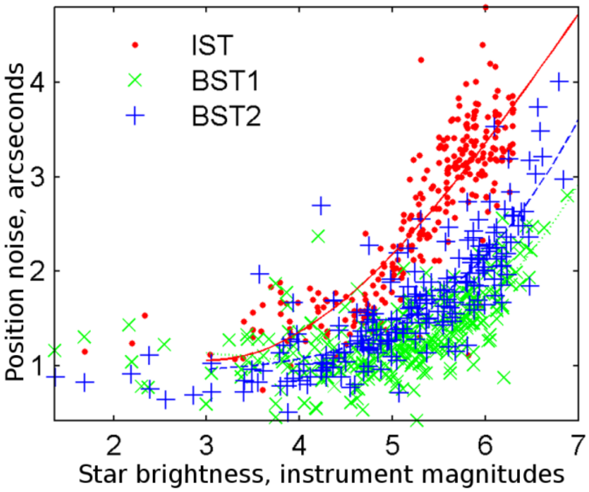

**Fig.8 Measurement noise from ICESat star trackers**

Note that the identities of the stars used for noise estimation do not appear in the estimation process such that the noise estimation can be performed before and independently from star identification. Essentially the noise estimation process is completed by tracking some selected spots within the sensor FOV which leaves only the question of the temporal variation of the angle separation between those spots.

The simplest implementation is clearly a batch estimation process in which a large batch of interstar variances $\sigma_{xy}^2$ are stored over time and then a single least squares estimate of the individual star positions variances $\sigma_a^2, \sigma_b^2, \sigma_c^2, \sigma_d^2, \ldots$ is calculated. Extension to a sequential algorithm and implementation is clearly both possible and practical but may not be worthwhile unless there is evidence that the noise depends on time as well as star brightness. If the noise is time varying a sequential method capable of tracking the variations may be worthwhile. Otherwise, a lookup table of noise as a function of star brightness should be sufficient based on heritage and simulation studies.

### 4.1.8 SST Quaternion Measurement

The two spacecraft star trackers are supporting components to the LRS stellar-side as the SSTs provide attitude estimates that are useful for interpreting and using the LRS star telemetry and are particularly important with the LRS stellar-side experiences solar blindness Each SST outputs an attitude estimate and uncertainty for its own coordinate frame. In practice the measurement model needed to interpret and SST attitude estimate is simply the estimated rotation $\mathbf{A}_b^{ST}(\mathbf{A}_b^{SST})^T$ between the SST and LRS stellar-side coordinate frames, and the error model represents the uncertainties $\mathbf{R}_{SST}$ and $\sigma_{SST}^2$ in $\mathbf{A}_i^{SST}$ and $\mathbf{A}_b^{SST}$.

The ATLAS frame $\mathbf{A}_i^{ATLAS}$ is associated with simulation, modeling, and truth values. It is an abstract and ideal frame that is not necessarily tied to a specific sensor or empirical measurements. Pointing truth can be expressed as two time series representing the true attitude of the ATLAS frame $\mathbf{A}_i^{ATLAS}$ and the true laser unit vector(s) in the ATLAS frame.

A spacecraft frame $\mathbf{A}_i^{SC}$ is defined for onboard attitude control. The spacecraft frame is defined and effectively owned by Orbital ATK, the spacecraft vendor. Working toward optimal compatibility between the ATLAS frame and the spacecraft frame ~~there~~ some general conventions have been established for use whenever practical (for the ATLAS frame, spacecraft frame, body frame, etc).

1. X axis along the centerline of the spacecraft and positive out through the ATLAS instrument.
2. Y axis opposite from the solar array.
3. Z axis parallel to the ATLAS telescope line of sight.

In the reference attitude mode (with ATLAS forward and the spacecraft behind) the X,Y,Z axes are aligned with the natural orbit frame roll, pitch, yaw axes and the overall angular rate is approximately -229 arcsec/sec on Y (pitch).

Artificial telemetry is generated for the SSTs based on their reference alignments $\mathbf{A}_{ATLAS}^{SST1}$ and $\mathbf{A}_{ATLAS}^{SST2}$. The telemetry simply consists of the attitudes given by

$$\mathbf{A}_i^{SST1} = \mathbf{A}_{ATLAS}^{SST1}\mathbf{A}_i^{ATLAS} \tag{4.1.52}$$

$$\mathbf{A}_i^{SST2} = \mathbf{A}_{ATLAS}^{SST2}\mathbf{A}_i^{ATLAS} \tag{4.1.53}$$

Alignment variations $\mathbf{a}_{SST1}(t), \mathbf{a}_{SST2}(t)$ and noise $\boldsymbol{\eta}_{SST1}, \boldsymbol{\eta}_{SST2}$ are added to give

$$\mathbf{A}_i^{SST1} = \mathbf{A}(\mathbf{a}_{SST1}(t))\mathbf{A}_{ATLAS}^{SST1}\mathbf{A}_i^{ATLAS} + \boldsymbol{\eta}_{SST1} \tag{4.1.54}$$

$$\mathbf{A}_i^{SST2} = \mathbf{A}(\mathbf{a}_{SST2}(t))\mathbf{A}_{ATLAS}^{SST2}\mathbf{A}_i^{ATLAS} + \boldsymbol{\eta}_{SST2} \tag{4.1.55}$$

The reference alignments $\mathbf{A}_{ATLAS}^{SST1}$ and $\mathbf{A}_{ATLAS}^{SST2}$ are based on values provided by Orbital ATK.

$$\mathbf{A}_{ATLAS}^{SST1} = \begin{bmatrix} -.5 & -.7071 & .5 \\ -.5 & .7071 & .5 \\ -.7071 & 0 & -.7071 \end{bmatrix}^{\mathbf{T}} \tag{4.1.56}$$

$$\mathbf{A}_{ATLAS}^{SST2} = \begin{bmatrix} .5 & -.7071 & -.5 \\ -.5 & -.7071 & .5 \\ -.7071 & 0 & -.7071 \end{bmatrix}^{\mathbf{T}} \tag{4.1.57}$$

In the ATLAS coordinate frame, the SST LOS vectors are $SST1 = [0.5 \quad 0.5 \quad -0.7071]^T$ and $SST2 = [-0.5 \quad 0.5 \quad -0.7071]^T$. The LRS stellar-side LOS vector is $ST = [0 \quad 0 \quad -1]^T$. This creates a pyramid geometry with each SST LOS $45^\circ$ from the LRS ST LOS and $60^\circ$ from the other SST LOS. Another perspective on SST geometry is that the LRS ST LOS is along the spacecraft frame -Z axis and the SST LOSs are in their own SST plane. Take the plane defined by the spacecraft X,-Z axes and rotate it about the X axis by 35.26 degrees towards the Y axis (so away from the solar array). This is the SST plane. Within the SST plane, the SST LOSs are 60 degrees apart. One is 30 degrees forwards towards the X axis, one is 30 degrees back towards the -X axis.

## 4.2 Gyro Telemetry and Model Parameters

The SIRU is used to propagate the attitude estimate forward in time between measurement epochs from the LRS. In practice, propagation covers the time span between two measurement updates. SIRU output is recorded at 50 Hz, providing pointing information at higher frequencies than the 10 Hz star observations. With a precision on the order of tenths of an arcsecond, it also provides higher angular resolution. Despite the bandwidth and precision of the instrument, SIRU attitude propagation is associated with the growth of pointing uncertainty, while the LRS and SSTs are associated with reduced pointing uncertainties. Over shorter time scales the error characteristics of the SIRU dominate the uncertainties and drive their growth, appearing directly in the filter as process or state noise.The gyro observations represent changes of direction over time. Past observations are required to interpret new observations and functionally the gyros act as a memory unit. By contrast, the star trackers observe directions in space and are memoryless in the sense that information from the past is not required to interpret new observations, each one is independent.

The time tags of the 50 Hz LRS laser observations determine the time tags of the 50 Hz PPD product. This means that the time tags of the LRS laser observations are effectively a set of target times at which the processor needs to estimate the six laser pointing vectors and uncertainties. The 50 Hz SIRU output can be used used to propagate and interpolate the pointing estimates to the target time tags.

The SIRU consists of four hemispherical resonator gyros arranged with their sense axes forming an octahedral tetrad pyramid shape. The gyros are of the rate integrating type, outputting an angle expressed as an integer count which wraps as the output register overflows or underflows. One count is equal to 0.05 arcseconds. The overall unit is effectively a black box with four output registers updated at 100 Hz, one for each sense axis. The spacecraft records the values in the output registers asynchronously at 50 Hz, along with a time tag.

The angular output is transformed into rates by calculating the angular change per unit time in a preprocessor. The same preprocessor edits out repeated records, outliers, and other problem data. One reason for converting from angles to rates is that the filter state represents attitude and rate but requires the rate to come from an external source. No attempt is made to model the rotational dynamics of the spacecraft and integrate the angular accelerations. Instead, rates are taken directly from the SIRU. This process is referred to as model replacement.

In model replacement, the dynamical model found in many Kalman filters is replaced by empirical rate observations. The contribution to rate knowledge from the filter is the time-varying rate bias correction $\hat{\mathbf{b}}$ estimated during the measurement updates using the information in the LRS star observations and the SST attitude observations. This is particularly important because $\hat{\mathbf{b}}$ absorbs the effects of SIRU alignment variations. Variations of $\mathbf{A}_b^{SIRU}$ appear directly as variations in $\hat{\mathbf{b}}$.

SIRU output is used for several specific, discrete tasks within the implementation of the processor:

1. Propagating the body frame attitude estimate $\mathbf{A}_i^b$ forward in time from one star update to the next.
2. Calculating the state transition matrix $\mathbf{\Phi}$ for propagation of the state covariance $\mathbf{P}$ forward in time from one star update to the next.
3. Propagation of LRS star and laser observations over short time intervals (<<0.1 seconds). These are effectively small corrections to align time tags and closely related to simple interpolation.
4. Monitoring for higher-frequency pointing variations (jitter).

More indirectly, parameter estimates characterizing the SIRU also appear directly in the process noise matrix $\mathbf{Q}$ and determine the growth of body frame attitude uncertainty between star updates.

### 4.2.1 SIRU Geometry and Coordinate Frame Definitions

Several high-level SIRU characteristics can be inferred from Orbital ATK and Northrup Grumman documentation. Figure 12 illustrates the Orbital ATK spacecraft coordinate frame with +Z in the nadir direction, +Y opposite the solar array (orbit normal direction and pitch axis), and +X out of the page (velocity direction and roll axis). The first question is how does the SIRU frame (gyro unit coordinate frame) relate to the spacecraft frame?

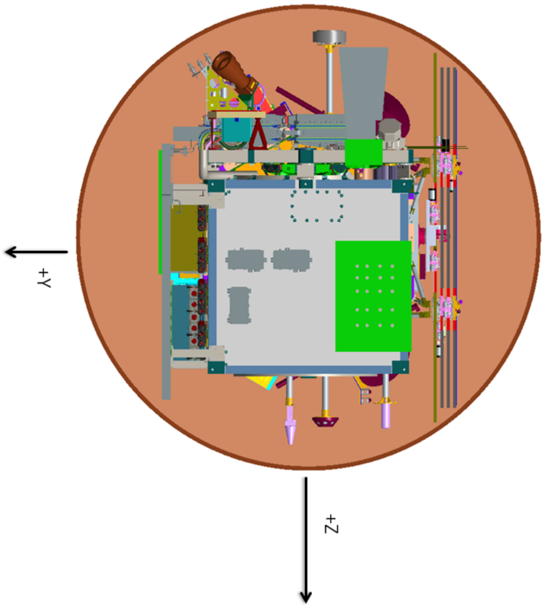

**Fig.9 Orbital ATK spacecraft frame and SIRU (upper left).**

Figure 13 is taken from Orbital ATK documentation of the Instrument Mounted Spacecraft Component (IMSC) and shows an early SST orientation that has since been changed. The IMSC is a natural semi-empirical (physical but without direct sensor measurements) definition because it is a compact and stable structure, and carries the SIRU and SSTs.

Comparing the three IMSC support feet or brackets to other figures indicates that the Orbital ATK spacecraft frame +Y direction is to the right. This orientation and the details of the SIRU agree with Figure 14 below.

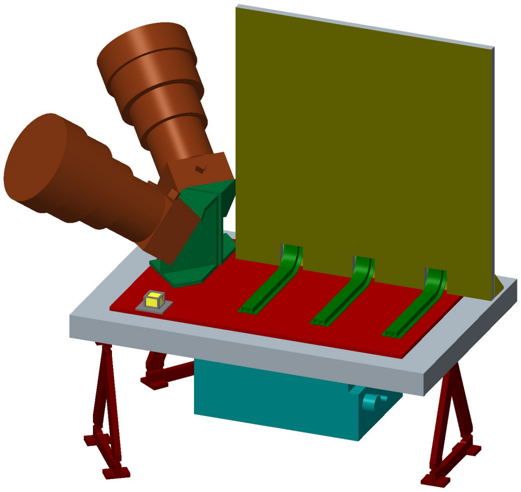

**Fig.10 IMSC and SIRU. OSC spacecraft frame +Y is towards the right.**

Figure 14 is taken from NG documentation and shows the SIRU coordinate frame definition. This definition seems to agree with the Orbital ATK spacecraft frame in the previous two figures. The ~~inference~~ working assumption here is that the SIRU frame and spacecraft frame are meant to be aligned and have similar axes and definitions. If this assumption is incorrect, it is probably wrong by a simple 90° or 180° rotation about the +Z axis and does not have a qualitative effect on the discussion below. The actual coordinate transformation between SIRU frame and spacecraft frame has been provided by the Orbital ATK and will be used in the real PPD processing.

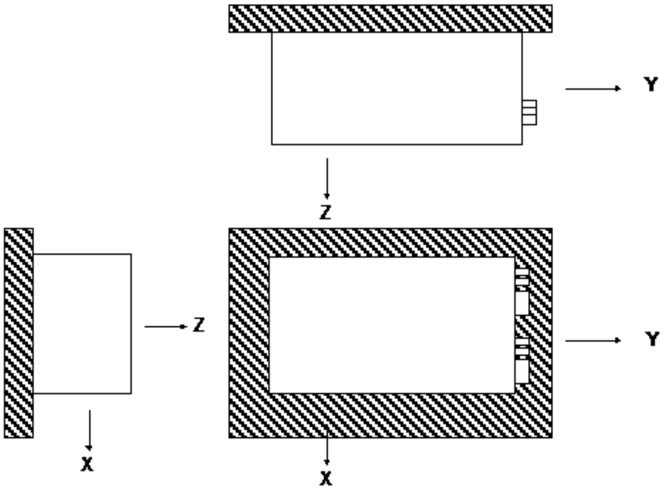

**Fig.11 SIRU coordinate frame. This seems to match the OSC spacecraft frame.**

Figure 15 is from NG documentation and shows the sense axes relative to the SIRU frame (and therefore the spacecraft frame as well). In summary, the four sense axes symmetrically divide the four spacecraft frame roll and pitch directions (+X, +Y, -X, –Y). Each sense axis is $54.736^\circ$ from the roll and pitch axes (or their negatives). $\cos(54.736^\circ) = 0.5774$ so the sense axes measure $0.5774$ of the rotation about their neighboring roll and pitch axes.

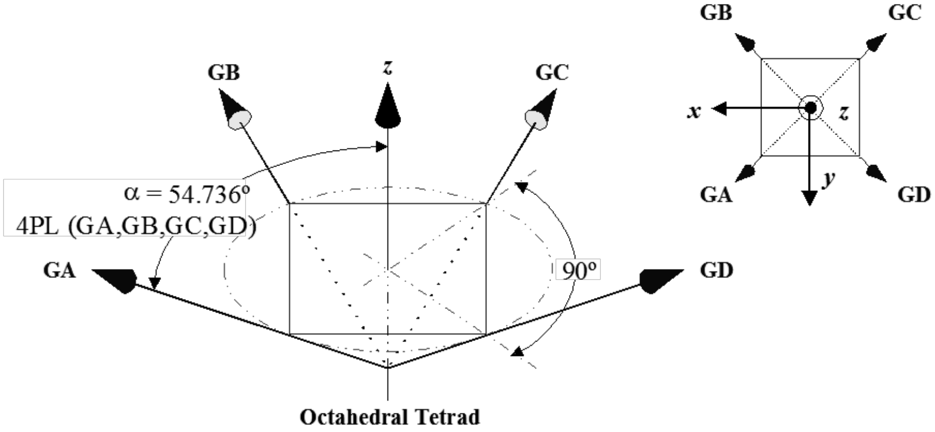

**Fig.12 SIRU sense axes**

The observed SIRU frame rate $\boldsymbol{\omega}_{SIRU}(t)$ expressed in the SIRU frame is given by

$$\mathbf{G}_{4\times 3}\boldsymbol{\omega}_{SIRU}(t) = \boldsymbol{\omega}_s(t) \qquad (4.2.1)$$

where $\mathbf{G}$ is a $4\times 3$ matrix relating the four sense axes rates $\boldsymbol{\omega}_s(t)$ to $\boldsymbol{\omega}_{SIRU}(t)$. For the simplest case $\mathbf{G} = \mathbf{W}^T$ where the ideal sense axes directions expressed in the gyro unit frame are the columns of $\mathbf{W}$ and $\boldsymbol{\omega}_{SIRU}(t)$ is given by

$$\mathbf{W}^T\boldsymbol{\omega}_{SIRU}(t) = \boldsymbol{\omega}_s(t) \qquad (4.2.2)$$

$$\boldsymbol{\omega}_{SIRU}(t) = (\mathbf{W}\mathbf{W}^T)^{-1}\mathbf{W}\boldsymbol{\omega}_s(t) \qquad (4.2.3)$$

The ideal sense axes directions expressed in the SIRU frame are the columns of $\mathbf{W}$ and NG documentation provides the following definition

$$\mathbf{W} = \frac{1}{\sqrt{3}}\begin{bmatrix} 1 & 1 & -1 & -1 \\ 1 & -1 & -1 & 1 \\ 1 & 1 & 1 & 1 \end{bmatrix} \qquad (4.2.4)$$

The estimated body frame rate $\hat{\boldsymbol{\omega}}$ expressed in the body frame is given by $\hat{\boldsymbol{\omega}} = (\mathbf{A}_b^{SIRU})^T \boldsymbol{\omega}_{SIRU} + \hat{\mathbf{b}}$, and if the body frame definition is equivalent to the Orbital ATK spacecraft frame then $\mathbf{A}_b^{SIRU} = \mathbf{I}$ and $\hat{\boldsymbol{\omega}} = \boldsymbol{\omega}_{SIRU} + \hat{\mathbf{b}}$.

### 4.2.2 Sense Axes Angular Counts and Angular Rates

The four sense axes are rate-integrating gyros and the SIRU outputs a vector $\boldsymbol{\theta}_s(t_k)$ of four angular counts with units of 0.05 arcseconds per count. The counts range from 0 to 65,535 and wrap on underflow or overflow. When counts increase past 65,535 they wrap to 0, and when they decrease past 0 they wrap to 65,535. Some significant angular count quantities for nadir pointing are shown in Table 3.

**Table 3 SIRU sense axis angular counts during nadir pointing**

| | 50 Hz, 0.02 seconds | 10 Hz, 0.1 seconds | 1 Hz, 1 second |
|---|---|---|---|
| Pitch axis, arcsec | 4.56 arcsec | 22.8 arcsec | 228 arcsec |
| Sense axis, arcsec | 2.63 arcsec | 13.16 arcsec | 131.65 arcsec |
| Sense axis, counts | 53 counts | 263 counts | 2632 counts |

In general, the significant information in the SIRU output is the angular increment $\Delta\boldsymbol{\theta}_s(t_k)$ from $t_k$ and $t_{k+1}$ given by

$$\Delta\boldsymbol{\theta}_s(t_k) \equiv \boldsymbol{\theta}_s(t_{k+1}) - \boldsymbol{\theta}_s(t_k) \qquad (4.2.5)$$

The angles must be unwrapped during the calculation of $\Delta\boldsymbol{\theta}_s(t_k)$ in order to get correct or even reasonable results. The four sense axis increments $\Delta\boldsymbol{\theta}_s(t_k)$ can be converted to three SIRU frame angular increments $\Delta\boldsymbol{\theta}_{SIRU}(t_k)$ by

$$\Delta\boldsymbol{\theta}_{SIRU}(t_k) = (\mathbf{W}\mathbf{W}^T)^{-1}\mathbf{W}\Delta\boldsymbol{\theta}_s(t_k) \qquad (4.2.6)$$

$\boldsymbol{\theta}_s(t_k)$ and $\Delta\boldsymbol{\theta}_{SIRU}(t_k)$ are expressed about the sense axes directions or SIRU frame axes. $\Delta\boldsymbol{\theta}_{SIRU}(t_k)$ is closely related to common roll-pitch-yaw Euler angles which are also expressed about the coordinate frame axes. This suggests that $\Delta\boldsymbol{\theta}_{SIRU}(t_k)$ is useful information in its own right (and $\Delta\boldsymbol{\theta}_s(t_k)$ as well by extension) since it reflects roll-pitch-yaw magnitude. This is particularly true over time intervals short enough that the SIRU frame does not change (rotate) significantly. Over short enough time intervals the SIRU frame can be propagated using $\Delta\boldsymbol{\theta}_{SIRU}(t_k)$ alone, without involving an angular rate $\boldsymbol{\omega}_{SIRU}(t_k)$ and integration.

Angular rates about each sense axis $\boldsymbol{\omega}_s(t_k) = \mathbf{f}(\Delta\boldsymbol{\theta}_s(t_k))$ and $\boldsymbol{\omega}_{SIRU}(t_k)$ are calculated as observed angular change per unit time.

$$\boldsymbol{\omega}_s(t_k) \equiv \frac{\boldsymbol{\theta}_s(t_{k+1}) - \boldsymbol{\theta}_s(t_k)}{t_{k+1} - t_k} = \frac{\Delta\boldsymbol{\theta}_s(t_k)}{\Delta t} \tag{4.2.7}$$

$$\boldsymbol{\omega}_{SIRU}(t) = (\mathbf{W}\mathbf{W}^T)^{-1}\mathbf{W}\frac{\Delta\boldsymbol{\theta}_s(t_k)}{\Delta t} \tag{4.2.8}$$

One of the advantages of angular rates $\boldsymbol{\omega}_s(t_k)$ and $\boldsymbol{\omega}_{SIRU}(t_k)$ is that the filter estimates their biases $\hat{\mathbf{b}}$ for correcting $\hat{\boldsymbol{\omega}}$ in $\hat{\boldsymbol{\omega}} = (\mathbf{A}_b^{SIRU})^T \boldsymbol{\omega}_{SIRU} + \hat{\mathbf{b}}$.

The 50 Hz SIRU output is monitored in both the time and frequency domains for evidence of high frequency pointing variations. Due to the sampling theorem, this evidence can be more qualitative than quantitative. Correlations with entering and exiting eclipse, solar panel motion, maneuvers, changes of ATLAS state, etc are of particular interest. An important question is which forms of the output are more useful and significant in practice: $\Delta\boldsymbol{\theta}_s(t_k)$, $\Delta\boldsymbol{\theta}_{SIRU}(t_k)$, $\boldsymbol{\omega}_s(t_k)$, or $\boldsymbol{\omega}_{SIRU}(t_k)$. In principle the information content in the four forms is equivalent. In practice, the ease of interpretation may vary.

### 4.2.3 Signal Processing

Time and frequency domain analysis of the SIRU output has a direct influence on the estimated pointing uncertainty, along with the expected performance as characterized by the pointing and jitter requirements. Jitter refers here to pointing variation at frequencies that are too high to be observed by the SIRU, but different hypothetical cases and their effects on the SIRU output and pointing uncertainty can be characterized. In other words, the estimated pointing uncertainties should reflect both all of the information content in the SIRU output, and the expected performance based on the pointing requirements. A significant question is how as much information can be extracted from the SIRU as possible.

The discussion here focuses on time and frequency domain signal processing for a generic signal time series $x(t_k)$ at sample times $t_k$ with approximately constant sampling intervals $\Delta t$ so that

$t_{k+1} - t_k \approx \Delta t$. Here $x(t_k)$ represents one component taken from of any of the time series $\Delta\boldsymbol{\theta}_s(t_k)$, $\Delta\boldsymbol{\theta}_{SIRU}(t_k)$, $\boldsymbol{\omega}_s(t_k)$, or $\boldsymbol{\omega}_{SIRU}(t_k)$. For example $x(t_k)$ can be the pitch component of $\Delta\boldsymbol{\theta}_{SIRU}(t_k)$ or $\boldsymbol{\omega}_{SIRU}(t_k)$, or the sense axis A component of $\Delta\boldsymbol{\theta}_s(t_k)$ or $\boldsymbol{\omega}_s(t_k)$. No distinction is necessary for the signal processing here; the signal here is simply a generic time series $x(t_k)$. In the interpretation of the results, the units associated with the signals should be carefully distinguished: $\Delta\boldsymbol{\theta}_s(t_k)$ and $\Delta\boldsymbol{\theta}_{SIRU}(t_k)$ are arcseconds or radians, $\boldsymbol{\omega}_s(t_k)$ and $\boldsymbol{\omega}_{SIRU}(t_k)$ are arcsec/s or rad/s.

In practice, we are primarily interested here in the high frequency components $x_H(t_k)$ within $x(t_k)$ and the first step is to remove the lowest frequency components $x_L(t_k)$ leaving

$$x_H(t_k) = x(t_k) - x_L(t_k) - b \qquad (4.2.9)$$

where $b$ is a constant bias and $x_H(t_k)$ is approximately zero-mean, $E\{x_H(t_k)\} \approx 0$, over longer timescales. The low frequency components in $x_L(t_k)$ represents trends, variations, and deviations from the constant $b$ over longer timescales. In short, removing the bias and low frequency components leaves the approximately zero-mean high frequency components $x_H(t_k)$.

The question here is how to estimate $x_L(t_k)$ in the time domain in order to subtract it from $x(t_k)$. One approach is to Fourier transform the time domain signal $x(t_k)$ into the frequency domain $X(\omega)$ and remove the low frequencies $X_L(\omega)$ using a frequency domain high-pass filter. Instead, the same effect will be achieved here by directly estimating $x_L(t_k)$ in the time domain for ease of physical interpretation.

One method for estimating $x_L(t_k)$ is a moving average (moving window average, boxcar average, etc). The moving average function is represented here by $ma_\alpha(\ )$ where the subscript $\alpha$ is a parameter for the amount of data to use for each average, or equivalently the averaging window size.

A more sophisticated method is locally weighted scatterplot smoothing (LOESS), represented here by the function $loess_{\alpha,\lambda}(\ )$. There are two parameters $\alpha$ and $\lambda$: $\alpha$ again represents the amount of data to use for each fit, and $\lambda$ is the degree of the local fit polynomial. When $\lambda = 0$ LOESS is exactly equivalent to the moving average function, $loess_{\alpha,\lambda=0}(\ ) = ma_\alpha(\ )$. For $\lambda = 1$ and $\lambda = 2$ linear or quadratic polynomials are fit within each data window. Examples of LOESS results for two time series are shown in Figure 16. In the figure on the right, LOESS results for different parameters $\alpha$ and $\lambda$ are shown in red and blue. Different low frequency ranges can be estimated and removed depending on the LOESS tuning.

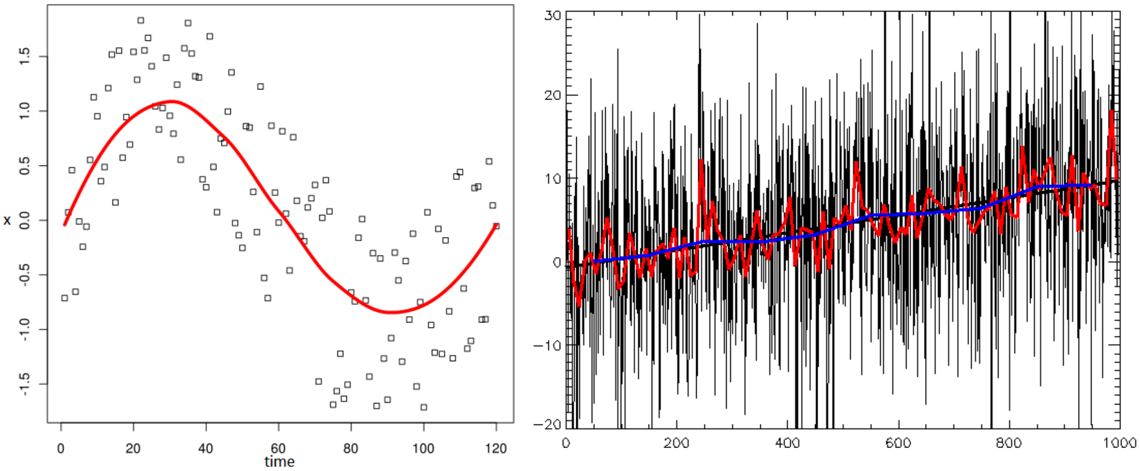

**Fig.13 Examples of LOESS results for the low frequency signals (red and blue) in two time series.**

With $x_L(t_k) = loess_{\alpha,\lambda}\left(x, t_k\right)$ and

$$x_H(t_k) = x(t_k) - loess_{\alpha,\lambda}\left(x, t_k\right) - b \qquad (4.2.10)$$

the approximately zero mean high frequency variations can be analyzed in the time domain $x_H(t_k)$ or Fourier transformed into the frequency domain $X_H(\omega)$.

With 50 Hz sampling of the SIRU output, the sampling theorem states that the usable bandwidth for detecting periodic signals is $50Hz/2 = 25Hz$. In practice, signals up to approximately $0.9(50Hz/2) = 22.5Hz$ may be detectable in $X_H(\omega)$ using the rule of thumb that about 0.1 of the usable bandwidth is lost to filter roll-off and noise. This is a useful amount of bandwidth for monitoring the time series $\Delta\boldsymbol{\theta}_s(t_k)$, $\Delta\boldsymbol{\theta}_{SIRU}(t_k)$, $\boldsymbol{\omega}_s(t_k)$, and $\boldsymbol{\omega}_{SIRU}(t_k)$. For example, the types of pointing variations observed on ICESat during solar array rotation (1 Hz and 3 Hz, Ref. [48]) should be easily detected and characterized in roll and pitch from $\Delta\boldsymbol{\theta}_{SIRU}(t_k)$ alone.

### 4.2.4 Measurement Model and Parameters

The SIRU measurement model combines the four observed sense axes rates into the three-component angular rate vector for the SIRU frame. This is a linear, geometric transformation, summing the contributions from the rates about the four sense axes to the rates about the three SIRU frame axes. It plays a role similar to the first-order pinhole camera model for the LRS, converting centroid positions to a three-dimensional vector observation.

The measurement model includes several types of corrections for each sense axes including geometric misalignment from the ideal octahedral tetrad, and scale factors of various types. Ground test values for these parameters are provided by NG, and parameter estimation is performed using flight data. Angular rate variations are required to make many of the parameters observable. Special SIRU calibration maneuvers will be performed, and the periodic ocean scan maneuvers may be usable as well.

The SIRU measurement model is the matrix $\mathbf{G}$ given by

$$\mathbf{G} = (\mathbf{I} - \mathbf{\Lambda})(\mathbf{W} - \mathbf{U}\mathbf{\Delta}_{\mathbf{v}} - \mathbf{V}\mathbf{\Delta}_{\mathbf{u}})^T \tag{4.2.11}$$

where $\mathbf{\Lambda} \equiv diag(\boldsymbol{\lambda})$ for scale factors $\boldsymbol{\lambda}_{4\times1}$ , and $\mathbf{\Delta}_{\mathbf{u}} \equiv diag(\mathbf{u})$ , $\mathbf{\Delta}_{\mathbf{v}} \equiv diag(\mathbf{v})$ for sense axes misalignments $\mathbf{u}_{4\times1}$ and $\mathbf{v}_{4\times1}$. The sense axes outputs are incorporated into the filter as the SIRU frame angular increment and angular rate

$$\Delta\boldsymbol{\theta}_{SIRU}(t) = (\mathbf{G}^T\mathbf{G})^{-1}\mathbf{G}^T\Delta\boldsymbol{\theta}_s(t) \tag{4.2.12}$$

$$\boldsymbol{\omega}_{SIRU}(t) = (\mathbf{G}^T\mathbf{G})^{-1}\mathbf{G}^T\boldsymbol{\omega}_s(t) \tag{4.2.13}$$

and the body frame angular rate estimate

$$\hat{\boldsymbol{\omega}} = (\mathbf{A}_b^{SIRU})^T\boldsymbol{\omega}_{SIRU} + \hat{\mathbf{b}} \tag{4.2.14}$$

The rate bias estimate $\hat{\mathbf{b}}$ is also classed as part of the measurement model. The rate bias for a sense axis is the observed rate when the true rate is zero. The time varying corrections $\hat{\mathbf{b}}(t)$ are critical and updated as frequently as possible. When the angular rates are approximately constant the effects of the model parameters in $\mathbf{G}$ are effectively absorbed in $\hat{\mathbf{b}}(t)$. The $\hat{\mathbf{b}}(t)$ term also plays an important alignment role by effectively absorbing the effects of variations in $\mathbf{A}_b^{SIRU}$ [12, 13].

The misalignment terms $\mathbf{\Delta}_{\mathbf{u}} \equiv diag(\mathbf{u})$ and $\mathbf{\Delta}_{\mathbf{v}} \equiv diag(\mathbf{v})$ correct for deviations of the sense axes away from the ideal octahedral tetrad pyramid shape defined by

$$\mathbf{W} = \frac{1}{\sqrt{3}}\begin{bmatrix} 1 & 1 & -1 & -1 \\ 1 & -1 & -1 & 1 \\ 1 & 1 & 1 & 1 \end{bmatrix} \tag{4.2.15}$$

The ideal sense axes directions expressed in the SIRU frame are the columns of the geometry matrix $\mathbf{W}$. A $\hat{\mathbf{u}},\hat{\mathbf{v}},\hat{\mathbf{w}}$ coordinate frame is defined for each sense axis, with the $\hat{\mathbf{w}}$ axis along the ideal direction and appearing as one of the columns in $\mathbf{W}$. The $\hat{\mathbf{u}}$ and $\hat{\mathbf{v}}$ axes can be defined by convention (agreement) or deterministic methods described in the literature [12, 14, 19]. The geometry matrices $\mathbf{U}$ and $\mathbf{V}$ are defined as

$$\mathbf{U}=\begin{bmatrix}\hat{\mathbf{u}}_1 & \hat{\mathbf{u}}_2 & \hat{\mathbf{u}}_3 & \hat{\mathbf{u}}_4\end{bmatrix} \qquad (4.2.16)$$

$$\mathbf{V}=\begin{bmatrix}\hat{\mathbf{v}}_1 & \hat{\mathbf{v}}_2 & \hat{\mathbf{v}}_3 & \hat{\mathbf{v}}_4\end{bmatrix} \qquad (4.2.17)$$

with the columns again expressing the ideal direction in the SIRU frame.

The deviation of each sense axis away from its ideal direction is expressed as a two-dimensional rotation vector $u,v$ in the plane orthogonal to the ideal direction. Collected together, the deviations for all the axes form the misalignment vectors $\mathbf{u}_{4\times1}$ and $\mathbf{v}_{4\times1}$.

The scale factor term $\mathbf{\Lambda}\equiv diag(\boldsymbol{\lambda})$ corrects for differences between the real and observed rate variations. If the real rate is varied as a linear ramp, the observed rate should also vary as a linear ramp with the same slope. The scale factor $\lambda_i$ is the correction for the *i*th sense axis. There are variations on this concept, such as symmetric scale factors that are the same for positive and negative rates, or asymmetric scale factors that are different for positive and negative rates [14, 19].

### 4.2.5 Error Model and Parameters

The SIRU error model describes stochastic processes contributing to the SIRU output. The error model is closely associated with the uncertainties in the pointing knowledge product. The dominant uncertainties appear in the filter as attitude and rate process noise, which are tied to the error model.

Kalman filter gyro error models are commonly based on parameter estimates for angular white noise (AWN), angular random walk (ARW), and rate random walk (RRW). The filter is assumed here to be of the model replacement type with gyros replacing dynamical modeling in the filter state equation.

In model replacement mode the SIRU measurements do not enter the filter via measurement updates, and error modeling does not enter the filter as measurement noise. Instead, SIRU error modeling enters via the process or state noise, and is characterized by parameters for AWN, ARW, and RRW. These parameters serve as approximations and simplifications for the parameters in a full gyro error model such as the IEEE standard model in reference [49].

Stochastic errors over short time scales are associated with AWN and ARW and can generically be associated with gyro noise (as opposed to gyro drift). Pointing uncertainty over short time scales is of special importance here because the SIRU provides all of the available shorter timescales (higher frequency) pointing information. SIRU noise, parameterized as $\sigma^2_{awn}$ and $\sigma^2_{arw}$, and the SIRU output recording rate of 50 Hz are the main limitations on 50 Hz pointing knowledge.

In practice the output from a rate integrating gyro held motionless in inertial space does not remain constant. AWN is a zero-mean Gaussian white noise variation of the output. Its parameter estimate is angular white noise variance $\sigma^2_{awn}$ and has units of radians$^2$. Its effects can be driven down by increasing the sample size.

ARW is a stochastic process described as integrated white noise and results in an angular bias in the output time series $\boldsymbol{\theta}(t_k)$. The angular bias growth is proportional to the root of the time span so slows over time. Its parameter estimate is angular random walk variance $\sigma^2_{arw}$ and has units of radians$^2$/second.

In the filter process noise matrix

$$\mathbf{Q}_k(t) = \begin{bmatrix} (\sigma^2_{awn} + t\sigma^2_{arw} + (t^3/3)\sigma^2_{rrw})\mathbf{I} & (t^2/2)\sigma^2_{rrw}\mathbf{I} \\ (t^2/2)\sigma^2_{rrw}\mathbf{I} & t\sigma^2_{rrw}\mathbf{I} \end{bmatrix} \qquad (4.2.18)$$

$\sigma^2_{awn} + t\sigma^2_{arw}$ are the dominant terms over short timescales. Over longer time scales the $\sigma^2_{rrw}$ terms become dominant. In MEKF-based alignment and attitude filtering, RRW is used to characterize bias instability and can generically be associated with gyro drift (as opposed to gyro noise). With 10 Hz observations from the LRS stellar-side and two SSTs, the filter does not experience long time intervals between measurement updates and the cumulative effects of gyro drift are kept small.

### 4.2.6 Filter Propagation

Propagation of the body frame attitude estimate $\mathbf{A}_i^b$ over a specified time interval is performed by integrating the body frame angular rate estimate $\hat{\boldsymbol{\omega}}$ given by

$$\hat{\boldsymbol{\omega}} = (\mathbf{A}_b^{SIRU})^T \boldsymbol{\omega}_{SIRU} + \hat{\mathbf{b}} \qquad (4.2.19)$$

Over a time interval $t_{k+1} - t_k$ short enough that $\hat{\boldsymbol{\omega}}$ is approximately constant, the propagation rotation vector is given by

$$\mathbf{a} = (t_{k+1} - t_k)\hat{\boldsymbol{\omega}}(t_k) \tag{4.2.20}$$

For $\mathbf{A}_i^b$ expressed as a quaternion $q_{ref}$ and the rotation vector $\mathbf{a}$ expressed as a quaternion $q(\mathbf{a})$ , propagation of the attitude and state from $t_k$ to $t_{k+1}$ is given by

$$q_{ref}(t_{k+1}) = q(\mathbf{a}) \otimes q_{ref}(t_k) \tag{4.2.21}$$

$$\hat{\mathbf{x}}(t_{k+1}) = \hat{\mathbf{x}}(t_k) \tag{4.2.22}$$

Attitude propagation when the assumption of constant $\hat{\boldsymbol{\omega}}$ is not valid if $t_{k+1} - t_k$ is too long or $d\hat{\boldsymbol{\omega}}/dt$ is too large. Note that these conditions can result if the SIRU telemetry has a high rate. In practice, with 50 Hz SIRU telemetry there may be times when the assumption that $d\hat{\boldsymbol{\omega}}/dt \approx 0$ over $t_{k+1} - t_k$ breaks down. The attitude can then be propagated using what is referred to here as the Inertial Navigation System (INS) method described in reference [18].

The INS method was designed with high frequency jitter and high gyro sampling rates in mind and is a relatively accurate way to calculate the rotation vector $\mathbf{a}$ in Eq. (4.2.21). Jitter and rapid maneuvers can cause an unwanted effect termed coning during attitude propagation. The INS method is based on the Bortz equation, the kinematic equation for the rate of change of a rotation vector $\mathbf{a}$ .

The Bortz equation for $d\mathbf{a}/dt$ is given by

$$\begin{aligned} d\mathbf{a}/dt &\approx \boldsymbol{\omega} + (\boldsymbol{\alpha} \times \boldsymbol{\omega})/2 \\ &\equiv \dot{\boldsymbol{\alpha}} + \dot{\boldsymbol{\beta}} \end{aligned} \tag{4.2.23}$$

where $\boldsymbol{\alpha} \equiv \int \boldsymbol{\omega} dt$ represents integrated angular rate and $\boldsymbol{\beta} \equiv \int (\boldsymbol{\alpha} \times \boldsymbol{\omega})/2 dt$ represents coning motion. When the coning motion is negligible $d\mathbf{a}/dt \approx \boldsymbol{\omega}$ which is equivalent to Eq. (4.2.20).

The objective of the INS method is to calculate the rotation vector $\mathbf{a}_m$ after a time interval $t_m$ from initial conditions $t_0 = 0$ and $\mathbf{a}_0 = \mathbf{a}(t_0) = \mathbf{0}$. The time interval $t_0$ to $t_m$ is termed the slow-cycle and in practice corresponds the total propagation interval, here the time between two filter measurement updates.

There are a number of sub-intervals termed the fast-cycle and defined by SIRU measurement. The index $l$ indicates which fast-cycle is currently being processed, beginning with $l = 0$ at $t_0 = 0$. The calculations in each fast-cycle staring with $l = 1$ are shown below, where $\boldsymbol{\alpha}_0 = \mathbf{0}$ and $\boldsymbol{\beta}_0 = \mathbf{0}$. In practice $\Delta\boldsymbol{\alpha}_l$ is a SIRU angular increment $\Delta\boldsymbol{\theta}_{SIRU}(t_k)$ from Eq. (4.2.5). In other words the INS method both assumes and is designed for rate-integrating gyro output.

$$\Delta\boldsymbol{\alpha}_l = \int_{t_{l-1}}^{t_l} d\boldsymbol{\alpha} \qquad (4.2.24)$$

$$\Delta\boldsymbol{\beta}_l = \frac{1}{2}\left(\boldsymbol{\alpha}_{l-1} + \frac{1}{6}\Delta\boldsymbol{\alpha}_{l-1}\right) \times \Delta\boldsymbol{\alpha}_l \qquad (4.2.25)$$

$$\boldsymbol{\alpha}_l = \boldsymbol{\alpha}_{l-1} + \Delta\boldsymbol{\alpha}_l \qquad (4.2.26)$$

$$\boldsymbol{\beta}_l = \boldsymbol{\beta}_{l-1} + \Delta\boldsymbol{\beta}_l \qquad (4.2.27)$$

When $t_l = t_m$ the fast-cycle calculations are complete and $\mathbf{a}_m$ is given by

$$\mathbf{a}_m = \boldsymbol{\alpha}_l + \boldsymbol{\beta}_l \qquad (4.2.28)$$

Essentially what the INS method provides that the basic propagation of Eq. (4.2.20) does not is the effect of the coning term $\boldsymbol{\beta}_l$.

For covariance propagation, the state transition matrix is given by

$$\boldsymbol{\Phi}_k(t) = \begin{bmatrix} \mathbf{R}(\mathbf{a}) & \mathbf{S}(\mathbf{a}) & & & \\ \mathbf{0}_{3\times3} & \mathbf{I}_{3\times3} & & & \\ & & \mathbf{I}_{3\times3} & & \\ & & & \mathbf{I}_{3\times3} & \\ & & & & \mathbf{I}_{3\times3} \end{bmatrix} \qquad (4.2.29)$$

$$\mathbf{R}(\mathbf{a}) = (\cos a)\mathbf{I} - \left(\frac{\sin a}{a}\right)[\mathbf{a}\times] + \left(\frac{1-\cos a}{a^2}\right)\mathbf{a}\mathbf{a}^{\mathrm{T}} \qquad (4.2.30)$$

$$\mathbf{S}(\mathbf{a}) = t\left[\left(\frac{\sin a}{a}\right)\mathbf{I} - \left(\frac{1-\cos a}{a^2}\right)[\mathbf{a}\times] + \left(\frac{a-\sin a}{a^3}\right)\mathbf{a}\mathbf{a}^{\mathrm{T}}\right] \qquad (4.2.31)$$

and the propagated covariance is $\mathbf{P}_{k+1} = \boldsymbol{\Phi}_k\mathbf{P}_k\boldsymbol{\Phi}_k^T + \mathbf{Q}_k$.

### 4.2.7 Tuning

There is an asymmetry in the use of the attitude and rate information reflecting a basic principle of attitude filtering: star (LRS stellar-side) or attitude (SST) observations enter through filter updates, and rate observations enter through filter predictions (propagations). The filter does not treat the rate observations as measurements but instead uses them to replace dynamical modeling in the state equation. A summary of the asymmetries is shown in Table 4.

**Table 4 Attitude filter asymmetries between attitude and rate observations**

| | Attitude obs | Rate obs |
|---|---|---|
| Filter phase | Update | Prediction |
| Noise type | Star/Quaternion noise | Rate bias instability |
| Noise represented in filter by | $\mathbf{R}$<br>Measurement noise | $\mathbf{Q}$<br>State process noise |

The filter tuning based on the star residuals is discussed in ICESat ATBD [38]. There are two knobs to turn for tuning: $\mathbf{R}$ and $\mathbf{Q}$. The emphasis put on filter updates is changed by varying $\mathbf{R}$. Smaller values in $\mathbf{R}$ mean there is less uncertainty in the attitude observations and results in larger update gains $\mathbf{K}$ and stronger update corrections of the filter state. The emphasis put on filter predictions is changed by varying $\mathbf{Q}$. Larger values in $\mathbf{Q}$ mean there is more uncertainty in the filter states and predictions and again results in larger update gains $\mathbf{K}$ and stronger update corrections of the filter state.

$\mathbf{Q}$ characterizes how attitude prediction uncertainty grows over time and is tied to the SIRU and complex measurement and error models. It is parameterized in the filter by $\sigma_{awn}, \sigma_{arw}$ and particularly by $\sigma_{rrw}$. Values are taken from the SIRU specifications and testing. With 10 Hz updates coming from the spacecraft star trackers the prediction time spans are relatively short. Over 0.1 second intervals, the predictions from the SIRU are relatively good and the question may reduce to how good are the attitude observations and how much should they be trusted. Filter tuning then becomes focused on $\mathbf{R}$ and the emphasis is placed on filter updates and attitude observations.

## 4.3 Laser Telemetry and Model Parameters

The LRS laser-side observes for six laser unit vectors $\mathbf{u}_{LT} = \mathbf{f}_{LT}(x, y, \mathbf{p}_{LT})$ in the laser-side coordinate frame (LT) at 50 Hz. The telemetry values are centroid positions $x, y$ on the detector with units of pixels. The FOV is $1.3^\circ \times 1.3^\circ$ ( $23.3 mrad \times 23.3 mrad$ ) and the detector is $1024 \times 1024$ pixels with approximately $9.385 arcsec/pixel$ ( $45.5 \mu rad/pixel$ ). The estimated alignment $\mathbf{A}_{LT}^{ST}$ between the laser-side frame and stellar-side frame is used to transform the laser unit vectors into the LRS stellar-side frame $\mathbf{u}_{ST} = \mathbf{A}_{LT}^{ST}\mathbf{u}_{LT}$.

The alignment $\mathbf{A}_{LT}^{ST}$ can be classed as part of the laser-side measurement model. In an ideal situation, with a stable and well known $\mathbf{A}_{LT}^{ST}$, the laser-side effectively observes the laser vectors directly in the LRS stellar-side frame $\mathbf{A}_{b}^{ST}$, which is connected with the ICRF by $\mathbf{A}_{b}^{ST}\mathbf{A}_{i}^{b}$. $\mathbf{A}_{LT}^{ST}$ is determined in ground testing and the geolocation error budget allocates $5.0 \mu rad$ for its variability. Variations of $\mathbf{A}_{LT}^{ST}$ may not be directly observable from flight data, but the effects should be significantly reduced by corrections to $\mathbf{A}_{LT}^{ST}$ from ocean scan calibration.

Based on the design and characteristics of the diffractive optics (DOE) the 6 beams produced from the single laser pulse will have a constant geometry relative to one another. As such, in the development of PPD algorithm, a one vector assumption is sufficient to specify all six beams using constant offset rotations. Extension to time-varying beam geometry is a straight forward increase in bookkeeping from one vector to six vectors.

### 4.3.1 6.25 Degree Yaw of the LRS

The spacecraft body frame $\mathbf{A}_{i}^{b}$ is assumed here to be defined similarly to the Orbital ATK spacecraft frame:

1. X axis along the centerline of the spacecraft and positive out through the ATLAS instrument.
2. Y axis anti-parallel to the rotation axis of the solar array.
3. Z axis parallel to the ATLAS telescope line of sight.

Note that the definition of ATLAS frame in Section 4.1.8 is identical to the spacecraft body frame here. For a general description of the attitude determination processing, the spacecraft body frame has rather abstract meaning; a reference frame that alignments of multiple sensors can be defined. Actual data processing requires the physical definition of the body frame.

The LRS as a whole is rotated by $6.25^\circ$ about its optical axes relative to the spacecraft body frame. The LRS laser-side line of sight (nadir pointing) is parallel to the body frame Z axis. Its X and Y axes are yawed $6.25^\circ$ from the body frame X and Y axes [38].

This yaw rotation is included in $\mathbf{A}_b^{LT}$ and does not have any other direct effects on the processor. Normally the LRS laser-side frame is effectively defined as the body frame by holding $\mathbf{A}_b^{LT}$ approximately constant. The $6.25^\circ$ LRS yaw is then effectively incorporated directly into the body frame attitude estimate $\mathbf{A}_i^b$. In this case, one can say that the spacecraft is yawed $6.25^\circ$ from the LRS and body frames, but the semantics have no practical significance.

The most critical question is if the processor adequately predicts the LRS star observations and interprets the LRS laser observations. The answer depends entirely on the accuracy of $\mathbf{A}_i^{ST} = \mathbf{A}_b^{ST}\mathbf{A}_i^b$. The effects of the $6.25^\circ$ yaw are absorbed in $\mathbf{A}_b^{ST}\mathbf{A}_i^b$. A laser-side unit vector $\mathbf{u}_{LT} = \mathbf{f}_{LT}(x, y, \mathbf{p}_{LT})$ in the laser-side frame is transformed into the stellar-side frame and the ICRF normally, $\mathbf{u}_{ICRF} = (\mathbf{A}_b^{ST}\mathbf{A}_i^b)^T \mathbf{A}_{LT}^{ST}\mathbf{u}_{LT}$.

### 4.3.2 LRS Alignment Variation

The motion of the laser-side observations (centroids or unit vectors) can be caused by the motion of the LRS as a whole relative to the ATLAS frame. This provides a possible method for detecting and characterizing LRS alignment variations even when there are no LRS stellar-side observations (during LRS stellar-side blinding). For example, if the laser-side observations are clearly moving but the laser beams are fixed in the ATLAS frame, i.e., beam steering mechanism (BSM) is constant, then what is actually moving is the LRS. This makes the LRS frame alignment $\mathbf{A}_b^{LT}$ observable and provides a basis for a parameter or state estimation of its time variations $\mathbf{A}_b^{LT}(t)$. The practical question is how frequently and easily the BSM data are available. The BSM motion is possibly derived from the relative motion between laser centroids and TAMS centroids.

### 4.3.3 Conversion of Centroids to Unit Vectors

As for the stellar-side, a laser-side measurement model $\mathbf{u}_{LT} = \mathbf{f}_{LT}(x, y, \mathbf{p}_{LT})$ including a quadratic radial term is provided by the LRS group. The model parameters are

$$\mathbf{p}_{LT} = [p_{LT1}, p_{LT2}, p_{LT3}, x_{LT0}, y_{LT0}] \tag{4.3.1}$$

The radial distance of a centroid from the laser-side principal point is

$$d = ((x - x_{LT0})^2 + (y - y_{LT0})^2)^{1/2} \tag{4.3.2}$$

A scaling factor $k$ is given by

$$k = p_{LT1}d^2 + p_{LT2}d + p_{LT3} \tag{4.3.3}$$

The $h, v$ coordinates of the unit vector are

$$h = \tan\theta_h = \tan(k(x - x_{LT0})) \tag{4.3.4}$$

$$v = \tan\theta_v = \tan(k(y - y_{LT0})) \tag{4.3.5}$$

and $\mathbf{u}_{LT} = [h \quad v \quad 1]^T / (h^2 + v^2 + 1)^{1/2} = \mathbf{f}_{LT}(x, y, \mathbf{p}_{LT})$.

There is a fundamental difference between the LRS laser-side and stellar-side with regard to on-orbit calibration. The stellar-side observes nearly ideal external reference points - the stars. Star observations provide adequate information for calibration, with a nearly uniform distribution over the star tracker focal plane given a large enough sample size. The information available for calibrating the laser-side on-orbit is much more limited.

The available references for calibration of the laser-side are the six laser spots and four reference signal TAMS spots. In other words, on-orbit calibration will necessarily depend on the geometry of the six laser spots and four reference signal spots. The angles between the reference signal TAMS spots are approximately constant. The same should be true for the angles between the laser spots. Comparing the true angles with the observed angles is a potential source of calibration information for estimating laser-side measurement model parameters.The positions of the spots on the focal plane are normally approximately static, making the spatial distribution of calibration information across the focal plane sparse. It is possible, in principle, to scan the laser spots over the FOV using the BSM to improve spatial coverage.

### 4.3.4 Noise Estimation Using the Triangle Method

In this section unit vectors are assumed to be represented by $h,v$ coordinates and all calculations are performed in the two-dimensional $h,v$ plane. Near the center of the FOV $h \approx \theta_h$ and $v \approx \theta_v$, so $h,v$ coordinates are approximately angular measures with units of radians.

The laser-side error model for laser unit vector observations $\mathbf{u} = \mathbf{u}_{LT}$ is $\mathbf{u} = \mathbf{h} + \boldsymbol{\eta}$ where $\mathbf{u}$ is the observed unit vector, $\mathbf{h}$ is the true unit vector, and $\boldsymbol{\eta}$ is zero-mean Gaussian white noise $E\{\boldsymbol{\eta}^T\boldsymbol{\eta}\} = \sigma_u^2\mathbf{I}$.

Measurement noise $\sigma_u$ is estimated based on variations of the angular separations between pairs of laser vectors. The variance of the separations between vectors $a$ and $b$ is equal to the sum of their individual noise variances $\sigma_{ab}^2 = \sigma_a^2 + \sigma_b^2$, where $\sigma_{ab}^2$ is calculated directly from a set of simultaneous measurements of vectors $a$ and $b$. For a set of simultaneous measurements of three vectors $a$, $b$ and $c$ the variances of the separations form 3 equations $\sigma_{ab}^2 = \sigma_a^2 + \sigma_b^2$, $\sigma_{ac}^2 = \sigma_a^2 + \sigma_c^2$, and $\sigma_{bc}^2 = \sigma_b^2 + \sigma_c^2$ with 3 unknowns $\sigma_a^2$, $\sigma_b^2$ and $\sigma_c^2$. For the 6 laser vectors, there are $6(6-1)/2 = 15$ angular separation variances $\sigma_{xy}^2$. The system of equations for the 6 unknown noise variances is over-determined and solved using least squares.

### 4.3.5 Alignment of Laser Tracker Frame and Ocean Scan Correction

The alignment $\mathbf{A}_{LT}^{ST}$ between the laser-side frame and stellar-side frame is a key factor in transforming laser-side observations $\mathbf{u}_{LT} = \mathbf{f}_{LT}(x, y, \mathbf{p}_{LT})$ into laser vectors $\mathbf{u}_{ICRF}$ in the ICRF

$$\mathbf{u}_{ICRF} = (\mathbf{A}_b^{ST}\mathbf{A}_i^b)^T \mathbf{A}_{LT}^{ST}\mathbf{u}_{LT} \qquad (4.3.6)$$

Assume that a reference alignment $\mathbf{B}$ is provided by ground testing and is a constant throughout the mission. If not, B is simply an identity matrix. A time-varying correction $\mathbf{C}(t)$ is included in the measurement model in order to incorporate flight data. By including $\mathbf{C}(t)$, the alignment becomes time dependent and given by

$$\mathbf{A}_{LT}^{ST}(t) = \mathbf{C}(t)\mathbf{B} \qquad (4.3.7)$$

so

$$\mathbf{u}_{ICRF} = [(\mathbf{A}_b^{ST}\mathbf{A}_i^b)^T \mathbf{A}_{LT}^{ST}]\mathbf{u}_{LT} = [(\mathbf{A}_b^{ST}\mathbf{A}_i^b)^T \mathbf{C}(t)\mathbf{B}]\mathbf{u}_{LT} \qquad (4.3.8)$$

Parameter estimation for $\mathbf{C}(t)$ using flight data plays a major role in improving the overall laser-side measurement model. In general, reflects results from ocean scan calibration and is referred to as the ocean scan correction.

This discussion of ocean scan calibration is based on Ref. [50], where an expression similar to Eq. (4.3.8) is given (Ref. [50] Eq. (2) with minor notational changes) by

$$\mathbf{u}_{ICRF} = \mathbf{A}_{SBF}^{ICRF}(t)\mathbf{A}_{SBFC}^{SBF}(t)\mathbf{A}_{LT}^{SBFC}\mathbf{u}_{LT} \qquad (4.3.9)$$

The objective of ocean scan calibration is an estimation of the rotation $\mathbf{A}_{SBFC}^{SBF}$. Comparing Eqs. (4.3.9) to (4.3.8), $\mathbf{C}(t) = \mathbf{A}_{SBFC}^{SBF}(t)$ for $(\mathbf{A}_b^{ST}\mathbf{A}_i^b(t))^T \int \mathbf{A}_{SBF}^{ICRF}(t)$ and $\mathbf{B} \equiv \mathbf{A}_{LT}^{SBFC}$. In other words, ocean scan calibration provides an estimate of the correction $\mathbf{C}(t)$.

### 4.3.6 Laser Pointing Product

The overall product is a set of 6 laser unit vectors in the ICRF $\mathbf{u}_{ICRF,i}(t_k)$ for $i = 1,...,6$ at each LRS laser-side observation time tag $t_k$.

$$\mathbf{u}_{ICRF,i}(t_k) = [(\mathbf{A}_b^{ST}\mathbf{A}_i^b(t_k))^T\mathbf{C}(t_k)\mathbf{B}]\mathbf{u}_{LT,i}(t_k) \qquad (4.3.10)$$

The product $\mathbf{u}_{ICRF,i}(t_k)$ at $t_k$ is fully specified by:

1. The 6 laser unit vectors $\mathbf{u}_{LT,i}(t_k)$ expressed in the laser-side frame using $h, v$ coordinates (or other convenient two-component representations).
2. The ocean scan correction $\mathbf{C}(t_k)$.
3. The attitude estimate $\mathbf{A}_i^b(t_k)$.

The significant question here is: what is the attitude estimate $\mathbf{A}_i^b(t_k)$ at the essentially arbitrary laser-side output time tag $t_k$?

Table 5 and Table 6 demonstrate propagation of the attitude estimate to the arbitrary time tags of laser-side observations and filter updates (star observations). The gyro observation time tags are included in the time series since the gyro observations provide the empirical basis for the propagation. The SIRU provides all of the available higher frequency pointing information and is necessarily the basis for propagation over short timescales.

The objective is to find the rotation vectors $\mathbf{a}_{k-1}^{k}$ from $t_{k-1}$ to $t_k$ representing the attitude change between successive pairs of time tags. All of the propagation information comes from the SIRU and is encoded into and transmitted by the rotation vectors.

Table 5 presents the overall structure of the propagation and the role of the rotation vectors but says nothing about where the rotation vectors come from (how they are estimated). That is the job of Table 6 which is entirely focused on estimating the rotation vectors. The explanatory discussion is included below each table.

**Table 5 Rotation vectors needed to propagate the attitude between obs.**

| $k$ | $t_k$, msec | $\Delta t$, msec | Obs | Attitude estimate | Need |
|---|---|---|---|---|---|
| 1 | 0 | - | Gyro | $\mathbf{A}_i^b(t_1)$ | - |
| 2 | 4.74 | 4.74 | Star (LRS) | $\mathbf{A}_i^b(t_2)_- = \mathbf{A}(\mathbf{a}_1^2)\mathbf{A}_i^b(t_1) \to \mathbf{A}_i^b(t_2)_+$ | $\mathbf{a}_1^2$ |
| 3 | 9.32 | 4.58 | Laser | $\mathbf{A}_i^b(t_3) = \mathbf{A}(\mathbf{a}_2^3)\mathbf{A}_i^b(t_2)_+$ | $\mathbf{a}_2^3$ |
| 4 | 20.01 | 10.69 | Gyro | $\mathbf{A}_i^b(t_4) = \mathbf{A}(\mathbf{a}_3^4)\mathbf{A}_i^b(t_3)$ | $\mathbf{a}_3^4$ |
| 5 | 29.34 | 9.33 | Laser | $\mathbf{A}_i^b(t_5) = \mathbf{A}(\mathbf{a}_4^5)\mathbf{A}_i^b(t_4)$ | $\mathbf{a}_4^5$ |
| 6 | 40.01 | 10.67 | Gyro | $\mathbf{A}_i^b(t_6) = \mathbf{A}(\mathbf{a}_5^6)\mathbf{A}_i^b(t_5)$ | $\mathbf{a}_5^6$ |
| 7 | 49.33 | 9.32 | Laser | $\mathbf{A}_i^b(t_7) = \mathbf{A}(\mathbf{a}_6^7)\mathbf{A}_i^b(t_6)$ | $\mathbf{a}_6^7$ |
| 8 | 53.48 | 4.15 | Star (SST2) | $\mathbf{A}_i^b(t_8)_- = \mathbf{A}(\mathbf{a}_7^8)\mathbf{A}_i^b(t_7) \to \mathbf{A}_i^b(t_8)_+$ | $\mathbf{a}_7^8$ |
| 9 | 60.01 | 6.53 | Gyro | $\mathbf{A}_i^b(t_9) = \mathbf{A}(\mathbf{a}_8^9)\mathbf{A}_i^b(t_8)_+$ | $\mathbf{a}_8^9$ |

This table shows a representative time series of events. The events consist of the arrival of incoming observations (telemetry) from the three types of sensors: star, gyro, and laser. The star observations provide filter updates as indicated by the notation $\mathbf{A}_i^b(t_k)_- \to \mathbf{A}_i^b(t_k)_+$ for the update of the predicted attitude $\mathbf{A}_i^b(t_k)_-$ to the updated attitude $\mathbf{A}_i^b(t_k)_+$.

To form the laser pointing product, the attitude estimates $\mathbf{A}_i^b(t_3)$, $\mathbf{A}_i^b(t_5)$, and $\mathbf{A}_i^b(t_7)$ for the laser observations at $t_3$, $t_5$, and $t_7$ are needed. The problem reduces to estimating the eight rotation vectors $\mathbf{a}_1^2$, $\mathbf{a}_2^3$, $\mathbf{a}_3^4$, $\mathbf{a}_4^5$, $\mathbf{a}_5^6$, $\mathbf{a}_6^7$, $\mathbf{a}_7^8$, and $\mathbf{a}_8^9$.

**Table 6 Estimation of the rotation vectors using the SIRU output**

| $k$ | $t_k$ , msec | Obs | Rate information | Estimate |
|---|---|---|---|---|
| 1 | 0 | Gyro $\boldsymbol{\theta}_s(t_1)$ | | - |
| 2 | 4.74 | Star (LRS) | | $\hat{\mathbf{a}}_1^2 = (t_2 - t_1)\hat{\boldsymbol{\omega}}_a$ |
| 3 | 9.32 | Laser | | $\hat{\mathbf{a}}_2^3 = (t_3 - t_2)\hat{\boldsymbol{\omega}}_a$ |
| 4 | 20.01 | Gyro $\boldsymbol{\theta}_s(t_4)$ | $\hat{\boldsymbol{\omega}}_a = \mathbf{H}(\boldsymbol{\theta}_s(t_4) - \boldsymbol{\theta}_s(t_1))/(t_4 - t_1) + \hat{\mathbf{b}}$ | $\hat{\mathbf{a}}_3^4 = (t_4 - t_3)\hat{\boldsymbol{\omega}}_a$ |
| 5 | 29.34 | Laser | | $\hat{\mathbf{a}}_4^5 = (t_5 - t_4)\hat{\boldsymbol{\omega}}_b$ |
| 6 | 40.01 | Gyro $\boldsymbol{\theta}_s(t_6)$ | $\hat{\boldsymbol{\omega}}_b = \mathbf{H}(\boldsymbol{\theta}_s(t_6) - \boldsymbol{\theta}_s(t_4))/(t_6 - t_4) + \hat{\mathbf{b}}$ | $\hat{\mathbf{a}}_5^6 = (t_6 - t_5)\hat{\boldsymbol{\omega}}_b$ |
| 7 | 49.33 | Laser | | $\hat{\mathbf{a}}_6^7 = (t_7 - t_6)\hat{\boldsymbol{\omega}}_c$ |
| 8 | 53.48 | Star (SST2) | | $\hat{\mathbf{a}}_7^8 = (t_8 - t_7)\hat{\boldsymbol{\omega}}_c$ |
| 9 | 60.01 | Gyro $\boldsymbol{\theta}_s(t_9)$ | $\hat{\boldsymbol{\omega}}_c = \mathbf{H}(\boldsymbol{\theta}_s(t_9) - \boldsymbol{\theta}_s(t_6))/(t_9 - t_6) + \hat{\mathbf{b}}$ | $\hat{\mathbf{a}}_8^9 = (t_9 - t_8)\hat{\boldsymbol{\omega}}_c$ |

The method for estimating the eight rotation vectors $\mathbf{a}_1^2$ , $\mathbf{a}_2^3$ , $\mathbf{a}_3^4$ , $\mathbf{a}_4^5$ , $\mathbf{a}_5^6$ , $\mathbf{a}_6^7$ , $\mathbf{a}_7^8$ , and $\mathbf{a}_8^9$ shown here is designed to incorporate gyro measurement model information represented by $\mathbf{A}_b^{SIRU}$ , $\mathbf{G}$ , and $\hat{\mathbf{b}}$ with $\mathbf{H} \equiv (\mathbf{A}_b^{SIRU})^T (\mathbf{G}^T\mathbf{G})^{-1}\mathbf{G}^T$ . The raw SIRU vectors $\boldsymbol{\theta}_s(t_k)$ are assumed to be unwrapped. Each $\boldsymbol{\theta}_s(t_k)$ contains four angular counts with units of 0.05 arcseconds per count. The counts range from 0 to 65,535 and wrap on underflow or overflow. Unwrapping simply means that $\boldsymbol{\theta}_s(t_k) - \boldsymbol{\theta}_s(t_{k-1})$ gives the correct, meaningful result $\Delta\boldsymbol{\theta}_s$ despite the wrapping in the raw data.

The estimated rotation vectors are essentially a linear interpolation between the four gyro observations, based on the estimated body frame angular rate.

Table 5 and 6 represents the parallel processing of the PPD for the laser pointing determination. Alternatively, the processing of the laser-side data can be processed after the attitude determination from the stellar-side is conducted beforehand. It is practically important because of the correction of the alignment variation between the laser-side and stellar-side should be applied with the calibrated information from ocean scan analysis. Figure 17 illustrates the subsequent computation of the laser pointing vectors after the stellar-side attitude computation (PAD) is conducted for a fixed time interval. The time interval for daily PPD product (ANC05) is 25 hours (30 minutes additions at the beginning and the end of the day).

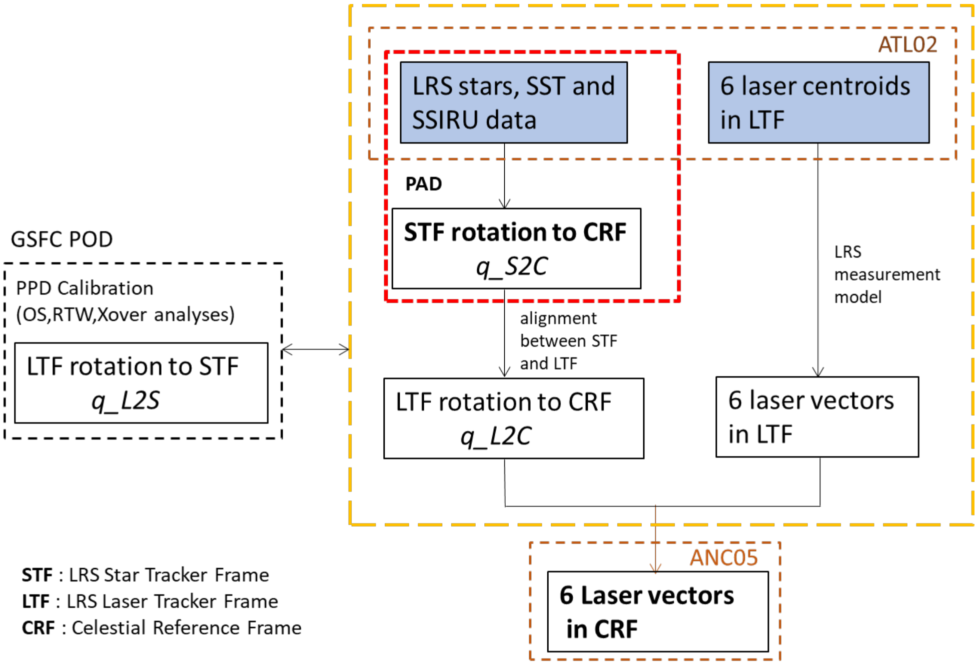

**Fig. 14 PPD flowchart: LRS laser-side data are combined with PAD solution**

# 5.0 PPD Simulation

Verification and performance analysis of the PPD algorithm is discussed here in the context of the overall position, pointing, and geolocation knowledge system. Evaluation of pointing knowledge can be divided into four high-level steps:

1. Input truth, generated from true position, pointing, and geolocation.
2. Artificial telemetry (LRS, SSTs, SIRU).
3. Test processing.
4. Output knowledge, performance analysis compares output knowledge with input truth.

The inputs consist of time series of true values for position, pointing, and geolocation. The time series represent the truth underlying artificial LRS, SST, and SIRU telemetry. The basic concept of the four evaluation steps is to generate artificial telemetry based on the truth, then process the telemetry for pointing knowledge. The difference between input truth and output knowledge is the error introduced by the sensors and processing and is the basis for performance analysis.

Subsets of the four steps can easily be emphasized for limited testing, for example, artificial telemetry and test processing in isolation (decoupled from the overall ground system). The focus here is on the most generalized configuration. In practice, output pointing knowledge and performance analysis are organic by-products of processing the artificial telemetry. During processing the estimated body frame attitude $\mathbf{A}_i^b$, observed laser unit vector(s) $\mathbf{u}_{LT}$, and ocean scan correction $\mathbf{C}(t)$ are readily available and the output pointing knowledge is simply

$$\mathbf{u}_{ICRF}(t_k) = (\mathbf{A}_b^{ST}\mathbf{A}_i^b(t_k))^T(\mathbf{C}(t_k)\mathbf{B})\mathbf{u}_{LT}(t_k) \qquad (5.0.1)$$

as discussed in Section 4.3.6. This is directly equivalent to the expression for the input truth

$$\mathbf{u}_{ICRF} = (\mathbf{A}_{ATLAS}^{ST}\mathbf{A}_i^{ATLAS})^T\mathbf{A}_{LT}^{ST}\mathbf{u}_{LT} \qquad (5.0.2)$$

The correspondences between estimated (or observed) and true values are

$$\mathbf{u}_{ICRF,estimated} \Leftrightarrow \mathbf{u}_{ICRF,true} \qquad (5.0.3)$$

$$\mathbf{u}_{LT,observed} \Leftrightarrow \mathbf{u}_{LT,true} \qquad (5.0.4)$$

$$\mathbf{A}_b^{ST}\mathbf{A}_i^b \text{ € } \mathbf{A}_{ATLAS}^{ST}\mathbf{A}_i^{ATLAS} \qquad (5.0.5)$$

$$\mathbf{CB} \text{ € } \mathbf{A}_{LT}^{ST} \qquad (5.0.6)$$

where Eqs. (5.0.3) and (5.0.4) are equivalent since they are linked by Eqs. (5.0.5) and (5.0.6).

The significant performance questions are the errors (differences) between the estimated and true attitudes ( $\mathbf{A}_b^{ST}\mathbf{A}_i^b$ and $\mathbf{A}_{ATLAS}^{ST}\mathbf{A}_i^{ATLAS}$ ) and between the observed and true laser vectors ($\mathbf{u}_{LT,observed}$ and $\mathbf{u}_{LT,true}$).

Regarding the simulation setting, the most significant source of known error for ICESat-2 PPD is the chromatic aberration in LRS stellar-side. The performance of the PPD eventually relies on the correction of the chromatic aberration (aka, color correction), and the color correction includes the nominal PAD (or the PAD includes color correction) at the beginning of the flight data processing. Once all the related parameters (color coefficients and optical parameters) are corrected for the reliable accuracies of the PAD solution, the overall processing will be simplified by not doing the color correction and by simply using the most recently estimated parameters. Then, the parameters are estimated regularly as a side work independently from the daily PPD processing to find out the possible change over time. In this chapter, we focus on the color correction simulation that is the broad meaning of the PPD simulation.

## 5.1 Coordinate Frames

Key coordinate frames conventional to the orbit and attitude systems are spacecraft frame $\mathbf{A}_i^{SC}$, body frame $\mathbf{A}_i^b$, ATLAS frame $\mathbf{A}_i^{ATLAS}$, and orbit frame $\mathbf{A}_i^{orbit}$.

A generic body frame $\mathbf{A}_i^b$ is associated with estimation, filtering, and knowledge rather than truth values and artificial telemetry. In practice, the body frame is equated with the attitude estimate for one or more attitude sensors. For our simulation, it is the LRS stellar-side frame.

One perspective on the ATLAS frame is that it represents attitude information that is useful in the widest context of the overall position, pointing, and geolocation ground system. Information of more limited interest is not included (for example LRS and SST alignments for generating artificial telemetry). Information that is useful outside of the pointing determination group is incorporated into the ATLAS frame and the input truth (Section 5.2). Information that is only of interest to the pointing group is restricted to the artificial telemetry. Therefore, 6.25° rotation of the LRS with respect to the ATLAS frame discussed in Sec. 4.3.1 is not relevant to the general PPD simulation and processing. It must be considered carefully, however, if the PPD product needs to be used in the other coordinate frames (e.g., RTA, MRF, IMSC, etc) outside the PPD system [1]. In that case, rotation from LRS to ATLAS frame has to be properly applied to the PPD product. Unless stated otherwise, here the body frame $\mathbf{A}_i^b$ is associated with the LRS frame, and the ATLAS frame $\mathbf{A}_i^{ATLAS}$ is obtained by the rotation of 6.25° from the LRS frame. The spacecraft frame is defined as identical to the ATLAS frame in the ICESat-2 PPD system.

$\mathbf{A}_i^{orbit}$ can be defined from the basic orbit parameters in Table 7.

**Table 7 Orbit characteristics**

| | Orbit, km | Period, sec | Period, min | Speed, km/s | Rate, arcsec/s |
|---|---|---|---|---|---|
| ICESat | 590 | 5779 | 96.33 | 7.56 | 224.3 |
| ICESat-2 | 496 | 5663 | 94.38 | 7.61 | 228.8 |

Approximating the orbit as circular, the simulated-truth position $\mathbf{r}$ and velocity $\mathbf{v}$ expressed in the Earth-Centered Inertial (ECI) frame can be used to define a local vertical and local horizontal coordinate frame with its $\hat{\mathbf{i}}$ axis parallel to $\mathbf{v}$, and its $\hat{\mathbf{k}}$ axis parallel to the nadir vector $-\mathbf{r}$.

$$\hat{\mathbf{i}} = \mathbf{v} / \|\mathbf{v}\| \tag{5.1.1}$$

$$\hat{\mathbf{j}} = \hat{\mathbf{k}} \times \hat{\mathbf{i}} \tag{5.1.2}$$

$$\hat{\mathbf{k}} = -\mathbf{r} / \|\mathbf{r}\| \tag{5.1.3}$$

$\mathbf{A}_i^{orbit}$ can be represented as a rotation matrix

$$\mathbf{A}_i^{orbit} = \begin{bmatrix} \hat{\mathbf{i}} & \hat{\mathbf{j}} & \hat{\mathbf{k}} \end{bmatrix} \tag{5.1.4}$$

The ATLAS frame incorporates the orbit frame $\mathbf{A}_i^{ATLAS}(t) = \mathbf{A}_{orbit}^{ATLAS}(t)\mathbf{A}_i^{orbit}(t)$ where $\mathbf{A}_{orbit}^{ATLAS}(t) = \mathbf{A}_n(t)\ldots\mathbf{A}_2(t)\mathbf{A}_1(t)$ are rotations that can represent ocean scans, off-nadir pointing, higher-frequency rotations of ATLAS as a whole, etc. After the additional rotations, the $\hat{\mathbf{i}}$ and $\hat{\mathbf{k}}$ vectors in $\mathbf{A}_i^{ATLAS} = \begin{bmatrix} \hat{\mathbf{i}} & \hat{\mathbf{j}} & \hat{\mathbf{k}} \end{bmatrix}$ will generally no longer be aligned with the velocity and nadir directions.

## 5.2 Simulated Orbit and Attitude Data

A realistic ICESat-2 dataset was provided by GSFC for algorithm test and evaluation. The data reflects the science mode ICESat-2 attitude, rate, position, and velocity for the 14-day interval at 1 Hz data. It also includes various pointing maneuvers planned for ICESat-2. Figure 18 illustrates the angular rate of the first 3 orbital periods of the data in roll, pitch, and yaw axes. Some simulated maneuvers are visible: Ocean scan maneuver for 20 minutes approximately from 5000 seconds in roll and pitch axes, and multiple vegetation target maneuvers in the roll axis. From this fundamental truth dataset, LRS stellar-side and SST data are generated at a 10-Hz rate and SIRU and LRS laser-side data at the 50-Hz rate. The higher rates are obtained by interpolation. Without measurement errors, these simulated data and attitude are the truth that can be used in the evaluation of PAD/PPD output in the test. Realistic data was created by adding measurement errors to the truth. The measurement errors for LRS, SIRU, and SST are based on the manufacturers or on-orbit flight performance analysis; LRS star measurement uncertainty is 17 $\mu$rad (1σ) [51]. The simulated uncertainties of SST quaternion are 7.3 $\mu$rad (1σ) respectively for x and y axes, 48.5 $\mu$rad (1σ) for z axis [52]. Gyro unit observation uncertainties are commonly characterized using three parameters: angular white noise $\sigma_{awn}$, angular random walk $\sigma_{arw}$, and rate random walk $\sigma_{rrw}$. Uncertainties for the ICESat-2 SIRU unit are specified by the manufacturer as $\sigma_{awn} = 1.454 \times 10^{-8}\, rad/Hz^{1/2}$, $\sigma_{arw} = 4.363 \times 10^{-8}\, rad/sec^{1/2}$, and $\sigma_{rrw} = 2.424 \times 10^{-11}\, rad/sec^{3/2}$ [53].

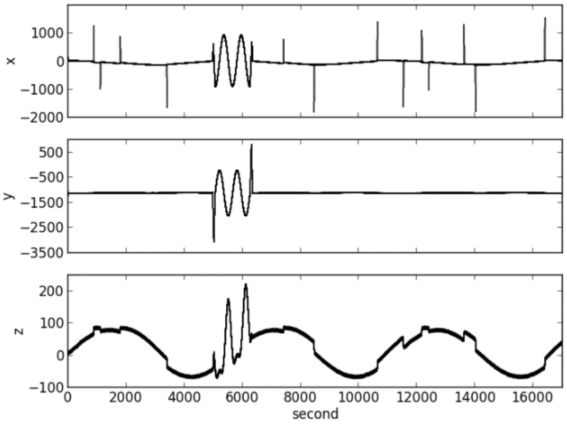

**Fig. 15 Angular rate of simulated orbit in arcsec/sec unit**

The LRS stellar-side gives star centroids in the pixel unit. The color correction formula in Eqs. (4.1.28-4.1.36) is converting the pixel data to angles. Simulation of the pixel data is an opposite process. Star centroids are generated first in angle unit from the 14-day data attitude, then the color error is added during the conversion of angles to pixel data. While the conversion from the pixel to angle is straightforward, the creation of pixel data from angles requires solving multi-variable non-linear equations.

Given a search point on the sky through the simulated orbit, the objective is to find the records from a star catalog that are near the search point. The star search method that is developed for ICESat PAD [34] continues to be used for the ICESat-2 PAD simulation for the realistic star data simulation. Appendix B introduces an alternative approach that could make the star search simpler near the poles.

Table 8 shows pre-launch color coefficients and optical parameters that were determined from the LRS night sky test data by LRS developers [42]. These numbers are used as truth in the pixel data simulation and are assumed unknown to users. The color correction is the procedure to find these values starting from the given initial values.

**Table 8 Pre-launch values for optical parameters and color coefficients**

| parameters | $x_0$ | $y_0$ | $f_0$ | $a_1$ | $a_2$ | $a_3$ | $b_1$ | $b_2$ | $b_3$ | $c_1$ | $c_2$ | $c_3$ |
|---|---|---|---|---|---|---|---|---|---|---|---|---|
| Values | 521 | 540 | 1 | 2.0842 | -3.7855 | 1.2293 | -0.4229 | 0.7559 | -0.1914 | 0.0208 | -0.0375 | 1.0132 |

## 5.3 Impact of Color Index Error

It is evident from Eqs. (4.1.34-4.1.36) that the accuracy of color indices directly affects the accuracy of estimated color coefficients, and consequently the quality of the attitude solution. Several different cases of the simulated color index error are listed in Table 9. Case 1 assumes that the color indices are available for all measured stars without error. From Case 2 to Case 5, the uncertainty is added to the color indices of all stars by the amount of the specified values.

**Table 9 Simulation cases based on color index uncertainty**

| Case # | 1 | 2 | 3 | 4 | 5 |
|---|---|---|---|---|---|
| Uncertainty ($1\sigma$) | No error | 0.02 for all stars | 0.03 for all stars | 0.04 for all stars | 0.10 for blue/red stars<br>0.04 for other stars |

Star measurements are simulated for each of 5 cases and used in the PAD processing. In the simulation, we assume that the initial values are unknown; zeros for all nine color coefficients, and (512, 512) for the optical center which is the geometrical center of 1024 by 1024 LRS pixels.

Simulation results are analyzed with the comparison of output parameters with their true values used in the data simulation.

Figure 19 shows the estimation error of the nine color coefficients from Case 1 simulation. Each point represents 1σ of the attitude error obtained from the processing of three orbital periods of LRS star measurements. The x axis is the iteration number, and y axis is coefficient error (the truth – estimated).

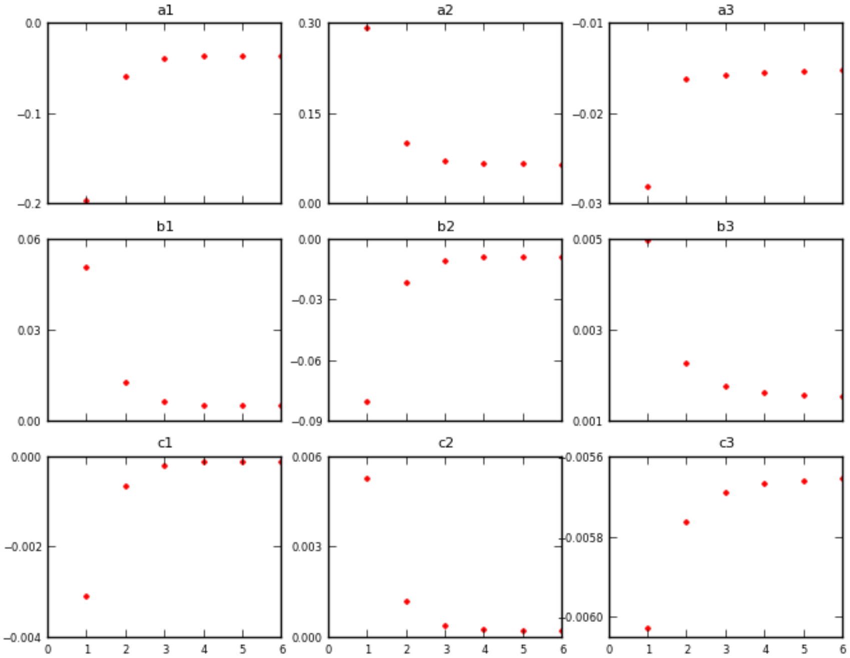

**Fig. 16 Color coefficient estimation error over iterations (Case 1)**

Figure 20 shows the estimation error of the nine color coefficients after the sixth iteration both in actual difference from the truth (upper plot) and in percentage of the difference (lower plot).

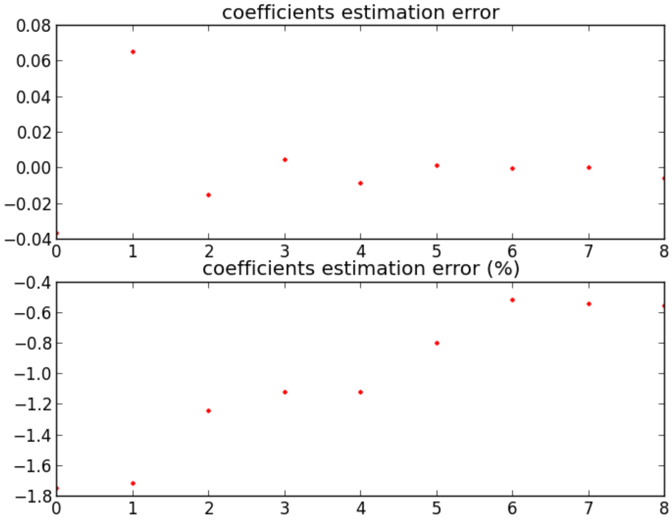

**Fig. 17 Estimation error of color coefficients after six iterations. From left(1), $a_1$,$a_2$, $a_3$, $b_1$, $b_2$, $b_3$, $c_1$, $c_2$, and $c_3$**

The estimation results of the optical center are given in the left plot of Figure 21. The optical center is initially off by -9 and -21 pixels from the true position, respectively for x (H) and y (V) axes. As expected, the errors decrease to near zero after a few iterations.

The color correction procedure summarized in Figure 10 includes two attitude determinations in each iteration. The right plot of Figure 21 illustrates attitude error (1σ) from each attitude determination over five iterations. The attitude error is very large at the beginning but reduces rapidly through multiple iterations.

On the other hand, the focal length immediately became 0.995 and no improvement is made after that one iteration. As an experiment, the star measurement uncertainty (17 $\mu$rad, 1σ) was removed from the simulated star data whereas all other conditions of Case 1 were kept. Then, in that situation the focal length estimation reached the true value 1. Therefore, it is believed that the limitation of the focal length estimation is caused by the measurement uncertainty of the star centroids that is independent of the chromatic aberration. This is also true for other parameters: by removing the measurement error of 17 $\mu$rad from Case 1, the estimates of the color coefficients, optical center, and attitude become much closer to the true values.

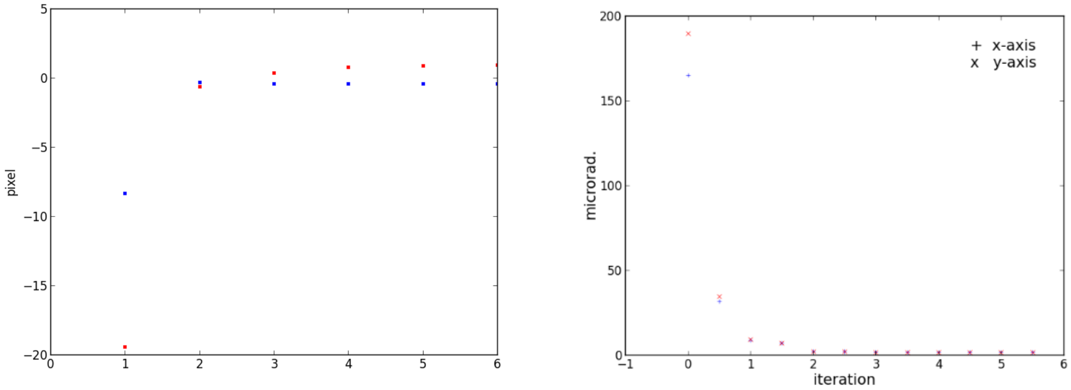

**Fig. 18 Optical center error (left) and LRS attitude error (right) through iterations.**

Although it is not possible to have exact color indices of the stars in mission star catalog, the results from Case 1 proves the reliable performance of the color correction algorithm. The impact of color index uncertainty is investigated based on the Cases 1 to Case 5 listed in Table 9. The results are shown in Figure 22 and Figure 23. In the right plot of Figure 23, each dot shows the root sum squared (RSS) value of roll and pitch attitude errors that contribute to the laser pointing vector directly; the -z axis of LRS stellar-side frame is ideally coincident with the +z axis of the laser-side frame. As the color index uncertainty increases, the error grows in all parameters.

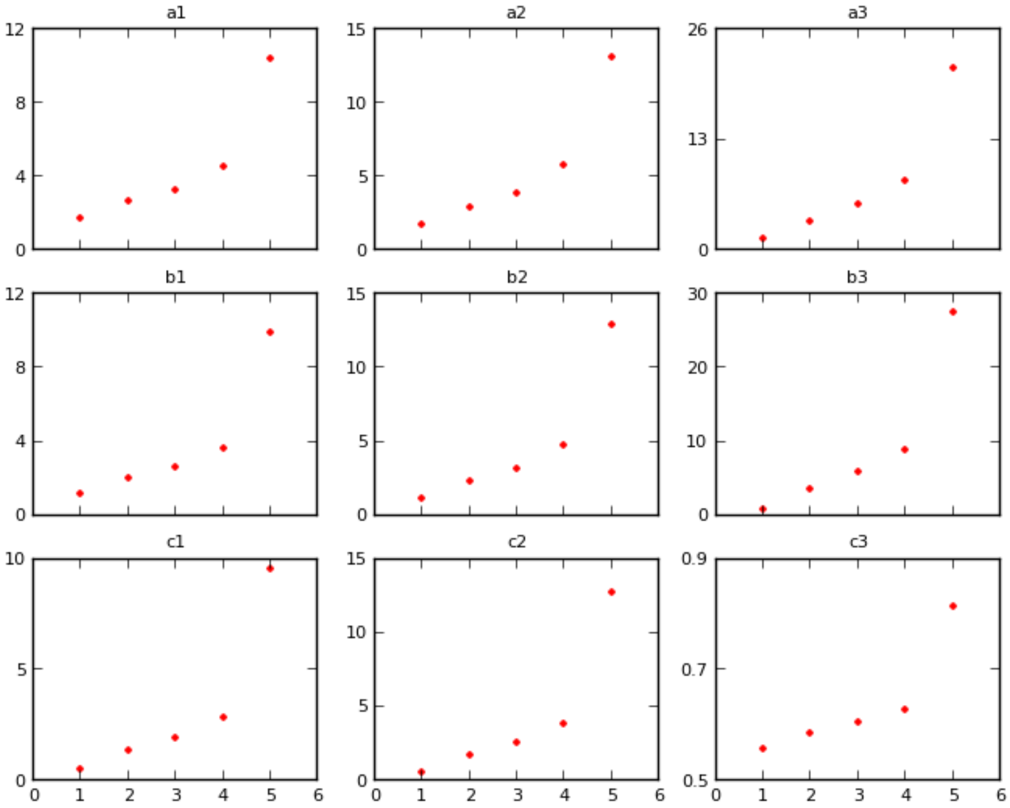

**Fig. 19  Estimation error of color coefficients for Case1 to Case5**

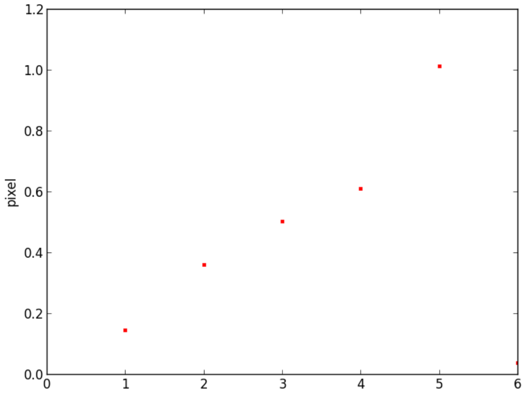

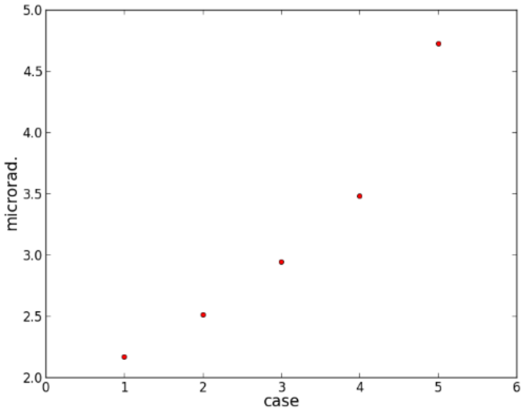

**Fig. 20 Optical center error (left) and LRS attitude error (right) for Case1 to Case5**

## 5.4 Full Sky Simulation

Simulations are conducted with 1° RA interval of the LRS boresight direction at the equator. The first three orbits of the 14-day data were used as the basis orbits. LRS FOV covers a 12° wide strip of the sky passing near the north and south celestial poles and the celestial equator. To move the 12° by 12° FOV viewed by the LRS without changing the basis orbits and attitude values, catalog star unit vectors $\boldsymbol{u}_{CRF}$ are artificially rotated by $-\alpha_{RA}$ in RA. This has the same effect on LRS observations as changing the ascending node of the orbit by $\alpha_{RA}$. For each RA, measurement data were simulated; LRS stellar-side stars (10Hz), SST quaternions (10Hz), and SIRU angular rates (50Hz). The simulated stars are brighter than magnitude 5.25 based on the expected LRS sensitivity, however, the mission star catalog has many more stars up to magnitude 6.0 by considering a possible variation of the LRS sensitivity. The color indices in the original LRS star catalog is regarded as the truth, and the color index error (Case 5 in Table 2) is added to the mission star catalog to reflect the anticipated uncertainty. The position error due to the chromatic aberration is added simulated star centroids using the color correction formula in Eqs. (4.1.28-4.1.36).

The color correction was applied to each RA with five iterations. The error in the attitude solution can be divided into two statistical numbers: mean and standard deviation. The mean value that is not zero is interpreted as attitude bias. If the optical center of the LRS is determined accurately, the attitude bias would be zero or negligible. If the optical center error is not negligible, the calibration method such as the range residual analysis by the ocean scan maneuver would be used to correct the bias. Therefore, attitude error that effectively restricts performance of the PAD is the standard deviation. Figure 24 shows the attitude errors gathered from the 5th iteration results of all 360 RA cases.

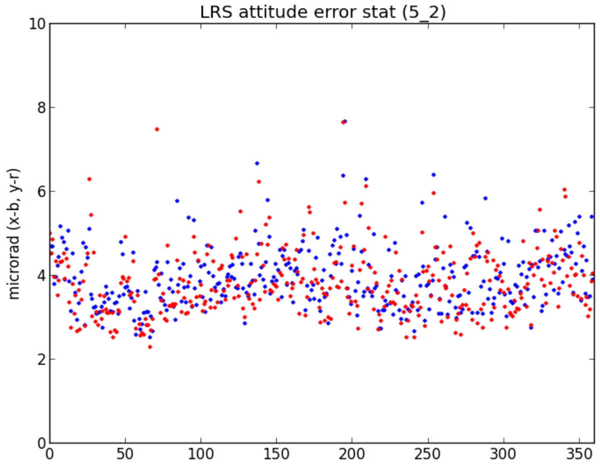

**Fig. 21  Full-sky simulation results: attitude errors in x and y axes**

From all results, the average error in roll axis is 3.93 μrad with 0.74 of 1σ. For pitch axis, the average is 3.80 μrad with 0.79 of 1σ. The RSS error of roll and pitch axes, illustrated in Figure 25, is 5.47 μrad. For comparison, attitude determination without the color correction resulted in considerably large errors; 162 $\mu$rad in roll and 168 $\mu$rad in pitch; 234 $\mu$rad RSS error.

Average number of the identified stars per FOV for each RA case is inversely plotted on Figure 25 over the attitude error. A general trend of attitude solution improvement along with the increased number of measured stars is apparent. The noticeable local differences from the general trend are apparent. One of the reasons for local differences is the fluctuation of a number of stars due to the irregular star distribution in the sky. As an example, the LRS can observe the stars up to 30 without the minimum restriction. This brings a large fluctuation of the available number of measured stars due to the irregular distribution of stars in our Galaxy. Figure 26 shows a typical case of the star measurement for three orbital periods of LRS data simulation;  the average number of observed stars per FOV is 6.24 with the 1σ value 3.67. In the sparse star region, the attitude solution tends to be degraded, whereas the chance of star identification error increases. For the PAD, how evenly the stars are distributed in the LRS FOV (i.e. 1σ value) is more important than how many stars are observed overall (i.e. mean value).

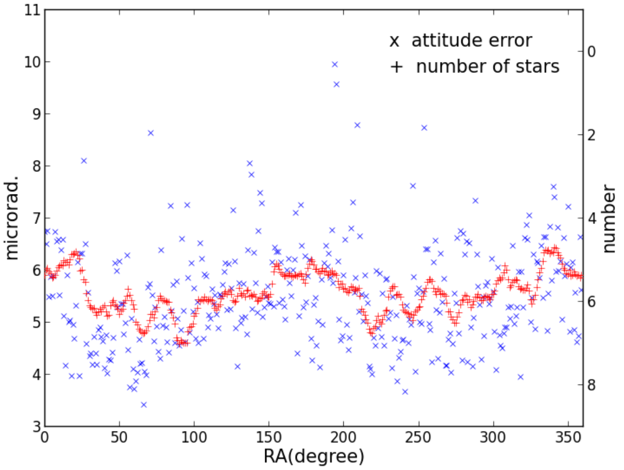

**Fig. 22 Full-sky simulation results: RSS attitude error (blue) and number of stars per FOV (red).**

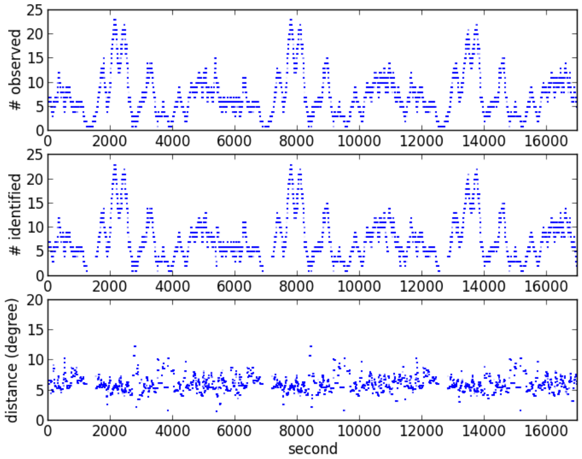

**Fig. 23 Number of measured(upper)/identified (middle) stars, and average distance (lower)**

Figure 23 (left) shows the impact of the color index uncertainty on the optical center estimation. The optical center error directly affects the attitude solution as the bias and passes down to the pointing determination bias. The range residual analysis from the ocean scan data at GSFC will provide the correction of the resultant bias as the PPD calibration. In the full sky simulation, optical center is initially at (512, 512) pixels, whereas the true optical center is at (521, 540) pixels. Figure 27 shows the optical center error after the color correction is completed with 5 iterations. The largest optical center error is near 800 μrad (≈ 4 pixels) in x axis and 400 $\mu$rad (≈ 2 pixels) in y axis. The average optical center error from the 360 RA cases is -8.19 $\mu$rad for x axis and 5.68 $\mu$rad for y axis, which implies that the optical center error is fairly a random error with nearly zero mean when simulations spread out over the whole sky. However, it would take about two years of data collection in order to cover the whole sky with ICESat-2 orbit. The optical center would change slowly with time and the calibration is available from the ocean scan analysis. A reasonable approach is that the PPD processes multiple day data to get the optical center estimates for each day first, then the averaged optical center is used the second processing of the same days for the consistency of the attitude/pointing bias in the PPD products. Once the corrected biases (or calibrated optical center) is available from the PPD calibration based on ocean scan analysis, the optical center estimation is no longer required in the PPD processing.

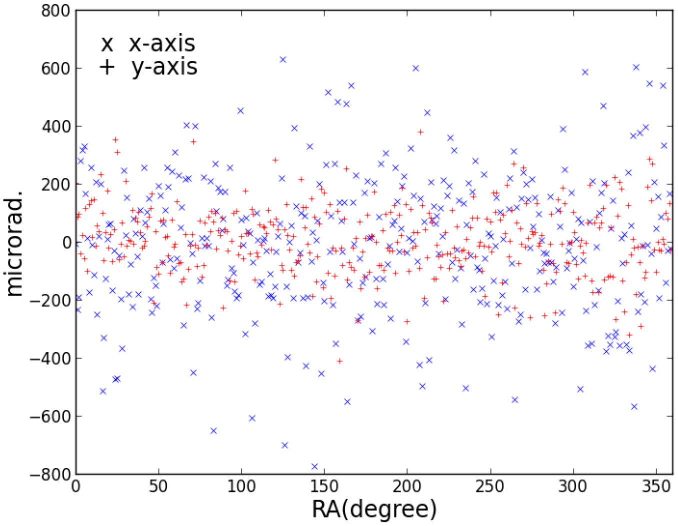

**Fig. 24 Optical Center errors from full-sky simulation**

## 5.5 Impact of Distortion

The distortion of the ICESat Instrument Stat Tracker (IST), shown in Figure 28, has both radial and tangential component. The color correction formula is based on the LRS measurement model that can observe the radial distortion. The color correction can be adversely affected if distortion exists on the LRS measurements because both distortion correction and color correction depend on the same information source: star position in ICRF or star catalog. Two different distortion models are considered in our investigation for the impact on the color correction. The IST distortion is stretched to 12° × 12° LRS FOV size from the original 8° × 8° IST FOV. The second distortion is a pure radial distortion with the maximum of 5 arcseconds (24 $\mu$rad) at the corners of the FOV, and zero at the center. Each distortion model is added to simulated star measurements with the chromatic aberration.

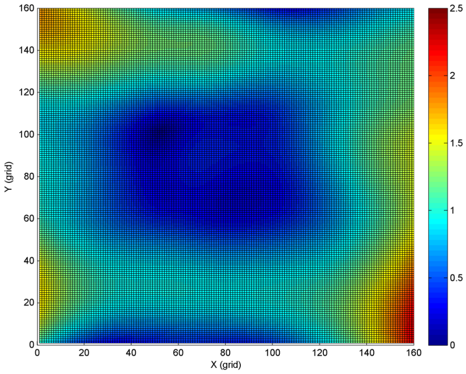

**Fig. 25 ICESat IST distortion map**

Fig. 29 illustrates attitude determination errors after the color correction for various simulation cases. The y axis shows the attitude determination error after the color correction. The numbers in x axis are multiple of the distortion error; N is for N times larger distortion than the original distortion described above. The largest distortion is by a factor of ten, 10 times greater than the original distortion, which means 50 arcseconds (≈ 242 $\mu$rad) maximum distortion at the corners of LRS FOV for the radial distortion and ~30 arcseconds (≈ 142 $\mu$rad) maximum for the IST distortion. The results show that the clear impact on the attitude solution from the IST distortion model, but no performance degradation from the pure radial distortion. It is the expected results because the color correction formula is the modification of the LRS ICD model (Section 4.1.2) that is designed to correct the radial distortion. On the other hand, it does not respond well to the tangential component distortion.

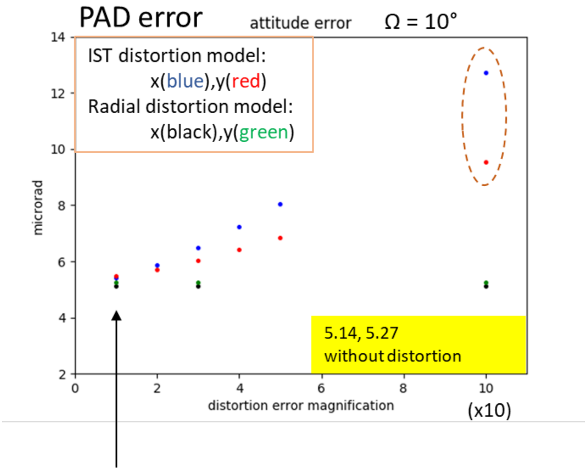

original distortion size (x01)
3 arcsec(max) for IST distortion
5 arcsec(max) for radial distortion

**Fig. 26 Attitude error vs. Distortion**

## 5.6 Color Index Improvement

The impact of the color index uncertainty on the color correction is obvious in Figure 22 and Figure 23. Further analysis of the tangential component distortion on the color correction (Figure 29) indicates that stars with a high color index error are more affected by the tangential distortion and degrade the attitude solution more significantly. In addition, detailed analysis of the full sky simulation result illustrated in Figure 25, manifests the correlation between the average attitude error and the number of blue and red stars. To improve the color correction and attitude solution, it is necessary to reduce the star color index uncertainty in the mission star catalog. The challenge with improving the impact of the uncertainty is identifying those stars that contain high color index errors.

By using the determined attitude and position of the measured star in the CRF, a graphical tool is developed to find the star with high color index error. The procedure is summarized in the flowchart in Figure 30. It starts with the color correction that provides best attitude solution using the color indices found in the mission star catalog.

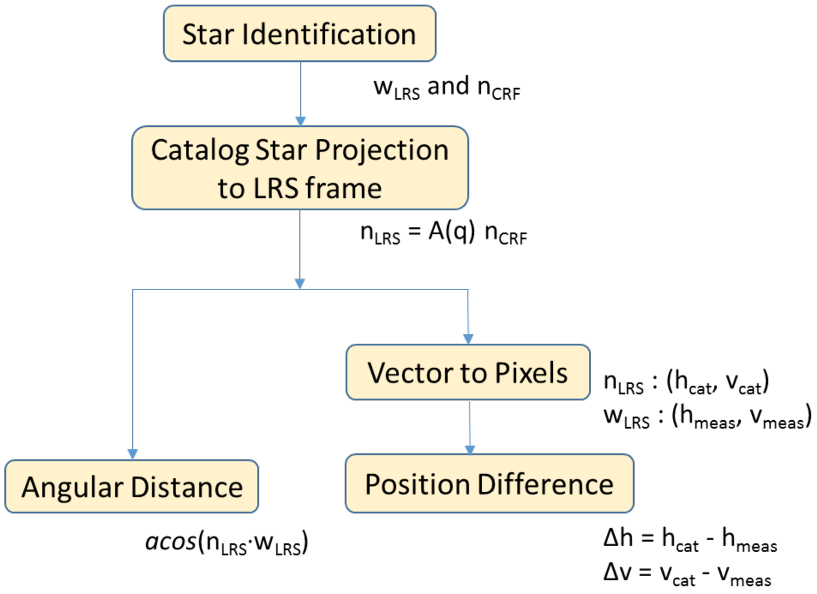

**Fig. 27 Distance between measured and predicted star positions**

The $n_{CRF}$ is the unit vetor of the measured star in the CRF. It is available through the star identification process. The $w_{LRS}$ is the corresponding unit vector measured in the LRS stellar-side frame. Note that the LRS coordinate frame is stellar-side frame in this section (i.e. $A_{CRF}^{LRS} = A_{CRF}^{ST}$). The estimated attitude in matrix, $A_{CRF}^{LRS}$, projects $n_{CRF}$ to the computed unit vector, $n_{LRS}$, in the LRS stellar-side frame, by

$$n_{LRS} = A_{CRF}^{LRS}\, n_{CRF} \tag{5.3.1}$$

Both $w_{LRS}$ and $n_{LRS}$ are unit vectors in the same LRS coordinate frame; one is measured, the other is predicted (Figure 31). The angular distance, $\Delta\theta$, or coordinate difference (Δh, Δv) should be zero or constant if there is no chromatic aberration (and distortion) present in the observation.

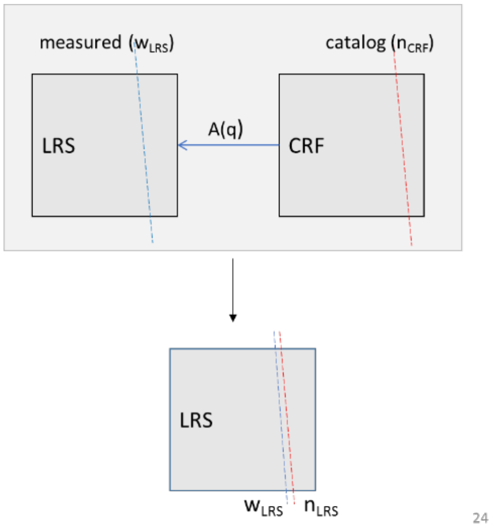

**Fig. 28 Measured and projected star coordinates**

If an accurate attitude solution is available through the color correction, $n_{LRS}$ and $w_{LRS}$ would be ideally parallel (or the constant distance) to each other with the noise from random measurement error. Figure 32 shows the $\Delta\theta$ vs. time plots from simulation: (a) with no chromatic aberration (b) with chromatic aberration before the color correction (c) with chromatic aberration after the color correction. Without chromatic aberration, the result conatins only measurement noises (17 $\mu$rad, 1σ). If the chromatic aberration exists without any correction, $\Delta\theta$ increases to nearly 1000 $\mu$rad- the maximum difference determined by the FOV size. With the color correction, $\Delta\theta$ is clearly reduced to the level of the star measurement error (17 $\mu$rad, 1σ), however, an unusually ~~y~~ large peak appears at about ~4700 seconds and repeats in subsequent orbits. At the time of the peak, 6 stars were identified and one of them (star 2503 in the mission star catalog) had high color index error; the color index (CI) in the star catalog is 1.607 while the true CI used for the simulation of the chromatic aberration is 1.927. It is a blue star that has a statistically large CI error (0.1, 1σ). In this case, the CI error is particularly large, -0.32.

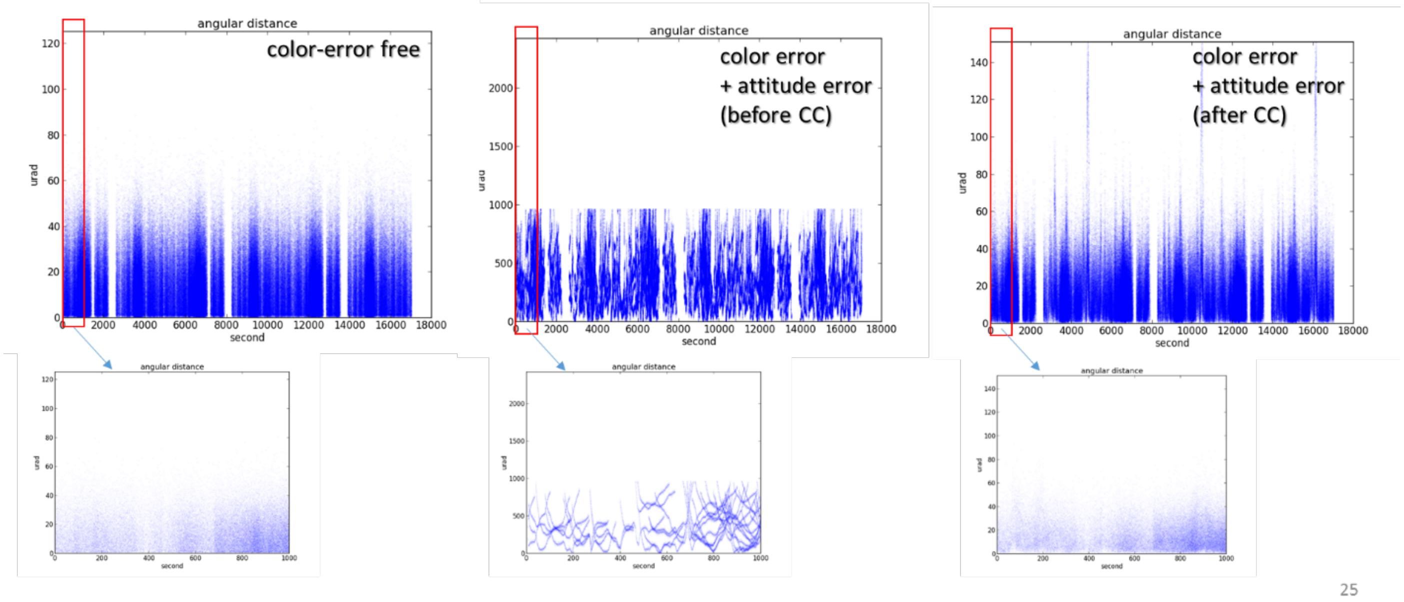

a) No color error b) before color correction c) after color correction

**Fig. 29 Angular distance between measured and predicted star coordinates**

Additional information for the star 2503 measurement is available by looking at the pixel distance Δh or Δv. The curves in Figure 33(a) show Δh vs. h: the estimated attitude is used for the upper curve and the true attitude is used for the lower curve. The pixel distance first decreases (to a low point of -100 $\mu$rad for the upper curve), as the star moves through the FOV, then returns to zero near the horizontal center of the FOV. The star pass through the second half of the FOV shows the opposite pattern. This high curvature is caused by a high CI error of -0.32. Most catalog stars have a CI error less than 0.2 in magnitude, and thus do not curve as much as star 2503.

The magnitude and direction of the CI error of star 2503 were modified in a few different ways; (b) -0.16 (half size), (c) +0.32 (opposite direction), (d) +0.16 (opposite direction and half size). The simulation results show that the direction and magnitude of the curvature are evidently correlated to the sign and magnitude of the CI error.

Star 2520 is one of the five other stars observed at the time period of star 2503 measurement, and its CI error is 0.09. The curvature of this star is relatively larger with the estimated attitude than with the true attitude (Figure 34(a)). By excluding star 2503 in the attitude determination, the curvature with the estimated attitude decreased and became similar to the true attitude case (Figure 34(b)). It indicates that high CI error of star 2503 caused degradation of attitude solution and it created the increased curvature to the other star at the same measurement time.

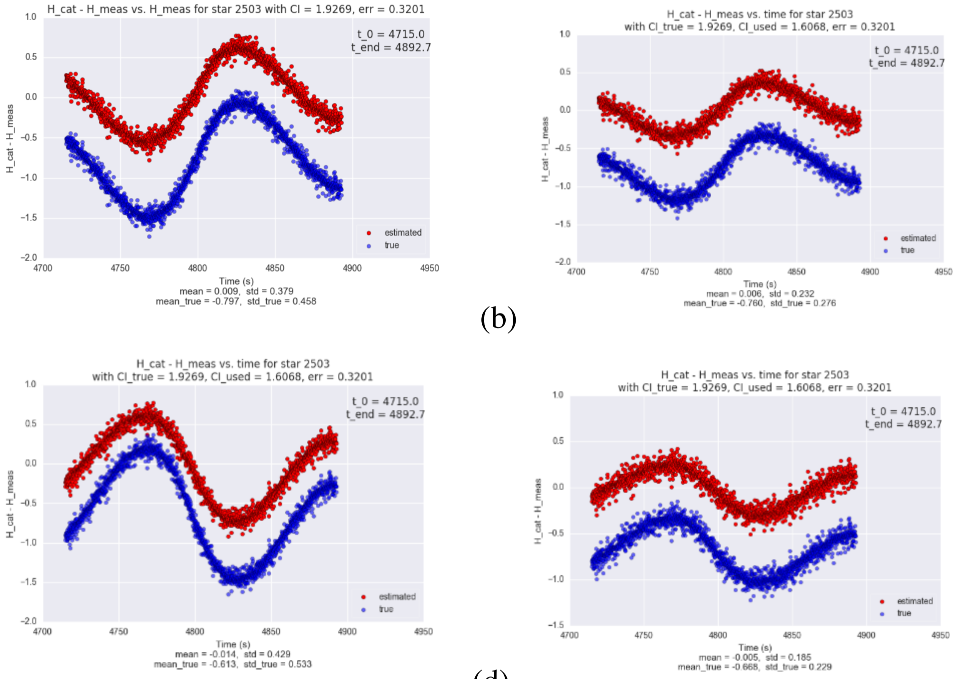

(a) (b)

(c) (d)

**Fig. 30 Pixel distance between measured and predicted star coordinates for star 2503**

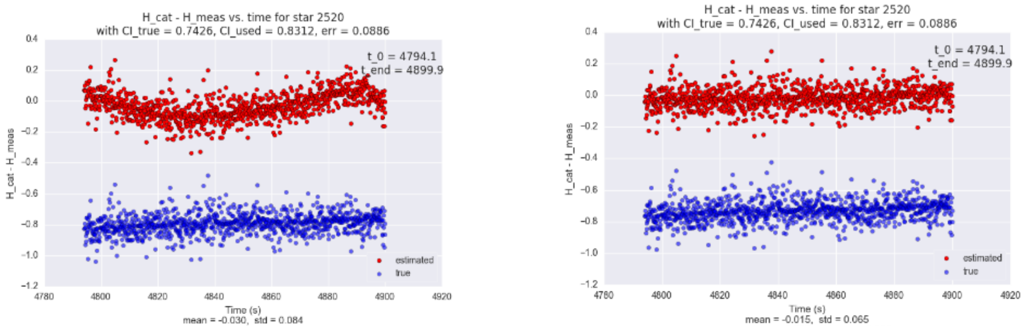

(a) (b)

**Fig. 31 Pixel distance between measured and predicted star coordinates for star 2520**

Discarding the stars with high CI error for an improved attitude solution seems to be a reasonable approach, however, it is usually unadvisable to reduce the number of usable stars. An alternative approach is to improve the CI value for stars with noticeably large CI error rather than exclude them from the attitude solution. This alternative allows for leveraging the otherwise omitted star's contribution to the attitude determination when considering other star's CI improvements As an example, using star 2503 with a true CI value resulted in a curvature decrease in the pixel distance plot with the estimated attitude. This decrease was not observed in the case where star 2503 was excluded from the analysis. Furthermore, analysis of this particular case also concluded that a~~n~~ previously unidentified star was successfully identified when the CI for 2503 was corrected rather than thrown out, as the number of usable stars increase to seven. This indicates that the use of star 2503 with the corrected CI is a better option than simply discarding it in terms of the overall attitude solution accuracy.

Without knowing the true CI values, the CI correction approach starts with searching for unusual peaks within the angular distance plot (Figure 32), then moves to the pixel distance plot (Figure 33) to evaluate those stars associated with the peaks. As the questionable peaks are removed or explained through the curvature analysis approach the CI estimate will continue to improve until all artifacts are addressed. Although a manual approach to CI improvement is certainly feasible it isn't practical given the amount of time and resources it would require. The method developed here for the automatic comparison of the measured curvature with the theoretical curvature calculated from the color correction formula mitgates the requirement for manual processing.

The range of expected CI error values between -0.35 and +0.35. The vast majority of stars have errors less than 0.2. For a range of 20 evenly spaced color errors between -0.35 and +0.35, the color correction formula produces a curve associated with each error, for each star. These curves are created using the boundary conditions for every star (starting and ending horizontal and vertical pixel positions), and assuming a linear pass through the FOV. For 1000 data points along this linear path, the color correction formula is applied to find the corrected horizontal pixel position by using every CI equal to one of the 20 errors plus the CI that was used in the attitude determination code.

In Figure 33(a), the blue data points represent the mean fit curve that is compared with the theoretical $\Delta x$ vs. $x$ curves produced by the color correction formula. A spline interpolation is used to extrapolate the mean values from 20 data points to 1000 data points. For each of the 20 theoretical curves, the root mean square (RMS) value between the curve and the interpolated Δh vs. h plot is calculated and recorded. Then, spline interpolation is used again, this time to create a function relating RMS vs. CI error. The CI error with an RMS closest to 0 is assumed to be the CI error of the star.

Figure 35 shows an example of this procedure for star 2503. Each colored curve represents the theoretical Δh vs. h for 2503 using a different CI error, given its starting position, ending position, and catalog CI (1.6068) value. The purple curve represents a CI of 1.2568 (CI error = -0.35). The red curve represents a CI/CI error of 1.9568/+0.35. The dashed line is the mean value of the calculated curve (blue dots from Figure 33(a)). An RMS calculation would show that the shape of the calculated curve is somewhere between the orange and red, which means the CI error must be between 0.35 and 0.175. With a spline interpolation of 20 curves, you can very accurately estimate the actual CI error.

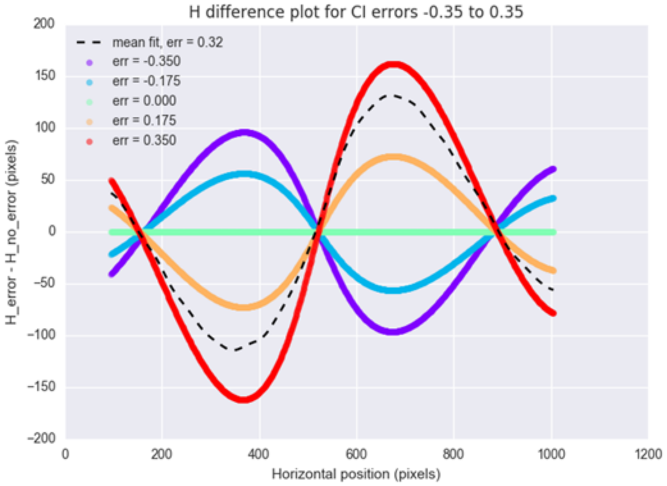

**Fig. 32 H difference plot for CI errors -0.35 to +0.35**

A known limitation of this method is its inability to account for the effects of attitude error. If the attitude error is large, it could cause a star's graphical data to show more or less curvature than its CI error would indicate- similar to the upper curve in Figure 33(a). However, the attitude solution improves with the iterative procedure by using the corrected color indices for the stars that have considerably large initial color index error. In each iteration, the cut-off value for the color index correction can be lowered with the improved attitude solution. This method was tested using multiple datasets, and for each one, the average CI error was cut approximately in half after three iterations. Only once was a star given a worse CI after the first iteration, and it was corrected by the second.

Table 10 shows an example of statistics from the iteration procedure. After each iteration, the limit for correcting CIs was decreased.

**Table 10 Statistics for color index correction**

| cutoff value | # of stars corrected | average CI error | EKF error (mean, 1σ) | QUEST error (mean, 1σ) |
|---|---|---|---|---|
| No cutoff | 0 | 0.02364 | 4.7229, 5.4262 | 8.7225, 9.5027 |

| | | | | |
|---|---|---|---|---|
| 0.08 | 11 | 0.018991 | 3.5785, 4.3407 | 7.2952, 7.1418 |
| 0.07 | 13 | 0.018106 | 3.5785, 4.3191 | 7.2967, 7.1278 |
| 0.06 | 20 | 0.015712 | 3.4169, 3.2737 | 7.1924, 7.0528 |

Since the overall attitude does not improve much after the first iteration, there is no justified reason to keep decreasing the limit. It is determined that one or two iterations are all that's really needed to meet the operational requirement, with the first iteration having a limit like 0.08 and the second having 0.06 or 0.05.

# 6.0 Ancillary Processing

The purpose of this section is to present the auxiliary processing before and after the primary PPD process. Flight telemetry is delivered from GSFC as ATL02 files and the PPD product is delivered to GSFC as ANC05 files. Both ATL02 and ANC05 files are in HDF5 format. The ATL02 file format is described in its data dictionary document provided by SIPS. The format of the ANC05 file is described in the POD Facility ICD [54] along with other input and output files between the UT ARL PPD group and GSFC. Unless otherwise stated, input/output data files here are focused on ATL02 and ANC05 files. Figure 36 summarizes overall PPD processing and data flow.

The quality of the PPD product is dependent on the quality of the input data and validation of the attitude/pointing determination results. Therefore these additional steps are as important as the main PPD processing. This ATBD document basically emphasizes the main algorithm of the PAD and PPD. Rather than describing all the details of the preprocessing and postprocessing, the general ideas and important concepts of preprocessing and postprocessing are discussed here in the context of the quality control of the PAD/PPD. The connection for file transfer between GSFC and UT ARL was already established and tested.

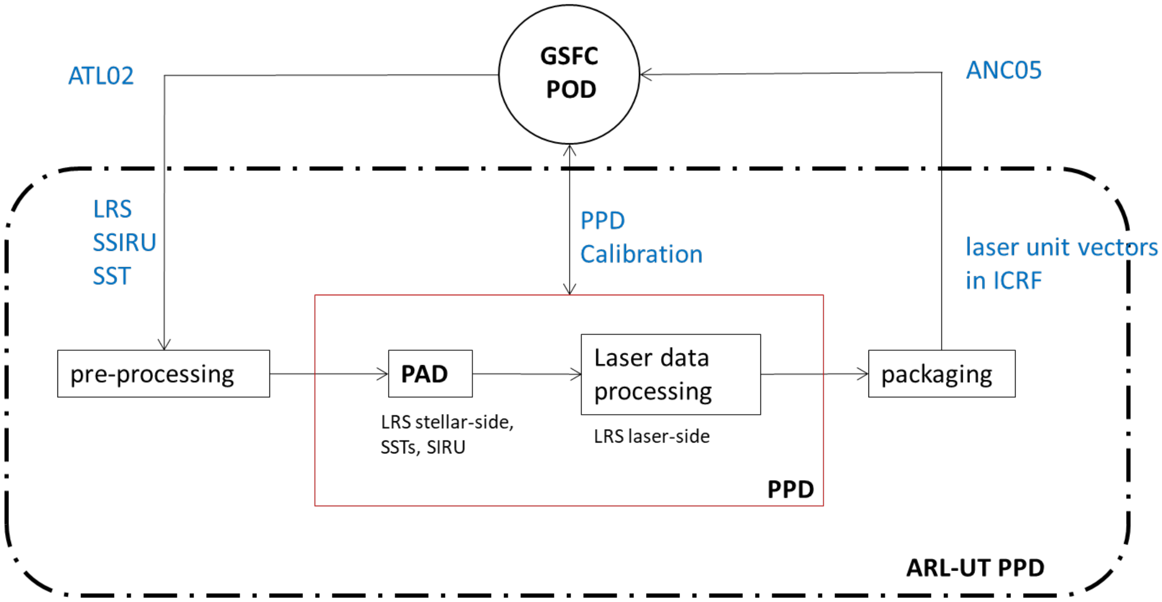

**Fig. 33 PPD Data Flow**

## 6.1 Preprocessing

Flight telemetry in ATL02 file is handled in a preprocessor that functions as an abstraction layer. When there is a change of telemetry format or multiple formats for the same telemetry, corresponding adaptations are made in the preprocessor but no changes are needed within the primary processing. After launch and in the early orbit, minor changes should be expected to the flight format and the interpretation of the ATL02 data may also change with the better understanding of the real flight data. Regardless of the cause, the preprocessing should be designed to deal with the change in the raw data so that the input/interface to the dedicated PAD/PPD processing is not affected by the change in ATL02. There were cases of this with the ICESat GLA04 flight format- a similar data packet to ATL02. For example, there was a change of the GLA04 definition for IST star position coordinates which had to be accommodated in the preprocessing algorithms. The preprocessor outputs should be stable representations of sensor observations for processing and adapt to the perfrable representation from the consideration of performance and clarity.

One of the most important functions of the preprocessor is to sort the sensor observations in timesuch that the output is a time-tag sorted event list of all observations (LRS, SST1, SST2, and SIRU) during a specified time interval $t_{start}$ and $t_{end}$. In addition to the sensor observations, the preprocessor extracts the auxiliary housekeeping information (e.g. LRS thermistor data, background noise, etc), LRS star/laser images (by request) and onboard solutions (attitude, position, and velocity) to separate files. In the daily PPD processing, the onboard attitude and velocity information are particularly important for the coarse attitude and stellar aberration corrections while the housekeeping and image data will be used for general analysis. ATL02 also contains other telemetries such as GPS and ATLAS that are bypassed by the PPD preprocessing workflow.

The information required for PPD is a compilation of data from multiple telemetry files. ATL02 is delivered in ~300 files for a daily product generation. A daily PPD product is required to contain 25 hours of laser pointing vectors, providing a full 24-hour solution with 30 minutes additional coverage in the beginning and ending of the daily span for overlap and consistency checks. The comparison of the overlap period in successive days are particularly useful for the sanity/quality check of the solution. The additional time at the beginning of the processing is particularly important to the Kalman Filter that normally passes through the transient period before reaching the stable condition. In addition, star data gaps often occur at the beginning of the 25 hours data chunk and the impact is alleviated with the overlap. Previous work with ICESat PPD established that a 30 minute buffer on each each of the daily packet is the adequate length to avoid the low quality PPD product in the situation where star data was not available at the beginning of the day due to sun blinding or sparse star regions, for example.

The data structure in the preprocessed data file has three key components per record:

1. Time-tag
2. Observation type, signifying how to handle the record and its associated observation.
3. Observation parameters, or a pointer to the observation parameters if they are located in a different data structure.

This intermediate or interface data structure provides practical abstraction between the telemetry and the primary PAD/PPD processor. The definitions of the observation parameters are processor dependent and decoupled from telemetry formatting.

ATL02 provides measurement data with the time-tags for all the data types as the elapsed time from the fixed epoch. Whereas only one time-tag is assigned to SIRU and SST measurement, the LRS data has three time-tags for each star or laser measurement. During the preprocessing, the multiple star measurements observed in several milliseconds range are aligned to 10Hz rate by the algorithm described in Section 4.1.3. For the SIRU, the raw angle data in four gyro measurement axes are converted to the rate data in three orthogonal axes ideally parallel to the LRS stellar-side.

## 6.2 Quality Check

The preprocessed data contains time-tag sorted parameters of all observations (LRS, SST1, SST2, and SIRU) during 26 hours time interval. The part of the preprocessing after sorting out the observations is the quality check (QC) of the input telemetry. The QC can be divided into the following categories based on the functions.

**Data gap detection**

Data ~~is often divided~~ gaps occur through natural causes (LRS star tracker sun blinding, sparse star region) as well as due to technical problems (time-tag alignment issues that cause short time-tag skips, telemetry malfunctions, etc). Long data gaps that can degrade the quality of the PPD product are reported within ANC05. The preprocessor (or main processor) fills in the short time-tag skips to prevent consequent outlier in the PPD product.

### Sanity checking

Non-optimal behavior of the instrument could deteriorate the quality of the data and could disrupt the PPD processing and/or produce degraded quality PPD solutions. As such, the standard PPD processing is configured to correct or reject data that is determined invalidIdentification of the invalid data is automated through 'sanity checking' within the PPD workflow..

The first attempt to sanity check focuses on the ATL02 flags. The LRS and SIRU observations rely on multiple binary flags to report the quality of each measurement. For example, the LRS stellar-side includes two binary flags: a trackstat bit, and a quality bit. A star pass is required to consist only of observations that satisfy both flags to indicate valid tracking and full accuracy. In principle, without this requirement, an otherwise good astronomical point source can be acquired and tracked by the LRS but be rejected because of insufficient observations that don't satisfy the quality flag. This can happen in practice for a star that is only marginally bright enough for LRS tracking. The LRS acquires the star and makes observations- triggering the trackstat flag but the accuracy is low and the quality bit is not set. This additional check was determined necessary based on experience with ICESat where  problematic stars were not identified using a single flag notification.

Another initial check is of star velocities across the FOV. These are calculated with two or more observations using the two-dimensional pixel coordinates. The velocity should be consistent to other stars in the FOV (or recently in the FOV) and with the estimated angular rate. Stars with inconsistent velocities are rejected as transients. The LRS housekeeping data in ATL02 includes star rate information as *srate* variables at 1 Hz rate for this purpose

SST telemetry in ATL02 provides a quality measurement of each quaternion computed by its internal processing as an alternate approach to using binary flags. The quality value is monitored in the preprocessing, and the actual star centroids are requested for detailed analysis if necessary.Some sanity checking is telemetry format dependent, but it is kept to a minimum to promote code maintainability and reuse. If there is a change of telemetry format, it should not break sanity checking configurations and quality monitoring functionality.

An example of the data monitoring forsanity checking is given in Figure 37. This particular check is for the Center of Integration (COI) time in simulated star data (Section 4.1.3). The LRS stellar-side COI time is of a particular importance. In ICESat star tracker telemetry, frequent time-tag errors were found;  time-tag skips, reversals, and duplicated data. These anomalies caused either breakdowns within the PAD processing chain or resulted in substantial attitude errors in the solution. It was determined that the cause of the problem was that the erroneous COI values were outside the anticipated range of values. For best practices, all of the time tag measurements will be monitored as it is a primary area of potential problems with the PPD workflow.

Unforeseen issues like the COI time error will require mitigation within the analysis and potentially how the data is utilized, especially when it is caused by hardware. Similar problems to those encountered during the ICESat mission could very well impact ICESat-2. In those cases the mitigation strategies have been established but adapation will be required for implementation to the current mission specifications. Other issues might arise for ICESat-2 that were not problems for its predecessor- those are the ones that don't have established fixes but are a focus in terms preparing for possible scenarios.

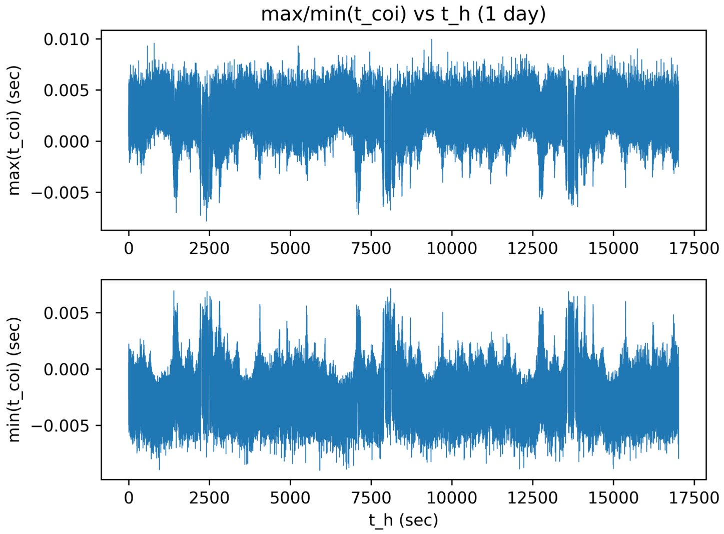

**Fig. 34 Maximum/minimum COI time at each LRS stellar-side Header time**

## Outlier detection

Outliers are data labeled valid data but still have values outside of the expected range. Unreasonably large peaks in the gyro rate, a star moving irregularly, and star coordinate outside the LRS FOV are typical examples of outliers. The majority of the outlier data will be edited out through preprocessing- sanity checks and outlier detection. Only when ICESat-2 is on-orbit will the outlier identification methods be refined and optimized based on the actual values of the data observables.

**Quality monitoring system**

The efficient way of QC is automatic reporting and visual monitoring of the input data. Measured parameters have values in the certain ranges. The results of the daily preprocessing are automated and routinely distributed via e-mails to the PPD technical team. For example, if the preprocessing detects abnormally large gyro rate, an e-mail notification will be generated with the emphasis of the special event in the title or header part of the email. Various plots regarding input data parameter trends such as LRS time-tags, gyro rates or SST quaternions are also automatically generated during the preprocessing and routinely reviewed by the PPD personnel.

Some QCs or data uncertainty analyses are applied after the primary PAD processing. For example, once star identification is complete and the subsequent PAD solution is generated, the triangle method (Section 4.1.7 and Section 4.3.4) provides the catalog entry number of any star that has large position errors. It will help to find out the possible cause of the PPD degradation: misidentification, high color index error, or distortion in the LRS optics, etc. to determine solutions, if needed.

These analyses that support PAD solution errors based on star identification are aided with a custom visulazation monitoring tool that measures and displays the star motion. The visualization tools are prepared for the verification of the star identification, the use in the color correction, and evaluation of the PAD/PPD.

As a consequence of the anomaly detection in LRS star/laser centroids in the preprocessing, the request can be made for the pixel image of the star/laser centroids if the detailed analysis is necessary as a QC of the input data. The ATL02 has the groups for image data, normally empty without wasting the disk space.

Note that some of the problems in ATL02 data will be reported to SIPS if the cause is not clearly understood or the correction should be made in the ATL02 or earlier stage.

## 6.3 Postprocessing

The evaluation of the PAD/PPD output, the generation of the ANC05 file following, putting the ANC05 file to the designated machine/directory, and archival of the important files for future analysis/reprocessing are considered as the postprocessing. For the PAD product evaluation, various methods such as star residuals (prediction vs. measurement), analysis of PAD boresights against gyro angles, comparison of EKF solution to QUEST solution, etc. will be used. The attitude determination by SST and SIRU data, without using the LRS stellar-side data, produces an independent attitude solution that can be used for the evaluation of the primary PAD.

Crucial calibration/validation methods for PPD biases, trends, and orbital variation errors are the range residual analysis from ocean scan maneuvers and short-period crossovers [50]. These techniques were successfully applied on the ICESat PPD and will be used again for the ICESat-2 PPD. The SF_2_LF (LRS stellar-side to laser-side rotation) quaternion file is essential to determine the LRS laser-side attitude from the stellar-side attitude. Ground based activites in the upper and mid-latitudes will utilized corner cube retroreflectors (CCR) placed in know locations at measured elevations. The CCR arrays will return a unique signature back to the satellite which can be analyzed to determine the accuracy of the geolocation and ultimately the quality of the pointing component at various locations within the orbit. These activities, and others planned for validation of the Level 1 mission requirements can be found in the ICESat-2 Project Science Office Post-Launch Global Validation Plan Document.

Before the upload of the final products to the machine accessible by the GSFC, the plots and statistics automatically generated during the processing are carefully reviewed by the PPD personnel. Unless the unusual event is detected, ANC05 file is uploaded along with and SF_2_J2000 (LRS stellar-side frame to J2000 CRF rotation) to the designated machine at UT ARL waiting for the acquisition by the GSFC. The content and format of the PPD products are defined in POD Facility ICD [54]. Archival of the critical files for possible analysis in the future or reprocessing is followed. The last two versions of the selected input/intermediate/output files are archived.

## 6.4 Sensor Failure

In the normal situation, the attitude determination based on SST and SIRU, without the inclusion of the LRS stellar-side data, is used for evaluation of the main PAD output. However, this is also a contingency plan that can be used as an alternative PAD in the worst case scenario: the failure of the LRS stellar-side. The failure of a single sensor does not necessarily mean complete PPD failure. One of the primary sensors in ICESat, Laser Reference Sensor, did not perform as planned, but the PPD overcomes the problem by properly updating the software with the redesigned algorithm [55]. If SIRU fails, the angular rates may be generated by using the alternative design of the filter, but the accuracy level is in doubt considering the importance of the SIRU data in the EKF propagation. Even though it would be challenging to meet the anticipated PPD requirement with alternative algorithm/software, the contingency plan to produce the best available estimates in the worst case situation is important.

## Glossary

**Ancillary inputs** refers to inputs that come from outside the ICESat-2 mission. Some examples are ephemeris data for the sun and moon (from JPL), fundamental star catalogs (SKY2000, Hipparcos), etc.

**ATLAS frame** the concept of an ATLAS frame comes up particularly in modeling and simulation of the overall geolocation process (level L2A product). It is an abstract and ideal frame. For ICESat there was often discussion of a GLAS frame and it was usually equivalent to a GLAS optical bench frame. For ICESat-2 the IMSC platform (carrying the SIRU and SSTs) is the obvious choice for an ATLAS frame.

**Bad stars** have LRS position measurements that are biased (from their reference positions given in the mission catalog) due to near-neighbor stars.

**Body frame** the term body frame may be local to the processor and filter, particularly the theory. A convention in attitude and alignment estimation theory to express the attitude as a rotation from the ICRF to the body frame $\mathbf{A}_i^b$. Here we express the star tracker alignments as rotations from this body frame $\mathbf{A}_b^{LRS}$, $\mathbf{A}_b^{SST1}$, $\mathbf{A}_b^{SST2}$. In general, in this document, the body frame is the same as the LRS frame, and often the ATLAS frame, and even the spacecraft frame (which is associated with the Orbital ATK onboard ACS).

**Calibration parameter inputs** refers to input parameters that are not included in the telemetry but are local to the ICESat-2 mission. They consist of ground testing and calibration information for the LRS, SST, and SIRU measurement and error models. Mission star catalogs can be loosely identified with the calibration inputs.

**Centroiding errors** or **high spatial frequency errors (HSFE)** are deviations away from the pinhole camera model that are a function of small changes of position on the focal plane, on the scale of individual pixels.

**Coordinate frames** these are abstract, ideal frames not directly associated with a sensor or empirical observations. In general, the **Body Frame** is associated with estimation, filtering, and knowledge. The **ATLAS Frame** is associated with simulation, modeling, and “truth”. The **orbit frame** is associated with the simplest orbit model. The **spacecraft frame** is associated with the Orbital ATK onboard ACS system.

**Distortion errors** or **low spatial frequency errors (LSFE)** refers here to deviations away from the simple pinhole camera model that are a function of the overall position on the focal plane [35, 37, 39].

**Error models** are stochastic equations involving random processes and represent uncertainties in sensor measurements and their interpretation.

**Filter cold start** means that default values for the states and uncertainties are used. An example is starting the filter without information from a previous run using telemetry that is nearby temporally.

**Filter warm start** means that state and uncertainty information from a previous run is available. The simplest case is starting a filter run using information from a previous run that is adjacent and even overlapping in time.

**Focal plane coordinates** represent unit vectors in an $\mathbf{i,j,k}$ sensor frame.

**Gyro telemetry** is received from the SIRU and used for propagation between measurement updates.

**High spatial frequency errors (HSFE)** or **centroiding errors** are deviations away from the pinhole camera model that are a function of small changes of position on the focal plane, on the scale of individual pixels

**Laser Telemetry** is received from the LRS laser tracker, which measures laser and reference spot centroids at 50 Hz.

**Laser Reference Sensor** consists of two trackers, referred as the **LRS star tracker** and the **LRS laser tracker**, joined back-to-back. The laser side functions like a star tracker, but observes artificial stars generated by the altimetry lasers and reference signals.

**Local Tangent Plane (LTP)** coordinates represent unit vectors in an $\mathbf{i,j,k}$ frame based on the body frame. Closely related to **sensor frame coordinates** or **focal plane coordinates** that represent unit vectors in an $\mathbf{i,j,k}$ sensor frame.

**Low spatial frequency errors (LSFE)** or **distortion errors** refers here to deviations away from the simple pinhole camera model that are a function of the overall position on the focal plane.

**Measurement Models** are deterministic equations for transforming and interpreting the sensor measurements.

**Mission Star Catalogs** are tied to the LRS star tracker. They can also be referred to as mission catalogs or LRS catalogs; the terms are completely equivalent here.

**Orbit frame** this is a basic LVLH frame for a circular orbit. It represents the simplest possible model $\mathbf{A}_i^{orbit}$ for the ATLAS frame attitude $\mathbf{A}_i^{ATLAS} = \mathbf{A}_{orbit}^{ATLAS}\mathbf{A}_i^{orbit}$ when $\mathbf{A}_{orbit}^{ATLAS} = \mathbf{I}$.

**Telemetry Inputs** refers to inputs from ATLAS and the spacecraft. These are the time series data sent from SIPS as HDF5 data files. They consist of 10 Hz LRS star measurements, 50 Hz LRS laser side measurements, 10 Hz quaternions and uncertainties from the two SSTs; 50 Hz SIRU measurements, ACS state estimates, temperature data, etc.

**Spacecraft frame** this frame is associated with the Orbital ATK onboard ACS. They express their alignments in the spacecraft frame so it is useful to keep in mind.

**Star Telemetry** is based on star measurements and is used to perform the filter measurement updates. It, therefore, determines propagation time intervals and filter cycle boundaries. It is a general term here for star measurements from the LRS and attitude estimates from the SSTs.

# Acronyms

| | |
|---|---|
| ACS | Attitude Control System |
| ARL | Applied Research Laboratories, The University of Texas at Austin |
| ARW | Angular Random Walk in gyro output |
| ATBD | Algorithm Theoretical Basis Document |
| ATLAS | Advanced Topographic Laser Altimeter System |
| AWN | Angular White Noise in gyro output |
| BSM | Beam Steering Mechanism |
| CI | Color Index |
| COI | Center of Integration |
| EKF | Extended Kalman Filter |
| FOV | Field of View |
| GLAS | Geoscience Laser Altimeter System |
| GSFC | Goddard Space Flight Center |
| HSFE | High Spatial Frequency Error |
| ICD | Interface Control Document |
| ICESat | Ice, Cloud, and Land Elevation Satellite |
| ICESat-2 | Ice, Cloud, and Land Elevation Satellite 2 |
| IMSC | Instrument Mounted Spacecraft Component |
| INS | Inertial Navigation System |
| IQR | Interquartile Range Q3-Q1 |
| IST | Instrument Star Tracker, ICESat |
| LF | LRS laser-side frame, the same as LT |
| LOESS | Locally Weighted Scatterplot Smoothing |
| LOS | Line of Sight, the optical axis of a sensor |
| LRS | Laser Reference Sensor |
| LRSICD | LRS Interface Control Document |
| LSFE | Low Spatial Frequency Error |
| LT (LTF, LF) | Laser Tracker Frame (LRS Laser-Side Coordinate Frame) |
| LTP | Local Tangent Plane coordinates for representing unit vectors |
| MEKF | Multiplicative Extended Kalman Filter |

| | |
|---|---|
| MMAE | Multiple-Model Adaptive Estimation |
| MRF | Master Reference Frame |
| NG | Northrop Grumman |
| PAD | Precision Attitude Determination |
| POD | Precision Orbit Determination |
| PPD | Precision Pointing Determination |
| PSO | Project Science Office |
| QC | Quality Check |
| RMS | Root Mean Square |
| RRS | Root Sum Squared |
| RRW | Rate Random Walk in gyro output |
| RTA | Receiver Telescope Assembly |
| SIMV9 | Simulation Version 9 (fundamental truth dataset from GSFC (Scott Luthcke) |
| SIPS | Science Investigator Led Processing System |
| SIRU | Space Inertial Reference Unit (it is scalable SIRU for ICESat-2) |
| ST (STF, SF) | Star Tracker Frame, (LRS Stellar-Side Coordinated Frame) |
| SST | Spacecraft Star Tracker or Sodern Star Tracker |
| TAMS | Telescope Alignment Monitoring System |

## References

[1] Saltzman, M., "Coordinate Systems Descriptions Report," ICESat-2-SYS-RPT-4972, Jun. 2017.

[2] Correll, T., ATLAS LRS Star Catalog, Jun. 5, 2015.

[3] ESA, *The Hipparcos and Tycho Catalogues*, ESA SP-1200, Noordwijk, Netherlands, 1997.

[4] Sande, C., Brasoveanu, D., Miller, A. C., Home, A. T., and Tracewell, D., "Improved Instrumental Magnitude Prediction Expected from Version 2 of the NASA SKY2000 Master Star Catalog," AAS 98-362, AAS Space Flight Dynamics, Advances in the Astronautical Sciences, Vol. 100, Univelt, 1998, pp. 765-778.

[5] Sande, C., Natanson, G., and Tracewell, D., "Effects of Uncataloged Near-Neighbor Stars on CCDST Operation," Proceedings NASA-CP-2005-212789, Proceedings of the NASA Goddard Flight Mechanics Symposium, 2005.

[6] Sande, C., Natanson, G., and Tracewell, D., "Effects of Uncataloged Near-Neighbor Stars on CCDST Operation," Goddard Space Flight Center, Maryland, 2005.

[7] Sande, C., Ottenstein, N., Tracewell, D., and Oza, D., "SKYMAP Requirements, Functional, and Mathematical Specifications," Report No. CSC-96-932-24, Computer Sciences Corporation, Falls Church, Virginia, Report CSC-96-932-24, Aug. 1999 1999.

[8] Sande, C. B., Warren, W. H., and Tracewell, D. A., "Recent Enhancements to and Future Plans for the SKY2000 Star Catalog," *Journal of the American Association of Variable Star Observers*, Vol. 29, No. 2, 2000, pp. 123-128.

[9] Lucke, R. L., Sirlin, S. W., and San Martin, A. M., "New Definitions of Pointing Stability: AC and DC Effects," *AAS Journal of the Astronautical Sciences*, Vol. 40, No. 4, 1992, pp. 557-576.

[10] Bayard, D. S., "A State-Space Approach to Computing Spacecraft Pointing Jitter," *Journal of Guidance, Control, and Dynamics*, Vol. 27, No. 3, 2004, pp. 426-433.

[11] Pittelkau, M. E., "Pointing Error Definitions, Metrics, and Algorithms," AAS 03-559, AAS/AIAA Astrodynamics Specialists Conference, Big Sky, MT, 2003.

[12] Pittelkau, M. E., "RIMU Misalignment Vector Decomposition," AIAA 2004-4856, AIAA Astrodynamics Specialist Conference, Providence, RI, 2004.

[13] Pittelkau, M. E., "Observability and Calibration of a Redundant Inertial Measurement Unit (RIMU)," AAS 05-105, AAS Space Flight Mechanics Meeting, Advances in the Astronautical Sciences, Vol. 120, Univelt, 2005, pp. 71-84.

[14] Pittelkau, M. E., "Calibration and attitude determination with Redundant Inertial Measurement Units," *Journal of Guidance, Control, and Dynamics*, Vol. 28, No. 4, 2005, pp. 743-752.

[15] Pittelkau, M. E., "Attitude Determination and Calibration with Redundant Inertial Measurement Units," AAS 04-116, AAS Space Flight Mechanics Meeting, Advances in the Astronautical Sciences, Vol. 119, Univelt, 2005, pp. 229-248.

[16] Markley, F. L., "Attitude Error Representation for Kalman Filtering," *Journal of Guidance, Control, and Dynamics*, Vol. 26, No. 2, 2003, pp. 311-317.

[17] Pittelkau, M. E., "Rotation Vector in Attitude Estimation," *Journal of Guidance, Control, and Dynamics*, Vol. 26, No. 6, 2003, pp. 855-860.

[18] Savage, P. G., "Strapdown Inertial Navigation Integration Algorithms Design Part 1: Attitude Algorithms," *Journal of Guidance, Control, and Dynamics*, Vol. 21, No. 1, 1998, pp. 19-28.

[19] Pittelkau, M. E., "Survey of Calibration Algorithms for Spacecraft Attitude Sensors and Gyros," AAS 07-295, AAS Astrodynamics Specialist Conference, Advances in the Astronautical Sciences, Vol. 129, Univelt, 2007, pp. 651-706.

[20] Gray, C. W., Herman, L. K., Kolve, D. I., and Westerlund, G. L., "On-Orbit Attitude Reference Alignment and Calibration," AAS 90-042, AAS Guidance and Control Conference, Advances in the Astronautical Sciences, Vol. 72, Univelt, 1990, pp. 275-292.

[21] Bayard, D. S., "An Overview of the Pointing Control System for NASA's Space Infra-Red Telescope Facility (SIRTF)," AIAA 2003-5832, AIAA Guidance, Navigation, and Control Conference, Austin, TX, 2003.

[22] Bayard, D. S. and Kang, B. H., "A High-Order Kalman Filter for Focal Plane Calibration of NASA's Space Infrared Telescope Facility (SIRTF)," AIAA 2003-5824, AIAA Guidance, Navigation, and Control Conference, Austin, TX, 2003.

[23] Li, R., Needelman, D., Fowell, R., Tsao, T.-C., and Wu, Y.-W., "Reusable Stellar Inertial Attitude Determination (SIAD) Design For Spacecraft Guidance, Navigation & Control," AIAA 2005-5928, AIAA Guidance, Navigation, and Control Conference, San Francisco, CA, 2005.

[24] Li, R. and Wu, Y.-W., "Absolute and Relative Attitude Determination for Multiple Payloads On Spacecraft," AIAA 2006-6048, AIAA Guidance, Navigation, and Control Conference, Keystone, CO, 2006.

[25] Pittelkau, M. E., "A Kalman Filter Approach to System Alignment Calibration," AAS 00-127, AAS/AIAA Space Flight Mechanics Meeting, 2000.

[26] Pittelkau, M. E., "Kalman Filtering for Spacecraft System Alignment Calibration," *Journal of Guidance, Control, and Dynamics*, Vol. 24, No. 6, 2001, pp. 1187-1195.

[27] Pittelkau, M. E., "Everything Is Relative In Spacecraft System Alignment Calibration," *Journal of Spacecraft and Rockets*, Vol. 39, No. 3, 2002, pp. 460-466.

[28] Pittelkau, M. E. and Dellinger, W. F., "Attitude Sensor Alignment And Calibration For The TIMED Spacecraft," AAS 03-153, AAS/AIAA Space Flight Mechanics Meeting, Ponce, Puerto Rico, 2003.

[29] O'Shaughnessy, D. and Pittelkau, M. E., "Attitude Sensor and Gyro Calibration for Messenger," NASA International Symposium on Space Flight Dynamics, NASA Conference Proceedings, Vol. NASA CP-2007-214158, NASA, 2007.

[30] Hanlon, P. D. and Maybeck, P. S., "Multiple-Model Adaptive Estimation Using a Residual Correlation Kalman Filter Bank," *IEEE Transactions on Aerospace and Electronic Systems*, Vol. 36, No. 2, 2000, pp. 393-406.

[31] Lam, Q. M., Hunt, T., Sanneman, P., and Underwood, S., "Analysis and Design of a Fifteen State Stellar Inertial Attitude Determination System," *AIAA Guidance, Navigation, and Control and Co-located Conferences*, AIAA 2003-5483, 2003, http://dx.doi.org/10.2514/6.2003-5483

[32] Markley, F. L., "Attitude Determination and Parameter Estimation Using Vector Observations: Application," *The Journal of the Astronautical Sciences*, Vol. 39, No. 3, 1991, pp. 367-381.

[33] Bayard, D. S., "High Precision Three-Axis Pointing and Control," in *Encyclopedia of Aerospace Engineering: Attitude Dynamics and Orbit Control of Spacecraft*. vol. 5 Part 26, R. Blockley and W. Shyy, Eds., ed Hoboken, NJ: Wiley-Blackwell Publishers, 2010, pp. 172-181.

[34] Bae, S, Smith, N., and Schutz, B. E., Precision Attitude Determination (PAD), GLAS ATBD Version 3.0, Center for Space Research, University of Texas at Austin, October, 2012.

[35] Liebe, C. C., "Accuracy performance of star trackers - A Tutorial," *IEEE Transactions on Aerospace and Electronic Systems*, Vol. 38, No. 2, 2002, pp. 587-599.

[36] Lam, Q. M., Woodruff, C., Ashton, S., and Martin, D., "Noise Estimation for Star Tracker Calibration and Enhanced Precision Attitude Determination," IEEE Information Fusion Conference, IEEE Conference Proceedings, IEEE, 2002, pp. 235-242.

[37] Wu, Y.-W. and Li, R., "Star Tracker Error Characteristics and Their Compensation Techniques," Proceedings NASA CP-2003-212246, Proceedings of the NASA Goddard Flight Mechanics Symposium, NASA-CP-2003-212246, 2003.

[38] Correll, T., "Laser Reference System (LRS) Command and Data Interface Control Document (ICD)," Revision B, ICESat-2-LRS-IFACE-1794, Nov. 2016.

[39] Griffith, T. D., Singla, P., and Junkins, J. L., "Autonomous On-orbit Calibration Approaches for Star Tracker Cameras," AAS 02-102, AAS Space Flight Mechanics Meeting, Advances in the Astronautical Sciences, Vol. 112, Univelt, 2002, pp. 39-57.

[40] Singla, P., Griffith, T. D., Crassidis, J. L., and Junkins, J. L., "Attitude determination and autonomous on-orbit calibration of star tracker for the gifts mission," AAS 02-101, Spaceflight Mechanics 2002, Advances in the Astronautical Sciences, Vol. 112, 2002, pp. 19-38.

[41] Smith, N., "Localized Distortion Estimation and Correction for the ICESat Star Trackers," M.S. Thesis, Aerospace Engineering, University of Texas at Austin, Austin, 2006.

[42] Semper, S., “Laser Reference System (LRS) Night Sky Test Report,” ICESat-2-LRS-RPT-4220, Oct. 2015.

[43] Arthur Gelb, *Applied Optimal Estimation*, The M.I.T. Press, Massachusetts, 1974, pp. 23-24.

[44] Samaan, M.A., Griffith, T., Junkins, J.L., “Autonomous on-Orbit Calibration Of Star Trackers,” *2001 Core Technologies for Space Systems Conference*, Colorado Springs, CO, 27-30 Nov. 2001.

[45] Mortari, D. and Neta, B., "K-vector Range Searching Techniques," Advances in the Astronautical Sciences, Vol. 105, Univelt Inc., 2000, pp. 449-463.

[46] Shuster, M. D., "Stellar Aberration and Parallax: A Tutorial," *Journal of the Astronautical Sciences*, Vol. 51, No. 4, 2003, pp. 477-494.

[47] Lauer, M., Jauregui, L., and Kielbassa, S., "Operational Experience with Autonomous Star Trackers on ESA Interplanetary Spacecraft," Proceedings NASA-CP-2007-214158, Proceedings of the 20th International Symposium on Space Flight Dynamics, NASA-CP-2007-214158, 2007.

[48] Yoon, S., Bae, S., and Schutz, B. E., "High Frequency Attitude Motion Of ICESat," AAS 05-108, AAS Space Flight Mechanics Meeting, Advances in the Astronautical Sciences, Vol. 120, Univelt, 2005, pp. 117-131.

[49] IEEE, "IEEE Std 647-2006 Standard Specification Format Guide and Test Procedure for Single-Axis Laser Gyros," ed: IEEE, 2006.

[50] Luthcke, S. B., Rowlands, D. D., McCarthy, J. J., Pavlis, D. E., and Stoneking, E., "Spaceborne Laser-Altimeter-Pointing Bias Calibration from Range Residual Analysis," *Journal of Spacecraft and Rockets*, Vol. 37, No. 3, 2000, pp. 374-384.

[51] Britt. J, “Geolocation Knowledge Budgets,” Revision G, ICESat-2-SYS- REQ-0450, ICESat-2 Controlled Document, Goddard Space Flight Center, Greenbelt, MD, 2015.

[52] Piot, D., Oddos-Marcel, L., Gelin, B., Thieuw, A., Genty, P., Martinez, P., and Airey, S., “Hydra Star Tracker On-board SPOT-6,” *American Astronautical Society,* AAS 13-046, 2013.

[53] Rozelle, D. M., “The Hemispherical Resonator Gyro: From Wineglass to the Planets,” *American Astronautical Society*, AAS Paper 09-176, Feb. 2009.

[54] Luthcke, S., Pennington, T., Rebold, T., and Thomas, T., "Interface Control Document (ICD) For Precision Orbit Determination (POD) Facility." Revision B, ICESat-2-FOPS-IFACE-4736, Feb. 2, 2018.

[55] Bae, S., Webb, C. E., and Schutz, B. E., “GLAS PAD Calibration Using Laser Reference Sensor Data,” *AIAA/AAS Astrodynamics Specialist Conference and Exhibit,* AIAA Paper 2004-4857, Aug. 2004. http://dx.doi.org/10.2514/6.2004-4857

[56] Fowell, R. A., Smith, N., Bae, S., and Schutz, B. E., "Bad Stars," AAS 09-012, AAS Guidance and Control Conference, Advances in the Astronautical Sciences, Vol. 133, Univelt, 2009, pp. 20-36.

[57] Smith, N., Fowell, R., Bae, S., and Schutz, B. E., "Improved Star Tracker Instrument Magnitude Prediction From ICESat Flight Telemetry," Paper AAS 11-086, AAS Guidance and Control Conference, Advances in the Astronautical Sciences, Vol. 141, Univelt, 2011, pp. 639-654.

[58] Smith, N., Bae, S., and Schutz, B. E., "Biased Star Tracker Measurements of Forty-Nine Stars from Flight Data," *Journal of Spacecraft and Rockets*, Vol. 47, No. 6, 2010, pp. 1023-1028.

[59] Smith, N., Bae, S., and Schutz, B. E., "Laser Reference Sensor Alignment Estimation from Star Observations," *Journal of Spacecraft and Rockets*, 2013 submitted 13.03.31.

[60] Smith, N., Bae, S., and Schutz, B. E., "Forty-Nine Biased Star Positions from ICESat Flight Data," Paper AAS 10-205, 20th Spaceflight Mechanics Meeting, San Diego, CA, 2010.

[61] Smith, N., Bae, S., Webb, C., and Schutz, B. E., "Laser Reference Sensor Alignment Estimation from Reference Signal Observations," *Journal of Spacecraft and Rockets*, 2013.

[62] Bae, S., Webb, C., and Schutz, B. E., "Star Tracker Misalignment Calibration for the ICESat Mission," AAS 06-107, AAS/AIAA Space Flight Mechanics, Advances in the Astronautical Sciences, Vol. 124, Univelt, San Diego, CA, 2006, pp. 113-124.

[63] Schutz, B. E., Bae, S., Smith, N., and Sirota, J. M., "Precision Orbit And Attitude Determination For ICESat," Paper AAS 08-305, F. Landis Markley Astronautics Symposium, Advances in the Astronautical Sciences, Vol. 132, Univelt, San Diego, CA, 2008, pp. 775-791.

# Appendix A. Pointing, Position and Geolocation

In practice, the laser unit vectors are empirically observed in the LRS laser-side frame. They are therefore thought of here as being fundamentally associated with the laser-side (laser-tracker) frame and represented by $\mathbf{u}_{LT}$. To represent pointing truth we want the true laser vectors $\mathbf{u}_{ICRF}$ in the ICRF and the intermediary $\mathbf{u}_{ATLAS}$ in the ATLAS frame.

The true ATLAS frame attitude is $\mathbf{A}_i^{ATLAS}$ and the true laser unit pointing vector(s) $\mathbf{u}_{ATLAS}$ and $\mathbf{u}_{ICRF}$ are given by

$$\mathbf{u}_{ATLAS} = (\mathbf{A}_{ST}^{LT}\mathbf{A}_{ATLAS}^{ST})^T\mathbf{u}_{LT} \tag{A.1}$$

$$\mathbf{u}_{ICRF} = (\mathbf{A}_i^{ATLAS})^T\mathbf{u}_{ATLAS} = (\mathbf{A}_{ST}^{LT}\mathbf{A}_{ATLAS}^{ST}\mathbf{A}_i^{ATLAS})^T\mathbf{u}_{LT} \tag{A.2}$$

The essential values for the overall position, pointing, and geolocation ground system are $\mathbf{u}_{ICRF}$ and $\mathbf{A}_i^{ATLAS}$. Information that is primarily of interest to the pointing group and is therefore restricted to the artificial telemetry is represented by the sensor alignments $\mathbf{A}_{ST}^{LT}\mathbf{A}_{ATLAS}^{ST}$. Note that given the true values for $\mathbf{u}_{ICRF}$ and $\mathbf{A}_i^{ATLAS}$, the laser unit vectors in the laser-side frame $\mathbf{u}_{LT}$ follow directly by

$$\mathbf{u}_{LT} = (\mathbf{A}_{ST}^{LT}\mathbf{A}_{ATLAS}^{ST}\mathbf{A}_i^{ATLAS})\mathbf{u}_{ICRF} \tag{A.3}$$

Equation (A.3) demonstrates that the $\mathbf{u}_{LT}$ can be viewed as a function of $\mathbf{u}_{ICRF}$ and $\mathbf{A}_i^{ATLAS}$

$$\mathbf{u}_{LT} = \mathbf{f}(\mathbf{u}_{ICRF}, \mathbf{A}_i^{ATLAS}) \tag{A.4}$$

Clearly $\mathbf{u}_{ICRF}$ and $\mathbf{A}_i^{ATLAS}$ are where position and geolocation information enter the true pointing. Representing the true ATLAS position vector as $\mathbf{r}$ and the true geolocation vector(s) as $\mathbf{s}$, the $\mathbf{u}_{ICRF}$, $\mathbf{A}_i^{ATLAS}$, and $\mathbf{u}_{LT}$ can be viewed as a function of $\mathbf{r}$ and $\mathbf{s}$

$$\begin{aligned}\mathbf{u}_{LT} &= \mathbf{f}(\mathbf{u}_{ICRF}(\mathbf{r},\mathbf{s}), \mathbf{A}_i^{ATLAS}(\mathbf{r},\mathbf{s})) \\ &= \mathbf{f}(\mathbf{r},\mathbf{s})\end{aligned} \tag{A.5}$$

Equation (A.5) represents the perspective adopted here, though the more common perspective is probably to describe geolocation as a function of $\mathbf{r}$, $\mathbf{u}_{LT}$, and $\mathbf{A}_i^{ATLAS}$ in

$$\mathbf{s} = \mathbf{s}(\mathbf{r}, \mathbf{u}_{ICRF}, \rho) = \mathbf{s}(\mathbf{r}, \mathbf{u}_{LT}, \mathbf{A}_i^{ATLAS}, \rho) \qquad (\text{A.6})$$

where $\varrho$ is laser range from the spacecraft to the ground. For time series of true attitudes and positions $\mathbf{A}_i^{ATLAS}(t)$ and $\mathbf{r}(t)$, there are associated time series of true angular rates $\boldsymbol{\omega}(t)$ and velocities $\mathbf{v}(t)$. They are classed as components of the overall state (though $\boldsymbol{\omega}(t) \equiv d\mathbf{A}/dt$ and $\mathbf{v}(t) \equiv d\mathbf{r}/dt$) to provide compatibility with the traditional state-space perspective, where a state equation of the form $d\mathbf{x}/dt = \mathbf{f}(\mathbf{x}, t, ...)$ equates the derivate of the state vector to a force model. The state-space perspective and state equation are somewhat deemphasized in pointing determination because no attempt is made to model the angular accelerations and torques.

# Appendix B. Search a Star Catalog for Stars

Given an arbitrary search point on the sky, the objective is to find the records from a star catalog that are near the search point. Complexity is only introduced by efforts to optimize or reduce the computational cost of the search and these efforts are often not necessary with modern ground-based computers. The key to the star search is the coordinates used to represent the search point and the star catalog records. The star search method that is developed for ICESat PPD directly uses RA and declination. The ICESat-2 PPD continues to apply the same approach for rigorous and realistic star data simulation. The description here focuses on the secondary search method that is not directly using RA and declination. This would make the star search simpler, particularly near the poles.

The coordinates are three-dimensional unit vectors in the celestial frame, and they are viewed simply as triplets of numbers between -1 and 1. The frame axes are: $\mathbf{z}$ axis pointing to the north celestial pole, $\mathbf{x}$ axis pointing to the vernal equinox, $\mathbf{y} = \mathbf{z} \times \mathbf{x}$. Star catalog records reduce to an integer record identifier and three coordinates x,y,z

**Table B-1 Examples of a star catalog reduced to x,y,z coordinates**

| record | x | y | z | Note |
|---|---|---|---|---|
| 1 | 1 | 0 | 0 | Star at vernal equinox |
| 2 | 0 | 0 | 1 | Star at north celestial pole |
| 3 | -.53 | -.21 | .65 | Some star |
| 4 | .86 | -.54 | .03 | Some star |

This allows the search to be decomposed into three simple independent sub-searches:

Sub-search 1. Find the set A of records with x values near the search point x value.

Sub-search 2. Find the set B of records with y values near the search point y value.

Sub-search 3. Find the set C of records with z values near the search point z value.

The intersection of sets A, B, and C are the catalog records near the search point. This completes the search. The only questions are related to how a sub-search is performed. The same sub-search method is used for each of the three sub-searches, with only the coordinate x,y,z changing. The remainder of this section discusses sub-search methods and optimizations. We note here that, for example, the K-vector search is one method for optimizing the sub-search method [45].

Within a sub-search, there is a list of $i = 1,...,n$ catalog coordinates $-1 \le c_i \le 1$ and a search point coordinate $s$. There is also an input parameter $r$ specifying the radius in radians about the search point inside which catalogs records are accepted as nearby. The lower bound $cmin$ and upper bound $cmax$ for acceptable $c_i$ values are given by:

If $s \ge \cos(r)$

$$\begin{aligned} cmin &= \cos(r)s - \sin(r)(1-s^2)^{1/2} \\ cmax &= 1 \end{aligned} \tag{B.1}$$

Elseif $s \le -\cos(r)$

$$\begin{aligned} cmin &= -1 \\ cmax &= \cos(r)s + \sin(r)(1-s^2)^{1/2} \end{aligned} \tag{B.2}$$

Else

$$\begin{aligned} cmin &= \cos(r)s - \sin(r)(1-s^2)^{1/2} \\ cmax &= \cos(r)s + \sin(r)(1-s^2)^{1/2} \end{aligned} \tag{B.3}$$

Matlab provides a function find( ) which can be used to find the $c_i$ between the lower and upper bounds in a single line of code. Without a find( ) function, an obvious approach is to first sort the list of $c_i$ values and then step through to find the first $c_i \ge cmin$ and the last $c_i \le cmax$. This type of sequential search in a sorted list is the basis of the K-vector search. It takes advantage of the ordering in the sorted list to fit a low-order polynomial function. The positions of the first $c_i \ge cmin$ and the last $c_i \le cmax$ can then be estimated by evaluating the polynomial rather than stepping sequentially through the list.

Using this method, a search is made of the mission star catalog for all observable stars near the LOS. The LRS line of sight is the $\mathbf{k}$ axis of the LRS attitude frame $\mathbf{A}_{ATLAS}^{ST}\mathbf{A}_{i}^{ATLAS}$. Candidate stars from the search are expressed as unit vectors in the LRS attitude frame by

$$\mathbf{u}_{ST} = \mathbf{A}_{ATLAS}^{ST}\mathbf{A}_{i}^{ATLAS}\mathbf{u}_{ICRF} \qquad \text{(B.4)}$$

For the $12^{\circ}$ LRS FOV the $h,v$ limits are

$$\tan(6\pi/180) = 0.105 \qquad \text{(B.5)}$$

Candidate stars with horizontal or vertical coordinates greater than 0.105 are outside of the FOV and discarded.

The remaining candidates are transformed by the measurement model

$$\mathbf{u}_{ST}^{'} = \mathbf{f}(\mathbf{u}_{LRS,}\mathbf{p}) + \mathbf{h} \qquad \text{(B.6)}$$

where the parameter vector $\mathbf{p}$ characterizes the deterministic errors and $\boldsymbol{\eta}$ is zero-mean Gaussian white noise $E\{\boldsymbol{\eta}^{T}\boldsymbol{\eta}\} = \sigma^{2}$. The measurement model and error model are discussed in Section 4.1.

# Appendix C. Star Passes and Mission Catalog

This section discusses the use of information from star observations at the level of individual unique stars (Sirius, Polaris, etc), their mission catalog records, and adaptive aspects of processing as a star passes through the LRS FOV. This is a higher-level perspective than the discussion of 10 Hz star tracker measurements from telemetry in Section 4.1 and is intended to provide a wider context for using stars in alignment and attitude filtering.

The mission catalog is tied to the LRS stellar-side alone and can also be referred to as the LRS catalog. The spacecraft star trackers are completely independent of the mission catalog. They are effectively black boxes containing their own manufacturer defined catalogs which have no relation to the mission catalog.

The plural term mission catalogs could be used here since there are at least two significant catalogs: one onboard the spacecraft for real-time attitude control, and one for ground-based processing. There will also be multiple versions of both of these catalogs as revisions and improvements are made over the life of the mission. The most recent version of the mission catalog for ground processing is the topic here unless noted otherwise.

The mission catalog contains reference parameters (star positions and instrument magnitudes) compiled specifically for interpreting the LRS star tracker telemetry. Significant sources for this information are the LRS star catalog, the Hipparcos catalog, NASA SKY2000 star tracker catalog, and flight data from LRS telemetry.

The catalog reflects what the LRS actually sees on the sky based on prelaunch night-sky test results, analytic methods using astronomical data and flight data from other missions, and LRS flight data after launch. It describes the apparent sky for the LRS, not the true sky. Catalog records correspond to the observed objects that the LRS acquires and tracks, not individual true astronomical objects. For example, a binary star system that is acquired and tracked as a single object by the LRS has a single record with parameters describing the location and brightness of the measured object, not separate records for both true objects in the binary system. Such cases and their corresponding records in the catalog are also referred to as blended objects or blended stars [4-7, 56-58].

An important question is whether the catalog includes all of the observed objects that the LRS can acquire. If the catalog has one record for each observed object it is an adequate representation of the apparent sky seen by the LRS. Prelaunch investigation was performed by the LRS developer to accurately predict the blended objects and recorded them into the LRS star catalog [2]. How to improve the mission catalog using actual star observation data is one of the main subjects here. The discussion includes the impact of problematic stars (regardless of blended or unblended) on attitude determination.

Note that we only discuss the LRS stellar-side (or star tracker) measurement in this section. LRS coordinate frame here is always indicating LRS stellar-side frame.

## C.1 Terminology and Conventions

The term star is used here for an object observed crossing the FOV. The set of observations is termed a star pass or simply a pass. The situation is more complex in a small fraction of cases but this terminology is convenient because most of the tracked objects are in fact astronomical point sources. With these conventions, a star can be a transient (dust particle, cosmic ray, satellite, etc) moving with a unique velocity across the FOV, or an object that is acquired, lost, and reacquired as it crosses the FOV. The object is still termed a star and the observations from multiple acquisitions make up a single pass.

The principle here is that the word star is simply a generic term for an object tracked by a star tracker. The focus is on the information content. If a star is actually a dust particle the information content is low and it should be classed as a bad star and rejected. If the star is truly an astronomical point source but the sensor observations are biased by nearby astronomical sources then the information content is higher but still problematic and the bias should either be corrected (preferably via the mission catalog record for the star) or rejected. A practical approach that detected biased stars during ICESat PPD based on star residual analysis is shown in Figure C-1(a). An example of the nearby (dim) star that causes the measurement bias of the primary (bright) star is illustrated in Figure C-1(b). Only when the star is an astronomical point source with unbiased sensor observations is the information adequate for performing filter updates.

The set of observations comprising a star pass is determined sequentially: if two sequential observations are nearby in space and time and have similar brightness values then they are the same star. Time gaps between observations can introduce complexity but the predictable ICESat motion and relatively high observation rate mean that linking star pass observations is not a practical problem

.

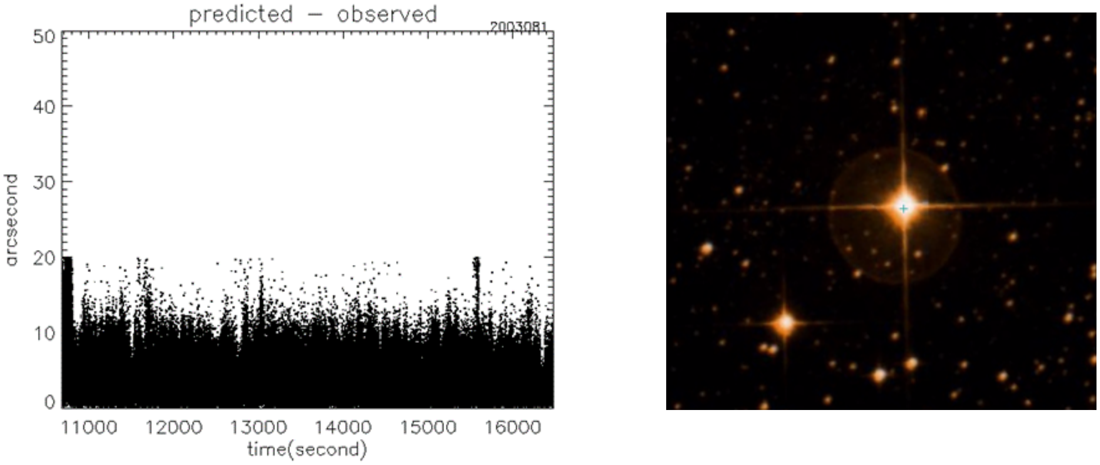

(a) Star residuals (b) primary and nearby star

**Fig. C-1 Star residuals indicating biased measurements and nearby star that causes bias of primary star measurement**

## C.2 Residuals

When a new star is observed at least two decisions have to be made: which mission catalog record is associated with the star, and should the pass observations be accepted for performing filter updates. These questions are answered as early in the pass as possible and ideally used for all of the following pass observations. In practice, additional decisions to accept individual observations are also made sequentially throughout the pass.

Identification and assessment are both based on residuals representing the differences between predicted and observed unit vectors. Residuals can be expressed in various forms, for example, a scalar angular separation or a three-dimensional vector difference. Here they are defined to be the two-component vector difference $\Delta\mathbf{u}$ between predicted and observed unit vectors expressed in $h, v$ coordinates (Section 4.1.1).

The predicted unit vector $\mathbf{u}_{pred}$ is based on the reference unit vector $\mathbf{u}_{ref}$ from the mission catalog, the estimated attitude $\mathbf{A}_i^b(t)$, and the estimated LRS alignment $\mathbf{A}_b^{LRS}(t)$. Normally the LRS frame (stellar-side Frame) is identified with the body frame by holding $\mathbf{A}_b^{LRS}(t)$ approximately constant so that

$$\mathbf{u}_{pred} = \mathbf{A}_b^{LRS}\mathbf{A}_i^b(t)\mathbf{u}_{ref} \tag{C.2.1}$$

and $\mathbf{u}_{pred}$ depends on the mission catalog $\mathbf{u}_{ref}$ and attitude estimate $\mathbf{A}_i^b(t)$ alone. This demonstrates the central role of the mission catalog. To identify a star, the catalog is searched for nearby candidates using the method discussed in Appendix B. Residuals are calculated for each candidate and the candidates are assessed using the adaptive criteria discussed in Section C.4.

For the predicted unit vector

$$\mathbf{u}_{pred} = [u_{pred,1} \quad u_{pred,2} \quad u_{pred,3}]^T = [h_{pred} \quad v_{pred}]^T \tag{C.2.2}$$

and the observed unit vector

$$\mathbf{u}_{obs} = [u_{obs,1} \quad u_{obs,2} \quad u_{obs,3}]^T = [h_{obs} \quad v_{obs}]^T \tag{ C.2.3}$$

the residual is given by

$$\Delta\mathbf{u}_{LRS} = [\Delta h \quad \Delta v]^T = [h_{obs} - h_{pred} \quad v_{obs} - v_{pred}]^T \tag{ C.2.4}$$

This residual is expressed in the LRS frame and is also the information needed for estimating deterministic corrections to the LRS stellar-side measurement model (Section 4.2.4 and 4.2.5).

A body frame residual $\Delta\mathbf{u}_{body}$ and celestial frame residual $\Delta\mathbf{u}_{ICRF}$ are computed along with $\Delta\mathbf{u}_{LRS}$. The $\Delta\mathbf{u}_{body}$ can be directly correlated with attitude and sensor alignment variations. The $\Delta\mathbf{u}_{ICRF}$ from multiple passes of a particular star can be combined for statistical analysis of bias and noise characteristics for improving the star's mission catalog record.

To compute $\Delta\mathbf{u}_{body}$ the predicted unit vector is

$$(\mathbf{u}_{pred})_{body} = \mathbf{A}_i^b(t)\mathbf{u}_{ref} \tag{C.2.5}$$

And the observed unit vector is

$$(\mathbf{u}_{obs})_{body} = (\mathbf{A}_b^{LRS})^T(\mathbf{u}_{obs})_{LRS} \tag{ C.2.6}$$

These two unit vectors are expressed as $h, v$ coordinates in a local tangent plane frame. The $\mathbf{i,j,k}$ axes of the local tangent plane frame are constructed based on the spacecraft frame $\mathbf{x}$ axes (the centerline from the spacecraft through the science instrument) and $(\mathbf{u}_{pred})_{body}$

$$\mathbf{j} = \mathbf{k} \times \mathbf{i} \tag{ C.2.7}$$

$$\mathbf{i} = \mathbf{x} \times (\mathbf{u}_{pred})_{body} = [1 \quad 0 \quad 0]^T \times (\mathbf{u}_{pred})_{body} \tag{C.2.8}$$

$$\mathbf{k} = (\mathbf{u}_{pred})_{body} \tag{C.2.9}$$

The body frame residual is given by

$$\Delta\mathbf{u}_{body} = [\Delta h_{body} \quad \Delta v_{body}]^T = [(h_{obs} - h_{pred})_{body} \quad (v_{obs} - v_{pred})_{body}]^T \tag{C.2.10}$$

See Section 4.1.1 for more discussion of local tangent plane coordinates.

To compute $\Delta\mathbf{u}_{ICRF}$ the predicted unit vector is

$$(\mathbf{u}_{pred})_{ICRF} = \mathbf{u}_{ref} \tag{C.2.11}$$

And the observed unit vector is

$$(\mathbf{u}_{obs})_{ICRF} = (\mathbf{A}_b^{LRS} \mathbf{A}_i^b(t))^T (\mathbf{u}_{obs})_{LRS} \tag{C.2.12}$$

These two unit vectors are expressed as $h, v$ coordinates in a local tangent plane frame on the celestial sphere that is aligned with astronomical RA and declination. The $\mathbf{i,j,k}$ axes of the frame are constructed based on the ICRF $\mathbf{z}$ axes (pointing to the celestial north pole) and $(\mathbf{u}_{pred})_{ICRF}$

$$\mathbf{j} = \mathbf{k} \times \mathbf{i} \tag{C.2.13}$$

$$\mathbf{i} = \mathbf{z} \times \mathbf{k} = [0 \quad 0 \quad 1]^T \times \mathbf{u}_{ref} \tag{C.2.14}$$

$$\mathbf{k} = (\mathbf{u}_{pred})_{ICRF} = \mathbf{u}_{ref} \tag{C.2.15}$$

The ICRF frame residual is given by

$$\Delta\mathbf{u}_{ICRF} = [\Delta h_{ICRF} \quad \Delta v_{ICRF}]^T = [(h_{obs} - h_{pred})_{ICRF} \quad (v_{obs} - v_{pred})_{ICRF}]^T \tag{C.2.16}$$

An array arrPassJ for pass $j$ is generated sequentially as each observation is processed. Each row contains a time tag, $\Delta\mathbf{u}_{LRS}$, $\Delta\mathbf{u}_{body}$, $\Delta\mathbf{u}_{ICRF}$ and $\mathbf{u}_{obs} = [h_{obs} \quad v_{obs}]^T$. The $\mathbf{u}_{obs}$ vectors are included in the array for estimation of distortion corrections (LRS measurement model deterministic corrections). After processing $n$ observations from pass $j$ the dimensions of arrPassJ are $n \times 9$.

## C.3 Pass Statistics

After a pass is complete its array is reduced to a relatively small set of statistics. The same reduction is performed at any time during the pass using the observations that have already been sequentially processed and stored in the array. The reduced pass statistics are used for identification and assessment and the question becomes what are effective and efficient statistics to include in the reduction.

The obvious candidates are the mean $\mu$ and square root of the variance $\sigma$ , and the median $Q2$ and associated quartiles $Q1, Q3$ . $\mu$ and $\sigma$ are straightforward but assume the residuals have a Gaussian distribution. This assumption can be a problem when there are significant trends or outliers in the residuals. The first, second, and third quartiles ( $Q1, Q2, Q3$ ) are termed robust statistics because they are less sensitive to the effects of outliers.

A practical difference is that $\mu, \sigma$ can be computed sequentially but $Q1, Q2, Q3$ cannot. $\mu, \sigma$ can be computed from the sequentially accumulated parameters $n, \Sigma x, \Sigma x^2$ . To compute $Q1, Q2, Q3$ a complete batch of residuals is required. For a star with thousands of passes and millions of total observations, each pass should be reduced to $Q1, Q2, Q3$ values rather than storing every residual.

There are 5 statistics $\mu, \sigma, Q1, Q2, Q3$ characterizing each of the 6 $h, v$ components in $\Delta \mathbf{u}_{LRS}$ , $\Delta \mathbf{u}_{body}$ , and $\Delta \mathbf{u}_{ICRF}$ for a total of 30 reduced statistics or parameters characterizing the pass. For pass $j$ with $n$ processed observations, the full $n \times 9$ pass array arrPassJ is reduced to a 31 component (including a time-tag) vector vecRedPassJ. This discussion assumes that adequate $Q2_{LRS}$ estimates are available and focuses on processing a single pass, referred to as the current pass, based on the $Q1_{pass}, Q2_{pass}, Q3_{pass}$ values of its residuals. Because of their importance for characterizing the filter status, the 6 $Q1_{LRS}, Q2_{LRS}, Q3_{LRS}$ values are added to each vecRedPassJ record for a total of 37 components.

An additional parameter is the interquartile range $IQR = Q3 - Q1$ . A standard robust definition of an outlier is given by

$$< Q1 - 1.5(IQR) \text{ or } > Q3 + 1.5(IQR) \qquad \text{(C.3.1)}$$

Outlier residuals are excluded from calculations of $\mu, \sigma, Q1, Q2, Q3$ based on an initial calculation of $Q1, Q2, Q3$ . Because the sensitivity of $Q1, Q2, Q3$ to outliers is relatively low, the initial and final $Q1, Q2, Q3$ values are usually the same.

Residuals are evaluated based on adaptive criteria that are sequentially adjusted for:

1. The current overall condition of the filter as determined empirically from the $Q1, Q2, Q3$ pass statistics for stars that were recently in the FOV. These overall values are maintained in $Q1_{LRS}, Q2_{LRS}, Q3_{LRS}$. The subscript LRS specifies that these values characterize the overall LRS attitude estimate, which is the key component of the filter state.
2. Whether a positive identification of the current pass (the pass being assessed) has been made. The binary identification value is represented by $ID_{pass}$ here.
3. The $Q1, Q2, Q3$ statistics for the previous residuals of the current pass. These values are maintained in $Q1_{pass}, Q2_{pass}, Q3_{pass}$.

The data structures and parameters used in pass identification and assessment are summarized in Table C-1.

A constantly recurring process is determination of the overall condition of the filter based on the $Q2_{LRS}$ values. Non-zero $Q2_{LRS}$ indicates a bias in the LRS attitude estimate

$$\mathbf{A}_i^{LRS} = \mathbf{A}(\mathbf{a}_{LRS})\mathbf{A}_b^{LRS}\mathbf{A}_i^b \tag{C.3.2}$$

Assuming that the LRS is identified with the body frame (because $\mathbf{A}(\mathbf{a}_{LRS})$ is held approximately constant at zero) this means a bias in the body frame attitude $\mathbf{A}_i^b$. For example, if the $Q2_{LRS}$ value for the $h$ residuals of recent passes is 10 arcseconds, then the $Q2_{pass}$ value for the $h$ residuals of the current pass are expected to be near 10 arcseconds. $Q2_{LRS}$ is calculated from the current and previous star passes over a memory interval of length $t_{memory}$. The oldest pass residuals included have time-tags $t_{timetag} > t_{current} - t_{memory}$.

**Table C-1 Data structures and parameters used in star pass identification and assessment**

| Object | Description |
|---|---|
| arrPassJ | Array for pass $j$ with rows comprised of a time-tag, $\Delta\mathbf{u}_{LRS}$, $\Delta\mathbf{u}_{body}$, $\Delta\mathbf{u}_{ICRF}$ and $\mathbf{u}_{obs} = [h_{obs} \quad v_{obs}]^T$, generated sequentially as each observation is processed. With $n$ processed observations the array is $n \times 9$. |

| | |
|---|---|
| vecRedPassJ | For pass $j$ with $n$ processed observations the $n \times 9$ arrPassJ is reduced to a 37 component (including a time-tag and $Q1_{LRS}, Q2_{LRS}, Q3_{LRS}$ values) vector vecRedPassJ. |
| binIDPassJ, $ID_{pass}$ | Binary value indicating whether a positive identification of pass J (including the current pass $ID_{pass}$) has been made. |
| $t_{memory}$ | $Q2_{LRS}$ is calculated from passes with time-tags $t_{timetag} > t_{current} - t_{memory}$. |
| $Q2_{LRS}$ | Median values of multiple pass residuals from recent passes. A non-zero value indicates a bias in the LRS attitude estimate. |
| $Q1_{LRS}, Q3_{LRS}$ | First and third quartile values of multiple pass residuals from recent passes. Used for outlier detection. |
| $Q2_{pass}$ | Median value of residuals from the current pass. If $Q2_{LRS}$ is approximately zero and $Q2_{pass}$ is non-zero then the current pass contains biased measurements and is a bad star. |
| $Q1_{pass}, Q3_{pass}$ | First and third quartile values of residuals from the current pass. Used to detect outliers within the current pass. |
| $L_{\Delta h}$, $L_{\Delta v}$, $L_{\Delta m}$ | Adaptive limits for the criteria (identification and assessment criteria). |

## C.4 Positive Identification

If $ID_{pass}$ is false then the pass needs to be positively identified. $\mathbf{A}_i^{LRS}$ is adequate for star identification because filter updates are coming from the star trackers. The mission catalog is searched for stars near $(\mathbf{A}_b^{LRS}\mathbf{A}_i^b)^T \mathbf{u}_{obs}$ using the search method described in Appendix B, Chapter 4 of ICESat PPD ATBD [34], or K-vector based method [45]. The search result with the smallest $(\mathbf{A}_b^{LRS}\mathbf{A}_i^b)^T \mathbf{u}_{obs} - \mathbf{u}_{ref}$ residual is the identification candidate.

Positive identification means that the observations are indeed of the star described by the candidate mission catalog record. With positive identification, if the residuals for the current pass

$Q2_{pass}$ include a bias while $Q2_{LRS}$ is near zero then the mission catalog record should be corrected and improved over time to better reflect the empirical LRS response to the real sky. In other words, positive identification is an important step in recognizing and characterizing bad stars.

Positive identification is based on the $Q2_{LRS}$ and $Q2_{pass}$ values for position residuals. In case the measurement of the star magnitude is sufficiently accurate, the positive identification is also based on the predicted and observed magnitudes $m_{pred} = m_{ref}$ and $m_{obs}$. The magnitude residual is defined by

$$\Delta m = m_{obs} - m_{pred} \tag{C.4.1}$$

The prediction $m_{pred}$ is taken directly from the reference value $m_{ref}$ provided by the mission catalog record. In effect, brightness can be the critical confirmation that the mission catalog record is correct and adequate. Because the magnitude residuals $\Delta m$ are not a function of the attitude estimate and filter state, there is less need for the type of statistical analysis and reduction represented by the median function $Q2()$. The available magnitude observations are simply compared with the prediction from the mission catalog.

It is useful however to monitor the magnitude residuals as a function of predicted (or reference magnitude). A function $\Delta m(m_{pred})$ is fit to a large batch of residuals and used as an estimate.

The three criteria for positive identification are

$$\left|Q2_{pass}(\Delta h) - Q2_{LRS}(\Delta h)\right| < L_{\Delta h} \tag{C.4.2}$$

$$\left|Q2_{pass}(\Delta v) - Q2_{LRS}(\Delta v)\right| < L_{\Delta v} \tag{C.4.3}$$

$$\left|\Delta m\right| < L_{\Delta m} \tag{C.4.4}$$

where the limits $L_{\Delta h}$, $L_{\Delta v}$, and $L_{\Delta m}$ effectively determine the strictness of the criteria. The same criteria are used in the next section for assessing individual observations with different values for $L_{\Delta h}, L_{\Delta v}, L_{\Delta m}$. These three values are the focus of the identification and assessment process. Implementation reduces to a question of adaptively setting appropriate $L_{\Delta h}, L_{\Delta v}, L_{\Delta m}$ values.

If the magnitude uncertainty is too large to use, the identification only depends on the position residuals. The discussion here includes the magnitude residuals for generality.

## C.5 Assessment for Use in Filter Updates

Assessment of the current pass and individual observations is based on the same criteria as positive identification, Eqs. (C.4.2) to (C.4.4). The difference is smaller values for $L_{\Delta h}, L_{\Delta v}, L_{\Delta m}$. The concept is that a star pass can be positively identified but then not used for filter updates because its residuals are abnormally high. In other words, only normal passes with relatively small $L_{\Delta h}, L_{\Delta v}, L_{\Delta m}$ should be used for filter updates.

There are three cases to consider. In case A the filter is performing a cold start and has not yet converged. Residuals from the LRS and spacecraft star trackers may be high. In case B a period without LRS stars observations is ending. Residuals from the spacecraft star trackers are low, but the LRS residuals may be high. This can be classed as a type of filter warm start since there are estimated, non-default states and uncertainties, but they may be stale and have high uncertainties depending on the length of the blinding. In case C the filter is converged and functioning normally with recent updates from the LRS and spacecraft star trackers. Residuals from the LRS and the spacecraft star trackers are low.

Table C-2 describes the three cases. Positive identification can be classed as a fourth case and is also included. The final column shows the adaptive values for the limits $L_{\Delta h}, L_{\Delta v}$. They are based on a scaling of the Interquartile Range (IQR) of the overall LRS residuals $Q3_{LRS} - Q1_{LRS}$. The IQR introduces the adaptive element into the criteria. The scaling factors $k_A, k_B, k_C, k_{ID}$ determine the relative tightness of the criteria. The scaling factors are found empirically from simulation and flight data. It is natural that

$$k_{ID} > k_A > k_B > k_C \tag{C.5.1}$$

representing the principle that the criteria become tighter as knowledge increases and uncertainty decreases.

**Table C-2 Cases for assessing star passes and positive identification**

| Case | Description | $Q2_{LRS}$ | SST residuals | $L_{\Delta h}, L_{\Delta v}$ |
|---|---|---|---|---|
| - | Positive Identification | Can be high or low | - | $k_{ID} \times IQR$ |

| | | | | |
|---|---|---|---|---|
| A | Filter is performing a cold start and has not yet converged. | High | High | $k_A \times IQR$ |
| B | A period without LRS stars observations is ending. | High | Low | $k_B \times IQR$ |
| C | Filter is converged and functioning normally with recent updates from the LRS and spacecraft star trackers. | Low | Low | $k_C \times IQR$ |

## C.6 Improving the Mission Catalog Using Archived Pass Statistics

As described above, there are 5 statistics $\mu, \sigma, Q1, Q2, Q3$ characterizing each of the 6 $h, v$ components in $\Delta\mathbf{u}_{LRS}$, $\Delta\mathbf{u}_{body}$, and $\Delta\mathbf{u}_{ICRF}$ for a total of 30 reduced statistics or parameters characterizing a pass. For pass $j$ with $n$ processed observations, the full $n \times 9$ pass array arrPassJ is reduced to a 31 component (including a time-tag) vector vecRedPassJ. Because of their importance for characterizing the filter status, the 6 $Q1_{LRS}, Q2_{LRS}, Q3_{LRS}$ values are added to each vecRedPassJ record for a total of 37 components. These vectors are computed and archived for millions of star passes, creating a significant database to mine for correlations and outliers.

The residuals expressed in the sky $\Delta\mathbf{u}_{ICRF}$ are of primary interest and significance. The objective is to improve the mission catalog by correcting the reference positions in the catalog so that the $\Delta\mathbf{u}_{ICRF}$ values

$$\Delta h_{ICRF} = (h_{obs} - h_{pred})_{ICRF} \qquad \text{(C.6.1)}$$

$$\Delta v_{ICRF} = (v_{obs} - v_{pred})_{ICRF} \qquad \text{(C.6.2)}$$

are normally approximately zero for all observed stars.

For pass $i$ the residuals are represented by the median values $Q2(\Delta h_{ICRF})_i$ and $Q2(\Delta v_{ICRF})_i$. The interquartile ranges

$$IQR(\Delta h_{ICRF})_i = Q3(\Delta h_{ICRF})_i - Q1(\Delta h_{ICRF})_i \tag{C.6.3}$$

$$IQR(\Delta v_{ICRF})_i = Q3(\Delta v_{ICRF})_i - Q1(\Delta v_{ICRF})_i \tag{C.6.4}$$

are measures of uncertainty in the residuals. The scale of the median residuals relative to their uncertainties is a measure of the overall significance $s_i$

$$s(\Delta h_{ICRF})_i = \frac{Q2(\Delta h_{ICRF})_i}{IQR(\Delta h_{ICRF})_i} = \frac{Q2(\Delta h_{ICRF})_i}{Q3(\Delta h_{ICRF})_i - Q1(\Delta h_{ICRF})_i} \tag{C.6.5}$$

$$s(\Delta v_{ICRF})_i = \frac{Q2(\Delta v_{ICRF})_i}{IQR(\Delta v_{ICRF})_i} = \frac{Q2(\Delta v_{ICRF})_i}{Q3(\Delta v_{ICRF})_i - Q1(\Delta v_{ICRF})_i} \tag{C.6.6}$$

of the pass in terms of improving the mission catalog. If the significance ratio is low then the result from the pass should have a relatively little effect on the catalog. If the significance is high the pass should be weighted up when correcting the catalog.

The measures of significance above only include uncertainty estimates for the residuals and by extension the observations. Uncertainties in the overall filter state should also be included. If the filter state uncertainties are high then large residuals can be expected and are not significant. The six $Q1_{LRS}, Q2_{LRS}, Q3_{LRS}$ values are used to estimate the filter uncertainties, particularly $Q2_{LRS}$ alone. Augmented significance measures are given by

$$s(\Delta h_{ICRF})_i = \frac{Q2(\Delta h_{ICRF})_i}{Q2(\Delta h_{LRS})_i + IQR(\Delta h_{ICRF})_i} \tag{C.6.7}$$

$$s(\Delta v_{ICRF})_i = \frac{Q2(\Delta v_{ICRF})_i}{Q2(\Delta v_{LRS})_i + IQR(\Delta v_{ICRF})_i} \tag{C.6.8}$$

This is directly analogous to how the Kalman filter uncertainty $\mathbf{HPH^T + R}$ combines the uncertainty from the filter states $\mathbf{HPH^T}$ with the uncertainty from the measurements $\mathbf{R}$.

With the median residuals $Q2(\Delta h_{ICRF})_i, Q2(\Delta v_{ICRF})_i$ and significance parameters $s(\Delta h_{ICRF})_i, s(\Delta v_{ICRF})_i$ for $i = 1,...,n$ passes of a particular star, and the analogous values for hundreds of other stars, it is straightforward to detect cases with significant biases. Stars with relatively high $Q2$ and $s$ values are flagged for assessment as possible bad stars. With flight experience, the detection thresholds are determined from the empirical probability distributions of the parameters. The biases represented by the high $Q2$ values can then be corrected in the mission catalog.

# Appendix D. Alignment Estimation by Method B

In the development and implementation of the alignment filter (EKF) for the PAD in Chapter 3, LRS stellar-side measurement is used to estimate LRS attitude and SST measurement models reduce to alignment rotations that relate the telemetered attitude estimates to the LRS stellar-side frame. The processor tracks these alignment rotations and SST error modeling involves parameter estimation for the alignment process noise in addition to the uncertainties in the telemetered attitude estimates.

There are advantages to associating the body frame with a sensor providing frequent and uninterrupted observations, particularly star or attitude observations that provide direct information from the celestial coordinate frame. One possibility is to use a combination of the SSTs since they acquire and track a large number of stars and are aligned in such a way that they will not both be blinded simultaneously.

The simplest case includes the spacecraft star trackers and SIRU alone, setting aside the LRS. In a sense, this shrinks the spacecraft down to the IMSC (Figure 13) and its three sensors. The true attitude $\mathbf{A}_i^{ATLAS}$ is conceptually tied to the IMSC and the true values for $\mathbf{A}_i^{ATLAS}$ are interpolated from the SIMV9 data that is described in Section D.1. The SST alignments are assumed to be constant. Errors introduced in the artificial telemetry are attitude noise (SST quaternion output noise) and rate noise (SIRU rate bias instability). The simulated LRS stars used in the LRS alignment estimation with respect to the ATLAS reference frame. The objective is to simultaneously track the ATLAS reference platform attitude and LRS alignment; in other words the rotations from the celestial frame to the reference platform frame and from the reference platform frame to the LRS frame. The reference platform is the IMSC, a small bench isolated from the main optical bench on three struts and carrying the two spacecraft star trackers and gyro unit. In reality, the observations from the three instruments are asynchronous but little fidelity is lost by modeling them as synchronous at 10 Hz, effectively reducing or compressing both the 50 Hz SIRU output and the overall complexity of the event list. Every 0.1 seconds the event list receives a rate vector from the SIRU and an attitude vector from each SST.

LRS attitude can be built by combining ATLAS platform attitude and LRS alignment before the attitude information is used for the LRS laser pointing determination. The approach (Method A), that is described in Chapter 3 (Theory), is tested in Chapter 5 (Simulation) with realistic complexity (asynchronous time-tags, 50Hz SIRU data, alignment variation, LRS laser data, chromatic aberration, etc). The simpler method here described as Method B, however, provides a quick study of several additional aspects as well as attitude filtering. The fundamental principles are not obscured by superficial complexity. The true attitudes $\mathbf{A}_i^{ATLAS}$ and rates are known. They are used to create artificial telemetry consisting of observed attitudes and rates with known error characteristics. The observations are filtered to estimate the attitude and rate. The differences between the truth and the estimates are the overall error. Overall error in the LRS attitude estimates from Method A is almost same as that from Method B if the chromatic aberration is not included in the LRS star measurements. In the worst case, Method B results in slight increase of attitude error within the geolocation error budget requirement with a comfortable margin. The results from the simpler case should also be applied to the general complex case with the different approach.

All spacecraft hardware is modeled here as two rigid bodies: the reference platform, and the LRS. The performance results presented here are based on Monte Carlo simulation of this first-order rigid body model, in which pointing knowledge involves three quantities: reference platform attitude, LRS alignment, and laser vectors in the LRS frame. The first-order model represents the most significant performance factors and allows secondary complexities to be represented as internal alignment variations and higher-order corrections.

At each point in simulated time, there are two reference platform attitudes and two LRS alignments: the truth from the simulation, and an estimate from processing simulated sensor observations. The term tracking refers here to the difference between estimated and true values, represented by a tracking error time series and RMS tracking error statistics. The focus of the results section is attitude and alignment tracking, with the assumption that in practice the laser vector observations are well calibrated and pointing knowledge is a function of attitude and alignment tracking performance.

## D.1 SIMV9 Truth Data

SIMV9 (Simulation Version 9) is a fundamental truth dataset from the geolocation group at GSFC. It provides the spacecraft frame attitude, rate, position, and velocity for a 24 hour interval that includes realistic pointing maneuvers of all types. The SIMV9 attitude truth frame $\mathbf{A}_i^{ATLAS}$ is defined here to be similar to the Orbital ATK spacecraft frame $\mathbf{A}_i^{SC}$ which is associated with the IMSC. Note that the SIMV9 data is different from the 14-day data (Section 5.2) used for the simulations in Chapter 5. It is the earlier version of the realistic simulation from GSFC than 14-day data.

The dataset provides a useful example for describing artificial telemetry and test processing, and it is treated a baseline or reference case here. It provides true attitudes and rates for $\mathbf{A}_i^{ATLAS}$ at 1 second intervals. After interpolation to 0.1 second intervals, these attitudes and rates are already closely related to the spacecraft star trackers and SIRU by the IMSC. The SSTs and SIRU are mounted on the IMSC, and the SIMV9 frame $\mathbf{A}_i^{ATLAS}$ is associated with the Orbital ATK spacecraft frame $\mathbf{A}_i^{SC}$ and therefore with the IMSC.

Generating artificial telemetry is a straightforward application of the measurement and error models from Chapter 4.0. The true attitude and alignments are known. The measurement models are used to introduce the sensor characteristics and deterministic errors. Stochastic errors (noise) are added and characterized in terms of the error models. The SIRU is more complex due to the nature of its observations and its role in the processor, as discussed in Section 4.2. Angular rates $\boldsymbol{\omega}_k$ are derived from $\mathbf{A}_i^{ATLAS}(t_k)$ and both are resampled to 0.1 second intervals to match the fundamental frequency of the star tracker observations and the overall tracking problem.

Figure D-1 shows rates of SIMV9 data. In roll, the two ocean scan maneuvers (A and C), target scans (B), and around the world scan (D) are apparent in the roll rate time series. The maneuver sequence is not representative of actual on-orbit operations but is convenient for studying scans and transitions.

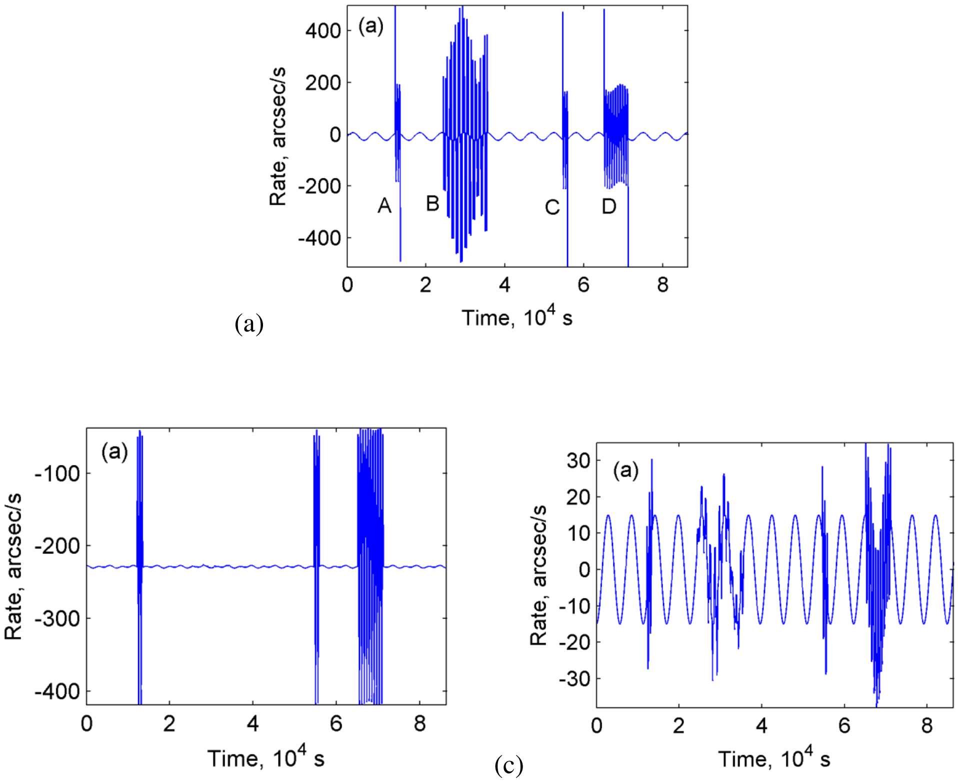

(a)

(b)

(c)

**Fig.D-1 SIMV9 Rates (a) Roll (b) Pitch (c) Yaw**

The results section focuses on roll tracking performance, and is representative of pitch tracking performance. Roll motion is equivalent to cross-track pointing and of first importance for laser spot geolocation and ICESat-2 science. The rate and acceleration variations are highest in roll as the calibration and target scans sweep the lasers across the ground track, particularly during target scans which are effectively pure roll (Figure D-1). Peak acceleration magnitudes are approximately 140 arcsec/$s^2$ as shown in Figure D-2.

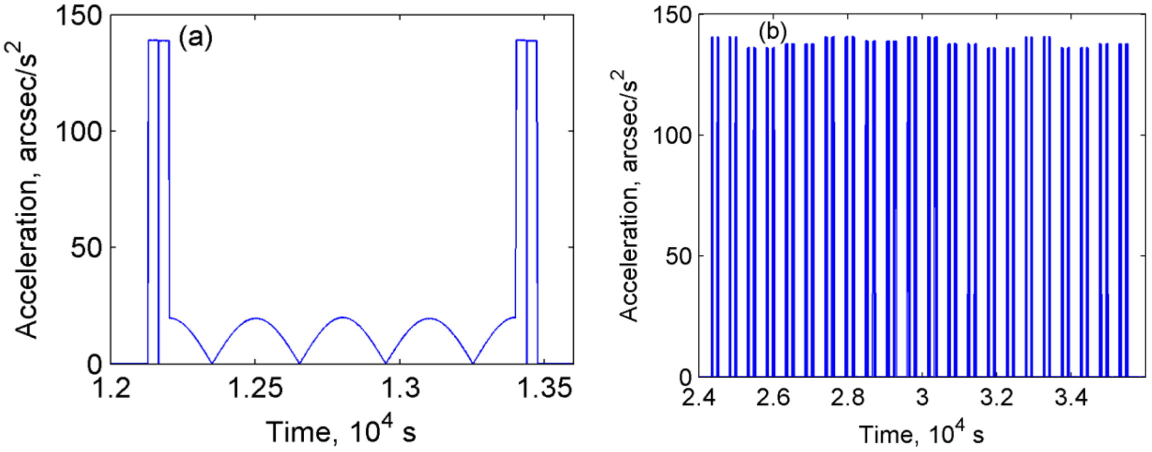

**Fig.D-2 Roll acceleration magnitudes during (a) ocean scan A and (b) target scan B.**

Two test cases used below for attitude tracking performance analysis are taken from the ocean scan shown in the left plot of Figure D-2. The baseline case with nadir pointing angular rates and small angular accelerations is from 12,000 to 12,065 seconds, just before the first acceleration peak. An upper-bound case with peak angular accelerations covers the first acceleration peak from 12,135 to 12,220 seconds.

## D.2 States and Observations

The time series of state estimated is generated by creating simulated sensor observations from the truth time series, including the effects of LRS motion, deterministic errors, and noise. The simulated sensor observations are then processed as artificial flight telemetry. Monte Carlo simulation runs for different LRS sensitivities and different regions of the sky provide information about the observation characteristics and the relationship between sensitivity and tracking performance. The results from multiple simulation runs are combined to characterize attitude and alignment tracking performance.

The processor is a Kalman filter that estimates reference platform attitude, gyro rate bias, and LRS alignment and is referred to here as an alignment filter [19, 26, 27]. Alignment filtering simultaneously predicts the measurements from all three star trackers (the LRS star tracker and the two spacecraft star trackers). The sparse LRS observations are effectively combined with the observations from the other two trackers. The measurement residuals are used to update the filter states, which represent the body frame attitude and time-varying corrections to the LRS reference alignment. The spacecraft star trackers are tied to the body frame by constant reference alignments. The combined states represent the attitudes of all three trackers. This type of alignment filtering is applicable to any configuration of vector sensors; if the vector observations can be predicted then the sensor alignments can be corrected.

There are two ATLAS reference platform attitudes: the simulation truth $\mathbf{A}_i^{ATLAS}(t)$, and an estimate $\mathbf{A}_i^{b}(t)$. Any expression that includes $\mathbf{A}_i^{ATLAS}(t)$ refers to simulation truth, and any expression that includes $\mathbf{A}_i^{b}(t)$ refers to estimated values. For example $\mathbf{A}_i^{LRS}(t)=\mathbf{A}(\mathbf{a}_{LRS}(t))\mathbf{A}_{ATLAS}^{LRS}\mathbf{A}_i^{ATLAS}(t)$ refers to the true LRS attitude and alignment, while $\mathbf{A}_i^{LRS}(t)=\mathbf{A}(\mathbf{a}_{LRS}(t))\mathbf{A}_{b}^{LRS}\mathbf{A}_i^{b}(t)$ refers to their estimated values. Note that the LRS frame in this section always represents the stellar-side or star tracker frame.

The true spacecraft star tracker (SST) attitudes are modeled as the product of a constant reference alignment $\mathbf{A}_{ATLAS}^{SST}$ and the reference platform attitude $\mathbf{A}_i^{ATLAS}(t)$

$$\mathbf{A}_i^{SST1}(t)=\mathbf{A}_{ATLAS}^{SST1}\mathbf{A}_i^{ATLAS}(t) \tag{D.2.1}$$

$$\mathbf{A}_i^{SST2}(t)=\mathbf{A}_{ATLAS}^{SST2}\mathbf{A}_i^{ATLAS}(t) \tag{D.2.2}$$

Time-varying corrections to the reference alignments $\mathbf{A}_{ATLAS}^{SST}$ are not modeled or estimated and the SST coordinate frames are effectively identified with the reference platform frame. Expressions for the estimated SST attitudes replace $\mathbf{A}_i^{ATLAS}(t)$ with $\mathbf{A}_i^{b}(t)$. A time-varying rotation vector $\mathbf{a}_{LRS}(t)$ representing small alignment corrections is included in the attitude models for the LRS

$$\mathbf{A}_i^{LRS}(t)=\mathbf{A}(\mathbf{a}_{LRS}(t))\mathbf{A}_{ATLAS}^{LRS}\mathbf{A}_i^{ATLAS}(t) \tag{D.2.3}$$

where $\mathbf{A}_{ATLAS}^{LRS}$ is the LRS reference alignment. The state vector is

$$\mathbf{x}(t)=[\mathbf{a}(t)^T \quad \mathbf{b}(t)^T \quad \mathbf{a}_{LRS}(t)^T]^T \tag{D.2.4}$$

where $\mathbf{a}(t)$ is the attitude error rotation vector and $\mathbf{b}(t)$ is the rate bias. These states are estimated sequentially using an alignment filter based on the standard attitude filter described in Section (3.3) with slight modifications as shown below.

The filter performs unconstrained estimation of the rotation vector $\mathbf{a}(t)$ during each measurement update phase while maintaining the overall body frame attitude estimate in the unit-norm reference attitude quaternion $q_b(t)$ with $\mathbf{A}_i^{b}(t)=\mathbf{A}(q_b(t))$. The true attitude $q_{ATLAS}(t)$ is modeled as $q_{ATLAS}(t)=q(\mathbf{a}(t))\otimes q_b(t)$ [13]. The measurement update phase assigns a finite value $\hat{\mathbf{a}}_+$ to $\hat{\mathbf{a}}(t)$ while the estimated quaternion retains its pre-update value $q_{b,-}$. The update information is moved from $\hat{\mathbf{a}}_+$ to a post-update reference $q_{b,+}$ and $\hat{\mathbf{a}}(t)$ is reset to zero so that $q(\hat{\mathbf{a}}_+) \otimes q_{b,-} = q(\mathbf{0}) \otimes q_{b,+}$.

The covariance matrix $\mathbf{P}$ is given by

$$\mathbf{P}_{9\times 9} \equiv E\{(\mathbf{x}-\hat{\mathbf{x}})(\mathbf{x}-\hat{\mathbf{x}})^{\mathrm{T}}\} = \begin{bmatrix} \mathbf{P}_{\mathbf{a}} & \mathbf{P}_{\mathbf{ab}} & \\ \mathbf{P}_{\mathbf{ab}} & \mathbf{P}_{\mathbf{b}} & \\ & & \mathbf{P}_{LRS} \end{bmatrix} \tag{D.2.5}$$

where $\mathbf{P}$ is partitioned into $3\times 3$ attitude $\mathbf{P}_{\mathbf{a}}$, rate $\mathbf{P}_{\mathbf{b}}$, correlation $\mathbf{P}_{\mathbf{ab}}$, and alignment $\mathbf{P}_{LRS}$ sub-matrices. In the continuous-time linearized state equation given by

$$\begin{bmatrix} \boldsymbol{\delta}\dot{\mathbf{a}} \\ \boldsymbol{\delta}\dot{\mathbf{b}} \\ \boldsymbol{\delta}\dot{\mathbf{a}}_{LRS} \end{bmatrix} = \begin{bmatrix} -[\boldsymbol{\omega}_{ref}\times] & \mathbf{I}_{3\times 3} & \\ \mathbf{0}_{3\times 3} & \mathbf{0}_{3\times 3} & \\ & & \mathbf{0}_{3\times 3} \end{bmatrix} \begin{bmatrix} \boldsymbol{\delta}\mathbf{a} \\ \boldsymbol{\delta}\mathbf{b} \\ \boldsymbol{\delta}\mathbf{a}_{LRS} \end{bmatrix} + \mathbf{I}_{9\times 9} \begin{bmatrix} \boldsymbol{\eta}_{arw} \\ \boldsymbol{\eta}_{rrw} \\ \boldsymbol{\eta}_{LRS} \end{bmatrix} \tag{D.2.6}$$

the rate bias $\boldsymbol{\delta}\mathbf{b}$ and alignment error $\boldsymbol{\delta}\mathbf{a}_{LRS}$ are driven by process noise alone, with $E\{\boldsymbol{\eta}_{arw}\boldsymbol{\eta}_{arw}^T\} = \sigma_{arw}^2\mathbf{I}$, $E\{\boldsymbol{\eta}_{rrw}\boldsymbol{\eta}_{rrw}^T\} = \sigma_{rrw}^2\mathbf{I}$, and $E\{\boldsymbol{\eta}_{LRS}\boldsymbol{\eta}_{LRS}^T\} = \sigma_{LRS}^2\mathbf{I}$. The discrete-time process noise matrix for a propagation interval $\Delta t \equiv t_{k+1} - t_k$ is given by

$$\mathbf{Q}_k = \begin{bmatrix} (\sigma_{awn}^2 + \Delta t\sigma_{arw}^2 + (\Delta t^3/3)\sigma_{rrw}^2)\mathbf{I} & (\Delta t^2/2)\sigma_{rrw}^2\mathbf{I} & \\ (\Delta t^2/2)\sigma_{rrw}^2\mathbf{I} & \Delta t\sigma_{rrw}^2\mathbf{I} & \\ & & \Delta t\sigma_{LRS}^2\mathbf{I} \end{bmatrix} \tag{D.2.7}$$

The LRS alignment process noise $\sigma_{LRS}$ is estimated using multiple model adaptive estimation as described in Section 3.3.4.

Simulated gyro unit rate observations are generated by adding measurement errors to the ideal rate time series $\boldsymbol{\omega}_k$, producing an observed rate time series $\boldsymbol{\omega}_{g,k}$. Gyro noise and rate bias are modeled by short term variations and long term trends in the rate error $\boldsymbol{\omega}_{g,k} - \boldsymbol{\omega}_k$. A basic model of the errors is $\boldsymbol{\omega}_{g,k} = \boldsymbol{\omega}_k + \mathbf{b}_k + \boldsymbol{\eta}_{arw}$ where $\boldsymbol{\eta}_{arw}$ is short timescale angular random walk in the gyro output with $E\{\boldsymbol{\eta}_{arw}\boldsymbol{\eta}_{arw}^T\} = \sigma_{arw}^2\mathbf{I}$. Random values $\Delta\mathbf{b}_k$ are added sequentially to the rate bias at each time step $\mathbf{b}_k = \mathbf{b}_{k-1} + \Delta\mathbf{b}_k$ with $E\{\Delta\mathbf{b}_k\Delta\mathbf{b}_k^T\} = \sigma_{\Delta\mathbf{b}}^2\mathbf{I}$. The parameter $\sigma_{\Delta\mathbf{b}}$ loosely characterizes the random walk of $\mathbf{b}_k$.

Gyro unit observation uncertainties are commonly characterized using three parameters: angular white noise $\sigma_{awn}$, angular random walk variance $\sigma_{arw}$, and rate random walk variance $\sigma_{rrw}$. Uncertainties for the ICESat-2 gyro unit are specified by the manufacturer as

$\sigma_{awn} = 1.454\times10^{-8}\,\text{rad/Hz}^{1/2}$, $\sigma_{arw} = 7.272\times10^{-10}\,\text{rad/s}^{1/2}$, and $\sigma_{rrw} = 2.424\times10^{-11}\,\text{rad/s}^{3/2}$. The angular parameters $\sigma_{awn}$ and $\sigma_{arw}$ are associated with short time scales and noise, and the rate parameter $\sigma_{rrw}$ is associated with longer time scales and rate bias. The growth in rate uncertainty is characterized by $\sqrt{t}\sigma_{rrw}$ and this value can be used as the basis for a model of $\Delta\mathbf{b}_k$, resulting in a parameter estimate of $\sigma_{\Delta\mathbf{b}} = 7.6\times10^{-12}\,\text{rad/s}$. However, $\sigma_{rrw}$ does not represent all of the factors involved in overall bias stability.

Another characteristic of the gyro unit specified by the manufacturer is a bias stability of approximately 5 arcseconds/hr $1\sigma$. Monte Carlo simulation is used to find the $\sigma_{\Delta\mathbf{b}}$ that results in an attitude tracking error of approximately 5 arcseconds $1\sigma$ after 1 hour of propagation. A set of $m = 12$ hypothetical $\sigma_{\Delta\mathbf{b}}$ values is tested by using each value for a set of $n = 90$ 1 hour attitude propagation runs, resulting in $mn = 1080$ total runs. The random walk of the rate bias is unique in each run, and the final attitude errors of all 90 runs for a given $\sigma_{\Delta\mathbf{b}}$ value represent its error distribution. The $\sigma_{\Delta\mathbf{b}}$ whose error distribution sigma is closest to 5 arcseconds is the best parameter estimate. Figure D-3 shows the error sigmas for the 12 $\sigma_{\Delta\mathbf{b}}$ values. $\sigma_{\Delta\mathbf{b}} = 8\times10^{-11}\,\text{rad/s}$ results in an attitude tracking error of 5 arcseconds/hr $1\sigma$.

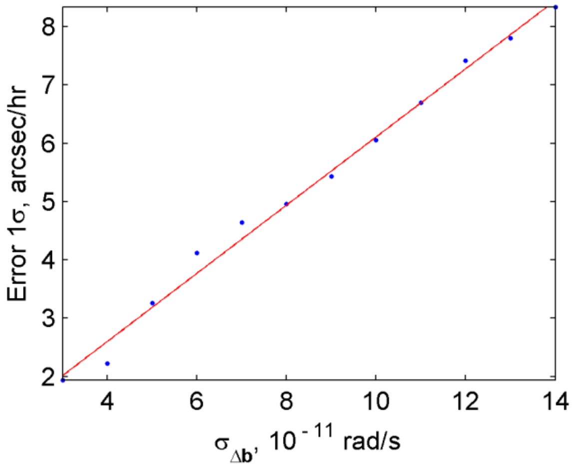

**Fig. D-3 Attitude tracking error per hour of propagation for various $\sigma_{\Delta\mathbf{b}}$ values.**

For filter state propagation, the gyro unit outputs time-tagged angular increments which are used to compute the rate observations $\boldsymbol{\omega}_g$. The filter models the rate as $\boldsymbol{\omega} = \boldsymbol{\omega}_g + \mathbf{b} + \boldsymbol{\eta}_{arw}$ where $d\mathbf{b}/dt = \boldsymbol{\eta}_{rrw}$. The state propagation rotation vector is $\mathbf{a} = \Delta t(\boldsymbol{\omega}_g + \mathbf{b})$ where the time interval is short enough that $\boldsymbol{\omega}_g$ is approximately constant. The discrete-time state transition matrix is given by

$$\mathbf{\Phi}_k = \begin{bmatrix} \mathbf{R}(\mathbf{a}) & \Delta t\mathbf{S}(\mathbf{a}) & \\ \mathbf{0}_{3\times 3} & \mathbf{I}_{3\times 3} & \\ & & \mathbf{I}_{3\times 3} \end{bmatrix} \qquad \text{(D.3.1)}$$

where $\mathbf{R}(\mathbf{a}) = \mathbf{I}\cos a - [\mathbf{a}\times]\sin a/a + \mathbf{aa}^{\mathbf{T}}(1-\cos a)/a^2$ and $\mathbf{S}(\mathbf{a}) = \mathbf{I}\sin a/a - [\mathbf{a}\times](1-\cos a)/a^2 + \mathbf{aa}^{\mathbf{T}}(a-\sin a)/a^3$. The propagated attitude estimate and state are $q_{b,k+1} = q(\mathbf{a}_p)\otimes q_{b,k}$ and $\mathbf{x}_{k+1} = \mathbf{x}_k$ and the propagated covariance is $\mathbf{P}_{k+1} = \mathbf{\Phi}_k\mathbf{P}_k\mathbf{\Phi}_k^T + \mathbf{Q}_k$.

The effective observations from the spacecraft star trackers are quaternions and are used to directly correct the estimated attitude state. Attitude tracking performance depends on the error characteristics of these quaternion observations over all but the shortest time scales, where rate and propagation errors dominate. The attitude observation errors are modeled here as white noise in the quaternions. Simulated attitude observations and attitude updates are discussed here for SST1 and the SST2 case is identical.

Simulated observations for SST1 are given by $q_i^{SST1} = q(\boldsymbol{\eta}_{SST})\otimes q_{ATLAS}^{SST1}\otimes q_i^{ATLAS}$ where $\boldsymbol{\eta}_{SST}$ is a rotation vector representing attitude observation uncertainties $\mathbf{R} = E\{\boldsymbol{\eta}_{SST}\boldsymbol{\eta}_{SST}^T\} = diag([\sigma_{SSTx}^2 \quad \sigma_{SSTy}^2 \quad \sigma_{SSTz}^2])$ and the constant reference alignment for SST1 is $q_{ATLAS}^{SST1}$. The observation uncertainties are specified by the manufacturer as $\sigma_{SSTx} = \sigma_{SSTy} = 1.5$ arcseconds and $\sigma_{SSTz} = 12.2$ arcseconds.

The filter prediction of the SST1 attitude is $q_{ATLAS}^{SST1}\otimes q_i^b$ and the observation residual rotation vector $\Delta\mathbf{y}$ is given by $[\Delta\mathbf{y}^T/2 \quad q_4]^T = q_i^{SST1}\otimes(q_{ATLAS}^{SST1}\otimes q_i^b)^{-1}$. Attitude updates are performed using the observation sensitivity $\mathbf{H} = \begin{bmatrix}\mathbf{A}_{ATLAS}^{SST1} & \mathbf{0} & \mathbf{0}\end{bmatrix}$, Kalman gain $\mathbf{K} = \mathbf{PH}^T(\mathbf{HPH}^T + \mathbf{R})^{-1}$, estimated state correction $\Delta\mathbf{x} = \begin{bmatrix}\Delta\mathbf{a}^T & \Delta\mathbf{b}^T & \Delta\mathbf{a}_{LRS}^T\end{bmatrix}^T = \mathbf{K}\Delta\mathbf{y}$, and covariance update $\mathbf{P}_+ = (\mathbf{I}-\mathbf{KH})\mathbf{P}_-$. The gyro rate bias update is $\mathbf{b}_+ = \mathbf{b}_- + \Delta\mathbf{b}$ and the updated attitude estimate is $q_{b+} = q(\Delta\mathbf{a})\otimes q_{b-}$.

Two angular acceleration cases are used to characterize attitude tracking errors: a baseline case with nadir pointing angular rates and small angular accelerations, and an upper-bound ocean and target scan case with peak accelerations. For each of the two acceleration cases, five uncertainty scaling factors 0.33, 0.5, 1, 2, and 3 are applied to $\mathbf{R}$. These 10 cases are used to characterize the sensitivity of attitude tracking error to both acceleration and observation noise. 50 Monte Carlo simulation runs were performed for each of the 10 cases.

Roll tracking RMS error values are given in the results section (Section D.5). Figure D-4 shows 0.05, 0.25, 0.5, 0.75, and 0.95 quantile breakdowns of the roll tracking error magnitudes. The central dots are the 0.5 quantiles or median values. The left plot is for the nadir pointing case with small angular acceleration, and the right plot is for the peak acceleration case.

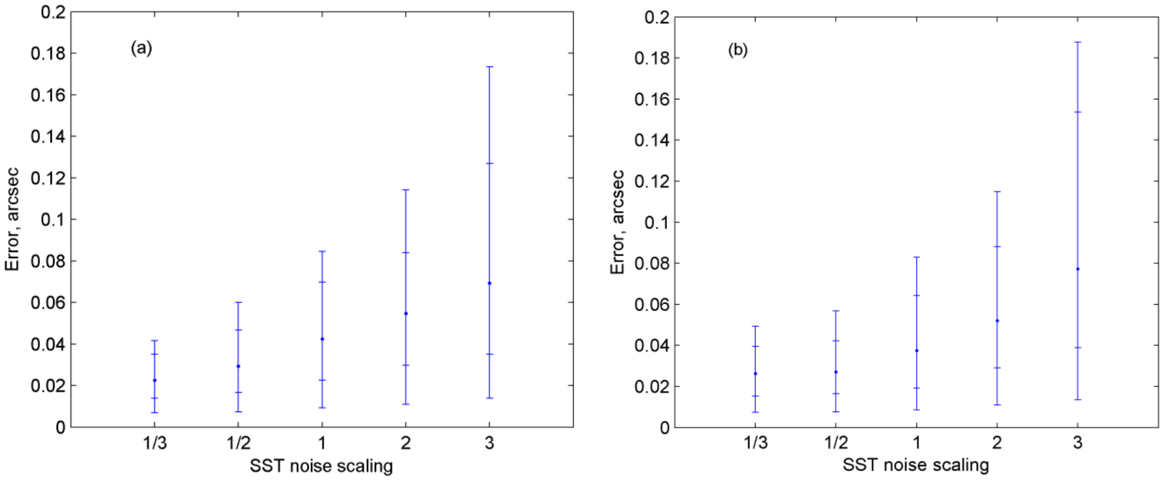

**Fig.D-4 Roll tracking error magnitude distributions for the (a) nadir pointing case and (b) peak acceleration case.**

Figure D-4 shows that, for the baseline observation noise and both acceleration cases, the median roll tracking error magnitude is approximately 0.05 arcseconds. Attitude tracking error magnitudes are similar in both the smaller and larger angular acceleration cases. With ATLAS reference platform attitude tracking errors on the order of 0.05 arcseconds, LRS star observations can be predicted accurately if LRS alignment tracking is also good.

## D.3 LRS Alignment Tracking

All information for LRS alignment tracking comes from star observations, and they are a primary source of alignment tracking errors, along with filter and numerical errors. The most significant issue is the quantity and distribution of observations across the sky; in other words, the sensitivity of the LRS and its ability to track dim stars. If only bright stars are acquired, there are periods without star observations during which the filter does not receive alignment updates and does not track the LRS alignment.

Another significant issue is deterministic errors and noise in the star observations. Deterministic errors such as distortion are corrected within the processor [57, 58, 59]. The effects of noise are reduced by observing more stars $n$, with uncertainty generally scaling by $1/\sqrt{n}$. Low sensitivity reduces $n$ and results in larger uncertainties.

There are also issues with individual stars and their mission catalog records. Normal stars have unbiased observations and catalog records. The exceptions are referred to here as bad stars and become more important as sensitivity decreases [56, 58, 60]. When the sensitivity is low there are more periods when only a single star is being tracked. This makes the filter more sensitive to bad stars since there are fewer normal stars to counteract their effects on filter updates.

The characteristics of the alignment variations can be classed as another source of alignment tracking errors. If the variations are especially complex it is natural to expect tracking errors to be larger. Monte Carlo simulations are performed for two cases here: a baseline sinusoidal motion, and a more complex case from ICESat flight data.

The true LRS attitude is $\mathbf{A}_i^{LRS}(t) = \mathbf{A}(\mathbf{a}_{LRS}(t))\mathbf{A}_{ATLAS}^{LRS}\mathbf{A}_i^{ATLAS}(t)$ and the estimated LRS attitude is $\hat{\mathbf{A}}_i^{LRS}(t) = \mathbf{A}(\hat{\mathbf{a}}_{LRS}(t))\mathbf{A}_{ATLAS}^{LRS}\mathbf{A}_i^{b}(t)$, where $\mathbf{A}_{ATLAS}^{LRS}$ is a constant reference alignment, and $\mathbf{a}_{LRS}(t)$ and $\hat{\mathbf{a}}_{LRS}(t)$ are small rotation vectors representing true and estimated LRS alignments respectively. LRS alignment tracking error is the rotation vector difference $\mathbf{e}(t) = \hat{\mathbf{a}}_{LRS}(t) - \mathbf{a}_{LRS}(t)$. When the attitude tracking error is small so that $\mathbf{A}_i^{ATLAS} \approx \mathbf{A}_i^{b}$, the alignment tracking error is approximately equivalent to the quaternion difference $q(\hat{\mathbf{A}}_i^{LRS}) \otimes q(\mathbf{A}_i^{LRS})^{-1} \approx [\Delta\mathbf{e}^T/2 \quad \mathrm{q}_4]^T$.

Simulated star observations are given by the observation model $\mathbf{y} = \mathbf{h}(\mathbf{u}_{obs}) = \mathbf{h}(\mathbf{A}_i^{LRS}\mathbf{u}_{ref}) + [\Delta h \quad \Delta v]^T + \boldsymbol{\eta}$ where $\mathbf{h}(\mathbf{u}) \equiv [u_1/u_3 \quad u_2/u_3]^T \equiv [h \quad v]^T$ and $\mathbf{u} = [h \ v \ 1]^T / \|[h \ v \ 1]\|$ take advantage of the unit constraint to transform between three-dimensional unit vectors $\mathbf{u}$ and the $h,v$ coordinate plane. The star catalog unit vector $\mathbf{u}_{ref}$ is expressed in the celestial frame. Deterministic errors are represented by $[\Delta h \quad \Delta v]^T$, and $\boldsymbol{\eta}$ is noise with an observation covariance of $\mathbf{R} = E\{\boldsymbol{\eta}\boldsymbol{\eta}^T\} = \sigma_{obs}^2\mathbf{I}_{2\times 2}$.

The observation sensitivity matrix representing the relationship of star observations to filter states is

$$\mathbf{H} = \frac{\partial \mathbf{y}}{\partial \mathbf{x}} = \frac{\partial \mathbf{h}}{\partial \mathbf{u}}\frac{\partial \mathbf{u}}{\partial \mathbf{x}} = \frac{\partial \mathbf{h}}{\partial \mathbf{u}}\begin{bmatrix} \dfrac{\partial \mathbf{u}}{\partial \mathbf{a}} & \mathbf{0} & \dfrac{\partial \mathbf{u}}{\partial \mathbf{a}_{LRS}} \end{bmatrix} \tag{D.5.1}$$

where from $\mathbf{h}(\mathbf{u}) \equiv [u_1/u_3 \quad u_2/u_3]^T$

$$\frac{\partial \mathbf{h}}{\partial \mathbf{u}} = \begin{bmatrix} 1/u_3 & 0 & -u_1/u_3^2 \\ 0 & 1/u_3 & -u_2/u_3^2 \end{bmatrix} \tag{D.5.2}$$

The factors $\partial\mathbf{u}/\partial\mathbf{a}$ and $\partial\mathbf{u}/\partial\mathbf{a}_{LRS}$ represent the sensitivity of star observations to ATLAS attitude and LRS alignment variations. Based on the derivations in Section 3.3. that follows Refs [26, 27],

$$\partial\mathbf{u}/\partial\mathbf{a} = \mathbf{A}_{ATLAS}^{LRS}[\mathbf{A}_i^{ATLAS}(t)\mathbf{u}_{ref}\times] \qquad \text{(D.5.3)}$$

$$\partial\mathbf{u}/\partial\mathbf{a}_{LRS} = [\mathbf{A}_{ATLAS}^{j}\mathbf{A}_i^{ATLAS}(t)\mathbf{u}_{ref}\times] \qquad \text{(D.5.4)}$$

Alignment updates are performed using the Kalman gain $\mathbf{K} = \mathbf{P}\mathbf{H}^T(\mathbf{H}\mathbf{P}\mathbf{H}^T + \mathbf{R})^{-1}$, estimated state correction $\Delta\mathbf{x} = \begin{bmatrix}\Delta\mathbf{a}^T & \Delta\mathbf{b}^T & \Delta\mathbf{a}_{LRS}^T\end{bmatrix}^T = \mathbf{K}\Delta\mathbf{y}$ and covariance update $\mathbf{P}_+ = (\mathbf{I} - \mathbf{K}\mathbf{H})\mathbf{P}_-$. The rate bias update is $\hat{\mathbf{b}}_+ = \hat{\mathbf{b}}_- + \Delta\hat{\mathbf{b}}$, the updated attitude estimate is $q_{b+} = q(\Delta\mathbf{a}) \otimes q_{b-}$, and the updated LRS alignment is $\mathbf{a}_{LRS+} = \mathbf{a}_{LRS-} + \Delta\mathbf{a}_{LRS}$.

The alignment process noise $\sigma_{LRS}$ in Eqs. (D.2.7) is the tuning parameter for alignment tracking and depends on the characteristics of the star observations and the LRS motion. More LRS motion means higher $\sigma_{LRS}$ values. However, as $\sigma_{LRS}$ increases alignment tracking becomes more sensitive to noise and other errors in the star observations. The objective is to find an adequate $\sigma_{LRS}$ for reacting to LRS motion and not reacting to star observation issues and errors. Different star observation characteristics, in particular, different LRS sensitivities, mean different $\sigma_{LRS}$ values. An example to find adequate $\sigma_{LRS}$ is shown in Section 3.3 (Table 2).

LRS alignment variation is expected to be periodic motion repeating with the orbital period of 5,670 seconds. Deviations from the orbital variation due to scan maneuvers are expected to be small but are an important question for more specialized studies. Evolution of the orbital variation is expected on time scales of days and weeks as the beta angle changes.

Two LRS motion cases are used here for Monte Carlo simulation: a baseline sinusoidal motion, and ICESat flight data. The baseline case includes a random initial phase so that the motion peaks at different times in each simulation run. Over a large set of runs, there will be peaks at or near every part of the orbit. The randomly distributed sinusoidal motions build up a map of performance characteristics with respect to the sky (numbers of stars, alignment tracking errors, etc) and provide increasingly uniform coverage as the number of simulation runs increase. The baseline amplitude is 10 arcseconds peak to peak.

ICESat flight data includes directly observed alignment variations that are used here as the basis for a class of realistic non-sinusoidal models [61-63]. On ICESat, the alignment between the LRS and instrument star tracker was directly observed by the LRS when a reference signal linking the LRS and IST coordinate frames was operating [62]. Figure D-5 shows LRS observations of the reference signal motion over one orbit.

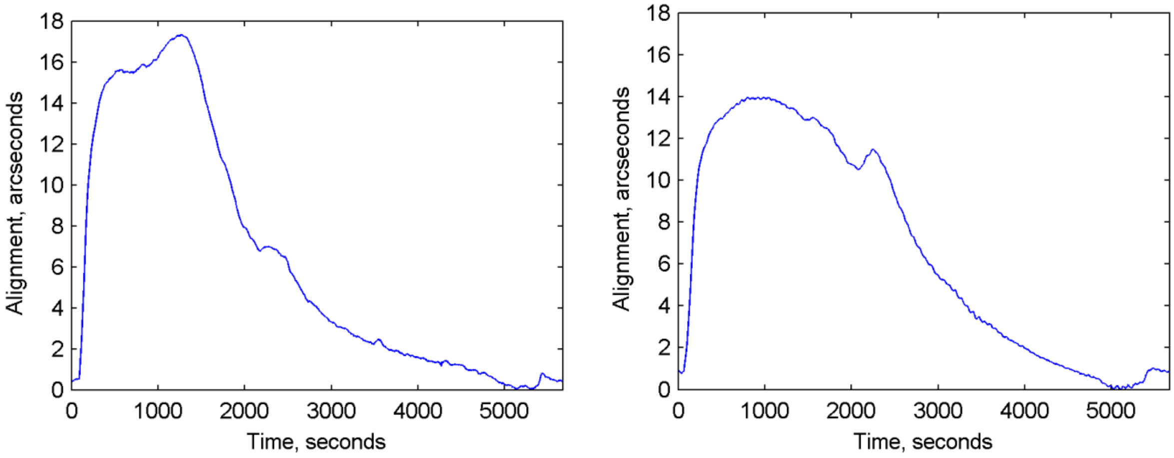

**Fig.D-5 ICESat flight data for LRS alignment orbital variation in (a) roll and (b) pitch.**

The ICESat 5,790 seconds orbital period is scaled to 5,670 seconds for ICESat-2. Because it provides a clear reference point, the jump or step-change due to entering sunlight is used to define $t = 0$ within the simulated orbital variation. In practice, the jump comes at the same phase of successive orbits, but again a random initial phase is used in each simulation run so that the jumps occur throughout the orbit, as for the baseline case.

The peaks in the two alignment cases are viewed as test signals that are input to the processor in order to study the output response. This is particularly true for the sharp jump in the ICESat case since it is close to a step-function. It is treated as a practical proxy for an impulse function for the purposes of driving a full range of processor responses and alignment tracking errors.

## D.4 Alignment Tracking Error

LRS alignment tracking error is a time series of rotation vector differences $\mathbf{e}(t_k) = \hat{\mathbf{a}}_{LRS}(t_k) - \mathbf{a}_{LRS}(t_k)$ between the estimated alignment $\hat{\mathbf{a}}_{LRS}$ and the simulation truth $\mathbf{a}_{LRS}$. By defining the LRS coordinate frame as LRS stellar-side frame the error rotation is expressed in LRS frame roll, pitch, and yaw $\mathbf{e} = [e_x \quad e_y \quad e_z]$. The LRS frame $z$ axis is zenith pointing and the spacecraft body frame $z$ axis is nadir pointing, so expressed in the body frame $\mathbf{e}_b = [e_{bx} \quad -e_{by} \quad -e_{bz}]$. As discussed in Section D.1 the focus here is normally on roll errors $e_k \equiv e_x(t_k)$. Roll and pitch results are similar. Yaw results are on a different scale because star observations are less sensitive to yaw.

A set of $i = 1,...,n$ runs are performed for every Monte Carlo simulation case, with $n$ normally 50 here. The roll error time series for each run $e_k(i)$ is sampled at 10 second intervals $j = 1,...,m$.

Within each 10 second sample $e_k(i,j)$ there are $k=1,...,100$ roll error values, matching the 10 Hz observation frequency. The mean $\mu(i,j) \equiv \sum_{k=1}^{100} e_k(i,j)/100$, and squared RMS $rms(i,j)^2 \equiv \sum_{k=1}^{100} e_k(i,j)^2/100$ are computed for each sample. The standard deviation $\sigma(i,j)^2 = rms(i,j)^2 - \mu(i,j)^2$ is computed as needed. This approach is directed towards computing overall results for sample $j$ from all $n$ Monte Carlo runs. Mean, RMS, and standard deviation values for sample $j$ are given by

$$\mu(j) = \sum_{i=1}^{n} \mu(i,j)/n \tag{D.6.1}$$

$$rms(j)^2 = \sum_{i=1}^{n} rms(i,j)^2/n \tag{D.6.2}$$

$$\sigma(j)^2 = rms(j)^2 - \mu(j)^2 \tag{D.6.3}$$

Results for all samples and all runs are given by

$$\mu = \sum_{j=1}^{m} \sum_{i=1}^{n} \mu(i,j)/mn \tag{D.6.4}$$

$$rms^2 = \sum_{j=1}^{m} \sum_{i=1}^{n} rms(i,j)^2/mn \tag{D.6.5}$$

$$\sigma^2 = rms^2 - \mu^2 \tag{D.6.6}$$

Time series of $rms(j)$ values for $n$ runs are a useful performance measure as demonstrated for one orbital period $j=1,...,567$ (5,670 seconds) in Figure D-6 to Figure D-8. The Monte Carlo simulation case here is the baseline sinusoidal alignment variation and LRS sensitivity 5.2. The plots on the left show $rms(i,j)$ for all $n=50$ runs, and the plots on the right show $rms(j)$. Figure D-6 to Figure D-8 show roll, pitch, and yaw respectively to demonstrate the similarity of roll and pitch and the difference of yaw. The overall RMS values calculated using Eq. (D.6.5) are roll 0.34 arcseconds, pitch 0.37 arcseconds, and yaw 3.04 arcseconds.

The broad distributions of results in the left-hand plots of $rms(i,j)$ reflect the random phases of the baseline sinusoidal alignment variations, making the results in each of the 50 runs differ significantly. The right-hand plots of $rms(j)$ is a cumulative result that reduces the effects of individual runs. In the limit as $n$ grows very large the $rms(j)$ plots show results that are effectively independent of individual runs.

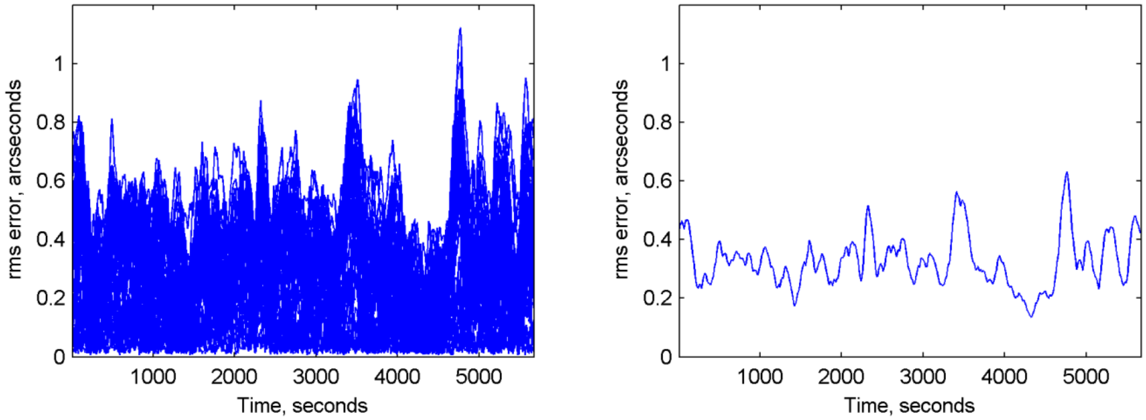

**Fig.D-6 Roll RMS errors for (a) each of 50 runs and (b) all 50 runs together.**

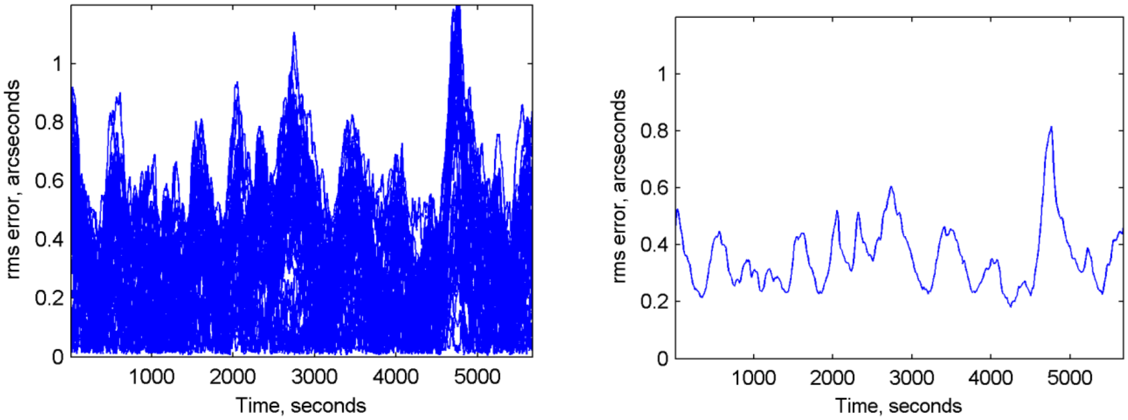

**Fig.D-7 Pitch RMS errors for (a) each of 50 runs and (b) all 50 runs together.**

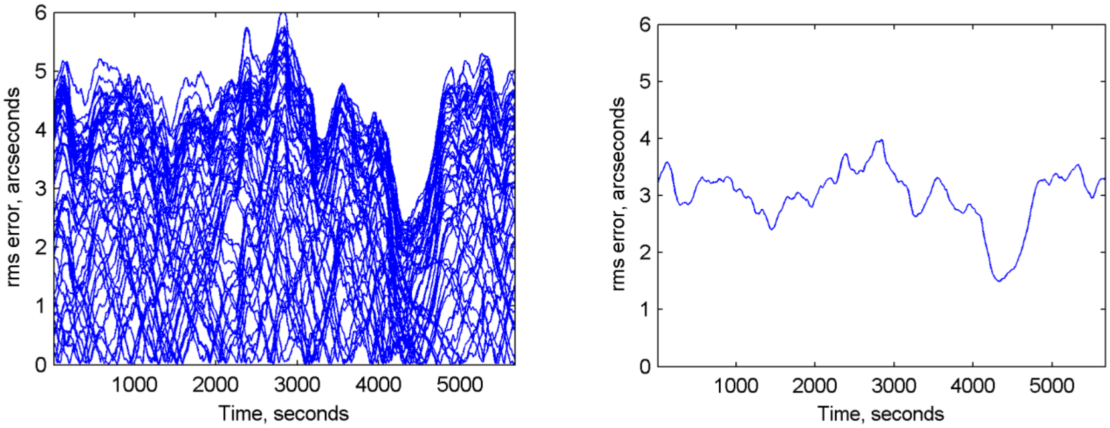

**Fig.D-8 Yaw RMS errors for (a) each of 50 runs and (b) all 50 runs together.**

Two features are apparent in Figure D-6 to Figure D-8. Beginning at 4,000 seconds the tracking errors decrease, followed immediately by an increase before 5,000 seconds. Figure D-9 shows the numbers of observed stars. The drop corresponds to a peak in the number of observed stars as the LRS line of sight passes through the Milky Way, and the increase corresponds to a star gap in which counts drop to 0 or 1. LRS sensitivity is 5.2 in this simulation. For lower sensitivities, the star peak is smaller and the star gap is larger.

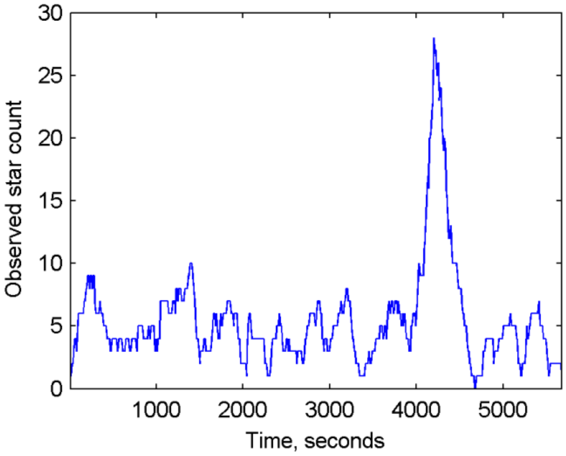

**Fig.D-9 Star counts for LRS sensitivity 5.2.**

Figure D-6 to Figure D-9 demonstrate the significance of observed star counts and therefore of LRS sensitivity. Star counts can be predicted using a star catalog and a model of LRS sensitivity; however, star counts alone provide no information about alignment and attitude tracking performance. Monte Carlo simulation simultaneously provides information about tracking performance (Figure D-6 to Figure D-8) and star counts (Figure D-9). It also provides detailed information about special cases such as long star gaps and the conditions under which near-neighbor stars are observed. Star gaps are directly characterized by the RMS tracking error time series. Over many simulation runs the randomly phased alignment variations act as test signals which produce output signals during star gaps. An analogy is searching for holes on a surface. Searching the surface spatially point-by-point is analogous to using a star catalog. Putting a light behind the surface is analogous to using tracking errors.

Near-neighbor stars are cases where the mission catalog record is a center of light prediction for two or more real stars. Figure D-10 shows a case which is important in the results section. The predicted center of light is at the origin, Skymap 7080327 is bright and near the center of light, and Skymap 7080200 is to the upper left. The radii of the circles are scaled to represent predicted instrument magnitude for the center of light and visual magnitude for the stars. Near-neighbors are identified here by the brightest member, so, for example, the case shown in Figure D-10 is referred to as Skymap 7080327.

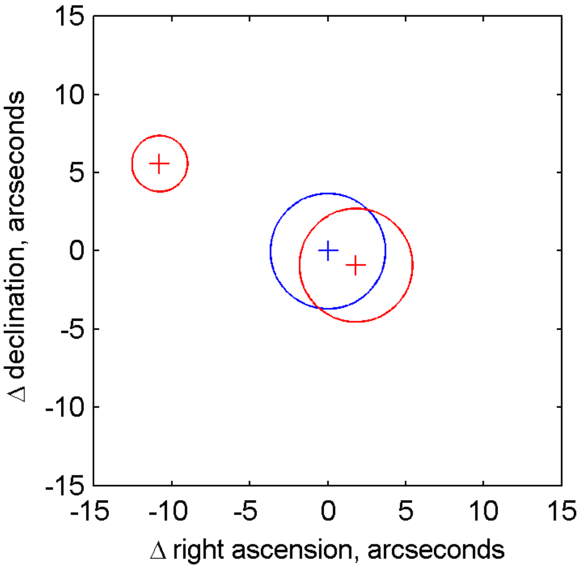

**Fig.D-10 Near-neighbor star Skymap 7080327.**

Near-neighbor stars are potential bad stars [56, 58, 60]. Center of light prediction depends on the LRS sensitivity and response to the brightness and color of each member star, as well as spatial geometry [57]. The detailed conditions in which a near-neighbor star is observed are also significant. If twenty stars are being observed, a small error in the center of light prediction for one near-neighbor star has little effect on the filter. If the near-neighbor star is the only star being observed, an error in the center of light prediction can propagate directly into the state estimate, as demonstrated below.

## D.5 Results

The overall uncertainty in LRS pointing knowledge is $\sigma_{LRS}^2 = \sigma_{ATLAS}^2 + \sigma_{aLRS}^2$ where $\sigma_{ATLAS}$ is reference platform attitude uncertainty and $\sigma_{aLRS}$ is LRS alignment uncertainty. LRS pointing refers here to roll, pitch, and the direction of the LRS line of sight in the celestial frame. Results for RMS attitude tracking errors are shown in Table D-1 and are used as an estimate of $\sigma_{ATLAS}$. The baseline value for reference platform attitude uncertainty adopted here is $\sigma_{ATLAS} = 0.06$ arcseconds.

**Table D-1 Reference platform RMS attitude tracking errors, arcseconds**

| Noise scaling | Nadir pointing | Peak acceleration |
|---|---|---|
| 0.33 | .03 | .03 |
| 0.5 | .04 | .04 |
| 1 | .06 | .05 |
| 2 | .1 | .08 |
| 3 | .15 | .13 |

Results for $\sigma_{aLRS}$ are based on a set Monte Carlo simulations in which the LRS views the full sky. The orbit inclination of $94^\circ$ means that the great-circle strip of sky observed by the LRS always includes the north and south celestial poles. Varying the RA of the ascending node $\alpha$ from $0^\circ$ to $180^\circ$ in $10^\circ$ steps $\alpha = 0^\circ, 10^\circ, \ldots, 170^\circ$ gives full sky coverage, with the ascending passes sweeping over half of the sky and the descending passes sweeping over the other half. Many of the results discussed here are for these 18 orbits, often with the addition of $\alpha = 180^\circ$ for comparison with $\alpha = 0^\circ$ and verification of periodic patterns in the results.

Figure D-11 summarizes roll axis results for the baseline LRS motion case. The left plot shows the number of star observations per orbit as a function of $\alpha$ and LRS sensitivity. The number of star observations is smallest for orbits near $\alpha = 0^\circ$ and largest near $\alpha = 90^\circ$. The right plot shows

$median(\sigma(j))$ (Eq. D.6.3) for roll over 50 simulation runs at each $\alpha$ and LRS sensitivity. The expected inverse relationship between sensitivity in the left plot and tracking performance in the right plot is clear.

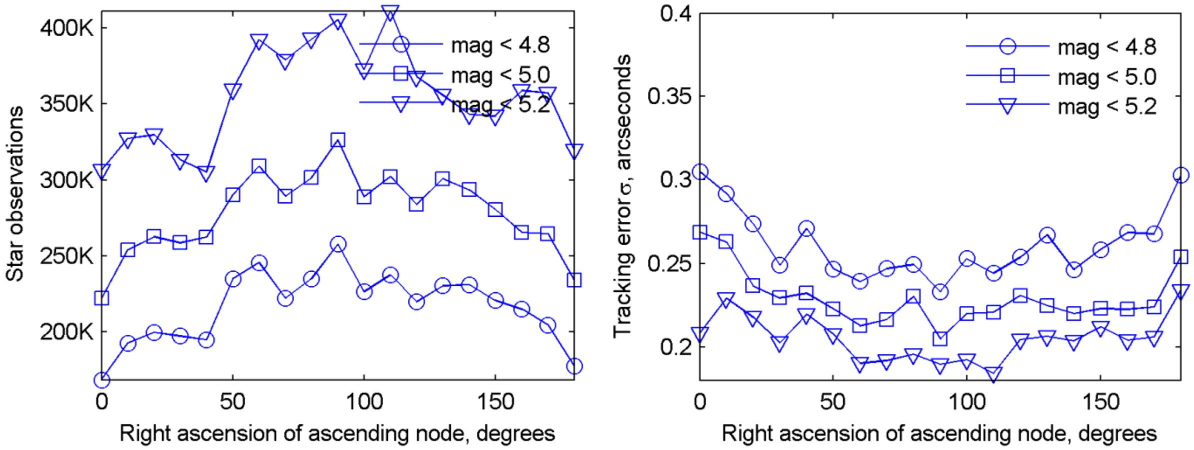

**Fig.D-11 Relationship of LRS sensitivity (left) and roll tracking error $median(\sigma(j))$ (right).**

Figure D-12 shows overall RMS (Eq. D.6.5) for roll over the same 50 runs as Figure D-11. The values in Figure D-12 are correlated with the $median(\sigma(j))$ values in Figure D-11 since the errors are approximately zero-mean with $rms(j) \approx \sigma(j)$. However, the RMS values are more sensitive to certain events than the $median(\sigma(j))$ values. The spike at $\alpha = 80^\circ$ is discussed in more detail below.

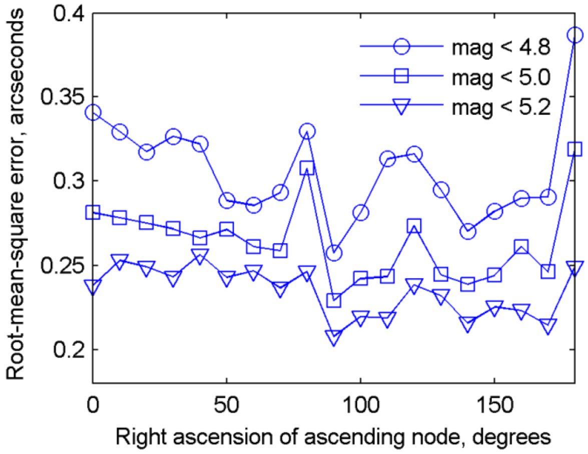

**Fig.D-12 RMS roll tracking error.**

Table D-2 gives the RMS roll tracking errors for both LRS motion cases, with the baseline case to the left and the ICESat flight data case to the right. As in Figure D-12, each RMS is computed from $50 \times 5670 \times 10 = 2.8 \times 10^6$ error values.

**Table D-2 RMS roll tracking error, arcseconds**

| | Baseline | | | ICESat | | |
|---|---|---|---|---|---|---|
| Node | 4.8 | 5 | 5.2 | 4.8 | 5 | 5.2 |
| 0 | 0.34 | 0.28 | 0.24 | 0.40 | 0.34 | 0.29 |
| 10 | 0.33 | 0.28 | 0.25 | 0.40 | 0.33 | 0.31 |
| 20 | 0.32 | 0.28 | 0.25 | 0.36 | 0.33 | 0.31 |
| 30 | 0.33 | 0.27 | 0.24 | 0.40 | 0.32 | 0.32 |
| 40 | 0.32 | 0.27 | 0.26 | 0.40 | 0.32 | 0.31 |
| 50 | 0.29 | 0.27 | 0.24 | 0.34 | 0.32 | 0.28 |
| 60 | 0.29 | 0.26 | 0.25 | 0.36 | 0.32 | 0.27 |
| 70 | 0.29 | 0.26 | 0.24 | 0.38 | 0.33 | 0.28 |
| 80 | 0.33 | 0.31 | 0.25 | 0.38 | 0.35 | 0.34 |
| 90 | 0.26 | 0.23 | 0.21 | 0.30 | 0.27 | 0.26 |
| 100 | 0.28 | 0.24 | 0.22 | 0.33 | 0.30 | 0.28 |
| 110 | 0.31 | 0.24 | 0.22 | 0.38 | 0.30 | 0.26 |
| 120 | 0.32 | 0.27 | 0.24 | 0.38 | 0.32 | 0.29 |
| 130 | 0.29 | 0.24 | 0.23 | 0.35 | 0.30 | 0.32 |
| 140 | 0.27 | 0.24 | 0.22 | 0.32 | 0.28 | 0.27 |

| | | | | | | |
|---|---|---|---|---|---|---|
| 150 | 0.28 | 0.24 | 0.23 | 0.33 | 0.31 | 0.28 |
| 160 | 0.29 | 0.26 | 0.22 | 0.36 | 0.33 | 0.26 |
| 170 | 0.29 | 0.25 | 0.21 | 0.34 | 0.30 | 0.26 |
| 180 | 0.39 | 0.32 | 0.25 | 0.42 | 0.39 | 0.30 |

Table D-3 characterizes overall LRS pointing knowledge uncertainty. It shows LRS pointing uncertainties $\sigma_{LRS} = (\sigma^2_{ATLAS} + \sigma^2_{aLRS})^{1/2}$ for the three LRS sensitivities, both motion cases, and three scalings (0.5, 1, 1.5) of the motion amplitudes.

**Table D-3 LRS pointing knowledge, arcseconds**

| LRS motion | Baseline | | | ICESat | | |
|---|---|---|---|---|---|---|
| scaling | 4.8 | 5 | 5.2 | 4.8 | 5 | 5.2 |
| 0.5 | 0.15 | 0.13 | 0.12 | 0.21 | 0.17 | 0.15 |
| 1.0 | 0.31 | 0.27 | 0.24 | 0.36 | 0.32 | 0.29 |
| 1.5 | 0.41 | 0.35 | 0.33 | 0.54 | 0.47 | 0.42 |

These results are for random phasing of the LRS motion during the simulation runs. The random phasing in effect puts equal weight on each region of the sky. This normalizes the results for comparison, but means that they are a type of upper-bound uncertainty estimate. In flight telemetry, the phasing of the LRS motion is approximately constant from one orbit to the next, not random.

Baseline uncertainty estimates such as $\sigma_{LRS} = 0.27$ arcseconds (Table D-3) characterize performance over the full sky. Local performance varies significantly, particularly in regions where there are fewer stars than normal. The RMS roll tracking error in Figure D-12 demonstrates a significant localized interaction between the star observations and alignment tracking errors in the spike at $\alpha = 80^\circ$.

Figure D-13 shows star count and RMS roll tracking error time series for the orbit at $\alpha = 80^\circ$. The 50 Monte Carlo runs use the baseline LRS motion case. The gap in star observations and resulting spike in tracking errors near 4,800 seconds is the source of the upward spike in Figure D-12. The results for the three LRS sensitivity cases 4.8, 5.0, and 5.2 are plotted together as three time series. The time series with fewer star observations and larger tracking errors is the sensitivity 4.8 case.

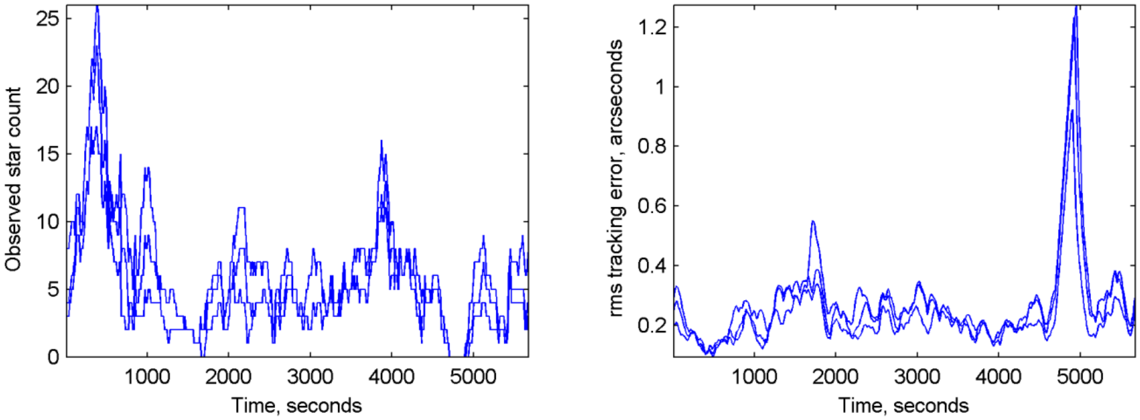

**Fig.D-13 Node 80° star observation counts (left) and RMS roll tracking errors (right).**

These time series represent a one-dimensional slice or sample of the full sky. If they are laid vertically side-by-side with similar time series for other ascending nodes, two-dimensional maps of the sky are built up, with the ascending node on the horizontal axis and time on the vertical axis. These sky maps are generated here by performing 50 Monte Carlo runs at each integer orbit node from 0° to 359°, with 10 second subsampling of each run. The resulting maps consist of a grid of $567 \times 360$ cells. The results from 180° to 359° are mostly redundant with the results from 0° to 179°, but there are small geometric differences between ascending and descending passes in a given region of the sky.

Figure D-14 to Figure D-16 show star observation counts and RMS roll tracking errors for the baseline LRS motion case and LRS sensitivities 4.8, 5.0, and 5.2. Results for each integer node from 0° to 180° are plotted. Node number forms the horizontal axis, from node 0° at the origin to node 180° on the right. The vertical axis is time with $t = 0$ seconds at the origin and 5,670 seconds at the top. At a given node, ascending from the horizontal axis to the top of the plot traverses the same type of time series as in Figure D-13. The spacecraft is passing through the ascending node at $t = 0$ seconds and the horizontal axis corresponds to declination 0°. At the top of the plot the spacecraft has returned to declination 0° by completing an orbit after passing the North Pole at $t = 1417$ seconds, the descending node at $t = 2834$ seconds, and the South Pole at $t = 4251$ seconds.

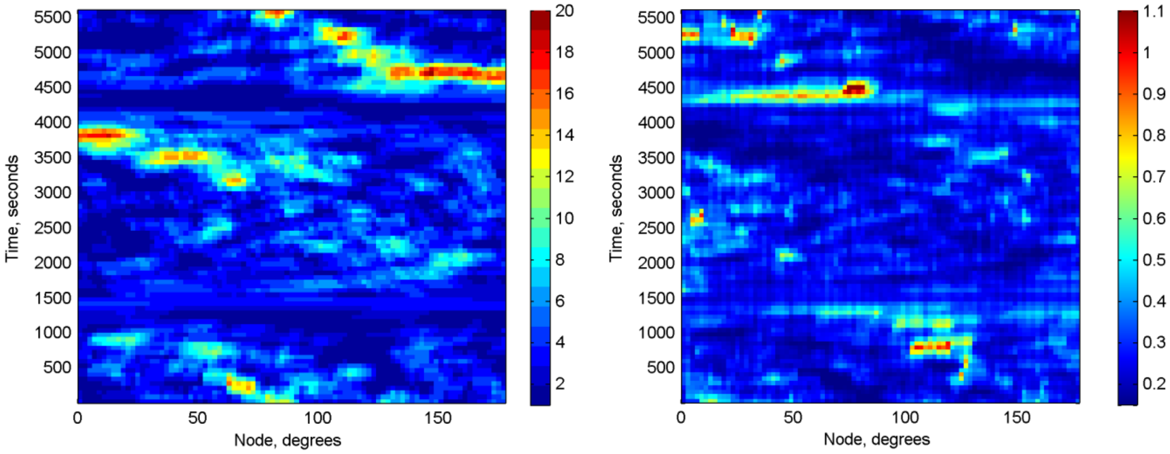

**Fig.D-14 LRS sensitivity 4.8 star counts (left) and RMS roll tracking errors in arcseconds (right).**

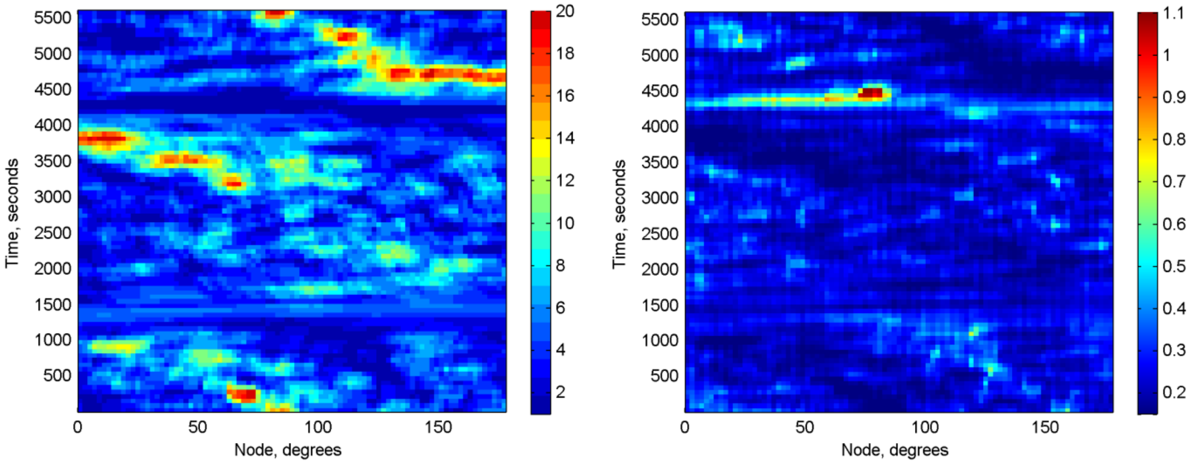

**Fig.D-15 LRS sensitivity 5.0 star counts (left) and RMS roll tracking errors in arcseconds (right).**

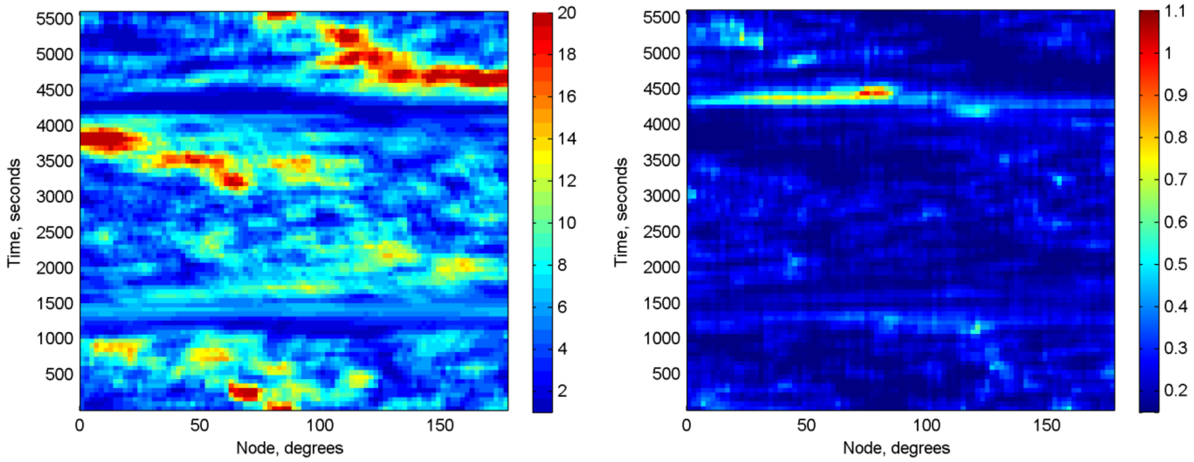

**Fig.D-16 LRS sensitivity 5.2 star counts (left) and RMS roll tracking errors in arcseconds (right).**

The $567 \times 360 = 204{,}120$ cells of the sky maps are used to characterize the overall abundances of star gaps and near-neighbor stars. Each cell represents 10 seconds of time and, so the cells are all equivalent for the purposes of determining how much time the LRS spends in star gaps or observing near-neighbor stars, despite the variable spatial overlap of adjacent cells. The cells have more spatial overlap on the sky at the celestial poles and less overlap at the celestial equator. Near the poles the cells from every orbit cover the same small region of the sky; they are similar to a set of rotated but essentially overlapping LRS fields of view. Table D-4 shows overall characteristics of the sky for the three LRS sensitivities.

Cells containing only a near-neighbor star are relatively rare and dominated by a handful of near-neighbors. This is significant because these are cases where biased center-of-light position predictions and bad stars are most problematic. In other words, only a handful of near-neighbor stars are potentially significant problems. Important examples are shown in Table D-5. Near-neighbor stars are identified here by the Skymap number of the brightest member star.

**Table D-4 Sky characteristics for maps with 204,120 cells**

| | Sensitivity | | |
|---|---|---|---|
| | 4.8 | 5.0 | 5.2 |
| Number of unique stars | 1,083 | 1,385 | 1,750 |
| Number of unique near-neighbor stars | 99 | 114 | 146 |
| Cells with no stars | 8,210 | 4,084 | 3,474 |
| Percentage of cells with no stars | 0.04 | 0.02 | 0.017 |
| Cells with a near-neighbor star | 53,214 | 61,632 | 78,666 |
| Percentage of cells with near-neighbor stars | 0.26 | 0.30 | 0.38 |
| Cells containing only near-neighbor stars | 918 | 481 | 246 |

**Table D-5 Counts of cells containing only a near-neighbor star**

| Sensitivity 4.8 | | Sensitivity 5.0 | | Sensitivity 5.2 | |
|---|---|---|---|---|---|
| Skymap id | Cells | Skymap id | Cells | Skymap id | Cells |
| 8460162 | 249 | 8460162 | 149 | 8460162 | 89 |
| 18560046 | 133 | 18560046 | 73 | 18560046 | 45 |
| 7080327 | 78 | 7080327 | 52 | 7080327 | 33 |
| 15340134 | 45 | 15340134 | 45 | 15340134 | 8 |
| 12560007 | 175 | 12560007 | 4 | - | - |
| 14410169 | 58 | 14410169 | 3 | - | - |
| - | - | 2590026 | 51 | 2590026 | 49 |
| - | - | 8120049 | 23 | 8120049 | 10 |

The tracking error maps for all three LRS sensitivities have a significant feature in common: a peak near node 80° and $t = 4500$ seconds caused by a region of the sky at RA 88° and declination -80° without observable stars, referred to here as a star gap. What makes this gap special is its duration in time for orbits with nodes between approximately 75° and 85°. Figure D-17 shows that, due to geometry, for these orbits the gap is approximately 250 seconds long due. The shape of the gap on the sky coincides with the direction that the spacecraft is traveling. Figure D-17 also shows a dot pattern indicating where the LRS is observing the near-neighbor star Skymap 7080327. For nodes between approximately 80° and 85°, it is the only observable star as the spacecraft leaves the gap.

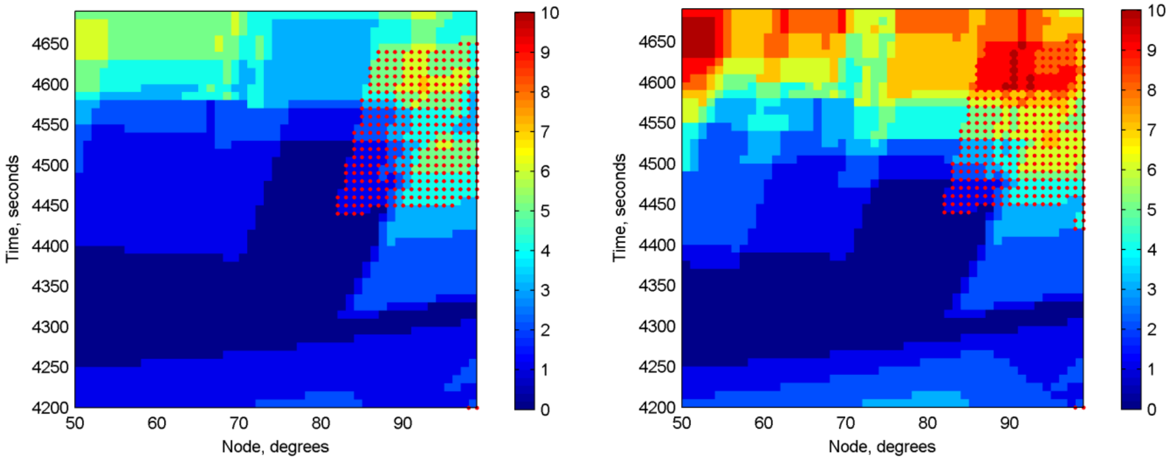

**Fig.D-17 Expanded view of star gap for LRS sensitivities 4.8 (left) and 5.2 (right).**

High resolution full-sky maps confirm that the situation in Figure D-17 is unusual both because of the size of the star gap and the adjacent isolated near-neighbor star. This situation is a good test case for studying the effects of both star gaps and problematic near-neighbor stars.

Figure D-18 shows the effects of near-neighbor stars with biased center-of-light position predictions (bad stars) on RMS alignment tracking error. The left plot in Figure D-18 shows the counts of observed stars near the star gap for orbit node 82° and LRS sensitivity 4.8. The star observed immediately after the main part of the gap, from 4,340 seconds to 4,500 seconds, is the isolated near-neighbor star Skymap 7080327. Another near-neighbor star is observed shortly before the gap, from 3,980 seconds to 4,170 seconds. The two near-neighbor stars are identified here by their brightest members: Skymap 7080327 and Skymap 16200091 respectively.

The right plot shows simulation results for three cases: a baseline case and two bad star cases. In the baseline case, both near-neighbor stars have unbiased center-of-light position predictions. In the two bad star cases, the center-of-light positions are both biased with a position offset of 1 arcsecond or 2 arcseconds. Each RMS tracking error time series combines the results from 50 simulation runs.

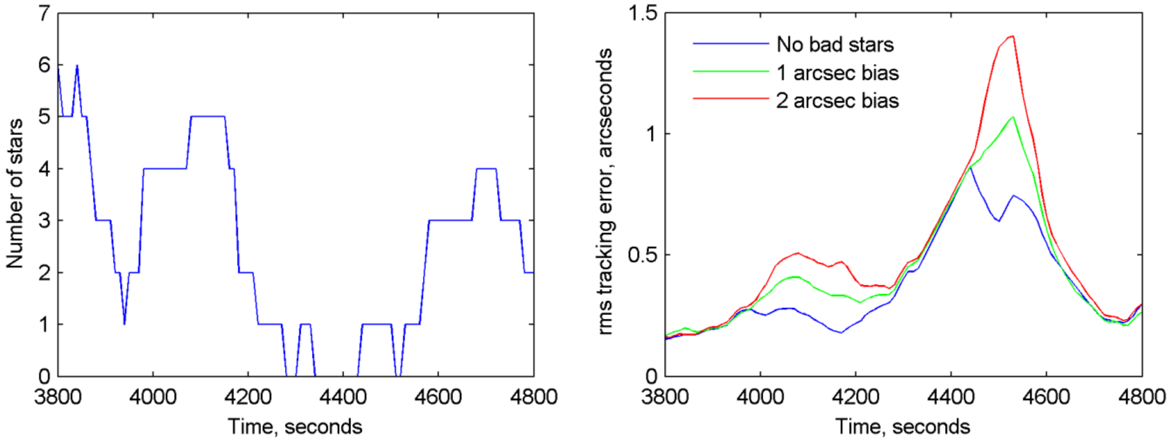

**Fig.D-18 Roll tracking error with bad stars near the star gap.**

Before the star gap, the effect of center-of-light bias for Skymap 16200091 is reduced by the filter updates from the other stars being observed simultaneously. In the star gap, however, the full effect of the bias for Skymap 7080327 is added to the previously accumulated effects of the gap.